Seismic velocity and elastic properties of plate boundary faults

by

Tamara N. Jeppson

A dissertation in partial fulfillment of

the requirements of the degree of

Doctor of Philosophy

(Geophysics)

at the

UNIVERSITY OF WISCONSIN-MADISON

2017

Date of final oral examination: 07/27/2017

The dissertation is approved by the following members of the Final Oral Committee:

Harold J. Tobin, Professor, Geoscience
Laurel B. Goodwin, Professor, Geoscience
Hiroki Sone, Assistant Professor, Geological Engineering
Clifford H. Thurber, Professor, Geoscience
Lucas Zoet, Assistant Professor, Geoscience

Abstract

The elastic properties of fault zone rock at depth play a key role in rupture nucleation, propagation, and the magnitude of fault slip. Materials that lie within major plate boundary fault zones often have very different material properties than standard crustal rock values. In order to understand the mechanics of faulting at plate boundaries, we need to both measure these properties and understand how they govern the behavior of different types of faults. Mature fault zones tend to be identified in large-scale geophysical field studies as zones with low seismic velocity and/or electrical resistivity. These anomalous properties are related to two important mechanisms: (1) mechanical or diagenetic alteration of the rock materials and/or (2) pore fluid pressure and stress effects. However, in remotely-sensed and large-length-scale data it is difficult to determine which of these mechanisms are affecting the measured properties. The objective of this dissertation research is to characterize the seismic velocity and elastic properties of fault zone rocks at a range of scales, with a focus on understanding why the fault zone properties are different from those of the surrounding rock and the potential effects on earthquake rupture and fault slip. To do this I performed ultrasonic velocity experiments under elevated pressure conditions on drill core and outcrops samples from three plate boundary fault zones: the San Andreas Fault, California, USA; the Alpine Fault, South Island, New Zealand; and the Japan Trench megathrust, Japan. Additionally, I compared laboratory measurements to sonic log and large-scale seismic data to examine the scale-dependence of the measured properties.

I conducted ultrasonic wavespeed measurements on drill core samples from the San Andreas Fault Observatory at Depth (SAFOD) and compared these measurements to sonic logs acquired in the borehole. This comparison showed that the properties of the structural core of the San Andreas Fault are scale independent, indicating that the fault core has intrinsically low velocity, even if no anomalous pore pressure is assumed, due to alteration and mechanical damage. In

contrast, laboratory average P- and S-wave velocities for the surrounding damage zone are up to 41% greater than the sonic log. This scale dependence and other observations indicate that macro-scale features dominate the damage zone's acoustic properties. Because no pressure anomaly was detected while drilling the SAFOD borehole, I infer that damage at a scale larger than core samples controls the elastic properties of the broader damage zone. Overall a ~40% reduction in velocity of the brittle fault rock relative to intact host rock is observed at lab, log, and field-scales.

Using outcrop and drill core samples from the Deep Fault Drilling Project, I measured ultrasonic wavespeeds to examine the properties of the Alpine Fault. I compared these measurements to borehole sonic logs to show that lab measurements on both drill core and outcrop samples are good proxies for measurements on *in situ* rocks. As with data from the San Andreas Fault, I observed a ~40% velocity reduction in the brittle fault rock relative to the surrounding host rock. Additionally I observed that the hanging wall host rock had high seismic anisotropy while the fault core was mostly isotropic. Based on examination of the rocks I determined that the reduction in velocity and anisotropy was due to an increase in clay alteration and micro-scale brittle deformational features. The brittle fault rock properties measured at both the Alpine and San Andreas Faults are similar, suggesting that large faults may evolve to have similar properties despite different protoliths.

Drill core samples from the Japan Trench were collected during Integrated Ocean Drilling Program Expedition 343. I acquired these samples from the frontal accretionary prism where large-magnitude shallow coseismic slip was observed during the 11 March 2011 (M_w 9.0) Tohoku-Oki earthquake. Laboratory ultrasonic wavespeed measurements on the drill core samples show that the sedimentary materials that compose the prism are very compliant, with a

shear modulus of 1.0-2.3 GPa. I compared my measurements from the Japan Trench to values from analogous shallow subduction zone drill core samples from other locations. I found that shallow subduction zone sediments in general have much lower rigidity than is commonly used in earthquake rupture simulation models. Using laboratory, log, and wide-angle seismic refraction data I developed a cross sectional model of elastic property variations in the Japan Trench.

The data in this dissertation provide the most comprehensive characterization of the seismic velocities and elastic properties of fault zone rocks currently available. My work shows that fault zone rocks at mature plate boundary faults tend to be significantly more compliant than surrounding crustal rocks and quantifies that relationship. The results of this study are particularly relevant to the interpretation of field-scale seismic datasets at major fault zones. Additionally, the results of this study provide constraints on elastic properties used in dynamic rupture models. These models can then be used to analyze how compliant fault materials will affect fault slip and ground motion, thus improving estimates of seismic and tsunami hazard.

Acknowledgements

First and foremost, I would like to acknowledge my Ph.D. advisor, Dr. Harold J. Tobin, for being my mentor. Thank you for giving me the opportunity to learn and work in a great environment and also providing many opportunities to get out of the lab and work in the field. I am grateful for your encouragement and continual support.

I am also grateful to the members of my committee, Dr. Laurel B. Goodwin, Dr. Hiroki Sone, Dr. Clifford H. Thurber, and Dr. Lucas Zoet for their interest in my work and willingness to provide comments and suggestion to help me improve my research.

Participating in IODP and ICDP drilling projects has been a big part of my time at the University of Wisconsin – Madison and my acknowledgments would not be complete without thanking all the people who have been involved in those projects and allowed me to be involved as well. You have all taught me so much about drilling, the many areas of geology, and how to collaborate. I am grateful for the many great scientific discussions we have had, the encouragement you have given, and the great experiences I have enjoyed.

Of the many friends and colleagues at Wisconsin who have helped me survive graduate school there are three who deserve special mention. I cannot fully express here how much I owe to my officemate and friend, Susanna Webb, who has shared ideas, suffered through many practice talks and freak out moments, and helped me stay sane. I cannot image grad school and Wisconsin without you so it's probably a good thing we are going to be in Texas together. I also want to thank Jonathan Graham III for helping me with lab work, sample prep, and XRD

analysis. I don’t think I could have gotten it all done without you. I owe a lot of thanks to JoAnn Tudge for teaching me a lot about well log analysis, helping me to learn Geolog, and answering many questions.

I would be remiss if I did not also acknowledge my undergraduate advisor at Utah State University, James Evans, as well. Thank you so much, Jim, for giving me so many opportunities to learn, for providing many opportunities to get involved in scientific research, and preparing me for grad school. I thank you for sharing your extensive knowledge and scientific insights with me. Most of all I thank you for encouraging me and for supporting an undergrad who had no idea what she was doing most of the time. I don’t know where I would be without your support.

Last, but by no means least, I would like to acknowledge my family. Mom and Dad, thank you for supporting me even when you had no idea what I was doing out here, for teaching me to working hard, and encouraging me to keep going. Thanks for believing in me.

Table of Contents

List of Figures

List of Tables

1 Introduction

Geophysically sensed physical properties of rock depend on intrinsic material properties, brittle damage, and *in situ* conditions. Due to fault zone processes, the physical properties of the rocks surrounding faults are commonly altered. This allows fault zones to be distinguished from the surrounding unaltered host rock by geophysical studies. In field-scale geophysical studies fault zones are commonly detected as low velocity zones. However, there is a need to quantitatively calibrate these large-scale studies with laboratory measurements to determine the properties and conditions that cause the remotely observed geophysical signatures. This correlation is needed to better assess fault mechanics, and ultimately earthquake hazard, and to link observations with physical process.

Measurements of elastic wavespeed can be especially useful for studying fault zones as wavespeed measurements can be conducted over a range of frequencies (seismic, sonic, ultrasonic), which allows the elastic properties of the fault zone to be examined at different scales. By comparing measurements made at multiple frequencies and examining the scale-dependence, inferences can be made about the causes behind the observed velocity variations. Furthermore the measured compressional and shear wavespeed and derived elastic moduli can be used as proxies for strength, other material properties, and fluid content.

1.1 Dissertation content

This dissertation focuses on the multi-scale analysis of fault zone physical properties at depth using wavespeed measurements from borehole logs and laboratory work with comparison to larger-scale seismic studies. The principal aims of this study are to: (1) determine fault zone velocity structure at several scales, (2) determine how geophysical observations are linked to intrinsic material properties and/or *in situ* stress conditions, (3) study the evolution of fault zone

physical properties from host rock to fault core, and (4) address whether physical property values used in earthquake models are applicable to real fault zones. The samples and data used in this study came from three plate boundary fault zones: the San Andreas Fault (SAF), California, USA; the Alpine Fault, South Island, New Zealand; and the Japan Trench megathrust, Japan.

Most of the chapters in this dissertation were prepared as manuscripts for journal publication (excluding this chapter) and, as such, can be read in isolation. However, preparing the chapters in this manner has led to some duplication within the dissertation, particularly in the introduction and methods sections.

Chapter 2 is a study of borehole sonic log data and laboratory ultrasonic velocity measurement of drill core samples acquired as part of the San Andreas Fault Observatory at Depth project. Due to the limited amount of core material available, many of the laboratory measurements were acquired by the Pennsylvania State University Rock Mechanics Group in conjunction with permeability experiments they were performing (members of the Pennsylvania State group are not listed as coauthors on this project because they only acquired the raw waveform data during their experiments and did not assist with processing or interpretation). *In situ* measurements of wavespeed define a low velocity zone associated with the fault. The laboratory measurements showed that the elastic properties of the damage zone are scale dependent whereas measurements on samples from the fault core are scale independent. It is inferred that damage at a scale larger than core samples controls the elastic properties of the broader damage zone, while the fault core is intrinsically low velocity due to alteration and small-scale mechanical damage. This chapter was published in 2015 in the *Journal of Geophysical Research: Solid Earth*.

Chapters 3 and 4 focus on the data from the Deep Fault Drilling Project (DFDP). The goal of DFDP was to penetrate the Alpine Fault at depth and acquire borehole logs and core samples across the fault. This goal was not achieved, as the borehole was terminated before the fault was reached and core samples were not obtained. As a result, the analysis of well log data presented in chapter 3 is much smaller than originally planned and drill core samples from an initial, shallow borehole were supplemented with an extensive suite of outcrop samples for the laboratory analysis presented in chapter 4.

Chapter 3 documents work done to process the sonic log data acquired in the host rock of the Alpine Fault, South Island, New Zealand during the second phase of DFDP and presents sonic log results. Borehole conditions and tool complications led to problems in the data so that the initial auto-picked slowness log was unusable. I used slowness-time semblance processing methods to improve data quality and pick a more robust slowness log. Analysis of the sonic log indicates that the elastic properties of the hanging wall host rock are relatively homogenous and are consistent with previously measured laboratory ultrasonic velocities.

Chapter 4 presents the results of laboratory ultrasonic velocity measurements performed on DFDP drill core samples and outcrop samples of Alpine Fault Zone rocks. As with chapter 2, I compared the measurements to sonic log data and larger-scale seismic studies. A 20 to 40% decrease in velocity is observed in the brittle fault zone rock relative to the host rock at multiple scales suggesting that the low velocity is due to intrinsic material properties and small-scale brittle damage rather than *in situ* temperature and pressure conditions. A decrease in seismic anisotropy is also observed in the fault core. Future work on the data could incorporate an elastic multi-layer model similar to that used by *Healy* [2008, 2009] to compare how the isotropic Alpine Fault and anisotropic San Andreas Fault cores may influence stress rotations. This

chapter will be submitted to a journal for publication soon. Alpine Fault outcrop specimens referenced in this thesis are in the collections of the Department of Geoscience, University of Wisconsin – Madison, under file number UW2037.

Laboratory ultrasonic measurements on samples from the Japan Trench accretionary prism are the focus of chapter 5. The samples were obtained during IODP expedition 362 (JFAST). Most of the samples examined in this chapter were analyzed at the University of Wisconsin-Madison Rock Physics Lab but one sample was analyzed at Kochi University by Yoshitaka Hashimoto. I observed that the elastic moduli I derived from the laboratory measurements are significantly different from values used in earthquake rupture simulations, which tend to ignore the accretionary prism altogether. This observation led to collaboration with Eric Dunham and his PhD student, Gabriel Lotto, at Stanford University, aimed at understanding the influence a compliant accretionary prism would have on fault slip and tsunami generation. The initial results of this collaboration were published as Lotto et al. in 2017 in *Earth and Planetary Science Letters*. Chapter 5 documents the laboratory results and the derivation of a realistic cross sectional model of rigidity variations in the Japan Trench for use by Lotto in further earthquake rupture simulations. This chapter will be submitted to a journal for publication soon.

2 San Andreas Fault Zone velocity structure at SAFOD at core, log, and seismic scales

Abstract

The San Andreas Fault (SAF), like other mature brittle faults, exhibits a zone of low seismic velocity hypothesized to result from fluid pressure effects and/or development of a damage zone. To address the relative contributions of these mechanisms in developing low velocity zones, we measured P- and S-wave velocity ultrasonically at elevated confining and pore pressures on core samples from the San Andreas Fault Observatory at Depth (SAFOD). We compared those data to wireline and seismic-scale velocities to examine the scale dependence of acoustic properties of the fault core and damage zone. Average laboratory P- and S-wave velocities of the fault gouge at estimated *in situ* conditions are 3.1 and 1.5 km/s respectively, consistent with the sonic log from the same intervals. These data show that fault core has intrinsically low velocity, even if no anomalous pore pressure is assumed, due to alteration and mechanical damage. In contrast, laboratory average P- and S-wave velocities for the damage zone are 4.7 and 2.5 km/s, up to 41% greater than the sonic log in the damage zone. This scale dependence indicates that stress conditions or macro-scale features dominate the damage zone's acoustic properties, though velocity dispersion could play a role. Because no pressure anomaly was detected while drilling the SAFOD borehole, we infer that damage at a scale larger than core samples controls the elastic properties of the broader damage zone. This result bolsters other independent lines of evidence that the SAF does not contain major pore fluid overpressure at SAFOD.

The material in this chapter has appeared in Jeppson, T. N., and H. J. Tobin (2015), San Andreas fault zone velocity structure at SAFOD at core, log, and seismic scales, *J. Geophys. Res. Solid Earth*, 120, 4983–4997, doi:10.1002/2015JB012043.

2.1 Fault zone physical properties

Mature brittle fault zones commonly consist of three main components: fault core, damage zone, and undamaged protolith host rock [*e.g., Chester and Logan,* 1987*; Caine et al.,* 1996*; Kim et al.,* 2004*; Faulkner et al.,* 2010]. The fault core, where the majority of displacement due to movement on the fault accumulates, may include slip surfaces, clay-rich gouge, cataclasite, and chemically altered zones. Damage zones in low porosity rock typically consist of networks of distributed fractures and faults surrounding the fault core. The density of structures in the damage zone generally decreases exponentially with distance from the fault core gradually transitioning into the host rock [*Vermilye and Scholz,* 1998*; Faulkner et al.,* 2010]. The exact distribution of the three fault zone components varies between faults and within individual fault zones. Therefore, fault zones are complex, heterogeneous, three-dimensional structures in the earth's crust with properties that vary both along strike and down dip.

To understand the structure, materials, strength, stress state, and fluid content in fault zones *in situ,* we rely on geophysically-sensed properties such as seismic wave velocity or electrical resistivity, ideally calibrated by direct sampling in boreholes. In this study we use data from the San Andreas Fault Observatory at Depth (SAFOD) borehole to examine the physical properties of the San Andreas Fault Zone as determined from borehole geophysical logs and laboratory measurements. Velocity measurements can be made over a range of frequencies, which permits detection of velocity structure at different scales. At the largest scale, seismic tomography and trapped wave studies use waves with frequencies of 1 to 100 Hz and measure velocity at scales of 10s of meters to kilometers [*Winkler, 1986; Trippetta et al.,* 2010; *Rider and Kennedy,* 2011]. Borehole sonic logs use 10 to 40 kHz waves and produce 10s of centimeter to meter scale velocity measurements [*Rider and Kennedy,* 2011]. Laboratory ultrasonic velocity measurements

record velocity at the smallest (centimeter) scale using frequencies in the hundreds of kHz to MHz range [*Winkler and Plona,* 1982*; Trippetta et al.,* 2010*; Rempe et al.,* 2013].

There are relatively few previous studies that have addressed fault zone velocity structure at multiple scales. Li et al. [2001] used seismic refraction to study the shallow velocity structure of the Punchbowl fault zone in California. They compared crack densities calculated from seismic velocities to observed microfracture densities and found good correlation, supporting the conclusion that velocity decrease across the fault zone was due to fault related damage. Rempe et al. [2014] compared shallow seismic and ultrasonic measurements from a strand of the San Andreas system. They detected a decrease in velocity across the fault similar to that detected by Li et al. [2001] at both scales. However, Rempe et al. [2014] also noticed a scaling effect between field and laboratory measurements; this scaling effect is more pronounced in rocks with a lower degree of deformation. They have suggested the difference in scaling is due to the dominance of macro- vs. micro-scale damage in different regions of the fault zone. Such scale dependence is not uncommon and has been seen outside of fault zones as well. In Triassic evaporates in central Italy Trippetta et al. [2010] measured velocities in the lab that were greater than the *in situ* log velocities and proposed that this difference is due to large-scale fracturing. Stierman and Kovach [1979] have noted that 5-10% macrocrack porosity can reduce *in situ* P-wave velocity by 30 to 50% relative to lab velocity for the same rock. In contrast, Gettemy et al. [2004] attributed a difference between seismic and ultrasonic velocities in the San Gregorio Fault zone to frequency-dependent velocity dispersion. However, for most of the lithologies examined, adjusting the ultrasonic velocities for dispersion did not bring the ultrasonic and seismic velocities into agreement. Overall, these studies indicate that, by comparing results from multiple methods of measurement, evidence has been found that fault damage zones in particular may

exhibit scale dependence caused by differences in fracture presence between micro- and macro-scales.

2.2 San Andreas Fault Observatory at Depth

The San Andreas Fault (SAF) is a right-lateral strike-slip fault in California and is part of a network of faults that forms the boundary between the North American and Pacific plates. The SAF is composed of many segments whose mechanical behavior is known to be either locked or creeping. In 2004 and 2005, the main borehole of the SAFOD project was drilled north of Parkfield, California (Figure 2.1a) to refine our understanding of fault zone structure and determine stress conditions and physical properties of the SAF. It targeted a portion of the SAF that is seismically active in the transition zone between locked and creeping segments [*Zoback et al.,* 2011]. At this location microearthquakes occur from 2 to 12 km depth [*Thurber et al.,* 2004*; Waldhauser et al.,* 2004].

The hole was drilled vertically to a depth of ~1.5 km through Quaternary and Neogene sedimentary rock and Cretaceous Salinian granite and granodiorite, then deviated to an angle of ~60˚ from vertical to target the location of the microearthquakes (Figure 2.1b). All depths reported here are measured depths (MD) along the borehole (rather than true vertical depth (TVD) below the surface) unless otherwise noted. Drilling of the main borehole occurred in two phases. Phase I ended at ~3 km and phase II continued to ~4 km [*Zoback et al.,* 2011]. The deviated portion of the hole passes through Neogene arkosic sandstones and into Cretaceous Great Valley sequence siltstones.

In the rock volume surrounding the SAFOD borehole, seismic tomography studies have long identified a decrease in velocity across the SAF [*Thurber et al.,* 2003, & 2004; *Zhang and Thurber,* 2005]. Later studies by Zhang et al. [2009] have imaged a 1 km wide zone near the

fault where velocity is reduced by up to 20% relative to the surrounding velocities. The fault zone was further constrained in trapped wave studies by Li et al. [2004] and *Li and Malin,* [2008] which have identified a 100 to 200 m wide low velocity zone (LVZ) near Parkfield where the velocity is reduced by up to 40% relative to the surrounding velocities.

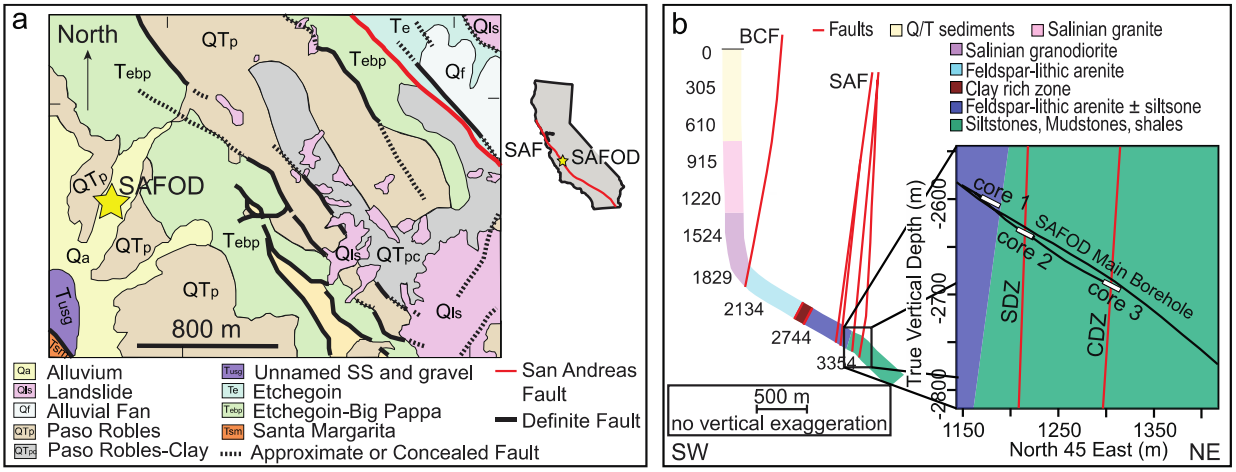

Figure 2.1*: (a) Location of the SAFOD drillsite near Parkfield, California. Modified from Thayer [2006]. (b) Simplified lithologic cross section of the SAFOD main borehole. Modified from Bradbury et al. [2007] and Zoback et al. [2011]. BCF – Buzzard Canyon fault; SAF – San Andreas fault. Inset shows a detailed section of the main borehole where it passes through the SAF, as well as the trajectories of the phase III sidetrack boreholes. White boxes show locations where core was taken.*

During and after drilling, geophysical logs were collected, and they revealed a 224 m wide zone of low velocity and resistivity (Figure 2.2) from 3190 to 3414 m [*Zoback et al.*, 2005, 2010, & 2011*; Jeppson et al.*, 2010]. The log P- and S-wave velocities (v_p and v_s) in this broad zone are 10 to 30% slower than the surrounding rock. This LVZ was interpreted to be the damage zone of the SAF. Within the broad LVZ, multiple narrow zones with even lower velocities (up to a 46% decrease) and resistivities were detected. Of particular interest are two zones at 3192 m and 3302 m where v_p dropped to 2.48 km/s and 2.43 km/s, respectively. These localized zones are 1 to 2 m wide in the logs.

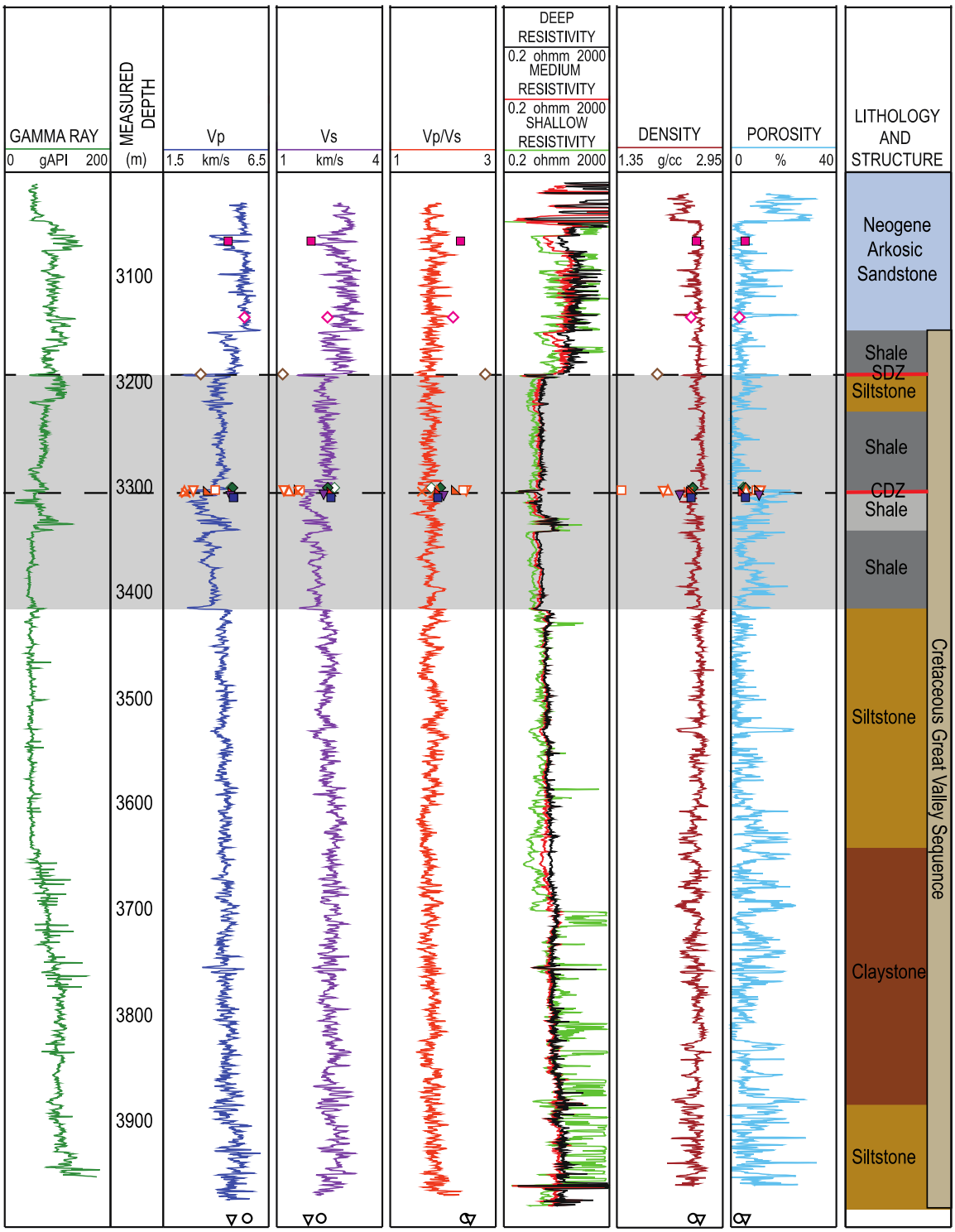

Figure 2.2: *Selected geophysical logs and cuttings-based lithologic column as a function of measured depth along the Phase II SAFOD borehole (approximately the range shown in the box in Figure 2.1b to the bottom of the hole). The light gray shaded region shows the location of the LVZ. Black dashed lines indicate locations of the SDZ and CDZ. Lab data reported in section 2.4 are shown as points with symbols and colors correlating to those used in Figure 2.4. In general lab and log velocities are similar, especially in the host rock and fault gouges.*

Repeated caliper measurements of borehole shape revealed that the steel casing was actively deforming at the exact locations of these two narrow LVZs. These areas were interpreted as localized deformation associated with the main strands of the modern SAF at this location, and are referred to as the Southwest Deforming Zone (SDZ) at 3192 m and the Central Deforming Zone (CDZ) at 3302 m [*Zoback et al.,* 2010, & 2011]. In 2007, during a third phase of drilling, sidetrack holes were drilled to retrieve 39.9 m of continuous core from 3 areas of the borehole (Figure 2.1b), including the SDZ and CDZ [*Zoback et al.* 2011]. Meter-scale zones of foliated fault gouge were found at depths corresponding to the SDZ and CDZ. These foliated gouge zones are composed of matrix-supported clasts (up to cm scale) of sedimentary rocks, similar to the Great Valley Block lithologies, and serpentinite [*Bradbury et al.,* 2011*; Holdsworth et al.,* 2011]. The clasts make up about 10% of the total gouge volume. The matrix is phyllosilicate-rich and ultra-fine-grained with a pervasive scaly foliation that wraps around the clasts at moderate to high angles relative to the core axis. These gouge zones were surrounded by sheared and fractured rock, supporting the interpretation that the SDZ and CDZ are active fault cores surrounded by a broad damage zone. The damage zone rocks are up to 50% clasts, contain fewer phyllosilicate minerals, and are considerably less deformed than the foliated gouges from the SDZ and CDZ [*Bradbury et al.,* 2011; *Holdsworth et al., 2011*].

Before drilling, it was proposed that the SAF correlated with a zone of high pore fluid pressure that could create a LVZ [*Rice,* 1992*; Unsworth et al.,* 1997*; Li et al.,* 2006*; Li and Malin,* 2008]. This hypothesis was thought to be supported by the presence of a high v_p/v_s ratio zone associated with a low v_p zone detected in tomographic inversion models of the fault zone [*Thurber et al.,* 2003] and high fluid content indicated by magnetotelluric studies [*Bedrosian et al.,* 2004*; Unsworth and Bedrosian,* 2004]. During SAFOD drilling there was no indication that the

borehole intersected a high pore pressure zone [*Zoback et al.*, 2011] and no substantial variations in v_p/v_s were observed over the depths of the LVZ in the sonic logging data [*Jeppson et al,* 2010] (it is noted, however, that high v_p/v_s zone in seismic tomography and low resistivity zone in magnetotelluric study were imaged at shallower levels than the SAFOD borehole penetration and therefore may not be related to the LVZ observed in the borehole logs).

Alternatively, the LVZ could be the result of mechanical damage and structural/mineralogical alteration caused by slip on the SAF [*Li et al.*, 2004*; Jeppson et al.*, 2010*; Zoback et al.*, 2011]. *In situ* and laboratory studies performed on many different lithologies have indicated that damage, ranging from micro- to meso-scale faults and fractures, may cause significant velocity reduction [*e.g., O'Connell and Budiansky,* 1974*; Stierman and Kovach,* 1979*; Gettemy et al.*, 2004*; Trippetta et al.*, 2010*; Jeanne et al.*, 2012*; Rempe et al.*, 2013]. It is also possible that compositional variations, including a lithologic change or fault-related clay development, could be the cause of the velocity reduction [*e.g. Tosaya and Nur,* 1982*; Kowallis et al.*, 1984*; Castagna et al.*, 1985*; Han et al.*, 1986].

Here, we report a suite of laboratory v_p, v_s, porosity, and density measurements collected at elevated confining and pore pressure on SAFOD core samples. These measurements are then used to derive dynamic elastic moduli. Through analysis of laboratory and logging data three main questions are addressed: (1) is the low velocity of the fault zone due to intrinsic properties of the rock or *in situ* stress conditions, (2) what is the likely cause of the scale dependence or independence of seismic wave velocity and the structures that control it in the fault zone rock, and (3) what implications does this have for the cause of the LVZ? Comparisons between laboratory and log data reveal that in some regions the physical property measurements are dependent on the scale of measurement whereas in other regions the obtained values are scale

independent. These results are examined in relation to previous seismic studies at and around SAFOD.

Table 2.1: *SAFOD core samples. Depths of Phase III cores were shifted to correspond to the main borehole.*

Sample Number	*Lithology*	*Drilling Phase*	*Orientation with respect to core axis*	*Measured Depth (m)*	*Shifted Depth (m)*
B12R5	Arkosic sandstone	II	Perpendicular	3065.29	- - -
E12	Greenish gray pebbly sandstone	III	Parallel	3142.58	3137.55
G27	Foliated fault gouge	III	Parallel	3196.578	3191.548
	Southwest Deforming Zone (SDZ)			*3192*	
G41a	Sheared siltstone & sandstone	III	Parallel	3295.19	3299.15
G41b	Sheared siltstone & sandstone	III	Perpendicular	3295.19	3299.15
G43	Foliated fault gouge	III	Parallel	3297.27	3301.23
G44a	Foliated fault gouge	III	Parallel	3297.94	3301.90
G44b	Foliated fault gouge	III	Perpendicular	3297.94	3301.90
G44c	Foliated fault gouge	III	Parallel	3297.94	3301.90
	Central Deforming Zone (CDZ)			*3302*	
G45	Foliated fault gouge	III	Unknown	3298.70	3302.66
G47	Sheared siltstone & mudstone	III	Perpendicular	3300.16	3304.12
G52	Massive siltstone to very fine sandstone	III	Perpendicular	3301.90	3305.86
G55	Sheared & fractured siltstone to very fine sandstone	III	Perpendicular	3304.34	3308.30
B3R7	Great Valley siltstone	II	Parallel	3991.66	- - -
B4R7	Great Valley siltstone	II	Parallel	3992.84	- - -

2.3 Methods

2.3.1 Ultrasonic velocity measurements

Samples of the SAFOD core were chosen to represent the major lithologies and structural domains present in the phase II mainhole core and phase III sidetrack cores, dependent on availability of the severely limited core material. We obtained samples of the SAFOD phase II and III core from nine different structural/lithologic units: (1) arkosic sandstone, (2) greenish-gray pebbly arkosic sandstone, (3) SDZ foliated gouge, (4) sheared siltstone and sandstone, (5) CDZ foliated fault gouge, (6) sheared siltstone to mudstone, (7) massive siltstone to very fine

sandstone, (8) sheared and fractured siltstone to very fine sandstone, and (9) intact siltstone (Table 2.1). Samples of Neogene arkosic sandstones (1 & 2) and Cretaceous Great Valley sequence siltstones (9) represent the host rock lithologies. The fault core is represented by samples of the SDZ and CDZ foliated gouge (3 & 5) with samples of the sheared and fractured rock surrounding the CDZ representing the damage zone (4, 6-8).

Following pulse-transmission techniques adapted from Birch [1960; 1961] and Christensen [1985], velocity measurements were performed under elevated confining stress and pore pressure on 15 core plugs of 25.4 - 38.1 mm diameter taken from the SAFOD cores (Table 2.1). During core subsampling, care was taken to avoid visible fractures, and, when possible, mutually orthogonal core plugs were taken from the core, within the restrictions imposed by severely limited core availability.

Laboratory ultrasonic velocity measurements were performed using a TEMCO pressure vessel with three 500 kHz central frequency piezoelectric transducers embedded in the endcaps (Figure 2.3). One transducer is for v_p and two are for mutually perpendicular v_s measurements. We used commercially available Isopar-H as the axial and confining fluid and saline water (Table 1A.1) for the pore fluid. Each velocity test was conducted with a constant pore pressure of 1 MPa while axial and confining pressures were adjusted so that v_p and v_s measurements were taken at a range of effective pressures. Some velocity measurements were recorded in combination with permeability experiments for which the protocol did not allow for pressure cycling or the measurement of velocity at lower pressure values. Confining pressure was kept at 200 kPa less than the axial pressure to maintain good sample coupling to the endcaps. Sample length was monitored for the duration of each velocity test using a linear potentiometer displacement transducer (LPT) attached to the axial ram. Final porosity and density were determined through

direct measurement of sample volume and wet and dry mass. These measurements, combined with the axial displacement, were used to estimate porosity and density changes during the experiment. Problems unloading the samples at the end stages of the experiments prevented the determination of porosity of two of these samples.

The largest uncertainty in the velocity measurement arises from non-parallel core faces and associated uncertainties in initial length measurements. The core faces can usually be smoothed and made parallel so there is less than 0.6 mm variability leading to 3% uncertainty in the length of the sample. The wave arrivals at low pressures are difficult to determine with precision due to poor sample-transducer coupling at low effective pressure. At low pressures there is a 2% uncertainty in picking the P-wave arrival. The S-wave arrival is more difficult to identify so there is a 6% uncertainty.

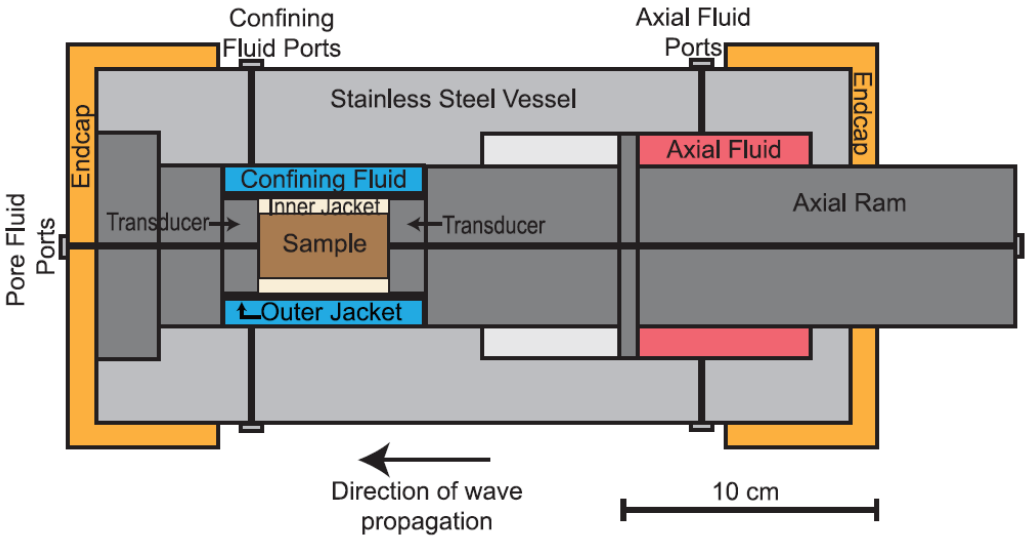

Figure 2.3: *Schematic of the triaxial pressure vessel used in our experiments.*

2.4 Results and discussion

In this section, we describe laboratory ultrasonic velocity measurements of SAFOD core; followed by a comparison of the lab data to log data and previous seismic studies of the area.

Detailed microstructural descriptions of the SAFOD core can be found in Bradbury et al. [2011], Holdsworth et al. [2011], and in the Core Photo Atlas (www.earthscope.org/safod).

2.4.1 Velocity measurements at elevated pressures

P- and S-wave velocity, porosity, and wet bulk density were measured for SAFOD core samples subjected to effective pressure ranging from 0.5 to 90 MPa. For some of the samples, velocity was measured over a cycle as pressure was increased in steps and then decreased through the same steps. These samples exhibit up to 8% hysteresis between the loading and unloading values. Variations in velocity and porosity with effective pressure for the core samples are shown in figure 2.4. For all samples, velocity increases and porosity decreases as the effective pressure is increased. The magnitude of change in velocity and porosity with effective pressure has been shown to vary with rock type and physical properties, and has been interpreted to indicate the closure of microfractures and pores [*Bourbie et al,* 1987*; Song et al.,* 2004], as well as alignment of clay grains in the minimum shear strength plane [*Tosaya,* 1982]. Most of the change in velocity occurs below 15 MPa, suggesting that the majority of the open microcracks and pores become closed over the pressure interval from 0.5 - 15 MPa. As a second change in slope is not seen at higher pressures we assume that these rocks have experienced greater than 70 to 90 MPa pressure at their maximum burial depth or have been cemented to give equivalent strength; therefore these experiments represent re-loading only. In general the velocities of the foliated fault gouges are very low (nearly all with $v_p < 4$ km/s, $v_s < 1.75$ km/s), relative to velocities of all other rock samples (nearly all with $v_p > 4$ km/s, $v_s > 1.75$ km/s). Generally, the porosities of the core samples are low, ranging between 3 and 8%. There are four exceptions: three samples from the gouge and one from the damage zone have porosities of 10 - 14%.

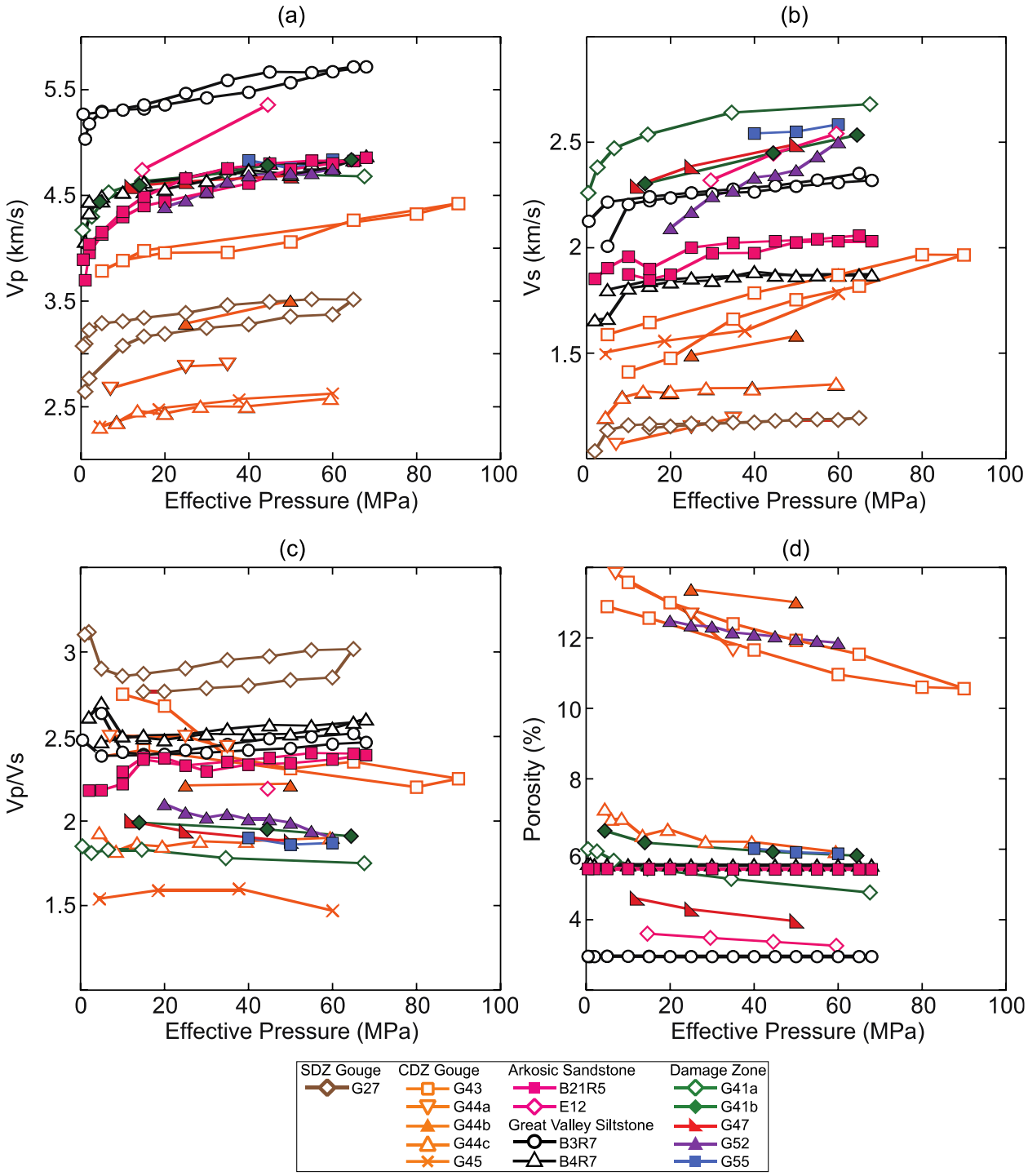

Figure 2.4: *Variations in (a) v_p, (b) v_s, (c) v_p/v_s, and (d) porosity measurements with effective pressure for SAFOD core samples. Velocities in the gouge are much lower than in other rock types. Solid symbols indicate that the long axis of the sample was oriented perpendicular to the core axis. Hollow symbols indicate that the long axis was parallel to the core axis and x's indicate sample orientation is unknown. This notation remains consistent throughout the paper.*

The v_p/v_s ratios were calculated from the measured velocities (Figure 2.4c). SDZ and CDZ gouges exhibit a wide range of v_p/v_s values (1.5 to 3.2). All other core samples fall into a slightly narrower range between 1.6 and 2.8. The Great Valley siltstones have high v_p values with relatively low v_s values, resulting in a high v_p/v_s ratio between 2.4 and 2.7, greater than all other non-gouge core samples. The wide range of v_p/v_s values in the gouge could be due to heterogeneities in the rock or to uncertainty in v_s measurements. However, the gouge v_p/v_s values are all within the range reported for sedimentary rocks by Brocher [2005] and for typical poorly consolidated marine sediments (v_p/v_s of 2.5 to 4) reported by Gettemy and Tobin [*2003*] and Hashimoto et al. [*2011*].

2.4.2 Velocity measurements at *in situ* pressure

To compare lab data to the SAFOD borehole logs, we used the v_p, v_s, porosity, and density values from the loading curve at the estimated *in situ* overburden stress. We assume this is close to the mean stress for a strike-slip stress state. We estimated the *in situ* overburden stress at the location of the actively deforming zones (2629.5 and 2684.5 m TVD) to be 42 MPa, assuming a bulk density of 2.60 g/cm^3, based on the average bulk density of Great Valley siltstones determined from SAFOD wireline logs, and hydrostatic pore fluid pressure conditions. While the actual *in situ* mean stress may be greater than 42 MPa [*Tembe et al.,* 2009; *Lockner et al.,* 2011], laboratory velocity curves remain relatively constant above 15 MPa for most of the samples. Therefore, the following analysis is not sensitive to the selection of a moderately different *in situ* mean stress state.

Figure 2.5 shows laboratory physical properties for the core taken close to the estimated *in situ* effective pressure. The core samples were divided into four groups based on lithology and fault-related damage states: (1) Neogene arkosic sandstones, (2) fault gouge, (3) damage zone, and (4)

Cretaceous Great Valley siltstones. The data at *in situ* effective pressures show that the foliated fault gouges have ultrasonic velocities substantially slower than the surrounding damage zone material (Figures 2.5 & 2.6). At 42 MPa pressure the gouge v_p is 17 to 63% slower than the v_p of the surrounding damage zone, which is on average 8% slower than the intact Great Valley samples. The arkosic sandstones have v_p between 4.6 and 5.4 km/s and v_s between 1.9 and 2.4 km/s. The damage zone has v_p between 4.6 and 4.8 km/s and v_s between 2.3 and 2.7 km/s. The Great Valley siltstone samples have v_p values of 4.7 and 5.4 km/s similar to the damage zone samples, but v_s values of 1.9 and 2.3 km/s, slower than most of the damage zone samples. In contrast, the gouges have v_p between 2.5 and 4 km/s and v_s between 1.2 and 1.7 km/s. As indicated by the v_p/v_s discussed in section 2.4.1 the v_p and v_s in the foliated fault gouge are as low as velocities for

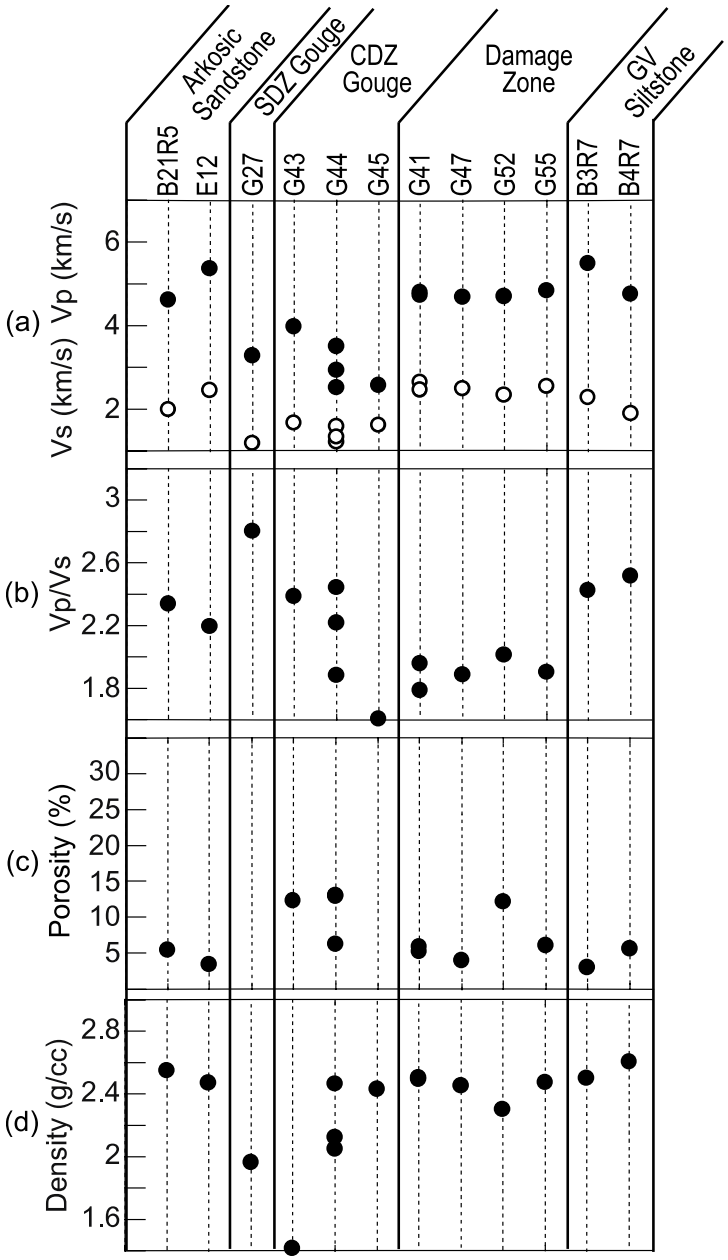

Figure 2.5: *Variations in (a) v_p (black) and v_s (white), (b) v_p/v_s, (c) porosity, and (d) density measurements for SAFOD core samples at approximately 42 MPa effective pressure. P-wave velocity in the fault gouge is up to 63% slower than in damage zone samples. Velocities in the damage zone are similar to host rock velocities.*

typical poorly consolidated marine sediments (v_p of 1.7 to 2.5 km/s; $v_s \leq 1$ km/s) [*e.g., Gettemy and Tobin, 2003; Hashimoto et al., 2011*]. The gouge is an incohesive, granular material [*Bradbury et al., 2011; Holdsworth et al., 2011*] and, based on velocity measurement, has properties similar to incohesive sediments.

Measurements of v_p and v_s on samples with different orientations with respect to the core axis were available for a sample of the CDZ gouge and a sample of the sheared siltstone and sandstone above the CDZ. These measurements were used to calculate a two dimensional directional anisotropy (core axis-parallel vs. core axis-perpendicular only). The sheared siltstone sample exhibits P-wave anisotropy of 1.5% and S-wave anisotropy of 7.5%. The foliated fault gouge is strongly anisotropic, with P-wave anisotropy of 33% and S-wave anisotropy of 28%. The slow direction occurs in gouge samples oriented parallel to the core axis and therefore, approximately perpendicular to the local foliation plane. The high degree of anisotropy in the gouge may be related to the development of a penetrative scaly fabric. Holdsworth et al. [2011] describes the fabric in neighboring samples as a "highly distinctive scaly fabric with numerous polished and striated foliation surfaces." In addition, Sills [2010] has noted that clasts in the gouge have a strong shape preferred orientation. In contrast, the scaly fabric is not present in the sheared siltstone sample, and the slow direction is not consistent between P- and S-waves or at different pressures. This indicates that for this sample the velocity difference between the two orientations may not be related to anisotropy but instead shows the natural variability of the sample.

2.4.3 Scaling: from laboratory to field–scale

2.4.3.1 Wave velocity

To compare the laboratory ultrasonic velocity measurements to the sonic logs, the locations of the core samples were first depth shifted to match log depth using the shift described in the Core Photo Atlas (www.earthscope.org/safod). As discussed in section 2.4.2, laboratory measurements conducted near an effective pressure of 42 MPa simulate the predicted *in situ* effective mean stress conditions experienced in the borehole. After shifting to align the coring sidetrack with the main hole that was logged, laboratory results and *in situ* log measurements were directly compared (Figures 2.2 & 2.6).

Most of the laboratory measurements are consistent with the log velocities, especially for the gouge and undeformed host rock. In the gouge, lab values at 42 MPa match log v_p and v_s values well. There is no indication that elevated pore fluid pressure and reduced effective stress is required to explain the magnitude of gouge velocity reduction relative to surrounding wallrock. In the damage zone however, the *in situ* pressure laboratory values differ from the log values. The damage zone samples yielded v_p and v_s values that are 9 to 41% and 1 to 32% higher, respectively, than the log values. There are three potential causes of the difference between laboratory and log velocities in the damage zone. They are: (1) a difference between simulated and *in situ* effective pressure and conditions, (2) frequency-dependent velocity dispersion, and (3) the presence of large-scale features not sampled at core scale.

Velocity depends greatly on effective pressure; therefore, the velocity difference could be due to differences in the laboratory versus *in situ* effective pressure and conditions. However, the velocity-pressure curves (Figure 2.4) indicate that the effective pressure at depth would have to be less than 10 MPa for most of the damage zone samples to have ultrasonic velocities as low as

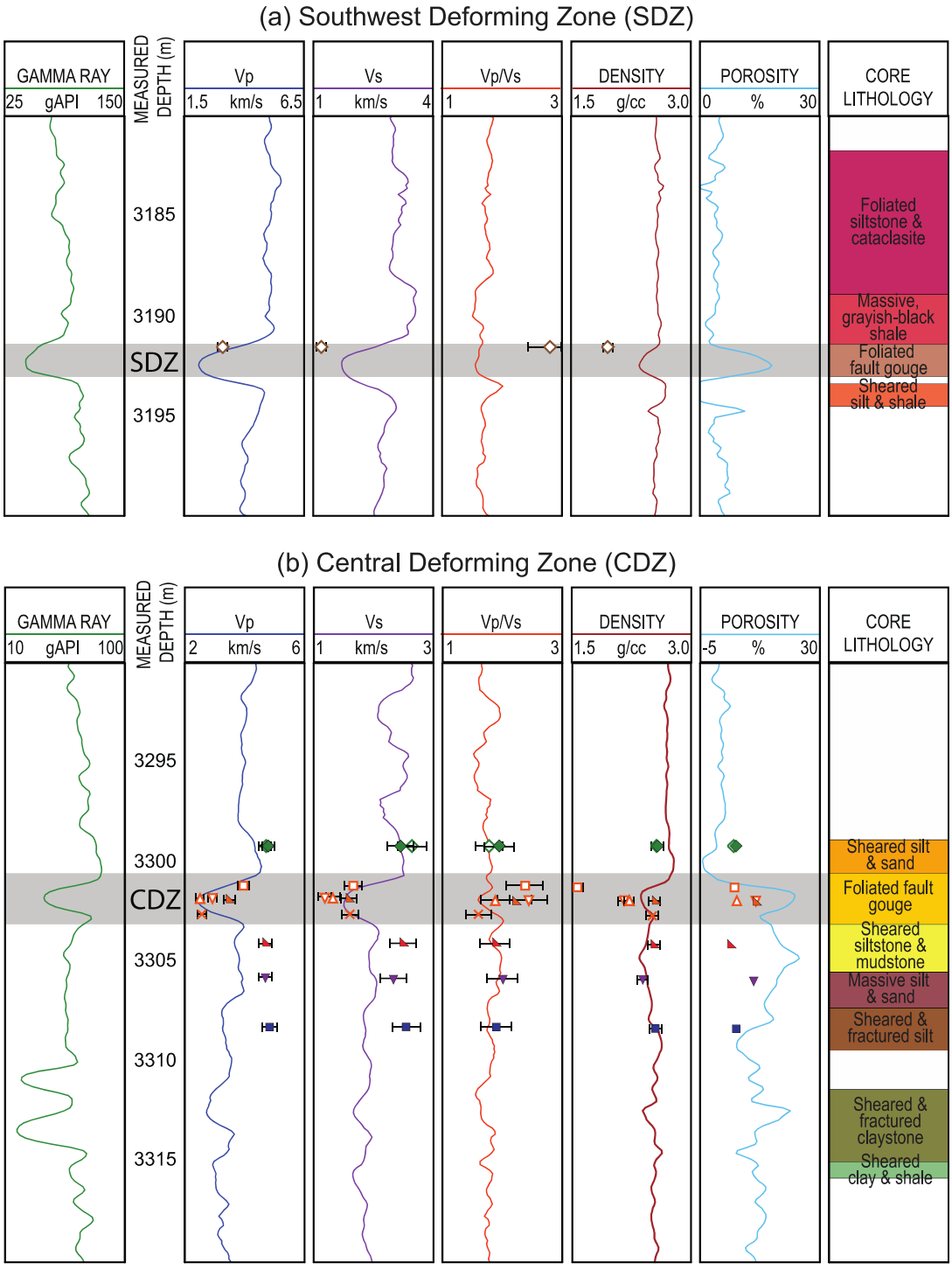

Figure 2.6: *Comparison of laboratory ultrasonic measurements and downhole sonic logs highlighting the (a) SDZ and (b) CDZ (gray shaded regions) as defined in the core. Lab data are shown as points with symbols correlating to those used in Figure 2.4 and core lithologies, as described in the SAFOD Core Photo Atlas, are also shown. Lab velocities are similar to log velocities in the fault gouges but in the damage zone the lab velocities are up to 41% higher than the log velocities. Error bars show errors of 5% in vp, 9% in vs, and 3% in density. Error bars representing a 5% error in porosity are smaller than the size of the sample markers.*

the log values. This equates to an overpressure ratio of λ =0.85 or greater. No such pressure anomaly has been detected. As there is good correlation between the lab and log velocities elsewhere in the borehole, it is likely that the conditions simulated in the laboratory are a good approximation of the conditions encountered in the borehole.

Alternatively, the velocity difference could be due to frequency-dependent velocity dispersion [*Winkler*, 1983 & 1986]. In saturated, porous, attenuating media, velocity is a function of frequency. Dispersion typically results in higher elastic moduli and thus higher velocities for high frequency waves [*Mavko et al.,* 2009]. Velocity dispersion is very likely to influence velocity scale dependence and lead to differences in the velocity measurement at seismic, sonic, and ultrasonic frequencies. The lack of scale dependence in the gouge may indicate that properties of the pores in the gouge allow the pore pressure to equilibrate more quickly. Measurements of the permeability of the SAFOD samples indicates that the damage zone permeability at 40 MPa is 10^{-21} to 10^{-17}, while the permeability of the SDZ and CDZ is 10^{-21} to 10^{-20} [Janssen et al., 2011; *Morrow et al.,* 2014]. This would indicate that the effects of velocity dispersion should cause the velocity difference between sonic and ultrasonic to be greater in the CDZ gouge, the opposite of what was found in the data. Therefore, it seems unlikely that dispersion is the cause of the damage zone scale dependence. However, Janssen et al. [2011] have found a high nanoscale pore body to pore throat ratio in the damage zone cataclasites, which would likely increase the effects of velocity dispersion. In order to fully address the potential for a velocity dispersion effect in the fault zone, we would need to estimate the velocity at low frequencies using dry ultrasonic velocities measurements. Unsaturated measurements were not conducted on these fragile samples, so frequency dispersion cannot be entirely

eliminated as a potential cause of the scale dependent acoustic properties of the damage zone. However, for the reasons stated above, we judge that it is unlikely to be the dominant effect.

Our preferred hypothesis is that the scale dependence in the damage zone is due to the presence of features at a spacing and scale too large to be sampled in the core plugs. Damage zones are formed from networks of small faults, veins, fractures, and other structures present over a range of scales [*Chester and Logan,* 1987*; Caine et al.,* 1996*; Shipton and Cowie,* 2003*; Kim et al.,* 2004*; Faulkner et al.,* 2010]. Sample preparation for laboratory experiments requires the rock to be relatively intact. Therefore, the 5 cm or smaller-scale samples used in laboratory measurements generally do not contain macro-scale deformation features such as small faults and fractures. We propose that the velocity reduction in the broader, damage zone (or LVZ) is the result of mechanical damage manifested by fractures at a scale larger than that sampled in core plugs and ultrasonic data [*e.g. Stierman and Kovach,* 1979*; Trippetta et al.,* 2010*; Jeanne et al.,* 2012*; Rempe et al.,* 2013].

In contrast, the scale independence of the velocity in the foliated gouge indicates that the greater velocity reduction seen across the SDZ and CDZ is a result of sample-scale features, observed in the gouge, including a penetrative, highly sheared and foliated scaly fabric, cm-scale and smaller clasts, ultrafine-grained phyllosilicates, and thin clay coatings of illite-smectite and chlorite-smectite minerals [*Schleicher et al.,* 2010; *Bradbury et al.,* 2011; *Holdsworth et al.,* 2011]. The gouges are strongly anisotropic, probably related to the development of a strong fabric in the rock, which likely contributes to the ultra-low velocities of the gouges. We propose that the ultra-low velocities of the SDZ and CDZ are due to the presence of micro-scale features.

2.4.3.2 Porosity, density, and v_p/v_s ratio

Comparing laboratory measurements of porosity and density to logging measurements is difficult due to significant differences in the way these properties are measured at the different scales. The logs do not directly measure bulk density and porosity. In this study, we used the Z-density log to estimate the *in situ* density downhole. The Z-density log approximates the bulk density based on the atomic number, which is determined from photoelectric absorption of gamma rays [*Ellis and Singer*, 2008]. The log porosity is then calculated from the density log. In general, the lab-derived densities are comparable to the log densities except in the SDZ and CDZ where the lab density is lower than the log (Figure 2.6). The lab-determined porosities fall within the same range as the log estimates, but they tend to be significantly lower than the log at the sample depth. The difference between the lab and log porosities is likely a result of macro-scale fracturing in the borehole creating a higher porosity. However, this does not explain why the lab density is lower than the log density in the gouge samples, which may indicate over estimation of the laboratory sample volume or errors in the log.

The laboratory-derived values of v_p/v_s are similar to log data except for the gouge, which exhibits a wider range in the lab values than is present in the log. This variability could be due to greater uncertainty in the v_s measurement, or to small-scale heterogeneities that are being sensed at the laboratory scale but are averaged over 60 cm at the log scale. Variations may be more prominent in the gouge samples due to variations in the size and concentrations of clasts present.

2.4.3.3 Elastic parameters

Dynamic bulk and shear moduli were calculated from laboratory-measured v_p, v_s, and density. There is a significant contrast between the moduli calculated for the gouge and all other samples from the SAFOD borehole (Figure 2.7). At the estimated *in situ* pressure (42 MPa), gouge samples exhibited bulk moduli of 5 to 21 GPa and shear moduli of 2.5 to 7 GPa. The shear and

bulk moduli in the gouges are on average 70% and 63% lower, respectively, than those of the damage zone. Modulus-porosity relationships show that the gouge samples plot in a cluster with low moduli and low porosity similar to the logging data from the SDZ and CDZ (Figure 2.8). Based on the measured velocities and computed elastic moduli, it is apparent that the foliated fault gouges are intrinsically different from any of the surrounding material. Of particular interest is the relationship between degree of deformation and bulk modulus that is apparent in Figure 2.7a. The bulk modulus is greatest for intact samples of the Great Valley and arkosic sandstone (>30 GPa) and lowest for samples of the fault gouge (<15 GPa). Samples from the damage zone plot between the two extremes (26 to 51 GPa). This suggests that the mechanical strength of the rock may also decrease with deformation. The striking difference in compliance of the gouge relative to the wall rocks bolsters arguments that the SAF creeps due to the presence of intrinsically weak fault materials rather than anomalous stress conditions [*Moore and Rymer*, 2007*; Carpenter et al.*, 2011*; Lockner et al*, 2011].

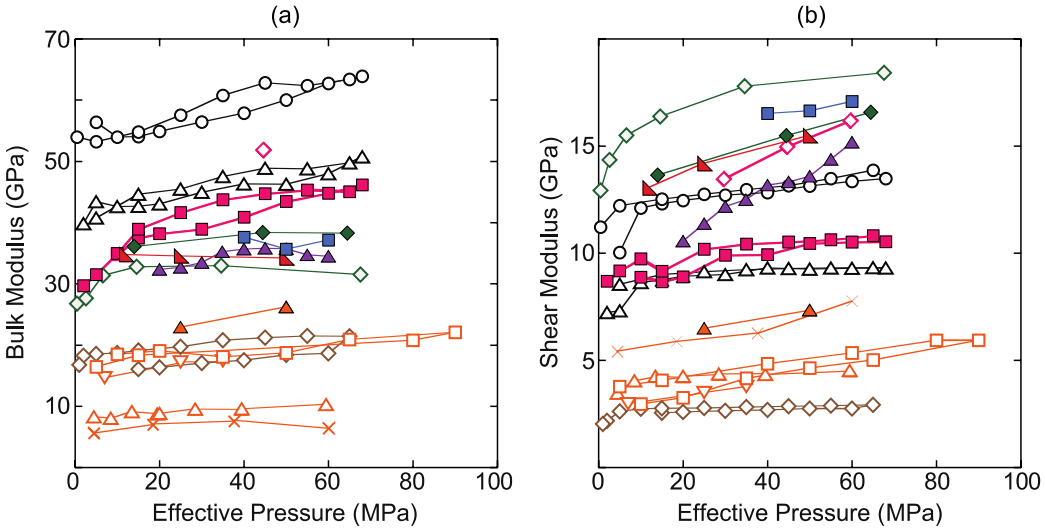

Figure 2.7: *Variations in (a) bulk and (b) shear moduli with effective pressure calculated from laboratory velocity and density data. Elastic moduli of the gouge samples are significantly lower than the elastic moduli of all other samples. Colors and symbols correspond to those in Figure 2.4. Foliated fault gouge samples, shown in orange and brown, plot well below all other samples measured.*

When elastic moduli are cross-plotted against porosity (Figure 2.8), samples of the intact host rock and damage zone plot in a region with high moduli and low porosity. Samples from the arkosic sandstones and Great Valley siltstones fall within the range of logging data from the corresponding lithology. The damage zone, however, has lab-derived elastic moduli that are consistently higher than the log-derived elastic moduli. This is interpreted as being due to differences in the wave velocity measurements caused by large-scale fractures and other features not present in the lab samples but present at field scales.

To determine the crack density needed to reproduce the observed elastic moduli in the damage zone we apply equations derived by Budiansky and O'Connell [1976] and Henyey and Pomphrey [1982] that relate the elastic moduli of uncracked rocks to the moduli of cracked rocks and the crack density. Assuming the velocities measured in the lab for rocks from the damage zone represent the velocities of the uncracked rock and the log velocities represent the cracked rock we calculated the nominal cracked and uncracked moduli of the SAFOD damage zone. The log values were averaged over 0.7 meters surrounding each core sample location and compared to the lab values. We then used the equations of Henyey and Pomphrey [1982] for wet cracks to determine the minimum crack density needed to produce the shear and Young's moduli that were observed for cracked rocks (*ie.*, the log moduli) from the moduli derived from ultrasonic lab samples.

These equations are developed for the long-wavelength limit (wavelength >> crack size). At SAFOD the majority of fractures seen in the resistivity image logs have apparent apertures on the order of 1 mm (M.D. Zoback 2008 personal communication) and the wavelength of the sonic log is on the order of 10 cm. For the laboratory data, the wavelength of the transducers used is on

the order of 10 mm and the microcracks in the core samples are intergranular (μm-scale). Thus the long-wavelength limit is valid at both scales.

Above the CDZ the velocity-derived cracked and uncracked moduli are very similar, so only a small crack density of 0 to 0.1 was needed to produce the cracked moduli. Below the CDZ, where there is greater separation between the cracked and uncracked moduli, higher crack densities of 0.3 to 0.9 were needed to reproduce the cracked moduli. The crack density is estimated as the average volume of the distorted strain field produced by a crack (crack length multiplied by the square of the crack width) divided by the total sample volume [*Henyey and Pomphrey*, 1982]. Real crack densities tend to fall between 0 and 1 so the crack densities estimated at SAFOD are reasonable and support the conclusion that the velocity difference in the damage zone is due to fracturing.

2.4.3.4 Comparison with seismic-scale studies

As discussed in section 2.2 the LVZ surrounding the SAF has been imaged in various tomography and trapped wave studies. The low spatial resolution of the tomography models generally results in an underestimation of the velocity reduction and overestimation of the fault zone width. Zhang et al. [*2009*] compared the velocities extracted from seismic models to the SAFOD logging data and found that the modeled velocities follow the general trends in the logs. However, the model velocities lack the small-scale variations and tend to underestimate the velocity. Zhang et al. [2009] suggest that a better estimation of velocity might be obtained by incorporating anisotropy. However, the limited anisotropy measurements obtained in this study do not necessarily support this hypothesis. The sonic log tool measures the velocities of waves propagating along the borehole wall and, in the case of SAFOD, approximately perpendicular to the local foliation plane. Therefore, sonic log velocities should provide a close to minimum

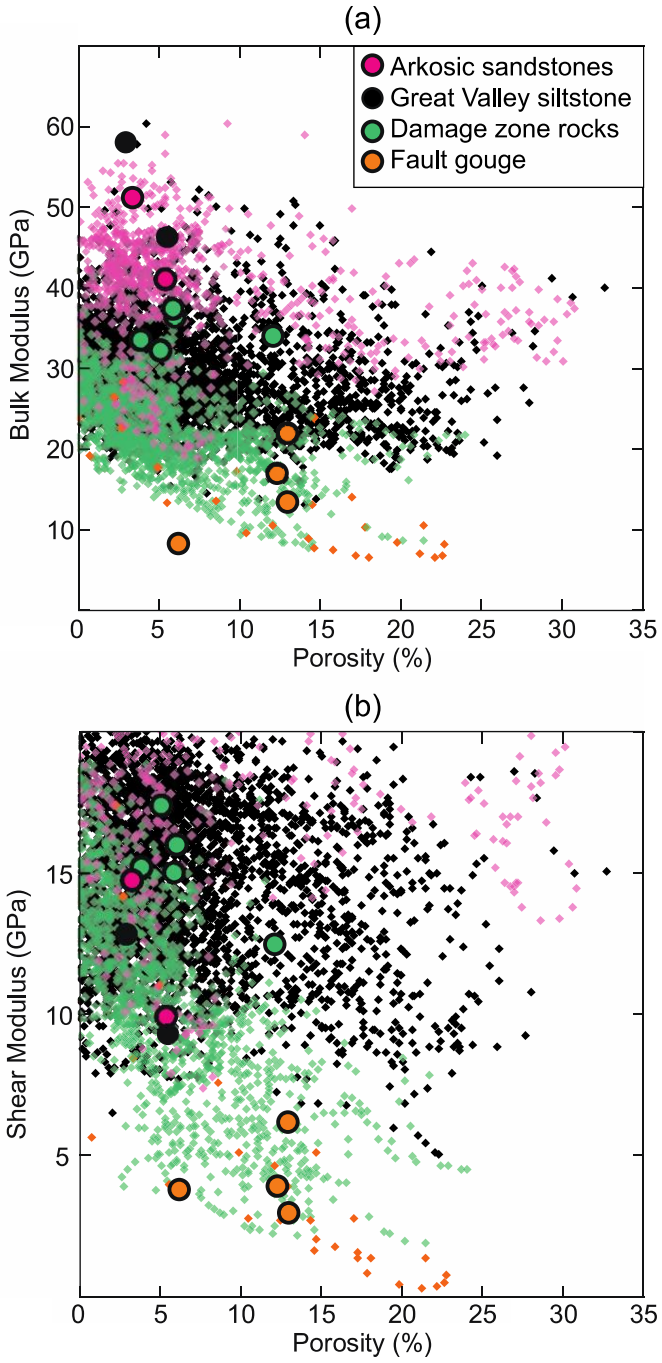

Figure 2.8: *Variations in (a) bulk and (b) shear moduli with porosity. Lab measurements are plotted as circles. Elastic moduli calculated from the lab data are similar to those calculated form the log data except for damage zone samples where the lab data tends to be higher. For reference, samples of the foliated fault gouge are plotted in orange. Small diamonds are the log derived elastic moduli from different lithologies and structural domains as indicated by color: arkosic sandstone (pink), Great Valley siltstone (black), damage zone (green), and SDZ and CDZ (orange).*

estimate of velocity. If directional anisotropy were the sole parameter affecting velocity, and assuming transverse isotropy, the averaged velocity obtained from seismic models would be greater than the SAFOD log velocity. However, this is not the case because the seismic-scale velocity is affected by large-scale variations in lithology and structures in the subsurface that are

not encountered by the sonic log. The seismic velocity is slower than the sonic log as it is an average velocity of these features, resulting in a smoothed velocity vs. depth relationship.

Fault zone trapped wave studies identify a LVZ with a width and velocity reduction similar to that seen in the sonic log. Li and Malin (2008) further constrained their model to image a 30 to 40 m wide fault core with velocity reduced by up to 40%, within a damage zone where velocity is reduced by up to 25%. At ultrasonic frequencies, the laboratory S-wave velocities of foliated fault gouges are 40-50% slower than the intact host rock samples, similar to both the logs and the trapped wave model. The data indicate that the low velocities of the SDZ and CDZ are the result of features that are present at all scales. In contrast, the 25% velocity reduction in the damage zone that is seen in field and log scale velocities, but not in laboratory measurements, supports the conclusion that the velocity reduction in the damage zone is due to large-scale fracturing and faulting not present at the cm-scale.

2.5 Conclusions

By examining geophysically sensed properties of fault zones at a variety of scales we begin to unravel the complex structure of fault zones at depth. At SAFOD, larger length-scale measurements (seismic to sonic log) detected a low velocity damage zone associated with the SAF while smaller length-scale measurements (sonic log to ultrasonic measurements) located individual fault core zones with properties that are significantly different from the surrounding material and result in extremely low velocities. Comparing v_p and v_s measured on cores at the same effective pressure across the fault zone shows that neither pore fluid pressure nor stress anomalies are required to explain the presence of the ultra-low velocity zones known as the SDZ and CDZ. Rather, the modification of rock fabric by brittle fault processes is sufficient to create the ultra-LVZs. We conclude that the velocity reduction seen across the SDZ and CDZ occurs

because of micro-scale damage and alteration, such as the development of clays and the scaly fabric (and related anisotropy) observed in the core, and not as a result of strongly heterogeneous *in situ* stress conditions.

For the 224 m wide surrounding damage zone, we found that the velocity measurements are scale-dependent. The elastic properties of the damage zone are similar to the intact host rock at small length-scales, but indicate that the rock is less rigid at larger length-scales. As no pore pressure anomaly was detected in the borehole, the velocity reduction seen at the field and log scale is most likely due to large-scale features such as fractures and small faults, which are not sampled in core plugs although, the effects of velocity dispersion cannot be eliminated as a factor.

A significant decrease in the elastic moduli of the foliated gouge relative to the surrounding material indicates that the gouge is considerably less rigid than the host and damage zone rock. This difference in compliance and lack of evidence indicating a zone of low effective stress support the argument that the SAF creeps due to intrinsically weak fault materials and not anomalous stress conditions.

Acknowledgements

Laboratory data used in this study were acquired at UW-Madison and PSU and are available from the author upon request. SAFOD log data was obtained from the International Continental Scientific Drilling Program (http://www-icdp.icdp-online.org/front_content.php?idcat=896). This work was funded by NSF grants EAR-0800648 and EAR-0746149 to H. Tobin. We thank Chris Marone and Demian Saffer for the use of their laboratory facilities at Pennsylvania State University. We also thank Hiroko Kitajima, Brett Carpenter, Andy Rathbun, Matt Fry, and Robert Valdez for running some of the ultrasonic velocity experiments. We also thank two

anonymous reviewers for their constructive comments and suggestions on an earlier version of the manuscript.

References

Bedrosian, P.A., M.J. Unsworth, G.D. Egbert, and C.H. Thurber (2004), Geophysical images of the creeping segment of the San Andreas fault: implications for the role of crustal fluids in the earthquake process, *Tectonophysics, 385*(1), 137-158, doi: 10.1016/j.tecto.2004.02.010.

Birch, F., (1960), The velocity of compressional waves in rocks to 10 kilobars, part 1, *J. Geophys. Res., 65*(4), 1083-1102.

Birch, F., (1961), The velocity of compressional waves in rocks to 10 kilobars, part 2, *J. Geophys. Res., 66*(7), 2199-2224.

Bourbie, T., O. Coussy, and B. Zinszneer (1987), *Acoustics of porous media*, Editions Technip, Paris, France.

Bradbury, K.K., D.C. Barton, J.G. Solum, S.D. Draper, and J.P. Evans (2007), Mineralogic and textural analyses of drill cuttings from the San Andreas Fault Observatory at Depth (SAFOD) boreholes: Initial interpretations of fault zone composition and constraints on geologic models, *Geosphere, 3*(5), 299-318.

Bradbury, K.K., J.P. Evans, J.S, Chester, F.M. Chester, and D.L. Kirschner (2011), Lithology and internal structure of the San Andreas fault at depth based on characterization of phase 3 whole-rock core in the San Andreas Fault Observatory at Depth (SAFOD) borehole, *Earth Planet. Sci. Lett., 310,* 131-144, doi: 10.1016/j.epsl.2011.07.020.

Brocher, T.M. (2005), Empirical relations between elastic wavespeeds and density in the earth's crust, *Bull. Seism. Soc. Am., 95*(6), 2081-2092, doi:10.1785/0120050077.

Budiansky, B., and R. O'Connell (1976), Elastic moduli of a cracked solid, *Int. J. Solids Structures, 12,* 81-97.

Caine, J.S., J.P. Evans, and C.B. Forster (1996), Fault zone architecture and permeability structure, *Geology, 24,* 1025-1028.

Carpenter, B.M., C. Marone, and D.M. Saffer (2011), Weakness of the San Andreas Fault revealed by samples from the active fault zone, *Nature Geoscience, 4,* 251-254, doi: 10.1038/ngeo1089.

Castagna, J.P., M.L. Batzle, and R.L. Eastwood (1985), Relationships between compressional-wave and shear-wave velocities in clastic silicate rocks, *Geophysics, 50*(4), 571-581.

Chester, F.M., and J.M. Logan (1987), Composite planar fabric of gouge from the Punchbowl Fault, California, *J. Struct. Geol., 9*, 621-634.

Christensen, N.I., (1985), Measurements of dynamic properties of rock at elevated temperatures and pressures, in *Measurements of Rock Properties at Elevated Pressures and Temperatures*, ASTM STP 869, edited by H.J. Pincus and E.R. Hoskins, pp. 93-107, Am. Soc. for Testing and Materials, Philadelphia.

Ellis, D.V., and J.M. Singer (2008), *Well Logging for Earth Scientists*, Springer, Netherlands.

Faulkner, D.R., C.A.L. Jackson, R.J. Lunn, R.W. Schlische, Z.K. Shipton, C.A.J. Wibberley, and M.O. Withjack (2010), A review of recent developments concerning the structure, mechanics and fluid flow properties of fault zones, *J. Struct. Geol., 32*, 1557-1575, doi: 10.1016/j.jsg.2010.06.009.

Gettemy, G.L., H.J. Tobin, J.A. Hole, and A.Y. Sayed (2004), Multi-scale compressional wave velocity structure of the San Gregorio Fault zone, *Geophys. Res. Lett., 31*, L06601, doi: 10.1029/2003GL018826.

Gettemy, G.L., and H.J. Tobin (2003), Tectonic signatures in centimeter-scale velocity-porosity relationships of Costa Rica convergent margin sediments, *J. Geophys. Res., 108*, B10,doi: 10.1029/2001JB000738.

Han, D., A. Nur, and D. Morgan (1986), Effects of porosity and clay content on wave velocities in sandstones, *Geophysics, 51*(11), 2093-2107.

Hashimoto, Y., H.J. Tobin, M. Knuth, and A. Harada (2011), Data report: compressional and shear wave velocity measurements on sediment in the hanging wall and footwall of megasplay fault, NanTroSEIZE Stage 1. *In Proc. IODP*, 314/315/316, edited by Kinoshita, M., Tobin, H., Ashi, J., Kimura, G., Lallemant, S., Screaton, E.J., Curewitz, D., Masago, H., Moe, K.T., and the Expedition 314/315/316 Scientists, Washington, DC (Integrated Ocean Drilling Program Management International, Inc.). doi:10.2204/ iodp.proc.314315316.217.2011.

Henyey, F.S., and N. Pomphrey (1982), Self-consistent elastic moduli of a cracked solid, *Geophys. Res. Lett., 9*(8), 903-906.

Holdsworth, R.E. E.W.E. van Diggelen, C.J. Spiers, J.H.P. de Bresser, R.J. Walker, and L. Bowen (2011), Fault rocks from the SAFOD core samples: Implications for weakening at shallow depths along the San Andreas Fault, California, *J. Struct. Geol., 33*(2), 132-144, doi: 10.1016/j.jsg.2010.11.010.

Janssen, C., R. Wirth, A. Reinicke, E. Rybacki, R. Naumann, H. Wenk, and G. Dresen (2011), Nanoscale porosity in SAFOD core samples (San Andreas Fault), *Earth Planet. Sci. Lett., 301,* 179-189, doi: 10.1016/j.epsl.2010.10.040.

Jeanne, P., Y. Guglielmi, and F. Cappa (2012), Multiscale seismic signature of a small fault zone in a carbonate reservoir: Relationships between v_p imaging, fault zone architecture and cohesion, *Tectonophysics*, *554-557*, 185-201.

Jeppson, T.N., K.K. Bradbury, and J.P. Evans (2010), Geophysical properties within the San Andreas Fault Zone at the San Andreas Fault Observatory at Depth and their relationships to rock properties and fault zone structure, *J. Geophys. Res.*, *115*, B12423, doi: 10.1029/2010JB007563.

Kim, Y., D.C.P. Peacock, and D.J. Sanderson (2004), Fault damage zones, *J. Struct. Geol.*, *26*, 503-517.

Kowallis, B.J., L.E.A. Jones, and H.F. Wang (1984), Velocity-porosity-clay content systematics of poorly consolidated sandstones, *J. Geophys. Res.*, *89*(B12), 10355-10364.

Li, Y., F.M. Chester, and J.E. Vidale (2001), Shallow seismic profiling of the exhumed Punchbowl fault zone, Southern California, *Bull. Seism. Soc. Am.*, *91*(6), 1820-1830, doi: 10.1785/0120000050.

Li, Y., and P.E. Malin (2008), San Andreas Fault damage at SAFOD viewed with fault-guided waves, *Geophys. Res. Lett., 35*(8), doi: 10.1029/2007GL032924.

Li, Y., J.E. Vidale, and E.S. Cochran (2004), Low-velocity damaged structure of the San Andreas Fault at Parkfield from fault zone trapped waves, *Geophys. Res. Lett., 31*, L12S06, doi: 10.1029/2003GL019044.

Li, Y., P. Chen, E.S. Cochran, J.E. Vidale, and T. Burdette (2006), Seismic evidence for rock damage and healing on the San Andreas Fault associated with the 2004 M 6.0 Parkfield earthquake, *Bull. Seism. Soc. Am., 96*(4B), S349-S363, doi: 10.1785/0120050803.

Lockner, D.A., C. Morrow, D. Moore, and S. Hickman (2011), Low strength of deep San Andreas fault gouge from SAFOD core, *Nature*, *472*, 82-85, doi: 10.1038/nature09927.

Mavko, G., T. Mukerji, and J. Dvorkin (2009), *The Rock Physics Handbook*, Cambridge University Press, Cambridge, UK.

Moore, D.E., and M.J. Rymer (2007), Talc-bearing serpentinite and the creeping section of the San Andreas fault, *Nature, 448*, 795-77, doi: 10.1038/nature06064.

Morrow, C.A., D.A. Lockner, D.E. Moore, and S. Hickman (2014), Deep permeability of the San Andreas Fault from San Andreas Fault Observatory at Depth (SAFOD) core samples, *J. Struct. Geol., 64,* 99-114, doi: 10.1016/j.jsg.2013.09.009.

O'Connell, R.J., and B. Budiansky (1974), Seismic velocities in dry and saturated cracked solids, *J. Geophys. Res., 79*(35), 5412-5426.

Rempe, M., T. Mitchell, J. Renner, S. Nippress, Y. Ben-Zion, and T. Rockwell (2013), Damage and seismic velocity structure of pulverized rocks near the San Andreas Fault, *J. Geophys. Res., 118*(6), 2813-2831, doi: 10.1002/jgrb.50184.

Rice, J.R. (1992), Fault stress states, pore pressure distributions, and the weakness of the San Andreas fault, *Int. Geophys., 51,* 475-503, doi: 10.1016/S0074-6142(08)62835-1.

Rider, M., and M. Kennedy (2011), *The Geological Interpretation of Well Logs*, Rider-French, Scotland.

Schleicher, A.M., B.A. van der Pluijm, and L.N. Warr (2010). Nanocoatings of clay and creep of the San Andreas fault at Parkfield California, *Geology, 38*(7), 667-670, doi: 10.1130/G31091.1.

Shipton, Z.K., and P.A. Cowie (2003), A conceptual model for the origin of fault damage zone structures in high-porosity sandstone, *J. Struct. Geol*., *25,* 333-344.

Sills, D.W. (2010), The fabric of clasts, veins, and foliations within the actively creeping zones of the San Andreas fault at SAFOD: Implications for deformation processes, M.S. thesis, Dep. of Geol. And Geophys., Texas A&M Univ., College Station, Texas, USA.

Song, I., M. Suh, Y. Woo, and T. Hao (2004), Determination of the elastic modulus set of foliated rocks from ultrasonic velocity measurements, *Engineering Geology, 72*, 293-308, doi: 10.1016/j.enggeo.2003.10.003.

Stierman, D.J., and R.L. Kovach (1979), An *in situ* velocity study: The Stone Canyon well, *J. Geophys. Res., 84*(B2), 672-678.

Tembe, S., D. Lockner, and T. Wong (2009), Constraints on the stress state of the Sand Andreas Fault with analysis based on core and cuttings from San Andreas Fault of Observatory at Depth (SAFOD) drilling phases 1 and 2, *J. Geophys. Res., 114*(B11), doi: 10.1029/2008JB005883.

Thayer, M. (2006), Structural geology of the San Andreas Fault Zone at Middle Mountain, near Parkfield, central California, M.S. thesis, Dep. Of Geological Sci., Arizona State Univ., Phoenix, Arizona, USA.

Thurber, C., S. Roecker, K. Roberts, M. Gold, L. Powell, and K. Rittger (2003), Earthquake locations and three-dimensional fault zone structure along the creeping section of the San Andreas fault near the Parkfield, CA: Preparing for SAFOD, *Geophys. Res. Lett., 30*(3), doi: 10.1029/2002GL016004.

Thurber, C., S. Roecker, H. Zhang, S. Baher, and W. Ellsworth (2004), Fine-scale structure of the San Andreas fault zone and location of the SAFOD target earthquakes, *Geophys. Res. Lett, 31,* L12S02, doi: 10.1029/2003GL019398.

Tosaya, C.A. (1982), Acoustic properties of clay bearing rocks, Ph.D dissertation, Dep. of Geophys., Stanford Univ., Stanford, California, USA.

Tosaya, C., and A. Nur (1982), Effects of diagenesis and clays on compressional velocities in rocks, *Geophys. Res. Lett., 9*(1), 5-8.

Trippetta, F., C. Collettini, S. Vinciguerra, and P.G. Meredith (2010), Laboratory measurements of the physical properties of Triassic Evaporites from Central Italy and correlation with geophysical data, *Tectonophysics*, *492*, 121-132.

Unsworth, M.J., P.E. Malin, G.D. Egbert, and J.R. Booker (1997), Internal structure of the San Andreas fault at Parkfield, California, *Geology*, *25*(4), 359-362, doi: 10.1130/0091-7613(1997).

Unsworth, M.J., and P.A. Bedrosian (2004), Electrical resistivity structure at the SAFOD site from magnetotelluric exploration, *Geophys. Res. Lett., 31*, L12S05, doi: 10.1029/2003GL019405.

Vermilye, J.M. and C.H. Scholz (1998) The process zone: A microstructural view of fault growth, *J. Geophys. Res., 103*(B6), 12223-12237.

Waldhauser, F., W.L. Ellsworth, D.P. Schaff, and A. Cole (2004), Streaks, multiplets, and holes: High-resolution spatio-temporal behavior of Parkfield seismicity, *Geophys. Res. Lett., 31*, L18608, doi: 10.1029/2004GL020649.

Winkler, K.W. (1983), Frequency dependent ultrasonic properties of high-porosity sandstones, *J. Geophys. Res., 88*(B11), 9493-9499.

Winkler, K.W. (1986), Estimates of velocity dispersion between seismic and ultrasonic frequency, *Geophys. 51*(1), 183-189.

Winkler, K.W., and T.J. Plona (1982), Technique for measuring ultrasonic velocity and attenuation spectra in rocks under pressure, *J. Geophys. Res.*, 87(B13), 10776-10780, doi: 10.1029/JB087iB13p10776.

Zhang, H., and C. Thurber (2005), Adaptive mesh seismic tomography based on tetrahedral and Voronoi diagrams: Application to Parkfield California, *J. Geophys. Res*, *110*(B04303), doi:10.1029/2004JB003186.

Zhang, H., C. Thurber, and P. Bedrosian (2009), Joint inversion for v_p, v_s, and v_p/v_s at SAFOD, Parkfield, California, *Geochem. Geophys. Geosyst.*, *10*, Q11002, doi:10.1029/2009GC002709.

Zoback, M.D., S. Hickman, and W. Ellsworth (2005), Overview of SAFOD phases 1 and 2: Drilling, sampling and measurements in the San Andreas Fault Zone at seismogenic depth, *Eos Trans. AGU*, *86*(52), Fall Meet. Suppl., Abstract T23E–01.

Zoback, M.D., S. Hickman, and W. Ellsworth (2010), Scientific drilling into the San Andreas Fault Zone, *EOS Trans. AGU, 91* (22), 197–204, doi: 10.1029/2010EO220001.

Zoback, M., S. Hickman, W. Ellsworth, and SAFOD Science Team (2011), Scientific drilling into the San Andreas fault zone - An overview of SAFOD's first five years, *Sci. Drill.*, *11*, 14-28, doi: 10.2204/iodp.sd11.02.2011.

2.6 Appendix

2A.1 Supplementary material

Introduction

The supplementary material provided here includes an expanded methods section, example waveforms with wave arrival determinations, and a table with data on the salinity of saturating fluid used in the experiments.

Expanded methods

Samples analyzed in this paper were measured either at the University of Wisconsin – Madison (UW) or at Pennsylvania State University (PSU). Similar methods were followed at both locations but with slight variations based on equipment set up. Hard, intact samples were prepared using a drill press and surface grinder while softer, delicate samples were prepared by hand with precision knives and sandpaper. Once the samples were trimmed, room-dry samples were loading into standard triaxial TEMCO pressure vessels available at both locations. Both locations used syringe pumps to control confining, axial, and pore fluid pressures. Samples were placed under a confining pressure of 1000 kPa before being saturated. Samples were saturated by creating a pressure differential across the sample. At PSU this was done by attaching a vacuum pump to one side of the sample and pumping brine (Table 2A.1.1) through at the other side. At UW the pressure differential was created by leaving one side of the sample open to atmosphere and pumping water through at the other end of the sample. In both cases once water began flowing out the open (or vacuumed) end of the sample that side was connected to the syringe pump so brine was flowing into both ends of the sample and pore pressure was increased to 500 kPa. Then the confining pressure was raised to 2 MPa and pore pressure was increased to 1 MPa before leaving the sample so saturate for ≥12 hours. After saturation, the confining pressure was raised to the measurement pressure and we allowed the sample to equilibrate after each pressure increase. Pore pressure was held constant at 1 MPa throughout the test to ensure that pore space gas was kept in solution. After equilibration, monitored by continuous measurement of pump volume and sample length using a linear potentiometer displacement transducer (LPT) attached to the axial ram, we recorded P- and S-wave speeds. Pulses were generated and recorded using 500 kHz central frequency piezoelectric transducers embedded in the endcaps. The setup of the transducers at UW allows three separate waveforms to be recorded (P, SH, and SV) (Fig. 2A.1.1) while at PSU only one waveform was recorded (Fig. 2A.1.2). To be consistent with the PSU data the SH- and SV-wave speeds measured at UW were averaged. The sample length used in calculating the wave speed was determined from the displacement recorded by the LPT.

The LPT displacement was also used to calculate an estimate of the density and porosity at pressure. The axial strain was calculated and we assumed that displacement was due to the

closure of pores and microcracks. Based on this assumption we subtracted the axial strain from the porosity to estimate the porosity at pressure. The LPT displacement was also used to estimate the sample length which was used to determine the sample volume at pressure and thus the density.

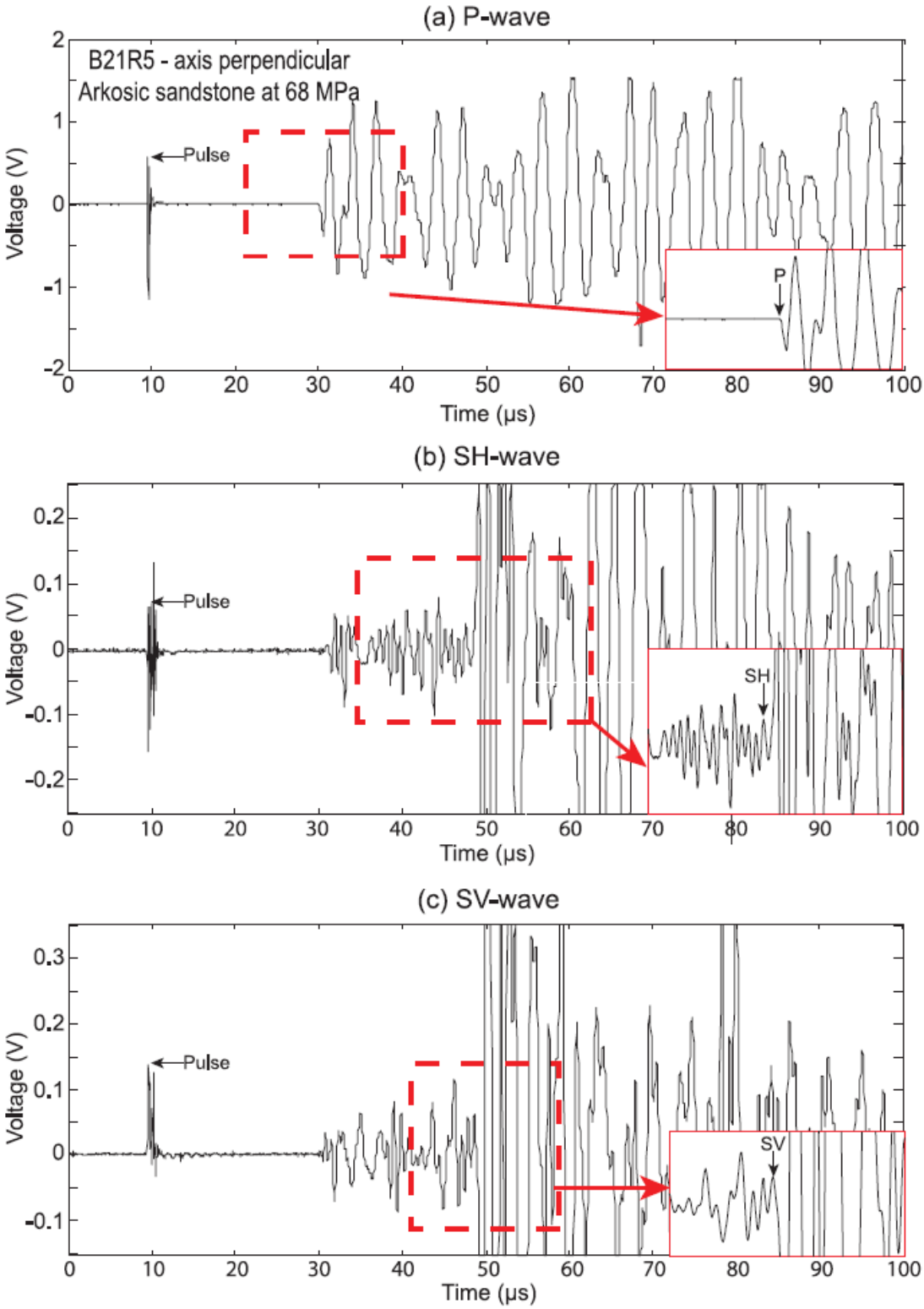

Figure 2A.1.1*: Example of raw waveforms measured at the University of Wisconsin-Madison with insets showing (a) P-, (b) SH-, and (c) SV-wave determinations.*

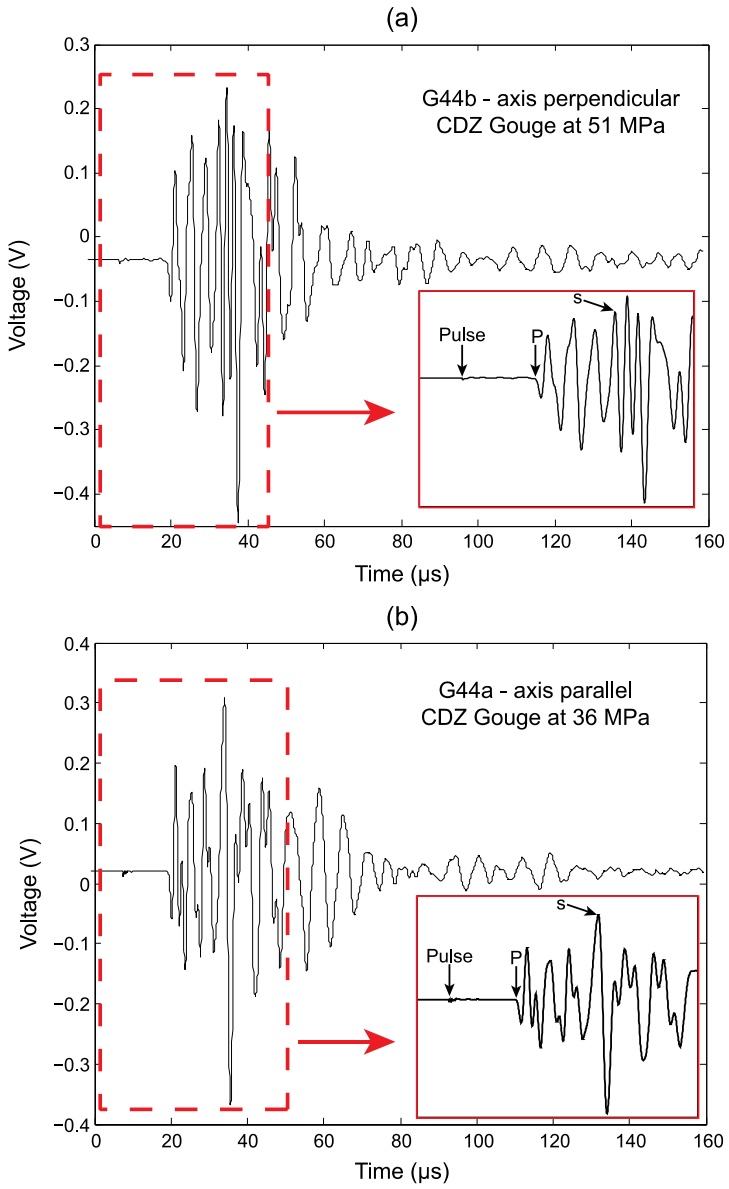

Figure 2A.1.2: *Example of raw waveforms measured at Pennsylvania State University with insets showing P- and S-wave determinations for (a) axis perpendicular and (b) axis parallel samples of the CDZ gouge.*

Table 2A.1.1: *Salinity of saturating fluid used in experiments.*

Salt	Concentration (g/L)
NaCl	14.5
CaCl	9.2
KCl	0.4

3 Analysis of Deep Fault Drilling Project phase 2 sonic log data

Abstract

I present an analysis of the sonic logging data acquired during the second phase of the Deep Fault Drilling Project (DFDP-2). Two different tools, the Mount Sopris 2PSA-1000 and QL40-FWS, were deployed in the borehole. Initial automatically determined slowness logs were clearly inaccurate so a more robust reprocessing of the data was needed. I reprocessed the raw sonic waveform data using semblance-time methods. This analysis showed that the data acquired using the 2PSA-1000 tool were unusable. However, reprocessing of the QL40-FWS data yielded slowness logs that provide a significantly better estimate of compressional and shear wave slowness. The average compressional and shear wave values are 68 μs/ft and 110 μs/ft, respectively, which correspond to velocities of 4.5 km/s and 2.8 km/s. The logs remain relatively constant throughout the borehole with some excursions related to fractures, borehole conditions, and tool settings, but no net downhole trends.

3.1 Introduction

The basic sonic logging tool transmits and receives sonic wave pulses that propagate in the wall rock, travelling largely parallel to the borehole axis. The received waveform data is recorded by the tool and can be used to determine the formation slowness, travel time per foot for a wave propagating through the formation. Many tool and software combinations do some initial automated processing of the waveform data. However, if the data quality is low, the initial results can be of poor quality and give inaccurate or meaningless slowness values, in which case it is necessary to manually check the sonic log data quality and process the data to obtain a robust estimate of the formation slowness. In this chapter I examine sonic log data obtained during the second phase of the Deep Fault Drilling Project (DFDP) located along the Alpine Fault on the West Coast of the South Island, New Zealand (Fig. 3.1).

3.1.1 Sonic logging

A brief review of sonic logging methods is provided here. More detailed discussions can be found in *Paillet and Cheng* [1991], *Ellis and Singer* [2008], and *Rider and Kennedy* [2011].

The wireline sonic tool is ideally suspended in the center of the borehole. A wave pulse is transmitted by the tool into the surrounding drilling mud. The wave propagates through the mud and is refracted at the borehole wall; the wave then travels through the formation close to the borehole wall. As the wave propagates through the formation, some of its energy is refracted back into the mud where it is detected by the tool's receivers. Much of the wave trajectory ends up being through the mud instead of the formation. To approximate the formation slowness two or more receivers are used to determine the normal moveout correction. Moveout refers to the effect of source-receiver distance on the wave arrival times. This effect is corrected for by fitting a line to a plot of arrival times versus source-receiver offset. As waves travelling to different

receivers should spend the same amount of time moving through the borehole mud so the slope of the line is the formation slowness averaged over the length of the receiver array.

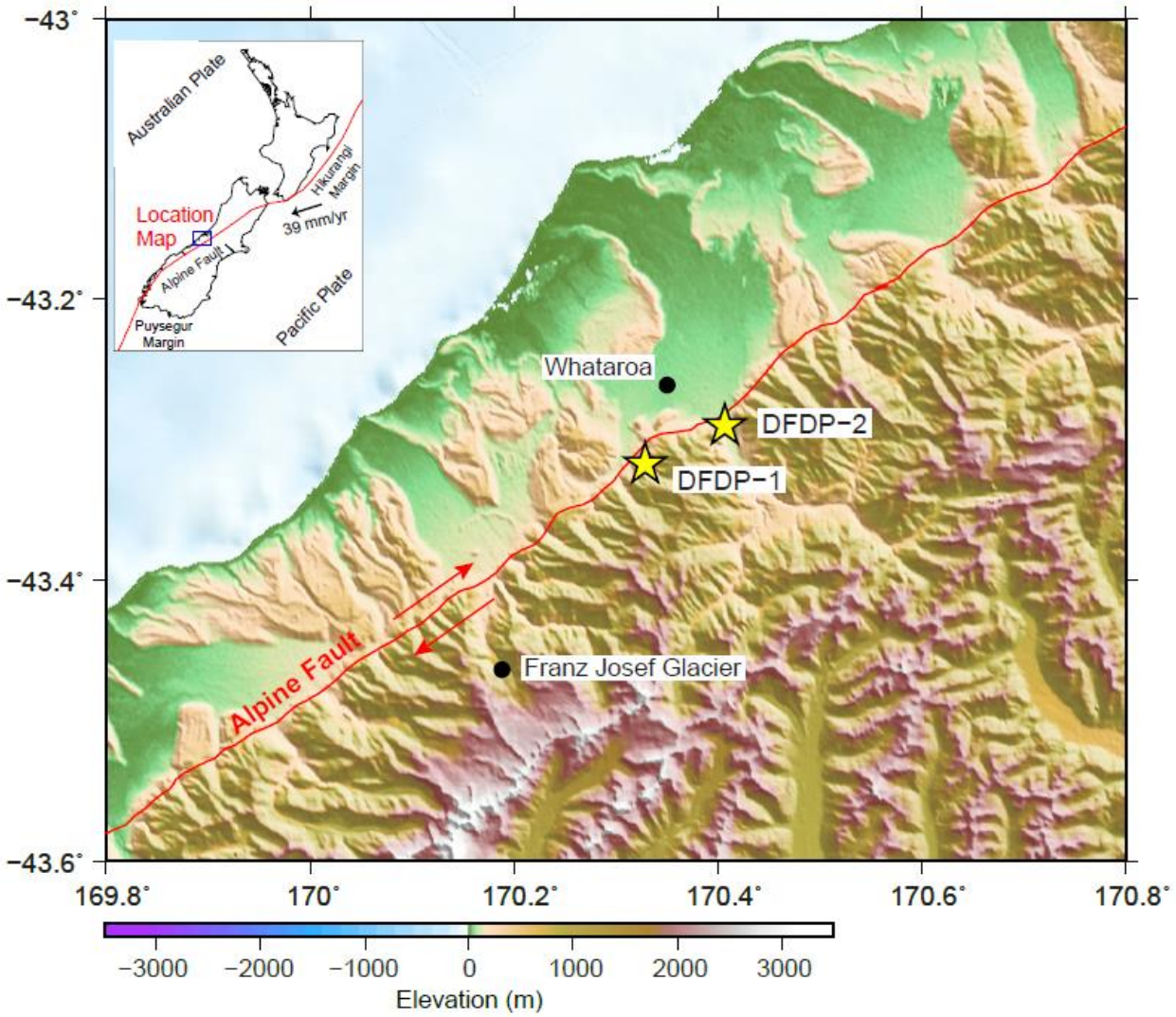

Figure 3.1: *Map showing the locations of the DFDP-1 and DFDP-2 boreholes (yellow stars).*

3.1.1.1 Sources

The transmitters used on sonic tools are commonly either monopole or dipole sources [*Rider and Kennedy*, 2011]. The monopole source emits a multi-directional compressional wavefront. The frequency of this wave is usually between 1 and 20 kHz. At the borehole wall the waves are converted into two refracted wave modes – compressional and shear. The monopole source

generates a compressional wave signal and a refracted shear wave is generated at the borehole wall, but it is only observed if the shear velocity of the formation is faster than the velocity in the drilling mud; this is known as a fast formation. If the formation shear velocity is slower than the mud velocity (slow formation) the refracted shear wave arrival is not observed. In the case of slow formations a dipole source must be used to obtain the formation shear wave velocity. A dipole source creates a directed pulse that generates a flexural wave. The flexural wave is dispersive, at low frequencies the velocity is approximately equivalent to the shear wave velocity of the formation. At higher frequencies, the velocity approaches the velocity of a Scholte surface wave propagating at the interface between the borehole fluid and wall [*Schmitt*, 1988]. The dipole source is usually operated in the frequency range of 1 to 6 kHz.

3.1.2 Deep Fault Drilling Project (DFDP)

The DFDP has occurred in two phases. The first phase (DFDP-1) occurred in early 2011 when two vertical boreholes were drilled into the Alpine Fault Zone at Gaunt Creek. The boreholes were drilled to depths of 100.6 m and 151.4 m using percussion techniques, wireline coring, and rotary drilling [*Sutherland et al.*, 2012; *Townend et al.*, 2013]. Following drilling, suite of wireline geophysical logs was acquired. The results of the logging program are presented in *Townend et al.* [2013].

In 2014 the second phase of DFDP drilling (DFDP-2) occurred in the Whataroa River Valley. A deviated borehole was drilled to a measured depth of 892 mbrt (meters below rig table, ~ 817 m true vertical depth) using conventional open-hole drilling and the dual-rotary methods [*Sutherland et al.*, 2015, 2017]. All depths mentioned in this paper are measured depths unless otherwise noted. Based on analysis of drill cuttings, the borehole penetrated a sequence of Quaternary gravel and lake silt underlain by Alpine schist, protomylonite, and mylonite of the

eastern (hanging wall) side of the Alpine Fault [*Toy et al.*, in review]. A suite of logging tools was deployed below casing (243.0 m) multiple times which allowed many sections of the hole to be re-logged. A total of 52 logging runs occurred over 20 logging sessions. The full logging program is discussed in *Sutherland et al.* [2015]. This chapter focuses on the processing of the sonic log data acquired over six runs using two different tools: the Mount Sopris 2PSA-1000 and QL40-FWS (Table 3.1; Table 3.2). The QL40-FWS has a monopole source and was the main sonic tool used.

Table 3.1: *Sonic tool specifications.*

Tool	Length (m)	Diameter (mm)	Sampling rate (us)	Number of receivers	Receiver spacing (m)	Transmitter-receiver offset (m)	Assigned measurement location	Max. Temperature (˚C)
QL40-FWS	2.14	50.00	4	4	0.20	0.60	transmitter	70
2PSA-1000	3.16	44.45	4	2	0.30	0.91	bottom of tool	70

Runs 12, 23, 45, and 49 were acquired using the QL40 9. During run 12 the QL40-FWS tool was run with the flow meter which required the tool string to be run four times from bottom of casing to 322 mbrt. The first two runs were conducted at a logging speed of 4 m/min and the last two runs were conducted at 8 m/min. For run 23 the first pass started at the bottom of casing and was interrupted at 334 mbrt due to communication problems. After restarting the tool a short upward pass was conducted to make sure the problem had been corrected. The third pass continued the downward motion from 330 mbrt to 390 mbrt. The final up going pass recorded continuously from 390 to 260 mbrt. During run 45 the temperature near the bottom of the hole exceeded the recommended maximum temperature for the tool. The first pass of the run started logging at a speed of 4 m/min but the speed was increased to 8 m/min below 770 mbrt where the temperature reached 78˚C and the pass was terminated at 812 mbrt when the temperature reached 82˚C. The

tool was brought up to shallower depths and two short passes were recorded around 750 mbrt and 699 mbrt. Run 49 was the final sonic tool run. The first pass recorded from bottom of casing to 823 mbrt where the temperature reached 79˚C. At this point a new pass was begun with a higher sampling interval (100 mm) and faster logging speed (18 m/min) to decrease exposure to the higher temperatures. This pass recorded from 823 mbrt to the final hole depth of 893 mbrt. The tool was then pulled up and the sample interval and logging speed were decreased before starting a third, up going, pass from 751 to 384 mbrt.

Table 3.2: *Sonic logging runs and tool settings.*

Run	Pass	Direction	Top depth (mbrt*)	Bottom depth (mbrt)	Tool	Mode	Frequency (kHz)	Logging speed (m/min)	Sampling interval (mm)
12	1	down	255.39	321.99	QL40-FWS	Mono	6	4	50
	2	up	255.06	321.96			6	4	50
	3	down	255.07	322.02			6	8	50
	4	up	254.92	321.97			6	8	50
23	1	down	262.12	333.72	QL40-FWS	Mono	6	4	50
	2	up	329.76	333.71			6	4	50
	3	down	329.76	389.96			6	4	50
	4	up	260.00	389.95			6	4	50
32	1	up	483.66	488.51	2PSA-1000	Mono	20	3	50
	2	up	406.42	487.92			20	2	50
	3	up	389.58	406.23			20	2.8	50
	4	up	320.80	389.05			20	2.9	50
	5	up	262.83	321.93			20	3	50
	6	up	481.75	488.25			1	3	50
	7	up	466.67	488.02			5	2.7	50
	8	up	263.58	488.33			1	3	50
33	1	up	458.15	488.10	2PSA-1008	Dipole	20	3	50
	2	up	262.22	457.92			15	3	50
45	1	down	260.38	812.13	QL40-FWS	Mono	6	variable	50
	2	up	749.98	750.43			6	4	50
	3	up	698.77	699.77			6	4	50
49	1	down	260.29	822.74	QL40-FWS	Mono	6	variable	50
	2	down	822.82	893.02			6	18	100
	3	up	384.13	750.73			6	4	50

*mbrt = meters below rotary table

The 2PSA has both dipole and monopole sources and was only deployed during runs 32 (monopole) and 33 (dipole). For run 32 the tool was set to monopole mode. The first pass was terminated after only logging 5 m because the gain was set too high. The second, third, and fourth passes were terminated at various depths due to communication problems and software crashes. The fifth pass recorded from 322 to 263 mbrt but still experienced communication problems. In an effort to improve data quality the sixth, seventh, and eighth passes were run to re-log the hole at a lower signal frequency. The sixth pass was run with a frequency of 1 kHz and was terminated due to a communication error. The frequency was increased to 5 kHz for the seventh pass but the signal did not show improvement so the pass was terminated and the eighth pass was run at 1 kHz from 488 mbrt to the bottom of casing. Prior to run 33, the tool was pulled out of the hole and set to run in the dipole configuration. The first pass was run at a frequency of 20 kHz and was terminated due to communication errors. The second run recorded from 458 mbrt to the bottom of casing with a 15 kHz frequency.

The initial slowness logs output by the QL40 tool software indicated the average compressional wave slowness is around 80 μs/ft but the logs are highly variable (Fig. 3.2). For the schists and mylonites in the area of the borehole it is expected that the slowness would range from about 50 to 90 μs/ft (6.1 – 3.4 km/s) for intact rock [cf., *Godfrey et al.*, 2000, 2002; *Christensen and Okaya*, 2007; *Guo et al.*, 2017]. The initial slowness logs are often outside of this range. Due to the unrealistic variation observed in the log it was deemed necessary to reprocess the raw waveform data. Additionally, separate P- and S-wave slowness logs were obtained during reprocessing of the data.

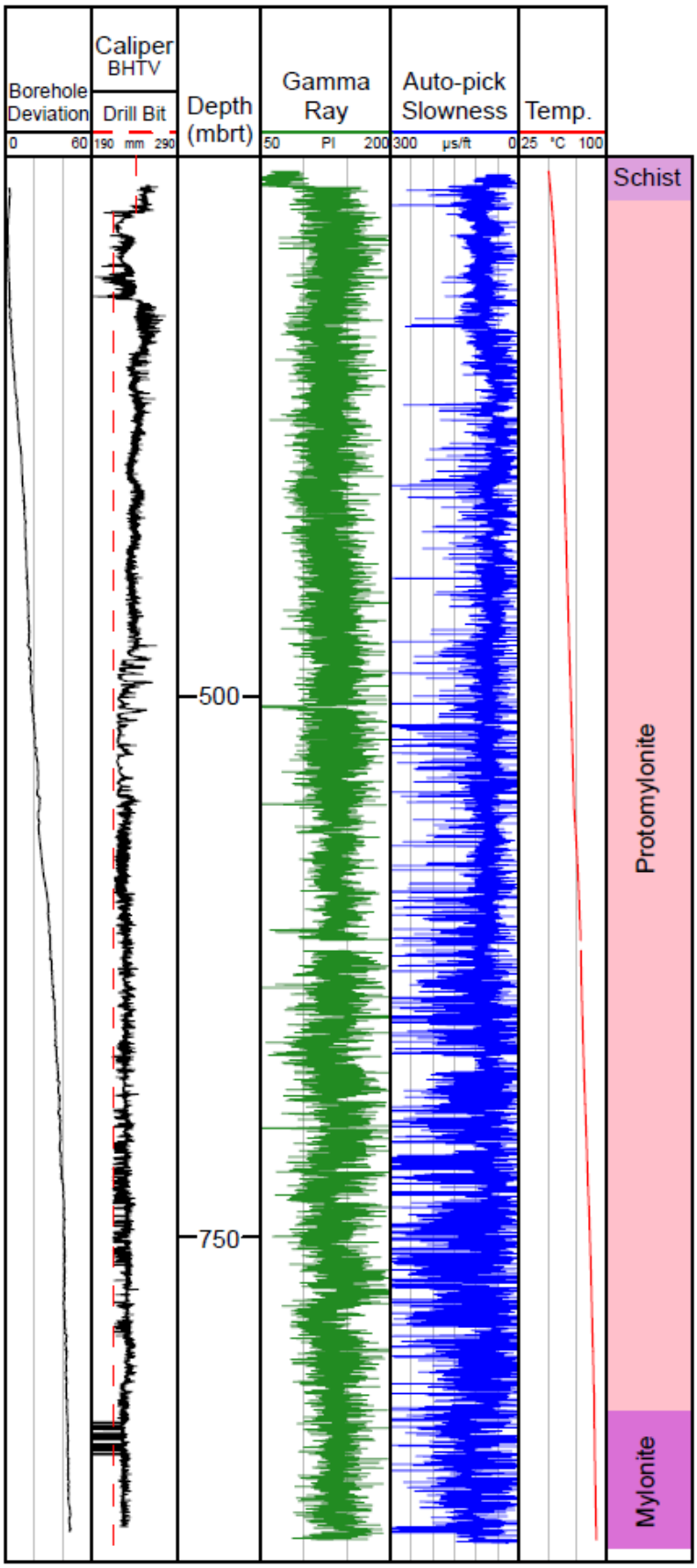

Figure 3.2: *Initial auto-picked slowness, selected wireline logs, and cuttings-based lithologic column as a function of measured depth along the DFDP-2B borehole. The auto-picked slowness is noisy, indicating the waveform data needed to be reprocessed.*

3.2 Full waveform sonic processing

I reprocessed the raw waveform data using the full waveform sonic module of Paradigm's Geolog software. This module uses slowness-time coherence processing to determine the formation slowness.

3.2.1 Data quality and preparation

The sonic log is very sensitive to borehole conditions and tool orientation. A large borehole, tilted tool, and washouts can result in significant attenuation and variations in the wave path length that will complicate the determination of the normal moveout correction [*Ellis and Singer*, 2008; *Rider and Kennedy*, 2011]. In severe cases the tool senses the borehole fluid instead of the formation. A caliper log should be used to evaluate the condition and shape of the borehole to determine areas where borehole conditions are likely to negatively affect the sonic log. However, due to the large deviation of the DFDP-2 borehole the arms of the mechanical caliper run in the hole had trouble opening correctly. An estimate of the caliper was obtained through analysis of borehole televiewer data (Fig. 3.2) [*Massiot*, 2017]. The televiewer data indicate that the borehole is enlarged by about 25 mm from 317 to 481 mbrt and by 11 mm from 481 mbrt to the bottom of the hole. The borehole has an approximately circular cross section and no breakouts were observed. This indicates that the borehole cross sectional shape should not have a significant effect on the sonic log, but the large diameter of the hole (~ 4 times the tool diameter) will increase attenuation. Additionally, the borehole deviates from vertical by up to 45˚; this deviation can cause the tool to be tilted or rest against one side of the borehole instead of being centered in the hole.

In general, waveforms acquired when the sonic tool was being pulled up are better than those acquired when the tool was being lowered into the hole because the speed at which the tool was moving was more consistent (Fig. 3.3). A slower logging speed is also preferred. For these

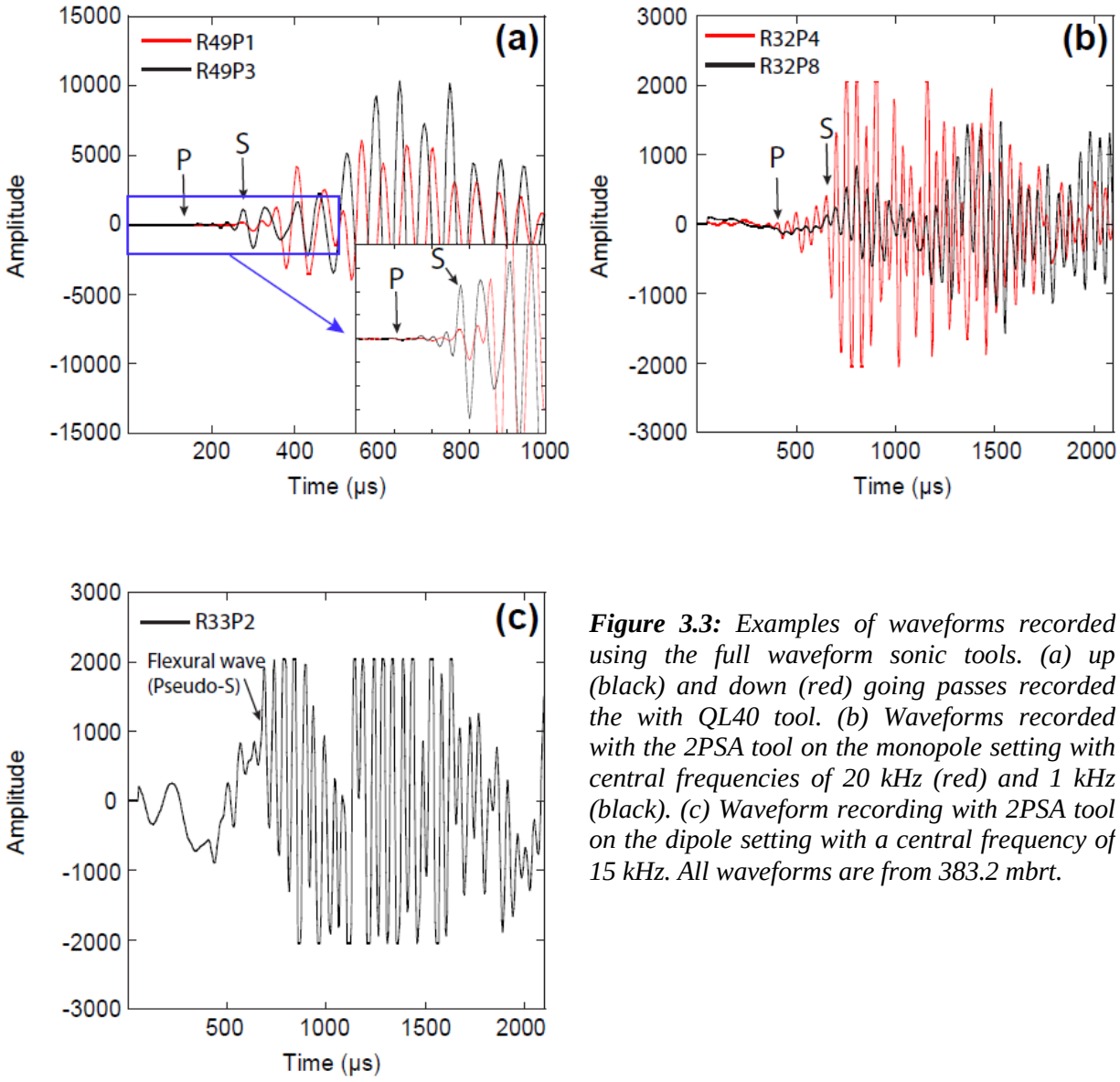

Figure 3.3: *Examples of waveforms recorded using the full waveform sonic tools. (a) up (black) and down (red) going passes recorded the with QL40 tool. (b) Waveforms recorded with the 2PSA tool on the monopole setting with central frequencies of 20 kHz (red) and 1 kHz (black). (c) Waveform recording with 2PSA tool on the dipole setting with a central frequency of 15 kHz. All waveforms are from 383.2 mbrt.*

reasons run 12 pass 2, run 23 pass 4, run 45 passes 2 and 3, and run 49 pass 3 are the preferred data files; however, they do not document the entire open hole. Run 49 passes 1 and 2 are the only passes through the hole below 750 mbrt, and both are down passes conducted at an above average logging speed (Table 3.2). The majority of energy is excited at frequencies between 10 and 30 kHz (Fig. 3.4). This range is higher than what is expected for the central frequency at which the tool was run. This is also on the high end of the recommended monopole frequency range. The high frequency will result in greater attenuation of the waveform making it more

difficult to identify the wave arrivals. Examining the waveforms acquired by the tools shows that the P-wave arrivals are very low amplitude (Fig. 3.3). In more advanced tools, each receiver has multiple elements and waveforms acquired by each element are summed to amplify signal and reduce noise, but that is not possible with these tools.

The repeated communication errors that occurred while running the 2PSA tool resulted in gaps in the data where no waveforms were acquired. This tool was run in monopole mode at both high (20 kHz) and low (1 kHz) frequencies. The gain appears to have been set too high during the high frequency runs, causing some of the peaks to be cut off, which may cause problems correlating the waveforms from different receivers (Fig. 3.3). Analysis of the waveform frequency spectrum shows that energy is excited over a broad range of frequencies, 0 to 30 kHz, regardless of tool settings (Fig. 3.4). When run in the dipole mode, the central frequency was set at 15 kHz or greater. This is much higher than the recommended frequency for dipole mode so the slowness of the generated flexural wave would have been faster than the formation's shear slowness due to frequency-dependent velocity dispersion. Additionally, the gain was still set too high causing parts of high amplitude wave peaks to be cut off, making it difficult to correlate across receivers. Due to these problems I do not examine the dipole data further.

After the data quality was examined the waveform data were formatted to match Geolog specifications. This required individual files acquired for each receiver to be compiled into one array file. The tool-specific parameters (Table 1) were stored with this file so that they were accessible to the software for calculations.

3.2.2 Pre-processing

Initially, the waveforms were processed without any filtering and subsequent processing iterations used bandpass filters to remove unwanted frequencies. I tested two main bandpass filters. The first removed frequencies outside of the 10 to 25 kHz range, where most of the

energy is excited for the QL40 and 2PSA high frequency waveforms. The second filter kept a lower frequency range of 5 to 15 kHz. Other frequency filters were tested but did not improve the quality of the results.

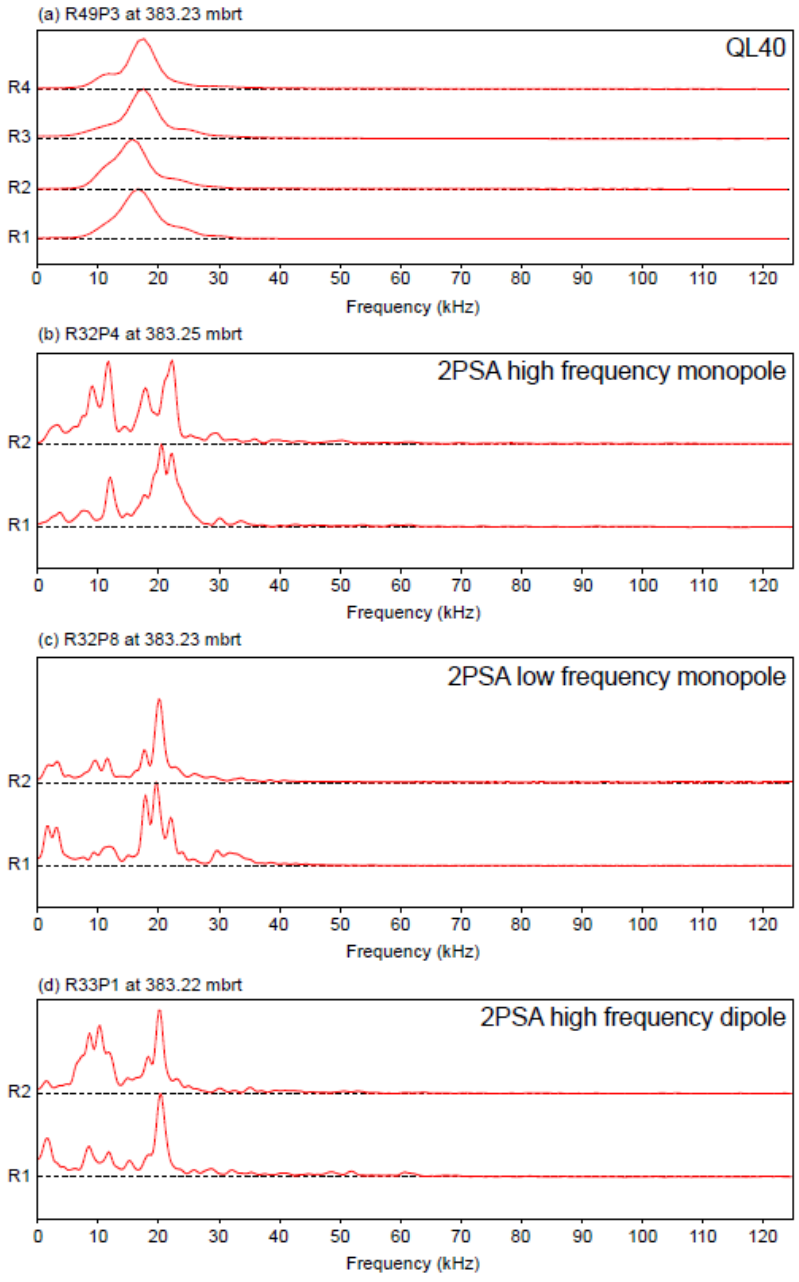

Figure 3.4: *Frequency spectra corresponding to waveforms collected by the QL40 and 2PSA tools at 383.2 mbrt. The QL40 tool has a narrow frequency spectrum (a) whereas the 2PSA has a broader frequency spectrum with a lot of energy excited around 20 kHz regardless of whether the tool settings were for a monopole source with a (b) high or (c) low central frequency or for a (d) dipole source with a high central frequency.*

3.2.3 Processing

Slowness-time semblance processing was performed using the Geolog module. The processing method determines the moveout correction required to obtain the maximum coherence between the waveforms acquired at each receiver at each depth. To do this the user defines a time window that is moved along the time axis of the waveforms at a specific time step. The time window must be wide enough to contain at least one period of the wave mode of interest. Two to five periods are recommended. A small time step will increase resolution but will also slow the processing time; a step of 20 μs, five times the waveform sampling rate of 4 μs, was selected to start with. It was later increased to 25 μs, which decreased the processing time without affecting data quality. At each time step the time window was rotated through a range of apparent velocities, also defined by the user, to correlate the waveforms. The coherence of the waveforms at each slowness and time step examined was determined and a semblance plot was created. A semblance plot is a contour map in the time-slowness domain that displays the calculated coherence (Fig. 3.5). The maximum coherence for each slowness at every measurement depth was compiled at each sample depth to form a projection log (Fig. 3.6). The processing constraints I used are provided in Table 3. Additional settings were tested but did not improve the results.

3.2.3.1 QL40

It is difficult to identify any clear wave arrivals in the projection log created using the unfiltered QL40 waveforms (Fig. 3.6). The coherence is rarely greater than 40%. The P-wave arrival is especially hard to identify, but the S-wave is more apparent at depths greater than 670 mbrt. The 10 to 25 kHz filter improves the data. The P-wave arrival is visible and coherence is increased but is still usually less than 40%. The low frequency filter (5 to 15 kHz) removes some of the smearing surrounding the P- and S-wave arrivals and increases the coherence in places,

especially the coherence of the tool arrival. However, this filter decreases the coherence of the P-wave arrival and the continuity of both the P- and S-wave arrivals, indicating that much of the desired signal is being removed.

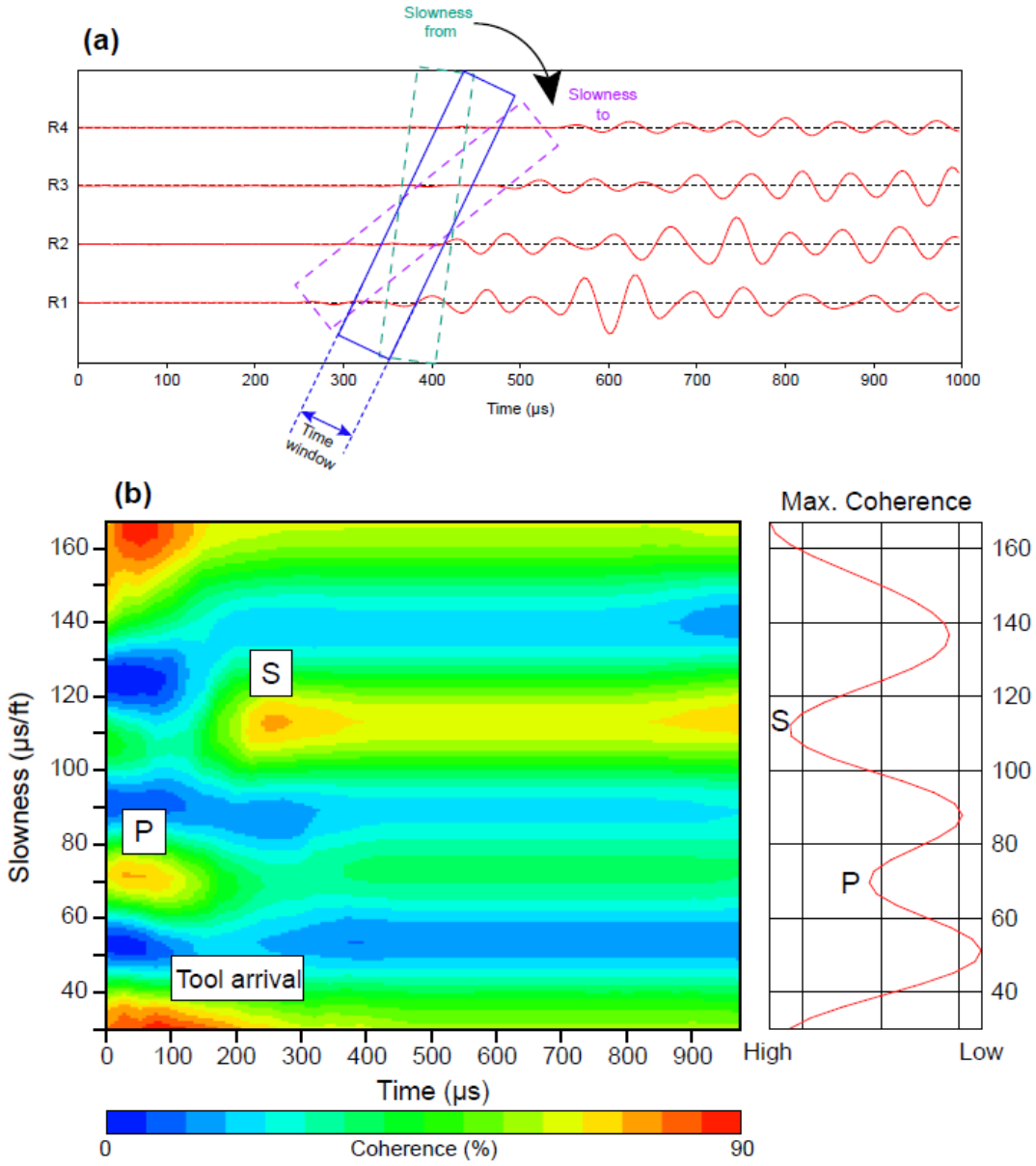

Figure 3.5: *a) Graphical representation of semblance processing in the slowness-time domain. A moving time window correlates the signal across the receivers. (b) Semblance plot for data acquired using the QL40 tool at 383.2 mbrt. A semblance plot is a contour plot of the calculated coherence in the slowness-time domain. The maximum coherences are used to generate a projection log.*

The low coherence of the arrivals could be caused by the tool being tilted in the borehole instead of parallel to the borehole wall. This tilt changes the distances the waves have to travel through the borehole to reach the different receivers such that different receivers may record varying amounts of travel time through the borehole mud. Since the processing method assumes the tool is centered and parallel to the borehole and travel time in the borehole mud is constant, it does not account for this additional variation in travel time.

Table 3.3: *Processing parameters used in Geolog.*

Time window	1600 μs
Time step	25 μs
Slowness from	30 μs/ft
Slowness to	170 μs/ft
Slowness step	3.48 /ft

I used the 10 to 25 kHz filtered projection to pick the slowness log. The other projection logs were referenced to help interpret areas of poor data quality. The initial picking was done automatically using the processing module. The auto-picked P- and S-waves were constrained to have a minimum v_p/v_s ratio of 1.3, preventing crossover of the P- and S-wave logs. Initial seed slownesses of 60 and 100 μs/ft were selected for P- and S-waves respectively. The automated picking software searches a 30 μs/ft window to either side of the seed value for the maximum coherence and corresponding slowness. I then manually reviewed the picked slowness logs and edited them if the picks were not realistic. This edited log was then used as a guide log for the automated picker and the search window was reduced to 20 μs/ft. If needed the log was again edited and rerun with a search window of 10 μs/ft. Finally the slowness logs were smoothed over 1 m using a moving average to remove anomalous spikes (Fig. 3.7).

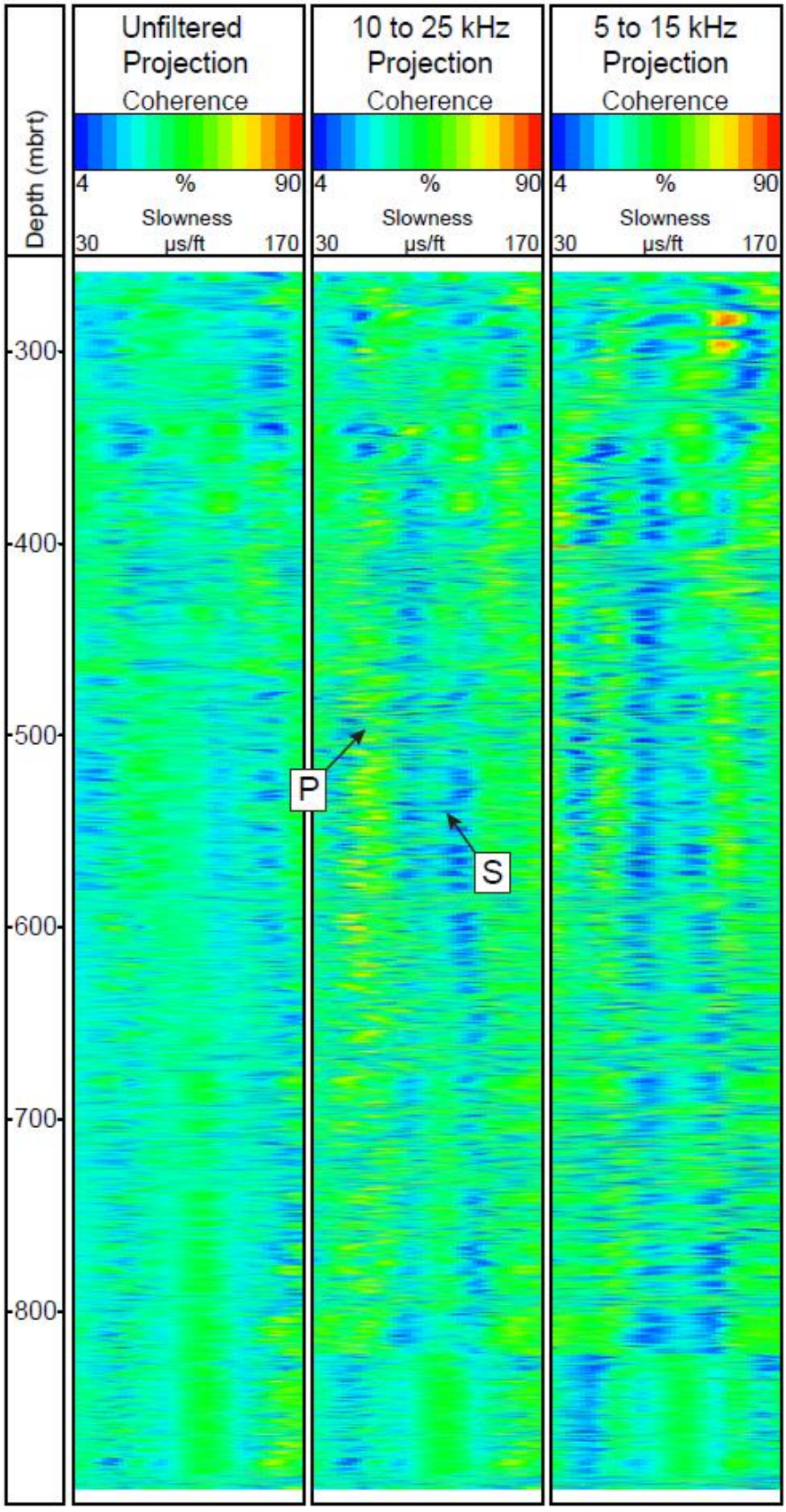

Figure 3.6: *Projection logs created using the unfiltered waveforms and waveforms passed through 10 to 25 kHz or 5 to 15 kHz bandpass filters. Waveforms were acquired using the QL40 tool.*

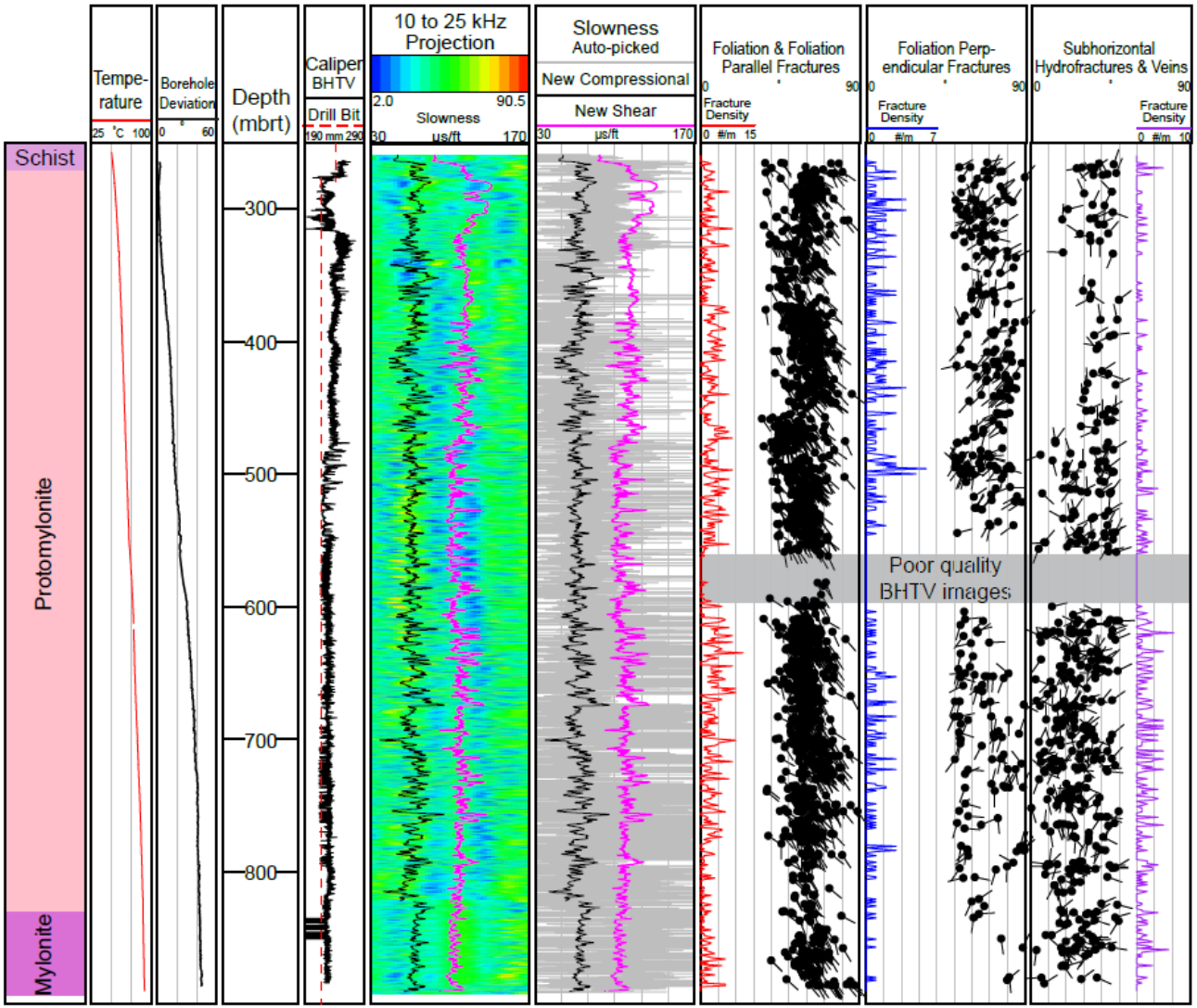

Figure 3.7: *Reprocessed P- and S-wave slowness logs, cutting-based lithologic column, and fracture data from Massiot [2017]. Reprocessed slowness logs provide a better estimate of formation slowness compared to the initial auto-picked slowness log. The gray shaded region indicates a zone where BHTV image quality prevented the identification of fractures and foliation.*

3.2.3.2 2PSA

Processing the monopole high frequency unfiltered waveforms resulted in numerous high coherency peaks in the projection plot. Due to similarity in appearance and spacing, these peaks appear to be multiples of each other (Fig. 3.8 & 3.9a). These coherence peaks are at slownesses that are faster than what is expected based on processing of the QL40 waveforms. Appling a frequency filter from 10 to 25 kHz did not remove the apparent multiples. I also tried running a narrower high frequency filter (15 to 25 kHz) centered around the tool's central frequency but that did not improve data quality. Running a low frequency filter removed most of the actual signal so wave arrivals were not observed in the projection. The semblance plots (Fig. 3.9a) show that the maximum coherence is found when a signal with a very late arrival time is correlated across waveforms recorded at different receivers. This signal arrives much too late to be either the P- or S-wave arrival.

The low frequency monopole data show occasional high coherence peaks (Fig. 3.8). Using the 10 to 25 kHz bandpass filter improves the signal quality by increasing the coherence but the peaks, like those of the high frequency monopole data, appear to be multiples (Fig. 3.9b). Running the lower frequency filter (5 to 15 kHz) again removes too much of the actual signal.

It is apparent the actual P- and S-wave arrivals are not being detected. The signals that are being correlated during processing are probably internal tool reflections. It is clear that the data obtained using this tool are of poor quality. The 2PSA tool is older than the QL40 and may have developed defects. Due to the poor data quality I did not pick the slowness logs for the 2PSA tool.

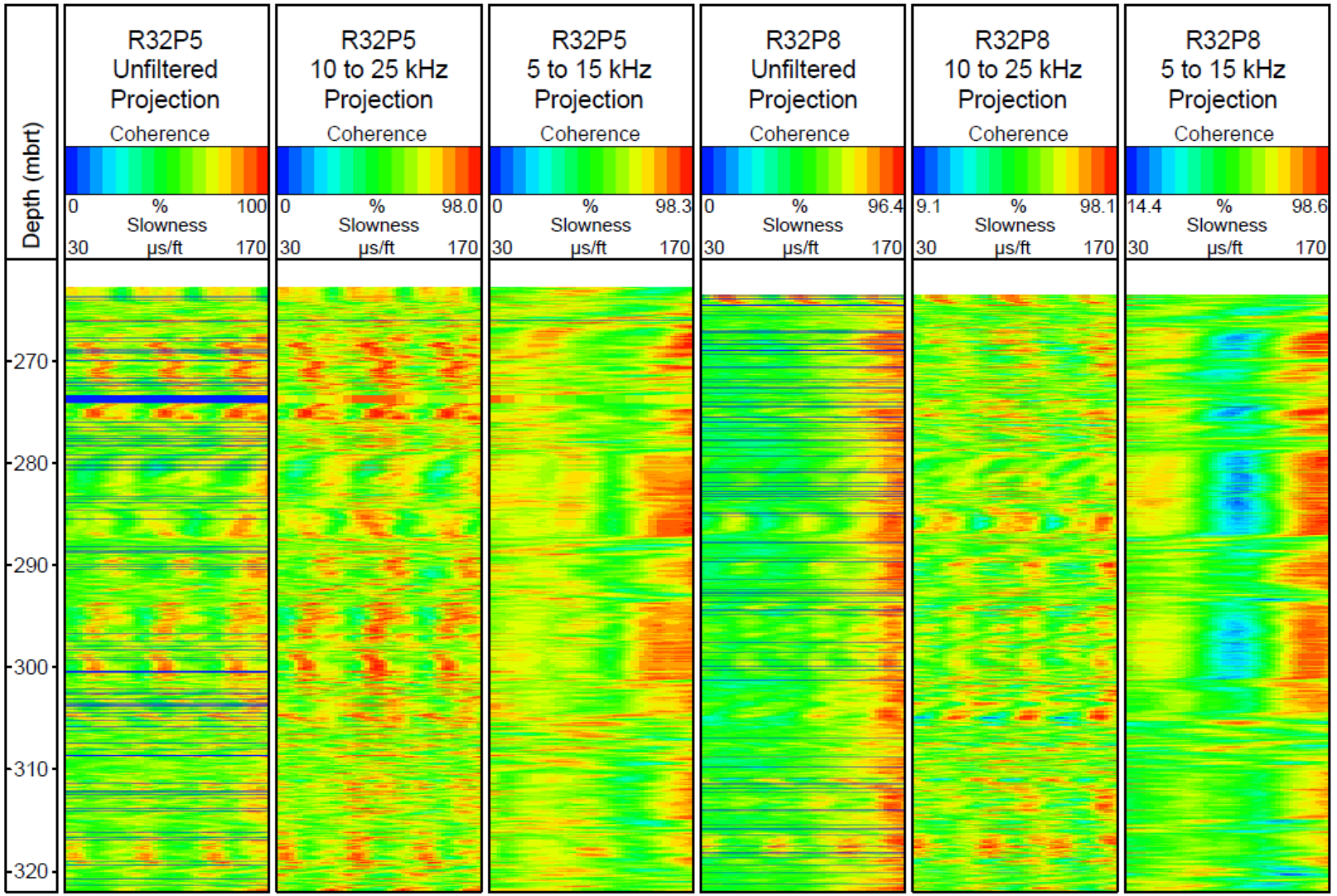

Figure 3.8: *Projection logs created using the unfiltered waveforms and waveforms passed through 10 to 25 kHz or 5 to 15 kHz bandpass filters. Waveforms were acquired using the 2PSA tool run with a monopole source.*

3.3 Discussion and conclusions

The automatically picked slowness jumped between P-wave, S-wave, tool, and potential Stoneley wave arrivals (Fig. 3.7). Careful reprocessing of the data has significantly improved the slowness logs by separating out the P- and S-wave slowness and removing unrealistically fast and slow excursions, although the data quality remains low. Slowness is relatively constant with depth, averaging around 68 μs/ft for P-waves and 110 μs/ft for S-waves, corresponding to velocities of 4.5 km/s and 2.8 km/s, respectively, with an average v_p/v_s ratio of 1.6. Seismic tomography, fault zone trapped waves, and laboratory data indicate the P- and S-wave velocities and v_p/v_s ratio at the depth of the borehole log should fall within ranges of 3.5 to 6 km/s, 2.3 to 3.7 km/s, and 1.5 to 2, respectively [*Godfrey et al.*, 2000, 2002; *Eberhart-Phillips and Bannister*, 2002; *Christensen and Okaya*, 2007; *Eccles et al.*, 2015; *Guo et al.*, 2017; *Chapter 4 this thesis*]. The Alpine Schist and mylonites have transverse to orthogonal anisotropy so the fastest velocities are measured when waves are propagating parallel to the foliation plane and the slowest velocities are obtained when wave propagation is perpendicular to foliation. The borehole intersects the foliation plane at an angle of 30˚ increasing to 90˚ with depth due to deviation of the borehole [*Massiot*, 2017]. The waves generated by the sonic tool were therefore propagating at an angle oblique to the foliation plane so, as discussed in chapter 4, the sonic log velocity falls between the two extrema measured in the lab on oriented samples. I do not observe a decrease is log velocity at depth related to changes in propagation angle with respect to foliation.

The slowness logs show that the acoustic properties of the Alpine Fault protomylonites are relatively homogenous. Analyses of cuttings acquired during drilling suggest there is a reduction in grain size with depth and an increase in chlorite + muscovite below 700 mbrt, but these

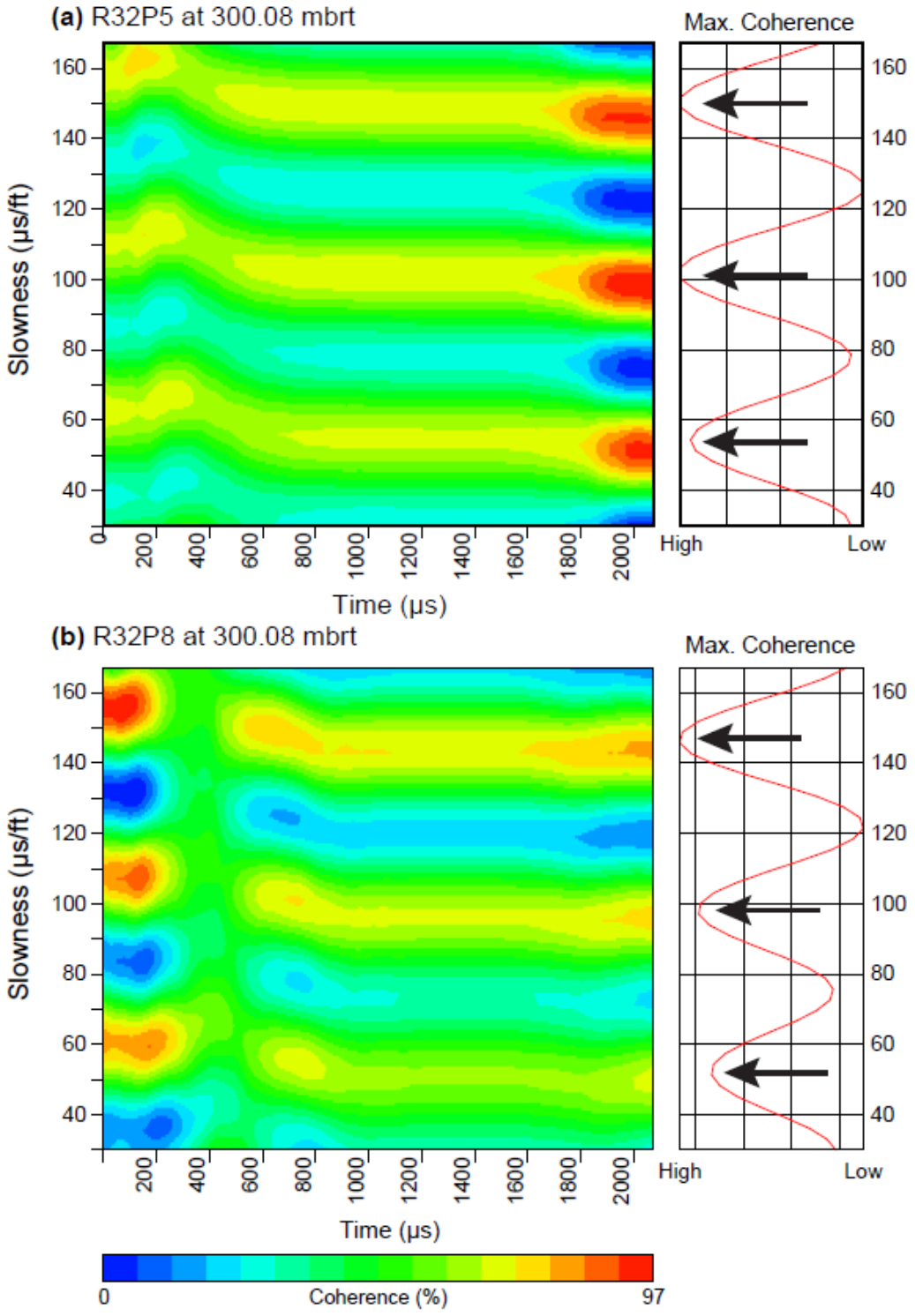

Figure 3.9: *Semblance plots at 300.08 mbrt for data acquired using the 2PSA tool run with a monopole source. Processing of the high (a) and low (b) frequency monopole data yields maximum coherences that do not correlate with expected P- or S-wave slownesses and appear to be multiples, as indicated by black arrows.*

variations may be due to variations in the drilling parameters instead of a lithologic change [*Toy et al.*, in review]. Overall, the cuttings indicate the borehole wall rock is relatively compositionally homogenous at this location, consistent with field observations of a fairly uniform hanging wall host rock for several hundred kilometers along strike [*Toy et al.*, in review; *Norris and Cooper*, 2007].

There are some notable excursions in the slowness log (Fig. 3.10). A zone of lower velocity from 279 to 303 mbrt is likely due to the high density of foliation perpendicular fractures observed in the televiewer images over this depth range [*Massiot*, 2017]. There is a slight downhole shift towards slower velocities and a decrease in variability at 475 mbrt that is most evident in the S-wave log. This shift corresponds to the depth of a shift in the BHTV-derived caliper that indicates the borehole diameter is smaller, suggesting that the shift in the sonic data is related to borehole conditions, rather than actual differences in rock properties. The greatest change in the slowness logs occurs in the P-wave slowness below 822 mbrt near the cuttings-defined boundary between the protomylonite and mylonite. At this depth the P-wave velocity decreases but there is no significant change in the S-wave, although the S-wave coherence peak is broad so there is uncertainty in the pick. This section was only logged during run 49 pass 2 and the tool settings were altered during this run to decrease the time spent above the recommend maximum temperature. The shift in slowness may be due to the transition from protomylonite to mylonite but such a sharp change in properties is unexpected for what is likely to be a gradual transition from protomylonite to mylonite. It is more likely that the shift in the slowness is an artifact caused by changes to the tool settings or the high temperature affecting the tool electronics. Smaller-scale, anomalously fast spikes in the data are related to poor data quality. High velocity

spikes at 701 and 754 mbrt correlate with high fracture density indicating that the decrease in data quality may be related to the presence of fractures.

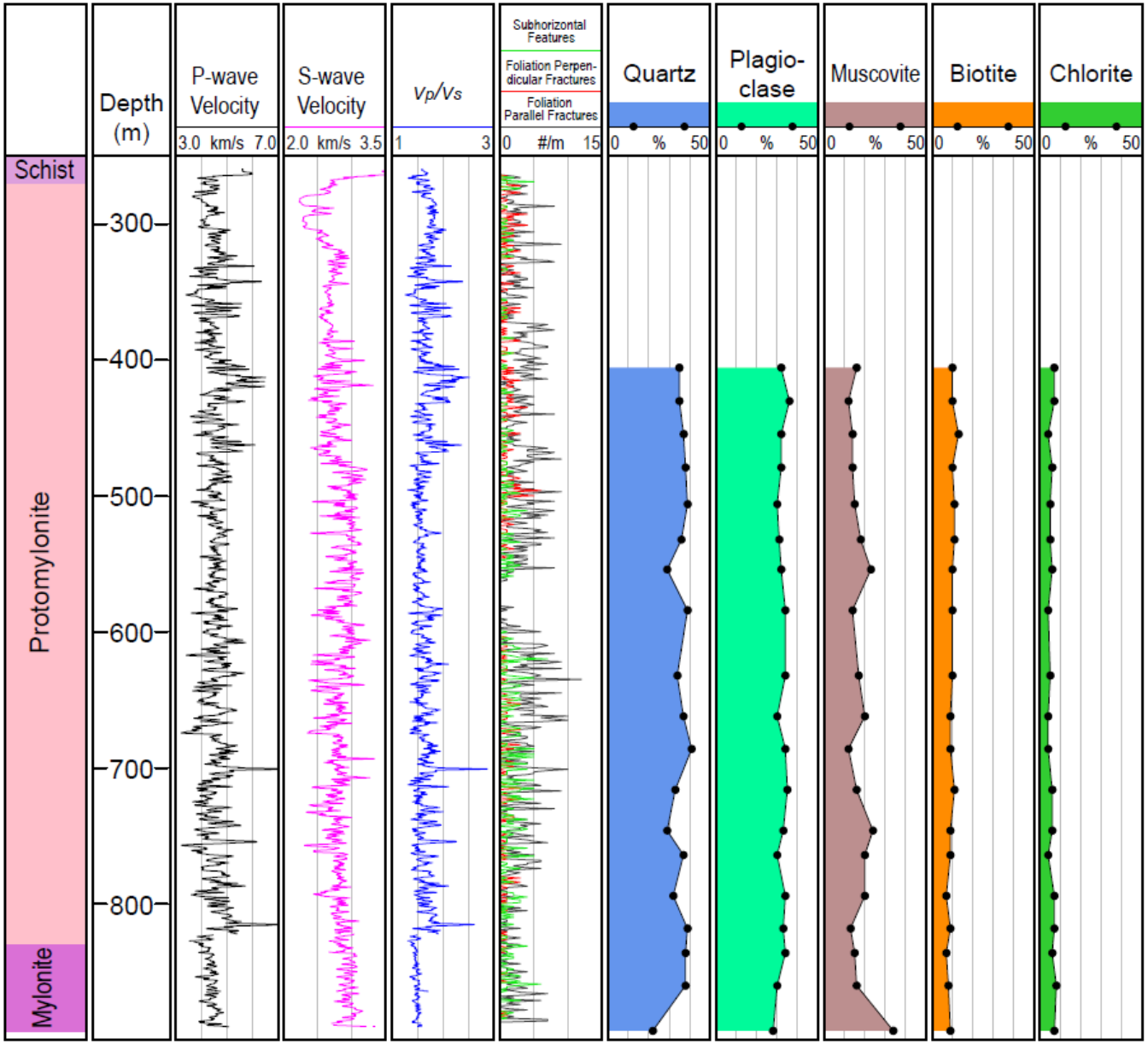

Figure 3.10: *P- and S-wave velocity, v_P/v_S ratio, fracture density, and results of XRD analysis of cuttings for the DFDP-2B borehole. Sonic log and compositional data indicate that the hanging wall host rock is relatively homogenous. XRD data from Toy et al. [in review].*

References

Christensen, N. I., and D. A. Okaya (2007), Compressional and Shear Wave Velocities in South Island, New Zealand Rocks and Their Application to the Interpretation of Seismological Models of the New Zealand Crust, A Cont. Plate Bound. Tectonics South Island, New Zeal., 123–155.

Eberhart-Phillips, D., and S. Bannister (2002), Three-dimensional crustal structure in the Southern Alps region of New Zealand from inversion of local earthquake and active source data, J. Geophys. Res., 107(B10), doi:10.1029/2001JB000567.

Eccles, J. D., A. K. Gulley, P. E. Malin, C. M. Boese, J. Townend, and R. Sutherland (2015), Fault Zone Guided Wave generation on the locked, late interseismic Alpine Fault, New Zealand, Geophys. Res. Lett., 42(14), 5736–5743, doi:10.1002/2015GL064208.Received.

Ellis, D. V., and J. M. Singer (2008), Well Logging for Earth Scientists, 2nd ed., Springer, Dordrecht.

Godfrey, N. J., N. I. Christensen, and D. a. Okaya (2000), Anisotropy of schists: Contribution of crustal anisotropy to active source seismic experiments and shear wave splitting observations, J. Geophys. Res., 105(B12), 27991–28007, doi:10.1029/2000JB900286.

Godfrey, N. J., N. I. Christensen, and D. A. Okaya (2002), The effect of crustal anisotropy on reflector depth and velocity determination from wide-angle seismic data: A synthetic example based on South Island, New Zealand, Tectonophysics, 355, 145–161, doi:10.1016/S0040-1951(02)00138-5.

Guo, B., C. H. Thurber, S. W. Roecker, J. Townend, C. Rawles, C. J. Chamberlain, C. M. Boese, S. Bannister, J. Feenstra, and J. D. Eccles (2017), 3-D P- and S-wave velocity structure along the central Alpine Fault South Island, New Zealand, Geophys. J. Int., 209, 935–947, doi:10.1093/gji/ggx059.

Massiot, C. (2017), Fracture system characterisation and implications for fluid flow in volcanic and metamorphic rocks, Victoria University of Wellington.

Norris, R. J., and A. F. Cooper (2007), The Alpine Fault, New Zealand: surface geology and field relationships, A Cont. Plate Bound. Tectonics South Island, New Zeal., 157–175.

Paillet, F. L., and C. H. Cheng (1991), Acoustic Waves in Boreholes, CRC Press, INC, Boca Raton, Florida.

Rider, M. H., and M. Kennedy (2011), The Geological Interpretation of Well Logs, 3rd ed., Rider-French, Scotland.

Schmitt, D. P. (1988), Shear wave logging in elastic formations, J. Acoust. Soc. Am., 84(6), 2215–2229, doi:10.1121/1.397015.

Sutherland, R. et al. (2012), Drilling reveals fluid control on architecture and rupture of the Alpine fault, New Zealand, Geology, 40(12), 1143–1146, doi:10.1130/G33614.1.

Sutherland, R. et al. (2015), Deep Fault Drilling Project (DFDP), Alpine Fault Boreholes DFDP-2A and DFDP-2B Technical Completion Report, Wellington.

Sutherland, R., J. Townend, V. G. Toy, P. Upton, J. Coussens, and DFDP2 Science Team (2017), Extreme hydrothermal conditions at an active plate-bounding fault, Nature, doi:10.1038/nature22355.

Townend, J., R. Sutherland, V. G. Toy, J. D. Eccles, C. Boulton, S. C. Cox, and D. McNamara (2013), Late-interseismic state of a continental plate-bounding fault: Petrophysical results from DFDP-1 wireline logging and core analysis, Alpine Fault, New Zealand, Geochemistry, Geophys. Geosystems, 14(9), 3801–3820, doi:10.1002/ggge.20236.

Toy, V., R. Sutherland, J. Townend, and DFDP2 Science Team (n.d.), Bedrock geology of DFDP-2B, Central Alpine Fault, New Zealand, New Zeal. J. Geol. Geophys., doi:10.1080/09500693.2010.511297.

4 Velocity structure of the Alpine Fault, New Zealand: The effect of brittle deformation and clay alteration on elastic properties of fault zones

Abstract

Major fault zones are commonly associated with seismically detected low velocity zones. In order to accurately interpret these low velocities zones and understand the processes that produce them, direct measurements of seismic wavespeed through fault zone rocks are needed. The Alpine Fault dominates the active transpressional plate boundary through the South Island of New Zealand. Rapid exhumation along the fault provides an opportunity to study near-surface rocks that have experienced similar histories to rocks currently present in the fault at mid-crustal depths. I examine the elastic properties of the Alpine Fault in Deep Fault Drilling Project (DFDP)-1 drill core samples and borehole logs from the shallow fault zone, DFDP-2 borehole logs from the hanging wall, and outcrop samples from a number of field localities along the central Alpine Fault. P- and S-wave velocities were measured at ultrasonic frequencies on saturated core plugs taken from DFDP-1 core and outcrops to construct a 1-D seismic velocity transect across the fault zone. Velocities were measured over a range of effective pressures between 1 and 60 MPa to determine the variation in elastic properties with depth and pore pressure. When possible, samples were cut in three orthogonal directions and S-waves were measured in two polarization directions on all samples to constrain velocity anisotropy. P- and S-wave velocities in the fault rock range from 2.5 to 5.0 km/s and 1.3 to 2.7 km/s, respectively, corresponding to a 20 to 40% decrease in velocity relative to the surrounding host rock. The hanging wall host rocks are very anisotropic while the fault core and footwall host rock are mostly isotropic. Comparison of laboratory, fault zone trapped wave models, and log velocity data show that the drill core and outcrop samples are good proxies for the *in situ* rocks, suggesting that the low velocity in the damage zone is due to microscale features, such as microfractures and clay content, present at all scales of measurement.

4.1 Introduction

Major fault zones are commonly detected as low velocity zones by seismic experiments [e.g., *Zhao et al.*, 1996; *Eberhart-Phillips and Bannister*, 2002; *Li and Malin*, 2008; *Cochran et al.*, 2009; *Eccles et al.*, 2015]. However, seismic experiments lack the resolution needed to detect fine-scale structural variations and link measured velocities to properties and processes within the fault zone. A reliable interpretation of seismic data depends on an accurate understanding of the elastic properties and seismic anisotropy of appropriate rock types and controls on variations in those properties. In this chapter I present measurements of compressional (P) and shear (S) wave velocities in three orthogonal directions, under simulated *in situ* conditions, for representative samples of drill core acquired during the first phase of the Deep Fault Drilling Project and outcrop samples from the central segment of the Alpine Fault Zone, South Island, New Zealand (Fig. 4.1). Emphasis is placed on the rocks within the fault zone as work has previously been done to characterize the elastic properties of the crustal rocks of the South Island [*Okaya et al.*, 1995; *Christensen and Okaya*, 2007] but the elastic properties of complexly altered rocks of brittle fault zones are comparatively poorly known.

4.1.1 Fault zone physical properties

In a simplified view, a mature brittle fault zone in low-porosity rocks in the upper crust consists of a fault core surrounded by a damage zone within undamaged protolith host rock [*Chester and Logan*, 1987; *Caine et al.*, 1996; *Kim et al.*, 2004; *Faulkner et al.*, 2010]. The fault core develops where the majority of displacement is accommodated in the fault zone. Due to large amounts of strain, the core typically contains gouge, cataclasites, and localized slip surfaces. The damage zone is a region of more distributed deformation, typically including a network of fractures, at various scales, and small faults whose density decreases exponentially with distance from the

fault core, leading to a gradual transition into the host rock [e.g., *Vermilye and Scholz*, 1998; *Faulkner et al.*, 2010].

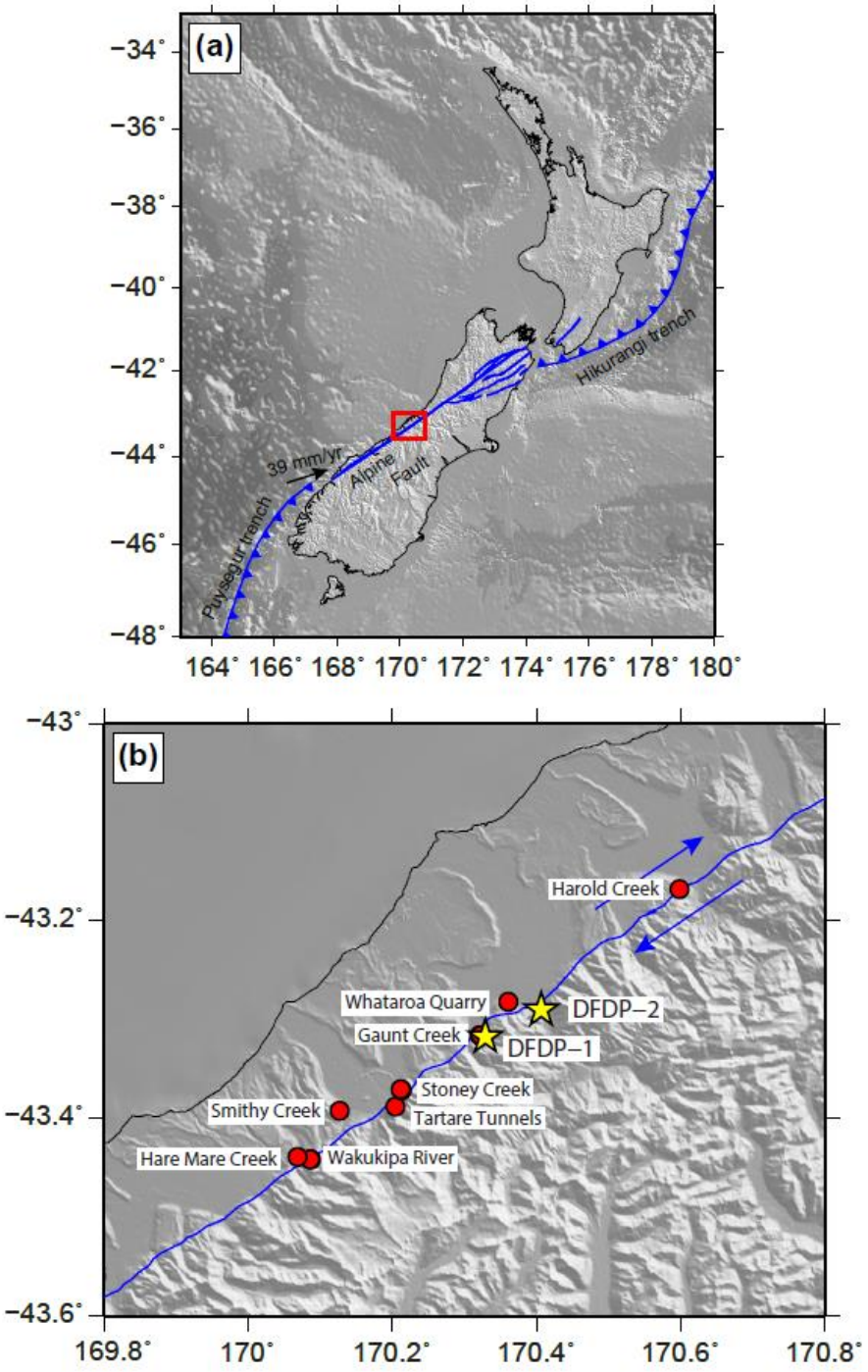

Figure 4.1: *(a) Tectonic setting of New Zealand showing the present plate vector (after Demets et al. [2010]). Red box outlines the area shown in figure 4.1b. (b) Location map of drill sites (yellow stars) and outcrops sampled in this study (red circles).*

The deformation mechanisms that operate within a fault zone combined with fluid flow can cause fault zone rocks to have properties that are significantly different from their protolith [*Mooney and Ginzburg*, 1986; *Chester and Logan*, 1987; *Ben-Zion and Sammis*, 2003; *Faulkner et al.*, 2010]. This difference in properties aids in the detection of fault zones using geophysical methods. Two important factors that influence the rock properties are (1) mechanical or diagenetic alteration and (2) pore fluid pressure and stress effects. A reduction in velocity with increasing fracture density has been predicted [*O'Connell and Budiansky*, 1974] and observed at laboratory, borehole, and seismic scales [e.g., *Birch*, 1960, 1961; *Stierman and Kovach*, 1979; *Li et al.*, 2001]. Additionally, the presence of fluids in the fault zone can lead to alteration of the protolith, resulting in the formation of new mineral phases, especially clays, [*Bruhn et al.*, 1994; *Velde*, 1995]. Theoretical estimates of the single crystal elastic moduli and velocities of clay [*Alexandrov and Ryzhova*, 1961; *Berge and Berryman*, 1995; *Katahara*, 1996] and measurement of clay-epoxy mixtures [*Wang et al.*, 2001] suggest that that the presence of clay would lead to faster velocities due to high elastic moduli (bulk modulus ~50 GPa, shear modulus ~20 GPa) However, measurement of clay aggregates yields lower elastic moduli (bulk modulus ~12 GPa, shear modulus ~6 GPa) [e.g, *Vanorio et al.*, 2003], suggesting that an increase in clay content in rock would result in a decrease in velocity, consistent with velocity measurements of clay-rich shales and sandstones [e.g., *Tosaya and Nur*, 1982; *Kowallis et al.*, 1984; *Castagna et al.*, 1985; *Han et al.*, 1986]. Fault zone processes can also alter hydraulic properties, increasing or decreasing fault zone permeability [e.g., *Carpenter et al.*, 2014; *Morrow et al.*, 2014, 2015], potentially leading to zones of elevated pore pressure [*Cox and Scholz*, 1988; *Chester et al.*, 1993; *Caine et al.*, 1996; *Lund Snee et al.*, 2014] and a decrease in velocity [*Bourbié et al.*, 1987; *Hofmann et al.*, 2005]. In order to determine the causes of remotely observed geophysical

signatures and understand the structure, material, strength, stress state, and fluid content in fault zones, geophysically sensed properties should be calibrated through direct sampling of the rock and comparison of measurements at different scales.

For example, the damage zone of the San Andreas Fault was observed in borehole logs from the San Andreas Fault Observatory at Depth (SAFOD) as a zone of low velocity and resistivity relative to the host rock [*Zoback et al.*, 2005, 2010, 2011; *Jeppson et al.*, 2010]. Based on geophysical observations at multiple scales and direct sampling of the rock it has been hypothesized that this difference in properties is caused by brittle deformation and clay alteration in the fault zone.

4.1.2 Characterizing an anisotropic medium

Many earth materials exhibit some degree of anisotropy, which can be enhanced at plate boundaries and other fault zones where shearing results in a preferred mineral alignment or tectonic stresses cause preferential creation and/or closure of fractures. Seismic waves travelling through an anisotropic medium will be affected by the direction of wave propagation, so a robust interpretation of the seismic data, whether it be locating earthquakes or processing tomographic images, requires inclusion of anisotropy. Despite recognition of the importance of seismic anisotropy our understanding of anisotropy in real rocks remains limited. Most of the work on constraining anisotropy in earth materials has been done on crystalline rocks [e.g, *Nur and Simmons*, 1969; *Wang et al.*, 1989; *Kern and Wenk*, 1990; *Okaya et al.*, 1995; *Godfrey et al.*, 2000; *Okaya and Christensen*, 2002; *Cholach et al.*, 2005; *Chan and Schmitt*, 2015]. Some work has been done on sedimentary rocks [e.g., *Johnston and Christensen*, 1995; *Louis et al.*, 2012; *Martínez and Schmitt*, 2013] but anisotropy in brittle fault damage zones has not been well studied. To my knowledge the only estimates of anisotropy in brittle damage zone materials from

direct measurement come from SAFOD. Based on cross-dipole sonic logs and laboratory measurements, the damage zone is anisotropic and the fault core appears to be more anisotropic that the surrounding host rock due to the development of a scaly clay fabric [*Boness and Zoback*, 2006; *Jeppson and Tobin*, 2015].

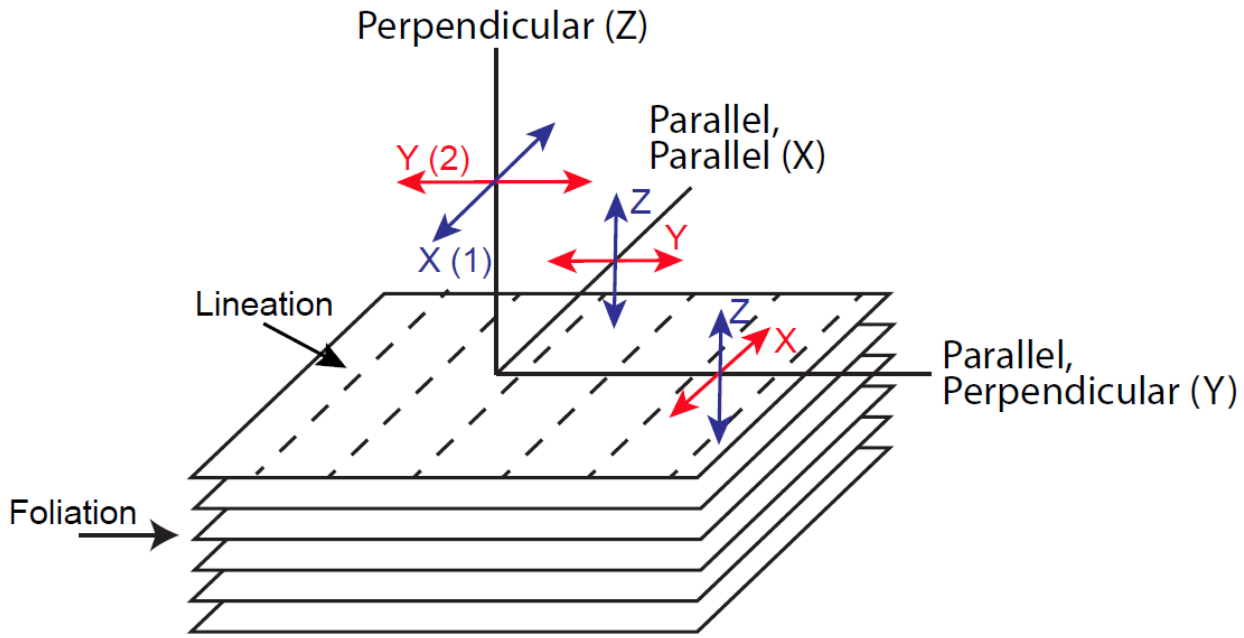

Figure 4.2: *Coordinate system defined with respect to visible foliation and lineation in hand specimens. The principal X and Y axes lie within the foliation plane but are parallel and perpendicular to lineation, respectively. The principal Z axis is perpendicular to the foliation plane. Velocity measurements taken along these axes are identified by both wave propagation (first subscript) and vibration directions (second subscript, red and blue arrows).*

Anisotropic materials are often described based on their symmetry. An isotropic medium has an infinite number of planes of symmetry and any loss of symmetry results in anisotropy. Full characterization of symmetry elements can require up to 779 individual velocity measurements, making it a difficult and time consuming process [*Pros et al.*, 1998; *Mah and Schmitt*, 2003]. Fortunately, the symmetry of a rock can be estimated from measurement of three orthogonal core samples. These cores are aligned with respect to foliation and lineation, where present, (Fig. 4.2) and wavespeed measurements in these directions are used to calculate the diagonal components

of the stiffness tensor, revealing the estimated symmetry. Wavespeeds are annotated with subscripts indicating propagation and vibration directions so that a P-wave traveling in the X-direction would be annotated as v_{xx} and an S-wave propagating in the X-direction but vibrating in the Y direction would be v_{xy}.

The stiffness tensor is a 6x6 matrix containing up to 21 independent elastic coefficients that are calculated from measured velocities and densities. The tensor is symmetric about the diagonal and is commonly written as:

$$C_{ij} = \begin{bmatrix} C_{11} & C_{12} & C_{13} & C_{14} & C_{15} & C_{16} \\ & C_{22} & C_{23} & C_{24} & C_{25} & C_{26} \\ & & C_{33} & C_{34} & C_{35} & C_{36} \\ & & & C_{44} & C_{45} & C_{46} \\ & & & & C_{55} & C_{56} \\ & & & & & C_{66} \end{bmatrix} \quad [1]$$

where the symmetric components below the diagonal are not shown for simplicity. Calculation of the elastic coefficients of the stiffness tensor is described in detail in *Mah and Schmitt* [2003]; here I present only the calculations that can be completed using measurements on three orthogonal cores. These components are:

$$C_{11} = \rho v_{xx}^2 \quad [2]$$

$$C_{22} = \rho v_{yy}^2 \quad [3]$$

$$C_{33} = \rho v_{zz}^2 \quad [4]$$

$$C_{44} = \rho v_{yz}^2 = \rho v_{zy}^2 \quad [5]$$

$$C_{55} = \rho v_{xz}^2 = \rho v_{zx}^2 \quad [6]$$

$$C_{66} = \rho v_{xy}^2 = \rho v_{yx}^2 \quad [7]$$

where ρ is the sample density. Additionally, for isotropic (infinite planes of symmetry), and transversely isotropic (i.e., hexagonal, one plane of symmetry) symmetry the off-diagonal component C_{12} can be calculated as:

$$C_{12} = C_{11} - 2C_{66} \quad [8]$$

Based on relationships among the diagonal components, the degree of symmetry can be estimated as isotropic, transversely isotropic or orthorhombic (three planes of symmetry). In these three cases the stiffness tensor simplifies to nine components:

$$C_{ij} = \begin{bmatrix} C_{11} & C_{12} & C_{13} & 0 & 0 & 0 \\ & C_{22} & C_{23} & 0 & 0 & 0 \\ & & C_{33} & 0 & 0 & 0 \\ & & & C_{44} & 0 & 0 \\ & & & & C_{55} & 0 \\ & & & & & C_{66} \end{bmatrix} \quad [9]$$

If $C_{11} \approx C_{22} \approx C_{33}$ and $C_{44} \approx C_{55} \approx C_{66}$ the material is quasi-isotropic; the full stiffness tensor can be derived from the measurements presented in this study because $C_{12} = C_{13} = C_{23}$. If two out of each set of three diagonal components are equal (e.g. $C_{11} \approx C_{22} \neq C_{33}$ and $C_{44} \approx C_{55} \neq C_{66}$) the material is transversely isotropic. The full stiffness tensor cannot be estimated from the measurements presented here because $C_{12} \neq C_{13} = C_{23}$. Additional wavespeed measurements with a propagation direction of 45˚ from the foliation are needed. Finally, if $C_{11} \neq C_{22} \neq C_{33}$ and $C_{44} \neq C_{55} \neq C_{66}$ the simplest symmetry possible is orthorhombic and 12 or more additional measurements in different orientations would be needed to fully derive the stiffness tensor [e.g. *Mah and Schmitt*, 2001, 2003].

Having the complete stiffness tensor allows the velocity of a wave propagating at any angle to be determined [*Thomsen*, 1986; *Mavko et al.*, 2009]. This is useful for comparison to *in situ* sonic logs and seismic measurements where wave propagation may not be parallel or perpendicular to foliation.

4.2 Alpine Fault, South Island, New Zealand

The Alpine Fault was selected as the field area for this study because the damage zone is relatively well exposed for a mature, very large offset, brittle plate bounding fault zone. Importantly, the fault zone rocks are derived from a nearly homogeneous protolith so the effects of mechanical deformation and chemical alteration can be easily isolated from the contribution of the host rock composition. Additionally, rapid uplift and exhumation along the fault has exposed rocks that were actively deforming at depth ~3 million years ago [*Little et al.*, 2002]. These exposed rocks provide a good proxy to materials currently deforming at mid-crustal levels and an opportunity to study processes and properties occurring at greater depths. Furthermore, the elastic properties and velocity anisotropy of the Alpine Fault host rock have been well studied [*Okaya et al.*, 1995; *Godfrey et al.*, 2000, 2002; *Christensen and Okaya*, 2007] so the focus of this study can be on the properties of the brittlely overprinted fault rock and the effect of fault zone processes on the evolution of elastic properties and seismic anisotropy. The Alpine Fault is also late in its seismic cycle and locked [*Sutherland et al.*, 2007; *Beavan et al.*, 2010], allowing a unique comparison to previous studies on the creeping segment of the San Andreas Fault which has recently experience coseismic slip and is also actively creeping.

The central segment of the Alpine Fault has been the recent focus of the Deep Fault Drilling Project (DFDP) [*Townend et al.*, 2009, 2013, *Sutherland et al.*, 2012, 2015, 2017; *Sutherland*, 2014]. Drill core samples, geophysical logging data, and seismic data have all been acquired as

part of the project, providing a wealth of information about the properties of the fault zone at a range of observation scales.

4.2.1 Tectonic setting and geology

The Alpine Fault is a 850-km long, dextral-reverse fault that cuts across the west coast of New Zealand's South Island and is part of a network of faults connecting the Hikurangi subduction zone in the northeast to the Puysegur subduction zone in the southwest (Fig. 4.1) [*Wellman*, 1955]. The late Quaternary oblique dextral-reverse slip rate on the fault is 27 ± 5 mm/yr, which accounts for two-thirds of the relative Pacific-Australian plate boundary convergence [*Norris and Cooper*, 2001; *Barnes*, 2009; *Langridge et al.*, 2010]. Multiple lines of evidence indicate that the Alpine Fault is capable of generating M_w 8 or larger earthquakes with a recurrence interval of 329 ± 68 years [*Bull*, 1996; *Sutherland et al.*, 2007; *Berryman et al.*, 2012]. Horizontal and vertical displacements of up to 8 m and 1.5 m, respectively, have been experienced during previous earthquakes [e.g., *Sutherland et al.*, 2007, and references therein]. The last Alpine Fault rupture, a M_w 7.9 that occurred in 1717 AD, is inferred to have ruptured 300 to 500 km of the fault [*Sutherland et al.*, 2007]. There is no evidence of significant interseismic creep above 12 km depth over the last 40+ years, indicating that the fault is locked and strain release is entirely coseismic [*Beavan and Ellis*, 2007; *Sutherland et al.*, 2007; *Beavan et al.*, 2010].

The central section of the Alpine Fault is the focus of this study. At the surface, the central section is partitioned into oblique thrust segments connected by strike-slip faults. Fault orientation varies between the different segments, but the average strike and dip is ~55˚, 45-60˚ SE [*Norris and Cooper*, 2007; *Stern et al.*, 2007]. Along the central section the dip-slip component of motion is maximized (10 mm/yr) and the central Alpine Fault trace delineates the

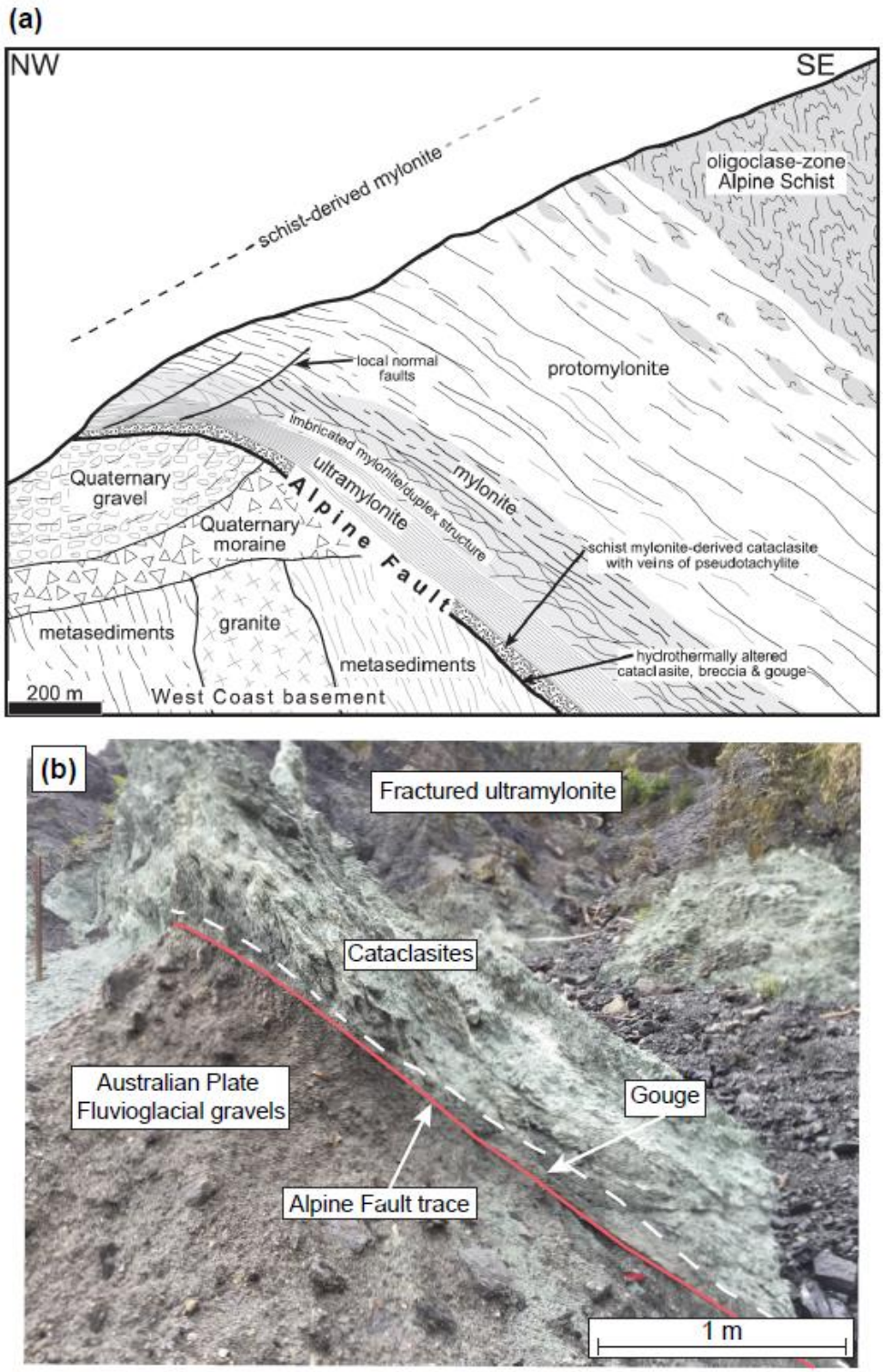

Figure 4.3: *Field relationships along the central Alpine Fault. (a) Schematic cross section, from Norris and Cooper [2007], of an oblique thrust segment compiled from multiple outcrop exposures (b) Field photograph of the Gaunt Creek fault scarp exposure. The Alpine Fault plane is indicated by the red line and the approximate upper boundary of the gouge is denoted by the dashed white line.*

western edge of the Southern Alps. Rapid exhumation along this portion of the fault over the last 5 to 8 Ma has exposed hanging wall rocks from up to 35 km depth [*Little et al.,* 2002, 2005; *Norris and Cooper*, 2003].

The structural relationships and lithologies exposed in outcrop vary along the Alpine Fault. Much work has been done to describe the observed field relationships [e.g. *Norris and Cooper*, 2007; *Barth et al.,* 2013]. I provide a brief description of these relationships here. The exposed hanging wall host rock includes a 1-km thick sequence of protomylonites, mylonites, and ultramylonites derived from the quartzo-feldspathic Alpine Schist, a subgroup of the Haast Schist (Fig. 4.3a) [*Little et al.*, 2005; *Cox and Sutherland*, 2007; *Norris and Cooper*, 2007; *Toy et al.,* 2008]. The mylonites formed due to ductile deformation of the Apline Schist as a result of shear on the Alpine Fault at depth. The degree of mylonitization increases towards the fault and mesoscopic fractures define a brittle damage zone that extends ~100 m from the fault plane [*Norris and Cooper*, 2007]. Within 20 to 30 m of the fault plane, the mylonites are overprinted by cataclasites which define the fault core (Fig. 4.3b) [*Norris and Cooper*, 2007; *Boulton et al.*, 2012]. The cataclasite zone transitions to a ~30 cm thick, phyllosilicate-rich gouge zone located immediately above a sharp fault plane, which is the principal slip surface. The damage zone is asymmetric, lying mostly in the hanging wall. Slip on the Alpine fault has juxtaposed the hanging wall rocks against Late Quaternary fluvio-glacial sediments, and older igneous and metasedimentary rocks in the footwall [*Norris and Cooper*, 2007; *Lund Snee et al.*, 2014].

4.2.2 Deep Fault Drilling Project (DFDP)

In early 2011, two vertical boreholes were drilled into the Alpine Fault Zone at Gaunt Creek as part of the first phase of DFDP (Fig. 4.1). Boreholes DFDP-1A and DFDP-1B were drilled ~80 m apart to depths of 100.6 m and 151.4 m, respectively, using percussion techniques, wireline

coring, and rotary drilling [*Sutherland et al.*, 2012; *Townend et al.*, 2013]. Following drilling, core samples were analyzed [e.g., *Toy et al.*, 2015] and a suite of wireline geophysical logs was acquired [*Townend et al.*, 2013]. These boreholes drilled only the damage zone of the fault. Six main lithologies were encountered. Listed from shallow to deep, they are: (1) Quaternary gravels, (2) hanging wall ultramylonite, (3) hanging wall cataclasite (foliated and unfoliated), (4) fault gouge and ultracataclasite, (5) footwall cataclasite, and (6) footwall gravels [*Toy et al.*, 2015].

In 2014 the second phase of DFDP occurred in the Whataroa River Valley with the goal of drilling through the entire fault zone at depth. The DFDP-2B borehole was drilled to a measured depth of 892-m (~ 817-m true vertical depth) using conventional open-hole drilling and dual-rotary methods [*Townend et al*., written communication, 2017]. The borehole penetrated a sequence of Quaternary gravel and lake silt, schist, protomylonite, and mylonite [*Toy et al.*, in review]. The Alpine Fault was not reached, but it is estimated to be within 200 to 400 m of the base of the borehole [*Sutherland et al.*, 2017; *Toy et al.*, in review]. Drill cuttings were collected and analyzed on site and a total of 32.22-m of core (mostly cement that was pumped into the borehole) was obtained [*Toy et al.*, in review]. A suite of geophysical logging tools was deployed in the borehole and a fiber-optic cable was installed between the casing and borehole wall so precise temperature measurements could be obtained [*Sutherland et al.*, 2017; *Townend et al.*, written communication, 2017].

4.3 Methods

4.3.1 Outcrop sample collection

To supplement limited core recovered during DFDP and obtain a suite of samples that are representative of the fault zone as a whole, I collected outcrop samples that were not heavily

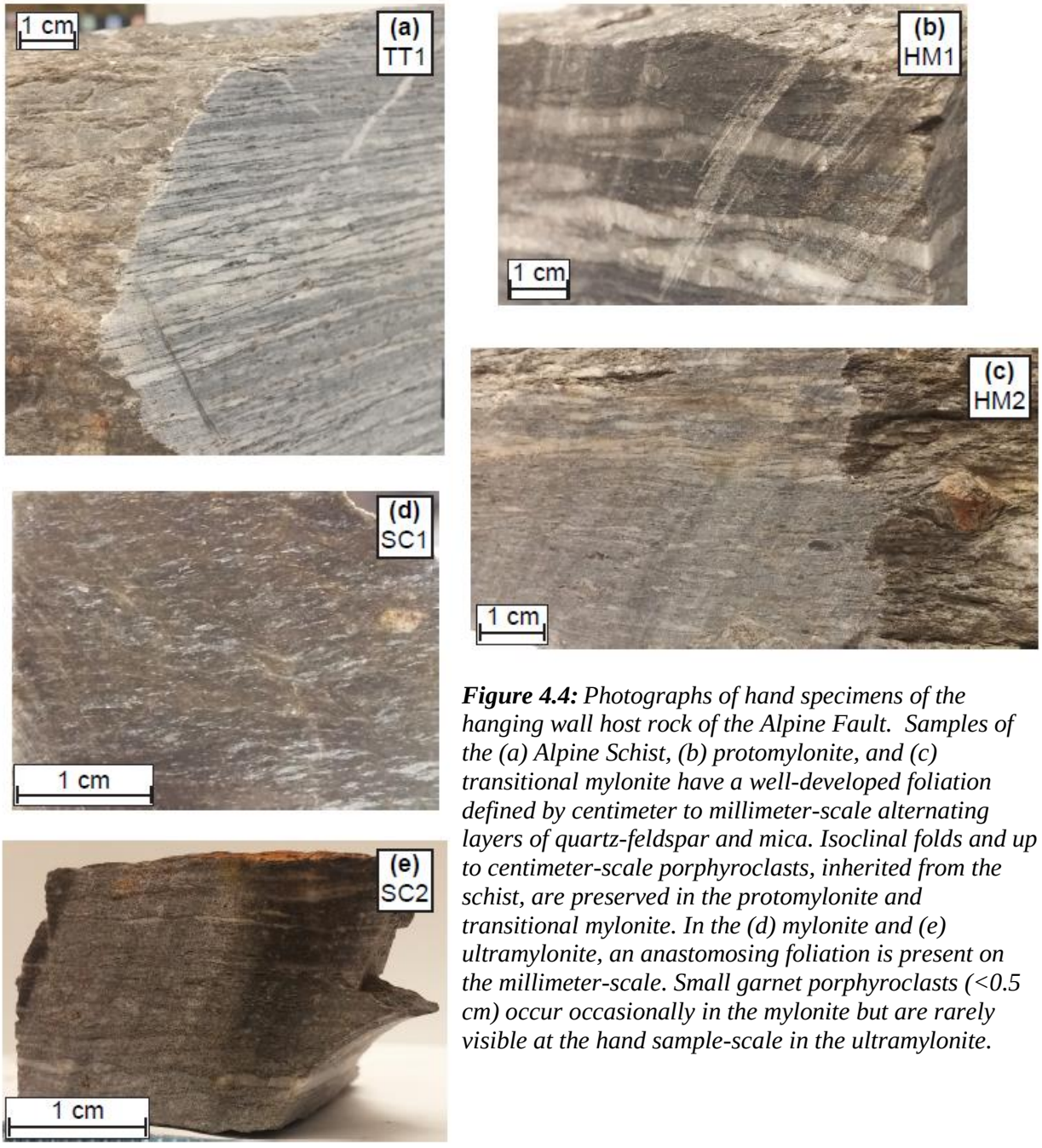

Figure 4.4: *Photographs of hand specimens of the hanging wall host rock of the Alpine Fault. Samples of the (a) Alpine Schist, (b) protomylonite, and (c) transitional mylonite have a well-developed foliation defined by centimeter to millimeter-scale alternating layers of quartz-feldspar and mica. Isoclinal folds and up to centimeter-scale porphyroclasts, inherited from the schist, are preserved in the protomylonite and transitional mylonite. In the (d) mylonite and (e) ultramylonite, an anastomosing foliation is present on the millimeter-scale. Small garnet porphyroclasts (<0.5 cm) occur occasionally in the mylonite but are rarely visible at the hand sample-scale in the ultramylonite.*

weathered and represented the major fault zone structural elements and lithologies present along the central segment of the Alpine Fault. A total of 16 outcrop samples, obtained from eight locations, were examined (Fig. 4.1b, Table 4.1). Samples were collected from the hanging wall host rock (Fig. 4.4; Alpine Schist and mylonitic sequence), damage zone (Fig. 4.5a; fractured

ultramylonite), fault core (Fig. 4.5 and 4.6; cataclasite, fault gouge, and ultracataclasite from a subsidiary footwall fault), and footwall host rock (Fig. 4.6; mylonite, monzonite, and granitic L-tectonite). I classify the fault rocks based on previous descriptions by *Boulton et al.*, [2012], *Toy et al.* [2015], and *Norris and Cooper* [2007], who used a modification of the nomenclature proposed by *Sibson* [1977].

4.3.1.1 Sample characteristics

4.3.1.1.1 Alpine Schist (protolith)

A sample of the quartzo-feldspathic Alpine Schist (TT1) was collected at the Tartare Tunnel. A subgroup of the Haast schist, the Alpine Schist is a high grade, garnet zone schist, that is likely Cretaceous in age, in which peak metamorphism predated the oblique Pacific-Australian plate boundary convergence [*Suggate*, 1961; *Grapes and Watanabe*, 1992; *Little et al.*, 2002]. The schists have a strong foliation defined by millimeter- to centimeter-scale alternating layers of quartz-feldspar and mica (Fig. 4.4a). The foliation dips ~60-70˚ SE, approximately parallel to the Alpine Fault. Near the mylonite this foliation is commonly crenulated by oblique shear bands (Fig. 4.7a) [*Little et al.*, 2002]. Undulose extinction observed in quartz grains and the presence of dextral shear indicators (Fig. 4.7b) places the schist near the boundary of the mylonitic zone of this locality [cf., *Little et al.*, 2002]. Microfractures occur in the quartz-rich layers at a high angle to foliation. The schist contains cm-scale garnet porphyroblasts.

4.3.1.1.2 Mylonitic sequence

The transition into the mylonitic zone is associated with a decrease in both the dip of the foliation and the mean grain size of the rock [*Little et al.*, 2002]. Samples of protomylonite (HM1) and transitional mylonite (HM2) were collected at Hare Mare Creek (Fig. 4.4b & c). In the protomylonite and transitional mylonite, a millimeter- to centimeter-spaced foliation defined by quartz-feldspar and mica layers is continuous and distinct (Fig. 4.7c). Isoclinal folds, garnet

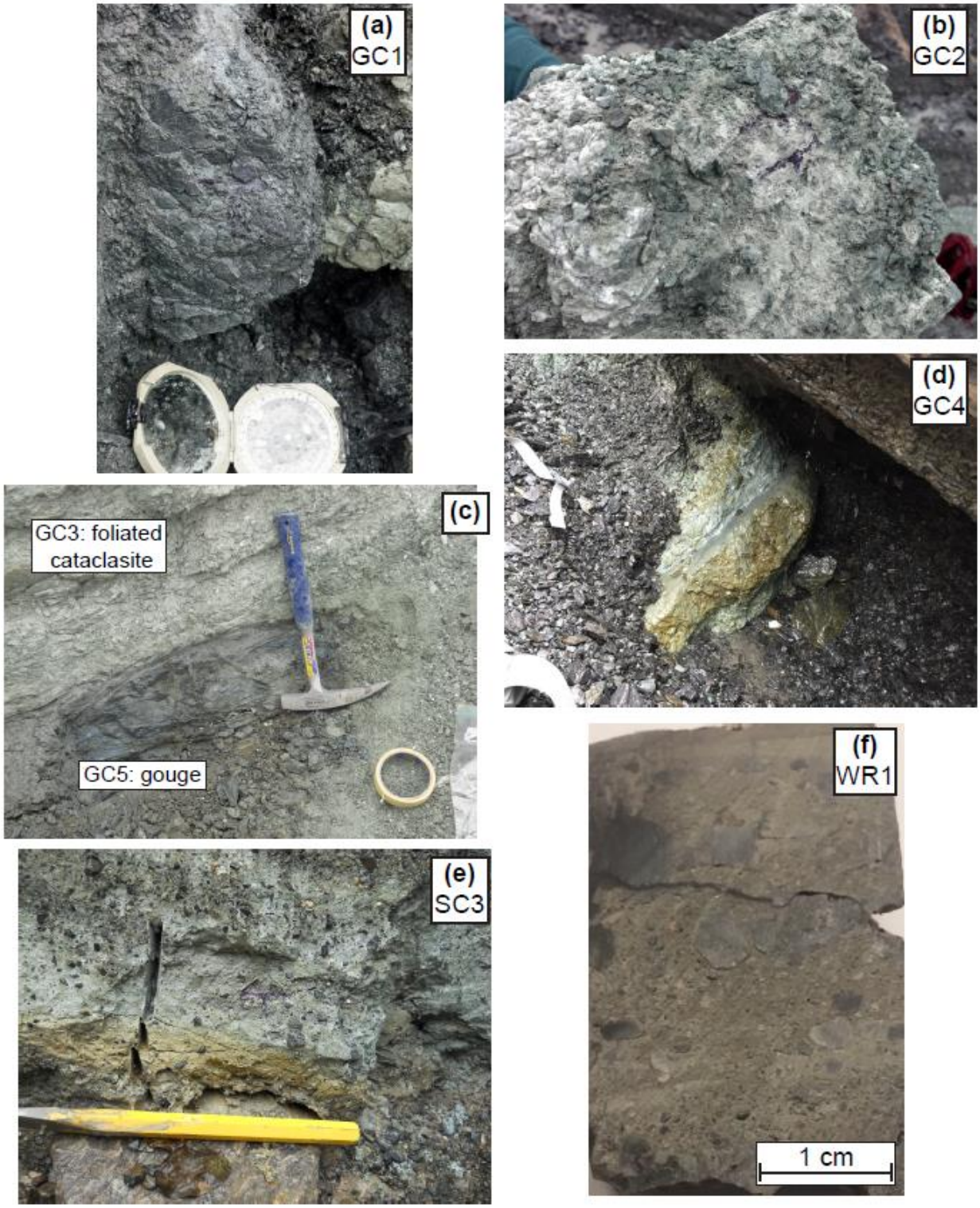

Figure 4.5: *Photographs of damage zone rocks. At Gaunt Creek samples of (a) fractured ultramylonite, (b) protocataclasite, (c) foliated cataclasite and (c, d) gouge were collected. Additional Gouge samples were collected at (e) Stoney Creek and (f) the Waikukupa Thrust.*

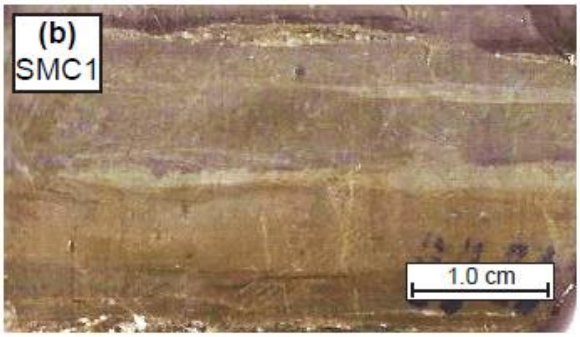

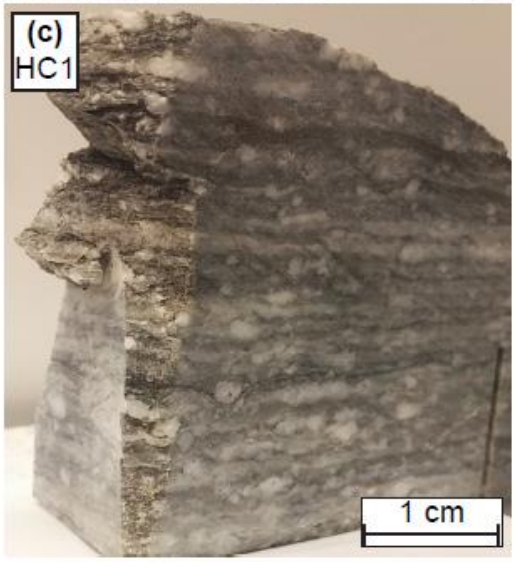

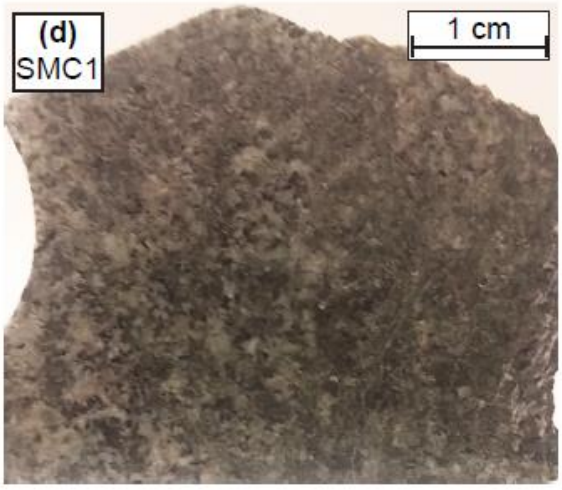

Figure 4.6: *Photographs of footwall rocks. (a) Ultracataclasite from subsidiary fault at Smithy Creek. (b) Cut surface of Smithy Creek gouge showing foliation (horizontal in image). Footwall host rocks are represented by (c) an augen mylonite sampled at Harold Creek, (d) a monzonite sampled at Smithy Creek, and (e) a granitic L-tectonite from the Whataroa Quarry.*

Table 4.1: *Outcrop samples collected on the central Alpine Fault with laboratory densities and velocities measured at 60 MPa.*

Sample	Location	Rock Type	Average Density (g/cm^3)			Minimum P-wave Velocity (km/s)			Maximum P-wave Velocity (km/s)			Minimum S-wave Velocity (km/s)			Maximum S-wave Velocity (km/s)		
TT1	Tartare Tunnels	Alpine Schist	2.66	±	0.05	5.31	±	0.16	6.21	±	0.19	2.96	±	0.09	3.70	±	0.11
HM1	Hare Mare Creek	Protomylonite	2.68	±	0.05	5.76	±	0.17	6.58	±	0.20	3.36	±	0.10	3.90	±	0.12
HM2	Hare Mare Creek	Transitional Mylonite	2.69	±	0.05	5.63	±	0.17	6.57	±	0.20	2.85	±	0.09	4.06	±	0.12
SC1	Stoney Creek	Mylonite	2.73	±	0.05	5.36	±	0.16	6.22	±	0.19	3.01	±	0.09	3.76	±	0.11
SC2	Stoney Creek	Ultramylonite	2.72	±	0.05	5.26	±	0.16	6.19	±	0.19	3.01	±	0.09	3.76	±	0.11
GC1	Gaunt Creek	Fractured Ultramylonite	2.15	±	0.13	4.17	±	0.17	4.97	±	0.20	1.55	±	0.06	2.38	±	0.10
GC2	Gaunt Creek	Protocataclasite	2.44	±	0.15	4.82	±	0.19	4.97	±	0.20	2.26	±	0.09	2.62	±	0.10
GC3	Gaunt Creek	Foliated Cataclasite	2.28	±	0.14	---	±	---	4.63	±	0.19	2.28	±	0.09	2.41	±	0.10
GC4	Gaunt Creek	Gouge	2.53	±	0.15	4.39	±	0.18	4.48	±	0.18	1.93	±	0.08	2.37	±	0.09
GC5	Gaunt Creek	Gouge	2.52	±	0.15	3.99	±	0.16	4.02	±	0.16	1.82	±	0.07	2.00	±	0.08
WR1	Waikukupa River	Gouge	2.48	±	0.15	4.51	±	0.18	4.73	±	0.19	2.34	±	0.09	2.50	±	0.10
SC3	Stoney Creek	Gouge	2.2	±	0.13	3.81	±	0.15	4.51	±	0.18	1.87	±	0.07	2.26	±	0.09
SMC1	Smithy Creek	Ultracataclasite	2.43	±	0.05	---	±	---	4.83	±	0.19	2.56	±	0.10	2.72	±	0.11
HC1	Harold Creek	FW Mylonite	2.67	±	0.05	5.69	±	0.17	6.23	±	0.19	3.27	±	0.10	3.62	±	0.11
WQ1	Whataroa Quarry	Granodiorite	2.64	±	0.05	5.89	±	0.18	5.98	±	0.18	3.35	±	0.10	3.54	±	0.11
SMC2	Smithy Creek	Monzonite	2.71	±	0.05	5.58	±	0.17	5.68	±	0.17	3.20	±	0.10	3.28	±	0.10

porphyroclasts, and oblique shear bands typical of the Alpine Schist sample are still observed in the protomylonite (Fig. 4.7d). Quartz and mica grains exhibit undulose extinction. Microfractures are present at a high angle to foliation. The transitional mylonite is distinguished from the protomylonite because the lineation trends 075-090˚, which is characteristic of the more deformed mylonites, rather than > 090˚, which is indicative of lineation inherited from the schists and is typical for the protomylonites [*Toy et al.*, 2012].

Mylonite and ultramylonite samples were collected from Stoney Creek (Fig. 4.4d & e). In the mylonite sample (SC1), a millimeter-scale anastomosing foliation is defined by alternating layers of quartz-feldspar and mica and the long axes of elongate grains (Fig. 4.7e). Proto-S surfaces are defined by the preferred orientations of micas (Fig. 4.7f). Quartz grains exhibit undulose extinction. Garnet porphyroclasts are up to 0.5 cm in diameter, but usually smaller (Fig. 4.4d). In the ultramylonite (SC2) an indistinct but continuous foliation is present. Millimeter-scale garnet porphyroclasts are rarely recognizable in hand sample and smaller-scale porphyroclasts are occasionally visible in thin section. The S-surfaces that are present in the mylonite are better developed in the ultramylonite and proto-C surfaces have begun to develop in the ultramylonite (Fig. 4.7g). Shear bands, with a sinistral-normal shear-sense, transect the foliation at a high angle (Fig. 4.7h), and foliation perpendicular microfractures are observed.

4.3.1.1.3 Damage zone cataclasites

In the damage zone, the ultramylonite is fractured and overprinted by cataclasis. A sample collected at Gaunt Creek (GC1; Fig. 4.5a) retains the mylonitic foliation, although it is heavily fractured and there are zones of cataclasis (Fig. 4.8a & b), analogous to structures exhibited by the brown-green-black ultramylonites sampled during DFDP-1 [*Toy et al.*, 2015]. A small fault in the sample records a sinistral-reverse sense of shear. Concentrated zones of micas and opaque

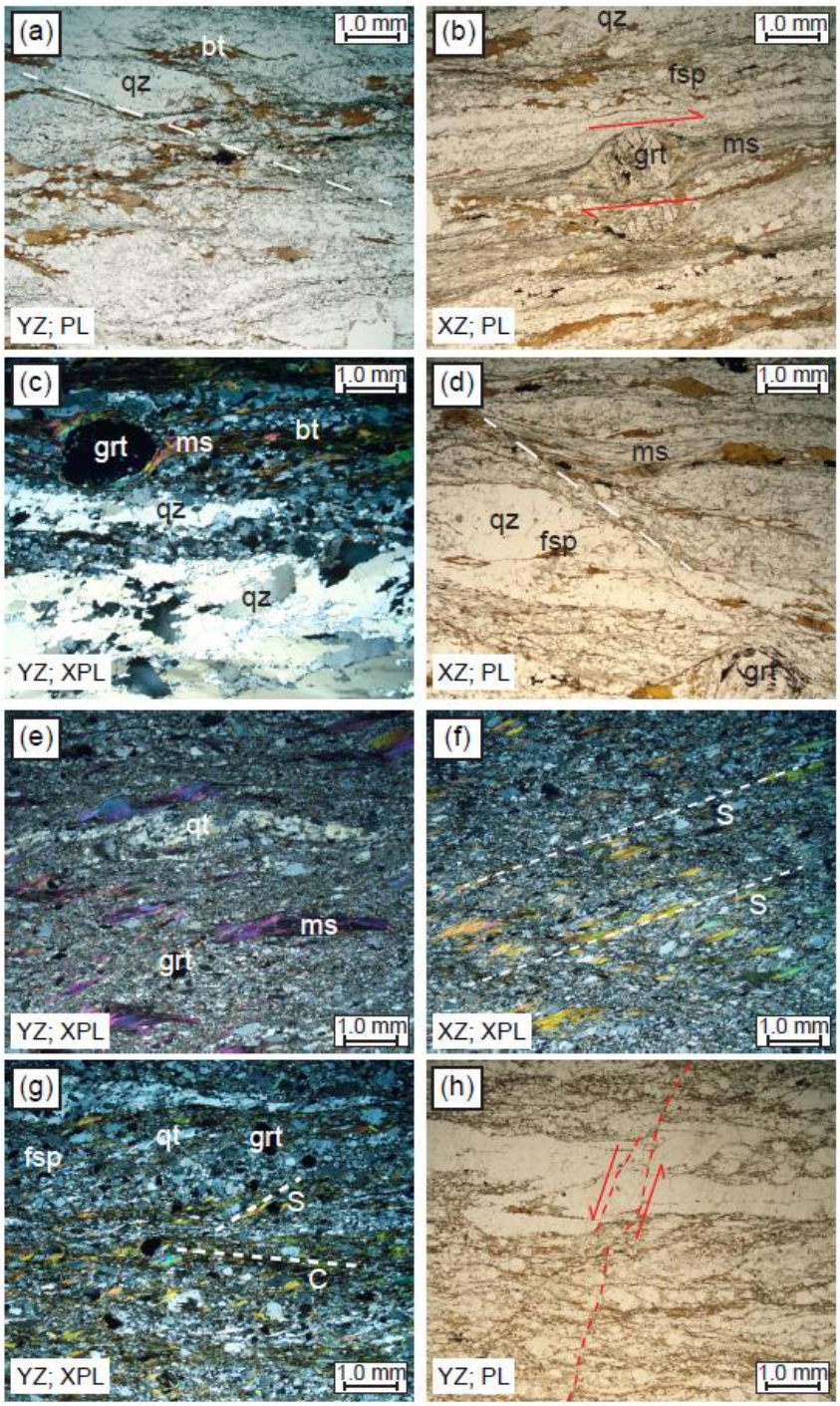

Figure 4.7: *Photomicrographs of the hanging wall host rock. (a) Oblique shear bands and (b) deformed garnet porhyroblast in the Alpine Schist indicate the sample was collected near the boundary with the mylonitic zone. (c) The protomylonite exhibits millimeter to centimeter-scale compositional bands and garnet porphyroclasts inherited from the Alpine Schist. (d) Oblique shear band in the protomylonite. (e) The mylonite is characterized by a millimeter-scale anastomosing foliation defined by elongate grains and alternating layers of quartz-feldspar and mica. (f) Proto-S surfaces in the mylonite are defined by micas. (g) S-C fabric in the ultramylonite. (h) High-angle, sinistral-reverse fracture transecting the foliation of the ultramylonite. Abbreviations for mineral labels are as follows: qz = quartz, bt = biotite, fsp = feldspar, grt = garnet, ms = muscovite; additionally, PL = plane polarized light, XPL = cross-polarized light, XZ = XZ plane, YZ = YZ plane - see figure 4.2.*

minerals define abundant pressure solution seams in the fractured ultramylonite. XRD analysis indicates the composition of the sample is 39 wt.% quartz, 29 wt.% plagioclase feldspar, 11 wt.% chlorite, and 21 wt.% illite. This represents a significant increase in clay minerals relative to the

host rock, in which clays are only present along fractures and weathered surfaces in the mylonitic zone [*Toy et al.*, 2015].

Two samples of pale-green cataclasite were collected from the fault core at Gaunt Creek (Fig. 4.5b & c). These rocks contain abundant fractures with a wide range of orientations [*Williams et al.*, 2016]. Sample GC2 is a protocataclasite that contains phyllosilicate-rich zones where the grain size has been significantly reduced by communition whereas in other places the sample is heavily fractured but grain size is not significantly reduced (Fig. 4.8c). Overall the fine-grained matrix is less than 50% of the rock. Angular clasts are present in the matrix-dominated zones. The mylonitic foliation has been significantly disrupted and a weak foliation defined by aligned phyllosilicates is present in places (Fig. 4.8d). GC3 is a foliated cataclasite, in which an anastomosing foliation defined by aligned phyllosilicates wraps around competent clasts (Fig. 4.8e). Previous work has shown that the composition of the cataclasite zone is variable but the clay-sized portion is dominantly composed of phyllosilicates; usually chlorite is most abundant followed by illite-muscovite [*Warr and Cox*, 2001; *Boulton et al.*, 2012; *Schleicher et al.*, 2015]. XRD analysis shows that the mineralogy of GC2 is 26 wt.% quartz, 40 wt.% plagioclase feldspar, 21 wt.% muscovite, and 13 wt.% chlorite + illite and GC3 is 43 wt.% quartz, 20% plagioclase feldspar, 23 wt.% chlorite, and 15% illite, in agreement with previous work [*Boulton et al.*, 2012]. Both of these samples are comparable to the upper cataclasites sampled in the DFDP-1 drill core [*Toy et al.*, 2015].

Additionally, a brown ultracataclasite sample (SMC1) was collected from a subsidiary footwall fault near Smithy Creek. The ultracataclasite (Fig. 4.6a) is cohesive and more indurated than the cataclasites from the Alpine Fault Zone. In hand sample, clasts are not visible and the rock is foliated (Fig. 4.6b). The composition of the sample is 12 wt.% quartz, 45 wt.% plagioclase

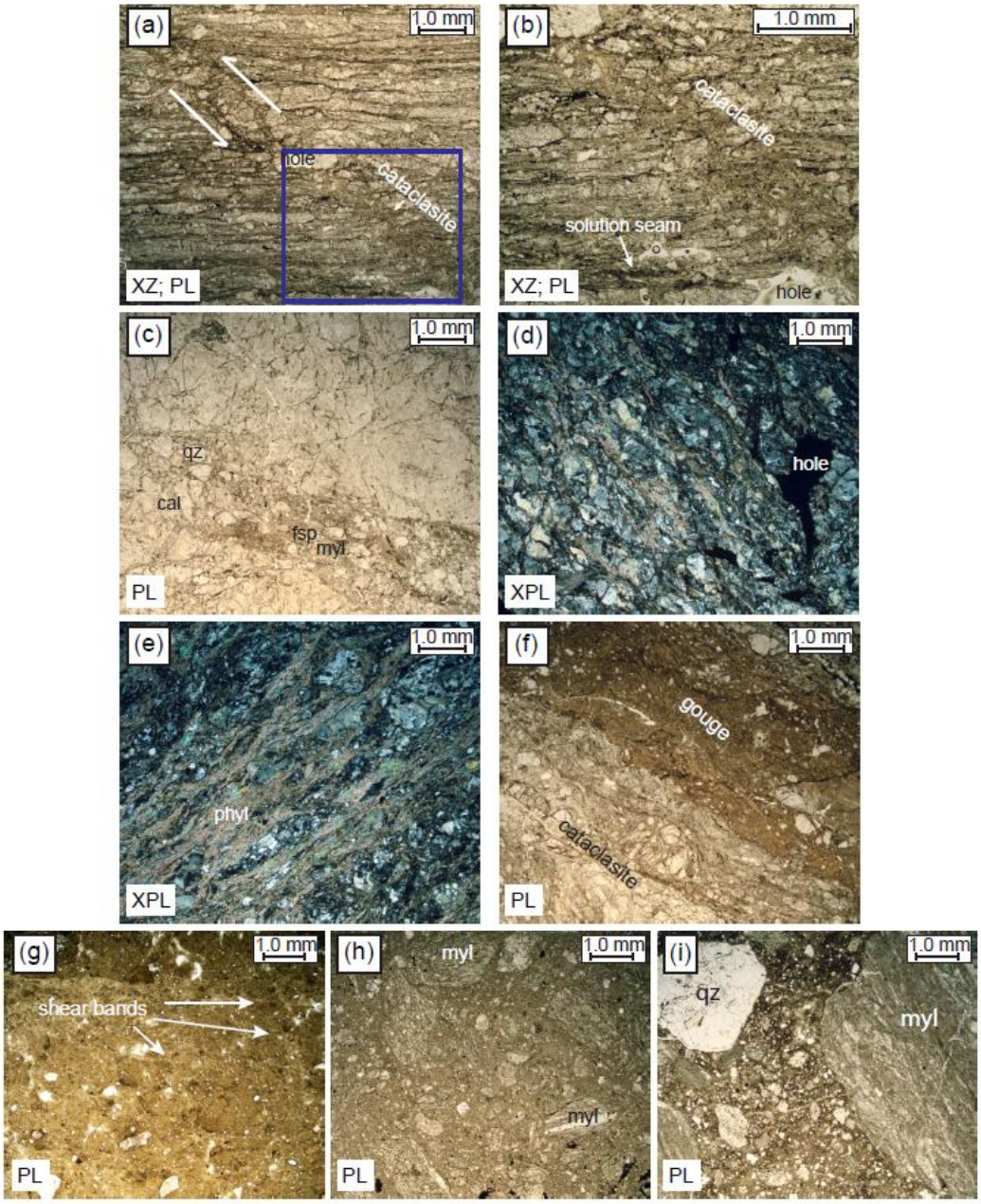

Figure 4.8: *Photomicrographs of damage zone samples. (a) Small fault and cataclasite zone in the fractured ultramylonite records a sinistral-reverse sense of shear. The blue box shows the location of the photomicrograph in figure 8b. (b) Cataclastic zone and pressure solution seams in the fractured ultramylonite. (c) Comminuted zone within the fractured rock mass of the GC2 protocataclasite. (d) Weak foliation, parallel to the fault plane, defined by phyllosilicates in GC2 cataclasite. (e) Anastomosing foliation defined by phyllosilicates in the GC3 foliated cataclasite. (f) Zones of cataclasite alternate with zones that are dominated by phyllosilicate-rich matrix in GC4 gouge. (g) Narrow shear bands filled with fine crystalline material within the Gaunt Creek gouge. (h) Mylonite and other rock fragments compose 30% of the Stoney Creek gouge. (i) Gouge from the abandoned Waikukupa Thrust containing clasts of mylonite and other rock fragments. Abbreviations for mineral labels are as follows: qz = quartz, fsp = feldspar, cal = calcite, phyl = phyllosilicate, myl = mylonite; additionally, PL = plane polarized light, XPL = cross-polarized light, XZ = XZ plane - see figure 4.2.*

feldspar, 25 wt.% pyroxene (augite), and 19 wt.% chlorite. The clay mineralogy is similar to the 25 wt.% chlorite and 3 wt.% illite measured on a proximal sample from the same outcrop [*Boles,* written communication, 2017].

4.3.1.1.4 Gouge

Four gouge samples were collected at Gaunt Creek, Stoney Creek, and the Waikukupa River. Samples from Gaunt and Stoney Creek are from the active trace of the Alpine Fault whereas the Waikukupa sample is from a thrust segment that was abandoned 20,000 years ago [*Norris and Cooper*, 1997]. These gouges are incohesive and vary in color from pale green to light brown (Fig. 4.5c-f). In hand sample, they are dominated by a fine-grained clay-rich matrix and contain less than 30% subangular, up to centimeter-scale, clasts that are mostly fragments of mylonite. Sample GC4 is a transitional sample with both cataclasite and gouge. Cataclastic zones alternate with gouge dominated by a phyllosilicate-rich matrix (Fig. 4.8f). There is a weak foliation defined by phyllosilicate bands in the cataclastic zones. Sample GC5 is almost entirely phyllosilicate-rich groundmass with less than 10% rock fragments (Fig. 4.8g). Narrow shear bands or microveins, filled with very-fine-grained crystalline material, define a weak foliation. The gouge sample from Stoney Creek (SC3) is 30 to 40% rock fragments within a phyllosilicate-rich matrix (Fig. 4.8h). The gouge is massive; occasionally a weak foliation is defined by the alignment of the long axis of the clasts. The WR1 gouge from the abandoned Waikukupa Thrust was sampled directly below the principal slip surface. It is massive and contains about 40% rock fragments (Fig. 4.8i). Due to the amount of rock fragments, SC3 and WR1 are better described as microbreccia. I refer to theses samples as gouges to be consistent with previous work that has been done on proximal samples. XRD analysis indicates the mineralogy of the gouges is dominantly quartz + K-feldspar + plagioclase + calcite + chlorite + illite-muscovite ± smectite [*Boles,* written communication, 2017.; *Warr and Cox*, 2001; *Boulton et al.*, 2012; *Schleicher et*

al., 2015]. Quantitative clay XRD analysis [*Boles*, written communication, 2017] on gouge samples from the same outcrops examined in this study indicates that the Stoney Creek gouge is 20 wt.% chlorite and 14 wt.% illite, the Gaunt Creek gouge is 18 wt.% chlorite and 18 wt.% illite, and the Waikukupa gouge is 13 wt.% chlorite and 25 wt.% illite.

4.3.1.1.5 Footwall host rocks

In general, the footwall of the Alpine Fault is more heterogeneous than the hanging wall, but it is not well exposed. I was able to obtain samples of rock types present in the footwall at three different locations. A footwall mylonite was sampled at Harold Creek (Fig. 4.6c). It is a quartzo-feldspathic augen mylonite with a foliation defined by micaceous and quartz-rich layers. Undulose extinction is observed in both quartz and feldspar grains. There are abundant feldspar porphyroclasts surrounded by recrystallized quartz and phyllosilicates (Fig. 4.9a). Porphyroclasts also host quartz and calcite veins (Fig. 4.9b). Some of the porphroclasts form boudinage structures. This mylonite was likely derived from Western Province granitoid protoliths [*Toy*, 2007]. At Smithy Creek I sampled a biotite-hornblende-two pyroxene monzonite (Fig. 4.6d) [*Lund Snee et al.*, 2014]. This lithology is massive but microfractures have a preferred, approximately vertical, orientation (Fig. 4.9c). Fractures are filled with opaque minerals and there is phyllosilicate fill in fractures within feldspar grains (Fig. 4.9d). Quartz grains in the sample exhibit undulose extinction. The final footwall lithology examined is a granitic L-S tectonite from Whataroa Quarry (Fig. 4.6e). This lithology has a strong lineation and a weaker foliation defined by quartzo-feldspathic rods surrounded by chlorite + biotite domains. The lineation is evident in the XZ plane, which parallels lineation (Fig. 4.9e); when looking at the YZ plane, the phyllosilicate domains are discontinuous (Fig. 4.9f). The sample contains abundant feldspar and quartz with some hornblende.

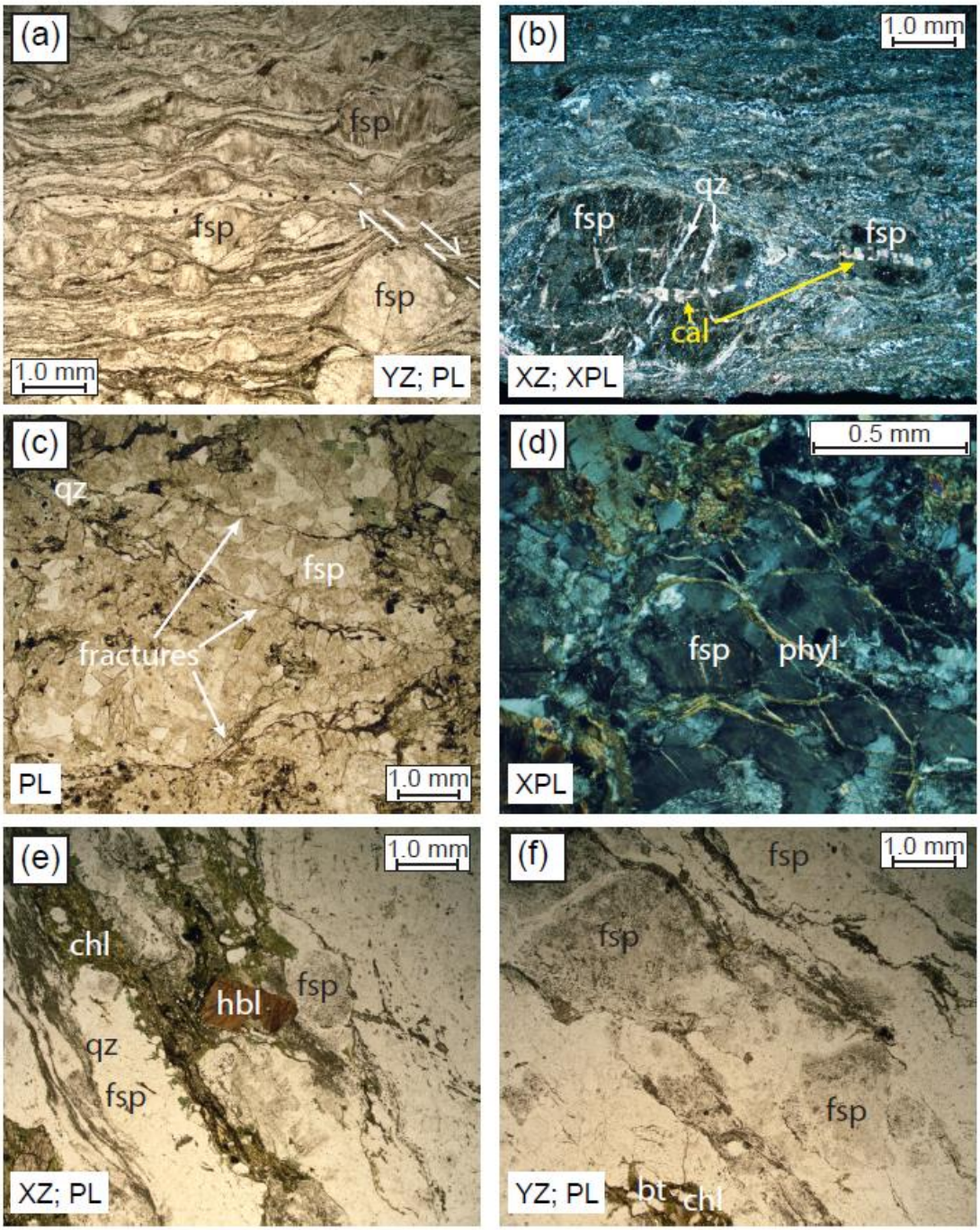

Figure 4.9: *Photomicrographs of Alpine Fault footwall host rock. (a) Abundant feldspar porphyroclasts deflect the foliation in the footwall augen mylonite. Shear band indicated by white dashed line. (b) Porphyroclasts in the augen mylonite contain quartz and calcite veins. (c) Aligned microfractures in monzonite, (d) Phyllosilicate vein within feldspar grain in the monzonite. (e) Phyllosilicate + amphibole and quartzo-feldspathic domains in the L-S tectonite in the XZ plane and YZ plane (f). Abbreviations for mineral labels are as follows: fsp = feldspar, qz = quartz, cal = calcite, hbl = hornblende, bt = biotite, chl = chlorite, phyl = phyllosilicate; additionally, PL = plane polarized light, XPL = cross-polarized light, XZ = XZ plane, YZ = YZ plane - see figure 4.2.*

4.3.2 Sample preparation

4.3.2.1 Outcrop samples

For the host rock specimens, 25.4 mm diameter cylindrical samples were prepared using a diamond bit drill press and surface grinder. Cylindrical samples from the damage zone specimens were cut to have either 25.4 mm or 38.1 mm diameters and, due to their incohesive nature, were prepared by hand using knives, an electric cutting tool, and sandpaper. When possible, three orthogonal specimens were obtain and oriented so that the axes of the cylinders were (1) foliation perpendicular (Z); (2) foliation and lineation parallel (X); and (3) foliation parallel, lineation perpendicular (Y) directions (Fig. 4.2). Due to the lack of clear lineation and difficulty in preparing the samples, most of the fault core samples have only two orientations: foliation perpendicular (Z) and foliation parallel (XY). In the event that a clear foliation was not visible, fault core samples were oriented relative to the fault plane. Additionally, the monzonite is massive, so one sample was taken in a vertical orientation, which is roughly parallel to the orientation of fractures, and the other two were oriented to be mutually perpendicular in the horizontal plane.

4.3.2.2 Drill core samples

Eight samples from the DFDP-1B borehole were also sampled for this study (Table 2). As with the outcrop samples, 25.4 mm diameter cylindrical specimens were cut from the drill core. These samples were oriented with respect to the drill core axis so that the specimen axis is either parallel (depth-parallel or vertical) or perpendicular (horizontal) to the borehole axis. All of these samples come from the Unit 6 lower cataclasites described by *Toy et al.* [2015]. These cataclasites contain millimeter-scale subangular to subrounded quartz-feldspar clasts, and are 10% to 70% matrix. Some of the sampled cataclasites are foliatited. The mineralogy is Quartz +

feldspar (plagioclase and orthoclase) + chlorite-muscovite + clays (illite/muscovite) ± biotite [*Toy et al.*, 2015].

Table 4.2: *Drill core samples from DFDP-1B.*

Sample	Depth (m)	Core	Section	Lithology	Average Density (g/cm^3)			Minimum P-wave Velocity (km/s)			Maximum P-wave Velocity (km/s)			Minimum S-wave Velocity (km/s)			Maximum S-wave Velocity (km/s)		
198	129.55	60	1	Cataclasite	2.22	±	0.13	4.35	±	0.17	4.40	±	0.18	2.24	±	0.09	2.80	±	0.11
382	130.01	60	2	Cataclasite	2.38	±	0.14	4.12	±	0.16	4.52	±	0.18	2.04	±	0.08	2.79	±	0.11
130	135.125	64	1	Cataclasite	2.25	±	0.13	4.35	±	0.17	4.87	±	0.19	2.29	±	0.09	2.60	±	0.10
316	139.59	67	1	Cataclasite	2.46	±	0.15	---	±	---	4.56	±	0.18	2.04	±	0.08	2.21	±	0.09
960	143.39	69	2	Foliated Cataclasite	2.20	±	0.13	4.33	±	0.17	4.61	±	0.18	2.19	±	0.09	2.76	±	0.11
410	143.45	69	2	Foliated Cataclasite	2.39	±	0.14	4.19	±	0.17	4.34	±	0.17	2.22	±	0.09	2.43	±	0.10
428	144	69	2	Cataclasite	2.59	±	0.16	4.86	±	0.19	4.86	±	0.19	2.46	±	0.10	2.79	±	0.11
384	144.1	69	2	Protocataclasite	2.26	±	0.14	4.70	±	0.19	6.52	±	0.26	2.10	±	0.08	4.12	±	0.16

4.3.3 X-ray diffraction analysis

X-ray diffraction (XRD) analysis was conducted on powdered samples of some of the damage zone rocks collected in the field. The analysis was performed at the University of Wisconsin – Madison S.W. Bailey X-ray Diffraction Lab on Scintag PAD V and Rikagu Rapid II diffractometers. The diffractometers are operated at 45 kV and 40 mA and 50 kV and 50 mA, respectively. Bulk sample diffraction patterns were collected from 3 to 75˚2θ. To determine the clay composition the powdered sample was mixed with water and heavy minerals were allowed to settle over 4 hours while the clay minerals remained in suspension. The suspended clays were then centrifuged to remove excess water and then spread over glass slides and allowed to dry. The clay diffraction patterns were collected from 3 to 40˚2θ. Preliminary quantitative estimates of the mineral composition were obtained by comparing the acquired diffraction patterns to patterns of various clay minerals from the American Mineralogist Crystal Structure Database (AMCSD).

Different crystal structures of a single mineral were overlain onto the acquired pattern to determine the best fit. Using Jade software, a statistical analysis is then run to compare the two patterns and provide an estimate of the weight percent of that mineral in the sample.

4.3.4 Laboratory ultrasonic wavespeed measurement

Following pulse-transmission techniques adapted from *Birch* [1960, 1961] and *Christensen* [1985], velocities through the cylindrical specimens were measured under elevated confining and pore pressure conditions at the University of Wisconsin-Madison Rock Physics Laboratory in the Department of Geoscience. Samples were loaded into a standard triaxial vessel (Fig. 4.10). For fault rock samples, a fine wire mesh was inserted at both ends to prevent extrusion of fine-grained sample material into the pore pressure ports when pressure was applied. Three 500 kHz central frequency piezoelectric transducers embedded in each endcap of the vessel were used as source-receiver pairs to generate the P-wave and two mutually perpendicular S-waves used in the wave propagation experiments. For foliation-parallel samples, transducers were oriented so that one vibration direction was parallel to the foliation and the other was perpendicular to foliation. In the following discussion I annotate the velocities so that the two S-waves, which propagate in the X-direction and vibrate in the Y- and Z-directions, respectively, will have velocities of v_{xy} and v_{xz}. Similarly, the S-waves that propagate in the Y-direction will be referred to as v_{yx} and v_{yz}. For foliation perpendicular samples, the vibration direction would ideally be oriented with respect to lineation. Due to difficulty in maintaining the lineation orientation during sample preparation, however, the vibration directions of foliation perpendicular samples are arbitrary so these velocities are annotated as v_{z1} and v_{z2}.

During our experiments, confining pressure, axial stress, and pore fluid pressure were independently controlled using three syringe pumps. Fresh water was used as a saturating fluid

whereas isopar-H was used as a confining fluid. An initial axial stress of 2 MPa was applied to each specimen followed by a confining pressure of 1.8 MPa. The 0.2 MPa difference between axial stress and confining pressure was maintained throughout the experiment to ensure good coupling between the sample liner and endcap. For fault rock samples, the specimen was then saturated by creating a pressure differential across the sample. One side of the sample was left open to atmospheric pressure and a 1 MPa pore pressure was applied at the other side. Once water began flowing out the open end of the sample, it was connected to the syringe pump so the saturating fluid flowed into both ends of the sample. Host rock samples were placed in a water bath for at least one week prior to being placed in the triaxial vessel and, once in the vessel, pore pressure was immediately applied to both ends of the sample without waiting for flow through.

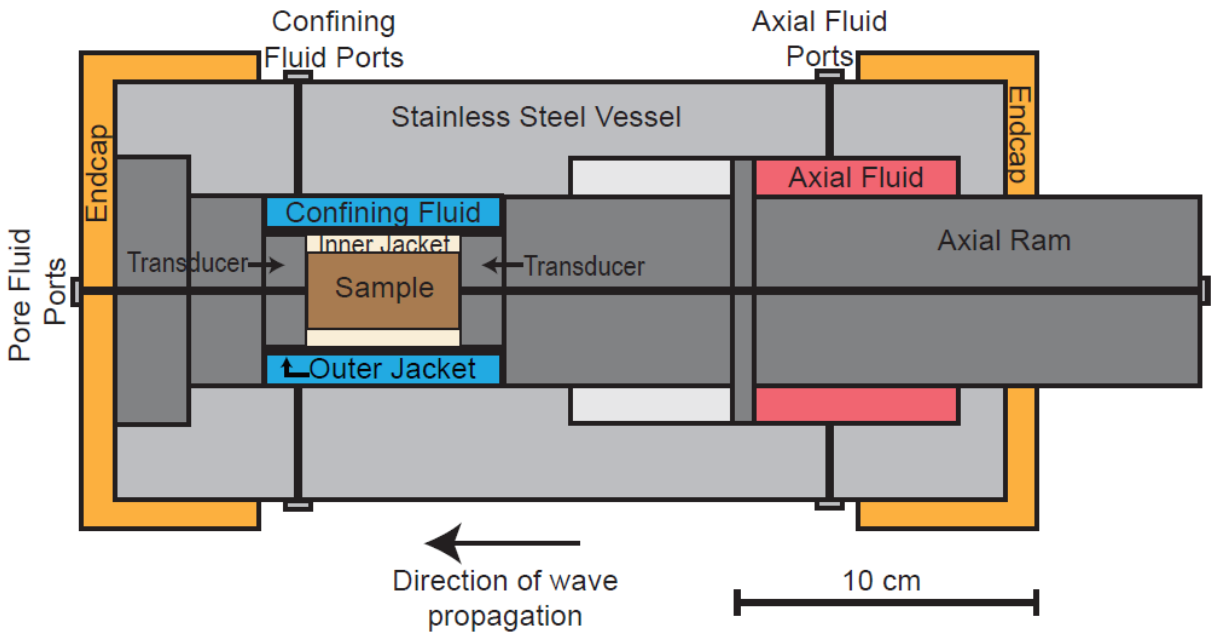

Figure 4.10: *Schematic of the triaxial pressure vessel at the University of Wisconsin-Madison.*

A pore fluid pressure of 1 MPa was maintained throughout the experiments to ensure that any remaining pore space gas was kept in solution. The specimen was allowed to saturate for ≥ 24

hours before the first ultrasonic velocity measurement was made. I then simultaneously increased the confining and axial pressure to obtain an effective pressure of 2 MPa and allowed the sample to equilibrate. Ultrasonic measurements were conducted at regular intervals between 1 MPa and 60 MPa. Following each pressure step the sample was allowed to equilibrate, as monitored by continuous measurement of sample length and pore volume change, before making an ultrasonic measurement. Measurements were made during both increasing and decreasing pressure paths. P- and S-wavespeeds were determined from time-of-flight measurements and the measured sample length. At low pressures, especially in the damage zone materials, the wave arrivals can be difficult to identify due to poor sample-transducer coupling. Additional uncertainty arises from non-parallel core faces and associated uncertainties in the length measurements. The length uncertainty is greater in the damage zone materials as theses samples had to be prepared by hand. Overall there is less than 3% uncertainty in the wavespeed measurement of the host rock and 4% uncertainty in the fault rock measurements.

Final porosity and density were determined through direct measurement of sample volume and wet and dry mass. Porosity was also measured using a helium porosimeter. These measurements, combined with the axial displacement, were used to estimate porosity and density changes during the experiment. The total sample volume was determined using both linear measurements using a vernier caliper and volumetric displacement methods. Because the damage zone samples are fragile and must be prepared by hand the sample diameter is not uniform. This results in a relatively high uncertainty of 6% in the density measurements and 7% in porosity measurements. In contrast, the host rock samples have less than 2% uncertainty in density and 3% in porosity.

4.3.4.1 Velocity anisotropy

The P-and S-wave velocity anisotropy around the Alpine Fault was determined from measurements made on the outcrop and drill core samples in the different wave propagation and vibration directions described above. The maximum anisotropy was calculated as:

$$Maximum\ anisotropy = \frac{(v_{max} - v_{min})}{v_{average}} \quad [10]$$

where v_{max} and v_{min} are the sample's minimum and maximum velocities and $v_{average}$ is the average of the velocities measured in the three orthogonal directions. This was calculated for both P- and S-waves when measurements were available in all propagation and vibration directions, although only one of either the Z1 or Z2 vibration directions was required as these measurements were not aligned.

4.4 Results and Discussion

4.4.1 P- and S-wave wavespeeds and pressure dependence

Typical velocity-pressure curves for the lithologies examined in this study are presented in figure 4.11. Velocity increases systematically with increasing effective confining pressure for all samples, but the damage zone/fault core samples exhibit greater sensitivity to changes in pressure than the samples taken from the surrounding host rock. This indicates that the fault rock is more compliant than the surrounding host rock. Furthermore the fault rock samples exhibit greater hysteresis between the loading and unloading curves. At 20 MPa, the average hysteresis for the fault rock samples is 10% compared to 3% for the host rock samples. The hysteresis suggests that the fault rocks experienced more permanent plastic deformation during the loading cycle than the host rock does.

Wavespeeds through the host rock samples are all similar. Over the range of examined pressures the velocities vary from 4.7 to 6.6 km/s for the P-wave and 2.3 to 4.1 km/s for the S-wave. These

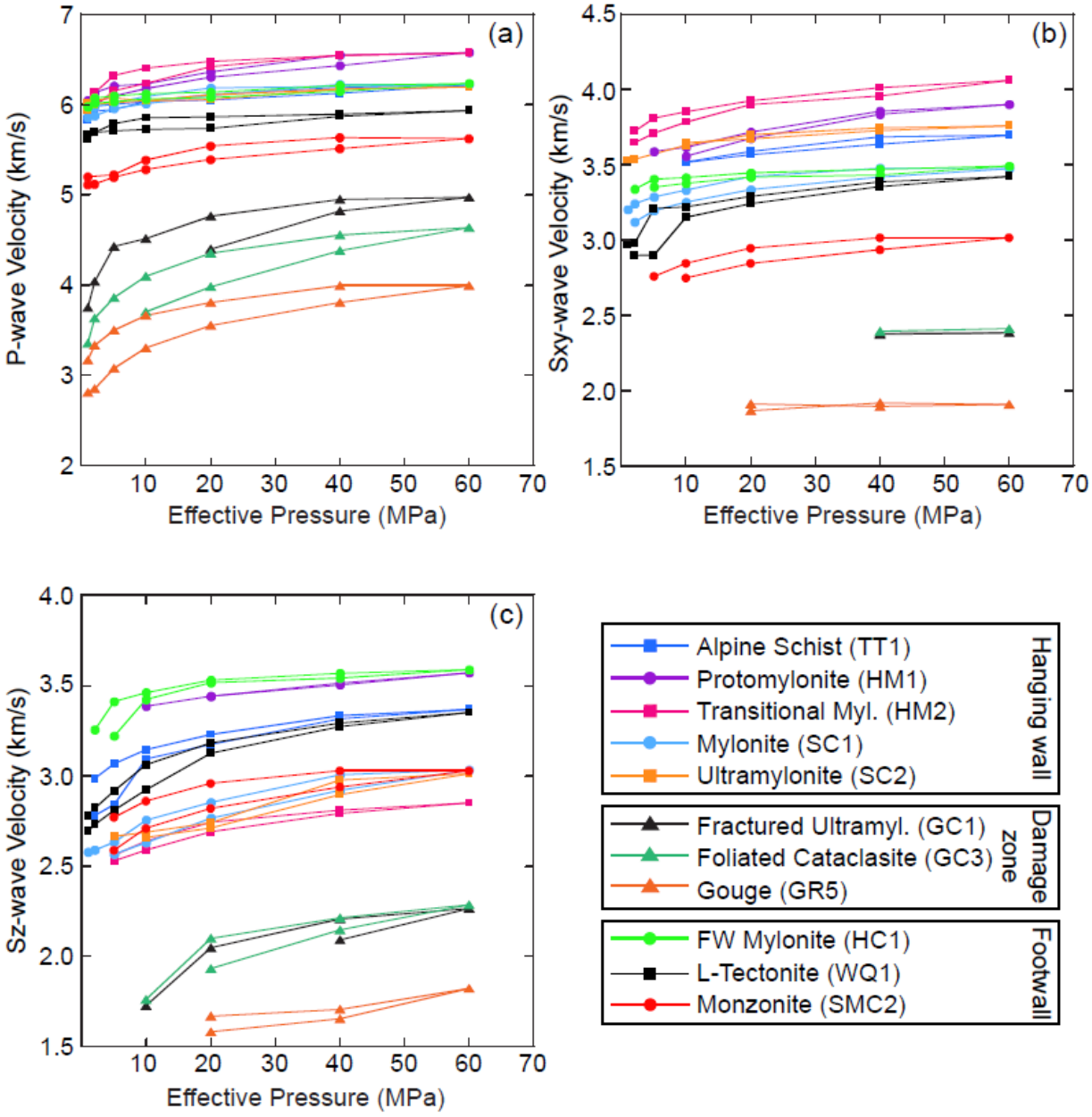

Figure 4.11: *Velocities measured on representative outcrop samples for (a) P-wave and (b & c) S-wave propagation in the X-direction with vibration direction (b) in the XY plane and (c) parallel to the Z-axis. Damage zone samples have significantly slower velocities than the surrounding host rock.*

wavespeeds are similar to those previously measured wavespeed measurements conducted on samples of the Alpine Schist and Alpine Fault mylonite [*Okaya et al.*, 1995; *Godfrey et al.*, 2000, 2002; *Christensen and Okaya*, 2007]. They are noticeably faster than wavespeeds though the

fault rocks, which range from 2.5 to 5.0 km/s for the P-wave and 1.3 to 2.7 km/s for the S-wave. At 60 MPa effective pressure, the average velocity difference in the fault rocks is a decrease of 23% for P-waves and 32% for S-waves relative to the host rock velocities. At 20 MPa this reduction increases to 32% and 43% for P- and S-wave respectively. The elastic properties of the damage zone lithologies are described in greater detail in the following sections.

4.4.1.1 Fractured mylonite and cataclasites

Measured P- and S-wave velocities of fractured mylonite and cataclasite samples obtained from outcrops range from 2.75 to 5 km/s and 1.6 to 2.6 km/s, respectively (Fig. 4.12a & b). P-wave measurements made in the X- (or XY) direction on samples of protocataclasite and fractured ultramylonite are similar, but the foliated cataclasite has the slowest velocity, suggesting a possible relationship between velocity and increasing degree of cataclasis. The Smithy Creek footwall ultracataclasite has P-wave velocities between 4.6 and 4.81 km/s and S-wave velocities between 2.4 and 2.76 km/s. The measured velocities for this non-Alpine Fault sample are faster and less pressure dependent than the Alpine Fault cataclasite samples because the sample is more indurated due to hydrothermal cementation [*Lund Snee et al.*, 2014]. The ultracataclasite S-wave velocity in the Z1 direction appears to increase with decreasing pressure, likely due to noise in the data obscuring the true wave arrival.

The velocity range measured in the outcrop cataclasites is similar to the range measured on the DFDP-1 drill core samples examined in this study (Fig. 4.12c & d) and in previous work by *Carpenter et al.* [2014]. Carpenter et al. [2014] documented P-wave velocities in the DFDP-1 cataclasites ranging from 2.3 to 4.4 km/s and S-wave velocities from 1.4 to 2.4 km/s. Most of the velocities I measured for the DFDP-1 core have a similar range (P-wave 2.4 to 4.9 km/s, S-wave 1.5 to 2.8 km/s) with one exception. The perpendicular 384 sample has a significantly higher

velocity (P-wave 5.7 to 6.5 km/s, S-wave 3.0 to 4.1 km/s). This sample is a protocataclasite and the majority of the sample volume is occupied by a single, large, ultramylonite clast, causing it to have elastic properties similar to the host rock.

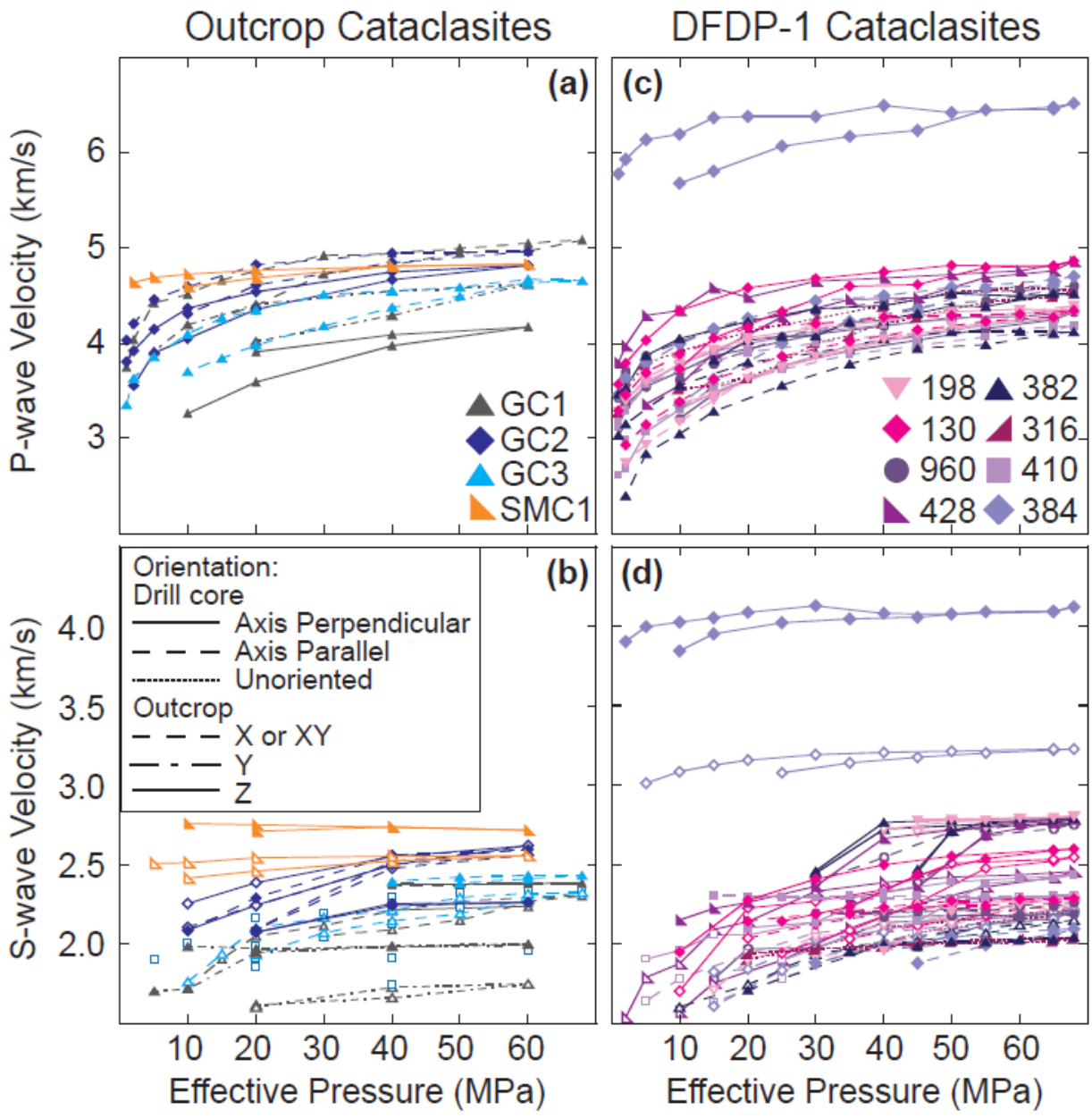

Figure 4.12: *(a) P- and (b) S-wave velocities measured in the X, Y, and Z-directions on the outcrop samples of fractured ultramylonite and cataclasite. (c) P- and (d) S-wave velocities measured on drill core samples of cataclasite oriented parallel or perpendicular to the drill core axis. S-wave vibration in the XY plane is indicated by solid symbols and vibration in the Z-direction is indicated by open symbols.*

4.4.1.2 Gouges

Four samples of fault gouge were examined (Fig. 4.13). Three of these samples (SC3, GC4, and GC5) came from the active trace of the Alpine Fault while the fourth sample came from the abandoned Waikukupa Thrust (WR1). Samples from the Alpine Fault and Waikukupa Thrust exhibit similar pressure sensitivity. The Alpine Fault gouges have the slowest P- and S-wave velocities ranging from 2.5 to 4.5 km/s and 1.3 to 2.4 km/s, respectively. A similar range in P- and S-wave velocities from 2.3 to 3.1 km/s and 1.3 to 1.5 km/s, respectively, was measured for gouge samples from DFDP-1 [*Carpenter et al.*, 2014]. The Waikukupa Thrust gouge is slightly faster, ranging from 3.2 to 4.7 km/s and 1.6 to 2.5 km/s for P- and S-waves, respectively.

Some of the velocity variations observed in the gouges may be related to fault healing. Seismic, geologic, and laboratory studies have provided evidence that fault healing occurs during interseismic periods and can result in increased wavespeed in fault zones [*Karner et al.*, 1997; *Olsen et al.*, 1998; *Bos and Spiers*, 2002; *Li et al.*, 2003, 2006; *Tenthorey et al.*, 2003; *Vidale and Li*, 2003; *Yasuhara et al.*, 2005]. The Stoney, Gaunt, and Waikukupa gouges can be directly compared as they are from the same fault zone, have experienced similar amounts of slip, and have the same protolith. The Stoney and Gaunt Creek gouges have the slowest wave speeds and experienced the most recent coseismic slip during the 1717 rupture [*Sutherland et al.*, 2007] whereas gouges from the Waikukupa Thrust, which was abandoned 20,000 years ago [*Norris and Cooper*, 1997] have faster wavespeeds.

The P- and S-wave velocities of the gouges from the active fault trace tend to be ~0.5 km/s slower than those of the cataclasites. In general, the gouges exhibit lower cohesion and slightly higher total clay content and porosity than the cataclasites [*Boles*, written communication, 2017; *Boulton et al.*, 2012] and it is expected that these characteristics would result in decreased

velocity [e.g., *O'Connell and Budiansky*, 1974; *Stierman and Kovach*, 1979; *Tosaya*, 1982; *Tosaya and Nur*, 1982; *Castagna et al.*, 1985; *Han et al.*, 1986].

Alpine Fault gouge wavespeeds are similar to those measured for gouges from the creeping segment of the San Andreas Fault, which have P-wave velocities between 2.3 and 4.5 km/s and S-wave velocities between 1 and 2 km/s [*Jeppson and Tobin*, 2015]. Both are large plate bounding faults that have experienced significant displacements, though they have different protoliths. The Alpine Fault gouges are slightly faster than the San Andreas gouges (up to 0.5 km/s difference). This difference could be related to fault healing since the sampled segment of the San Andreas Fault is actively deforming through creep. In contrast, the Alpine Fault is late in its seismic cycle and locked. However, there is also a difference in the clay composition of the gouges. The San

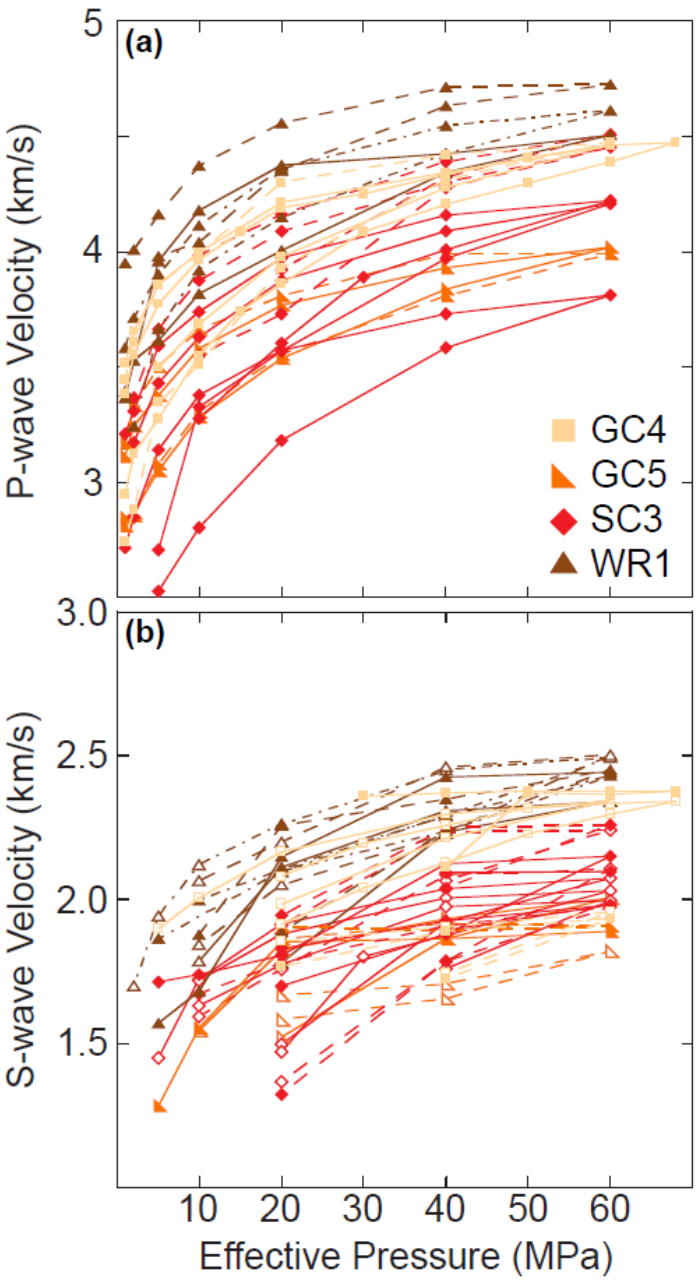

Figure 4.13: *(a) P- and (b) S-wave velocities measured in multiple orientations on the outcrop samples of fault gouge. Line styles indicate the measurement orientation as indicated in figure 4.12. S-wave vibration in the XY plane is indicated by solid symbols and vibration in the Z-direction is indicated by open symbols.*

Andreas gouges are dominantly composed of smectite, specifically saponite [*Moore and Rymer*, 2007; *Bradbury et al.*, 2011; *Holdsworth et al.*, 2011], which has lower elastic moduli than many other clay minerals [*Wang et al.*, 2001; *Vanorio et al.*, 2003] such as the chlorites and illites present in the Alpine Fault gouges.

4.4.2 Velocity anisotropy

In the host rocks, minimum P-wave velocities are consistently measured with the propagation direction perpendicular to foliation (Z-direction). Maximum P-wave velocities are measured when the propagation direction is parallel to both foliation and lineation (X-direction) (Fig. 4.14a). Maximum S-wave velocities are recorded when propagation is in the X-direction with vibration in the foliation plane (XY). When the vibration direction is perpendicular to the foliation (XZ or YZ) the velocity can be slower than for S-waves propagating in the Z-direction (Fig. 4.14b). Similar relationships with respect to orientation are observed in the damage zone samples, although the differences between measurements made in the different orientations is not as substantial, indicating a decrease in velocity anisotropy with fault related damage.

At pressures greater than 20 MPa, the magnitude of velocity anisotropy remains fairly constant especially in the host rock samples. In general, samples tend to be slightly more anisotropic at low pressures due to open microcracks, which close at greater pressures. Over the range of examined effective pressures, the velocity anisotropy varies by about 2 to 5%. This low magnitude of variation indicates that the velocity anisotropy is not controlled by microcrack orientation in these samples [*Christensen and Okaya*, 2007]. There are two exceptions to this trend. The maximum S-wave anisotropy for the Alpine Schist (TT1) decreases significantly from 20 to 10 MPa, likely due to uncertainty in the S-wave arrival picked at 10 MPa. At higher pressures the Z2-vibration direction is consistently the slowest S-wave, but at 10 MPa data

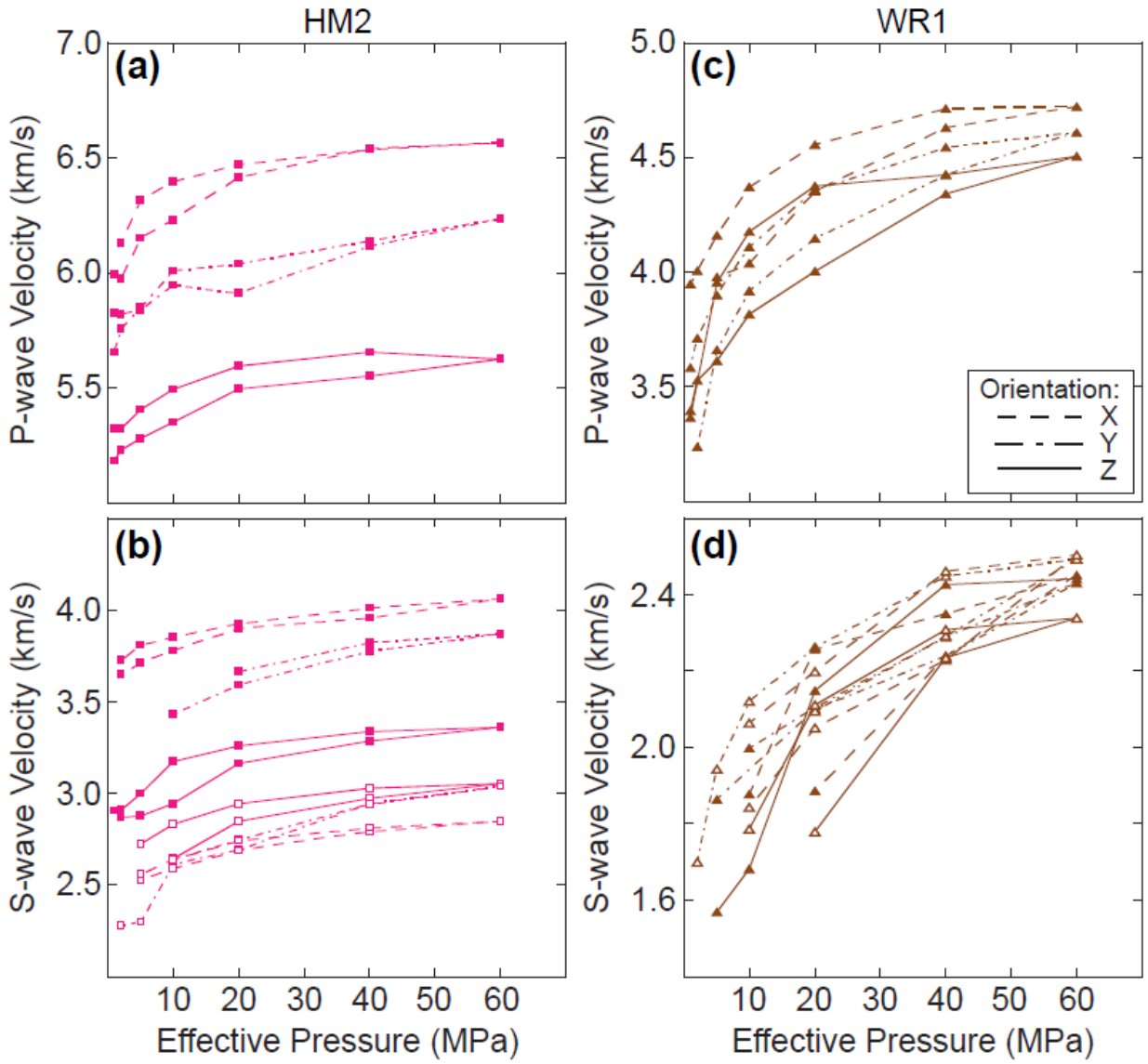

Figure 4.14: *(a) P- and (b) S-wave velocities measured on host rock sample HM2 in X, Y, Z directions show greater anisotropy than (c) P- and (d) S-wave velocities measured on gouge sample WR1 in the same orientations. S-wave vibration in the XY plane is indicated by solid symbols and vibration in the Z-direction is indicated by open symbols.*

quality decreases so the Z2 S-wave arrival could not be picked. The next slowest wave was the YZ S-wave but it is ~0.5 km/s faster than the Z2 wave resulting in a decrease in the anisotropy. The maximum S-wave anisotropy for the footwall mylonite (HC1) also decreases with decreasing pressure. This could be due to uncertainty in the S-wave picks or, as the sample is not

very anisotropic, open microcracks at low pressures may disrupt the weak anisotropy that is present due to mineral alignment.

Figure 4.15 summarizes the velocities and maximum anisotropy recorded at 60 MPa effective confining pressure for outcrop samples. This pressure is approximately the effective overburden stress at 1.5 to 2 km depth and was chosen to minimize uncertainty in velocity. In the hanging wall host rock the maximum P-wave anisotropy ranges from 13 to 16% and the S-wave anisotropy ranges from 15 to 36% at 60 MPa. Previous workers documented P-wave anisotropy of up to 27% in the Alpine Schist [*Okaya et al.*, 1995; *Godfrey et al.*, 2000, 2002; *Christensen and Okaya*, 2007]. This anisotropy is caused by well-developed foliations related to preferred mineral orientations. I do not observe the increase in anisotropy correlating with the degree of deformation in the mylonites that has been observed elsewhere [*Kern and Wenk*, 1990]. The non-mylonitic footwall host rock is not highly anisotropic. In these materials, the maximum P- and S-wave anisotropy is less than 10%. Of the footwall samples the mylonite is the most anisotropic but it is still less anisotropic than the hanging wall samples. The footwall mylonite contains many porphyroclasts that deflect the foliation, providing a lower velocity anisotropy than that of the hanging wall mylonites.

In the damage zone, there is greater variability but an overall decrease in anisotropy. GC1 has P- and S-wave anisotropies of 17 and 30%, respectively, similar to what is observed in the hanging wall host rock. Anisotropy is lower in the cataclasite and gouge samples where the P-wave anisotropy tends to be less than 10%. SC3 is anomalous, with a maximum P-wave anisotropy of 17%. The high anisotropy measured for SC3 is due to sample heterogeneity. Five samples of SC3 were measured, three in the Z direction and 2 in the XY direction; the P-wave velocities of these samples range from 3.8 to 4.2 km/s in the Z direction and 4.4 to 4.5 km/s in the XY

direction. This yields a range in the P-wave anisotropy from 7 to 16%. SC3 contains many relict mylonite and cataclasite grains that are not systematically distributed through the sample (Fig. 4.8). The velocity is affected by differences in the distribution of grains in the measured samples. In the cataclasites and gouges, S-wave anisotropy remains high (between 7 and 20 %).

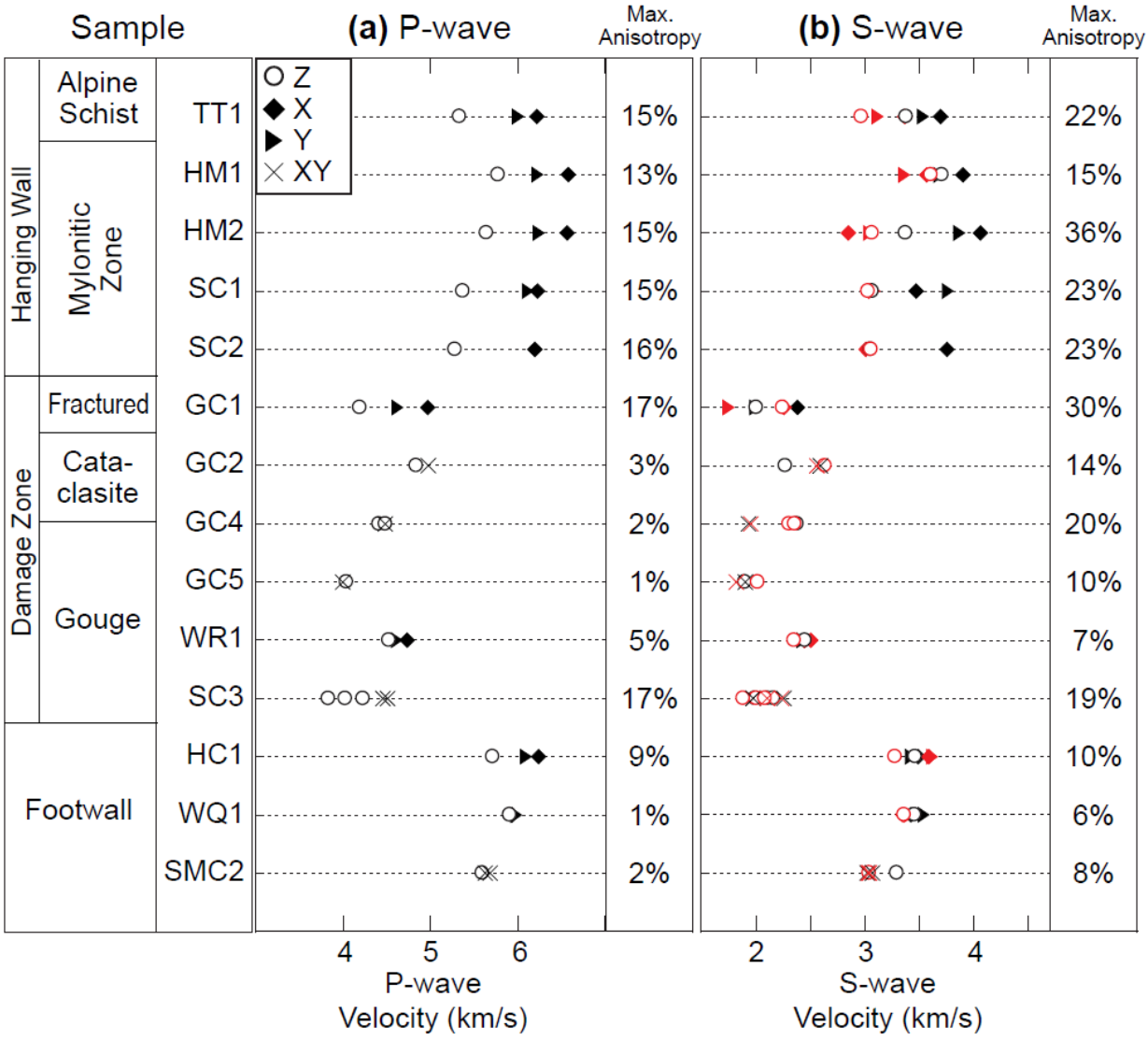

Figure 4.15: *Velocities for the Alpine Fault Zone rock illustrating seismic anisotropy. (a) P-wave and (b) S-wave velocities at 60 MPa. Open circles denote propagation perpendicular to foliation, solid triangles denote propagation parallel to foliation and perpendicular to lineation, and solid diamonds denote propagation parallel to both foliation and lineation. For S-waves, red denotes vibration is perpendicular to foliation (also Z2) and black denotes vibration parallel to foliation (also Z1). Percent anisotropy is calculated as indicated in equation 3.*

The variations in anisotropy observed in the damage zone correlate with the progressive disruption of the original mylonitic foliation by brittle deformation. GC1 retains its original mylonitic foliation and is highly anisotropic even though it has been heavily fractured (Fig. 4.8a & b). The anisotropy decreases in the cataclasites and gouge samples. In these samples the original foliation has been overprinted by brittle deformation and cannot be clearly identified. The weak discontinuous foliation that has developed in some of the cataclasite and gouge samples does not appear to have a significant effect on seismic anisotropy.

For both host and fault rock, the magnitude of the velocity difference between the different orientations is similar for both P- and S-waves, but the percent anisotropy is greater for the S-waves because the velocity values are smaller. Additionally, the maximum S-wave anisotropy combines both polarization directions, calculating separate maximum anisotropy for the different polarization directions reduces the maximum anisotropy, resulting in values similar to the P-wave anisotropy. The high S-wave anisotropies observed in the fault core rocks may be due to higher uncertainty in identifying the S-wave arrival in these materials. Previous workers have noted difficulty in consistently picking a reliable S-wave arrivals in measurements of fault core samples from the Alpine Fault [*Carpenter et al.*, 2014].

DFDP-1B cataclasite samples were aligned with respect to the core axis instead of foliation for better correlation with logging data. As the core was not oriented with respect to foliation, only a minimum estimate of the maximum anisotropy can be obtained. Wave propagation parallel to the core axis (depth parallel) tends to be slower than wave propagation perpendicular to the core axis (Fig. 4.16). I examine the maximum velocity anisotropy at 68 MPa as measurements at 60 MPa where not recorded for all the DFDP-2 samples. The maximum P-wave anisotropy at this effective pressure is less than 11% and the maximum S-wave anisotropy ranges from 9 to 56%.

The high S-wave anisotropies may not be realistic, as the waveforms for these samples are poor quality (Suppl. Fig. 4A.1.1) [c.f., *Carpenter et al.*, 2014].

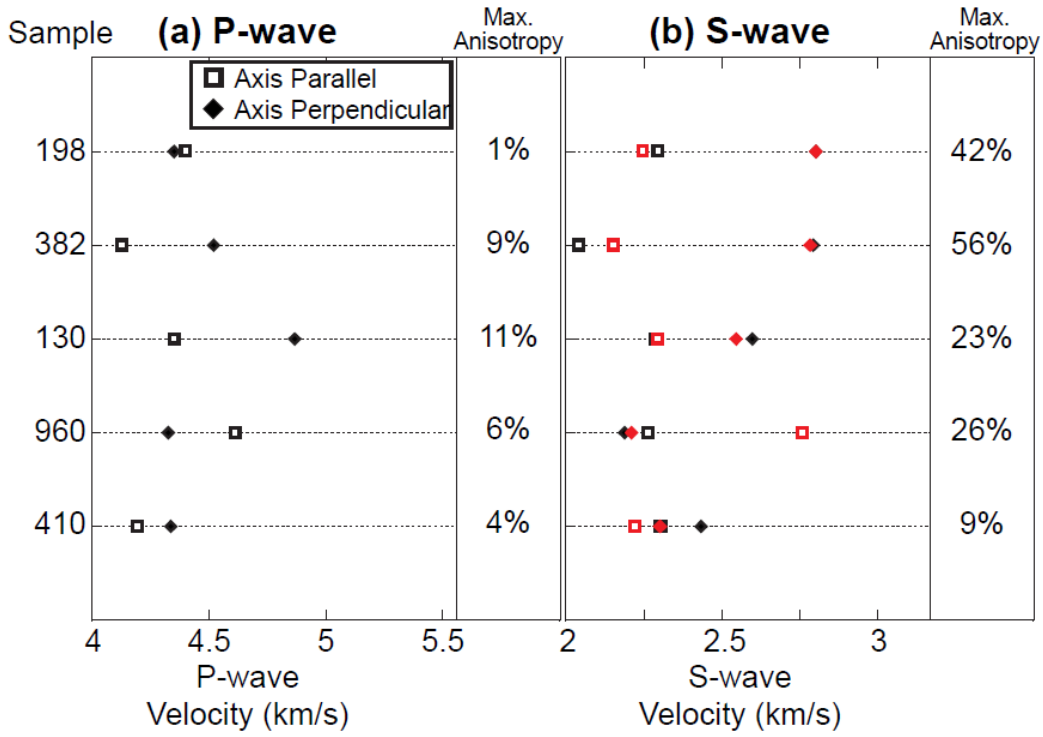

Figure 4.16: *Velocities for the DFDP-1B cataclasites illustrating seismic anisotropy. (a) P-wave and (b) S-wave velocities at 68 MPa. Open squares denote propagation parallel to the drill core axis, solid diamonds denote propagation perpendicular to the drill core axis. For S-waves, red and black denote two orthogonal but arbitrarily oriented S-wave vibration directions. Percent anisotropy is calculated as indicated in equation 3.*

4.4.2.1 S-wave splitting

A measure of S-wave splitting, taken as the simple difference between the two polarization directions measured for a single propagation direction, correlates well with other measures of anisotropy. In the hanging wall rock, S-wave splitting when propagation is in the foliation plane is 0.66 ± 0.29 km/s. Splitting when propagation is perpendicular to the foliation plane is 0.23 ± 0.18 km/s. The experimental uncertainty in determining the S-wave arrival is 3 to 4% or ~ 0.10 to 0.14 km/s. Thus S-wave splitting with propagation in the foliation plane is significant, indicating that the samples are at least transversely isotropic. Splitting is not always statistically

significant when propagation is perpendicular to foliation. In the Z-direction the schist shows the greatest magnitude of S-wave splitting, over 0.41 km/s, while the mylonite and ultramylonite show the least, less than 0.16 km/s. In the footwall rocks, S-wave splitting in the foliation plane is 0.11 ± 0.07 km/s and 0.16 ± 0.05 km/s perpendicular to the plane. As these values are the same within experimental uncertainty the footwall rocks may be isotropic. The fault rocks may also be isotropic as the S-wave splitting is 0.12 ± 0.11 km/s in the foliation plane and 0.11 ± 0.09 km/s perpendicular to the plane.

Table 4.3: *Diagonal components of the stiffness tensor and estimated symmetry for Alpine Fault outcrop samples. TI = transversely isotropic, ORTHO = orthorhombic, ISO = isotropic.*

Sample	C11	C22	C33	C44	C55	C66	Symmetry
TT1	101	95	77	26	30	36	TI
HM1	117	101	90	30	35	41	ORTHO
HM2	116	105	85	25	22	44	TI
SC1	107	100	79	26	25	33	TI
SC2	103	---	76	---	24	38	TI or ORTHO
GC1	59	33	43	5	12	14	ORTHO
GC2	60	---	57	---	16	16	ISO or TI
GC3	49	---	---	---	12	13	---
GC4	50	---	50	---	10	9	ISO or TI
GC5	37	---	44	---	8	8	ISO or TI
WR1	56	53	50	15	16	15	ISO
SC3	46	---	34	---	11	10	ISO or TI
SMC1	---	---	57	18	16	---	---
HC1	101	101	87	36	33	32	TI
WQ1	95	92	93	30	30	31	ISO
SMC2	86	88	84	25	25	25	ISO

4.4.2.2 Stiffness tensor and symmetry

The diagonal components of the elastic stiffness tensor were calculated from the observed velocities and densities (Table 4.3). As with velocity measurements, the moduli vary systematically with effective pressure, and there is a significant contrast between the properties of the fault rocks and surrounding host rock. The stiffnesses in the damage zone are about half those in the host rock, indicating that the fault rocks are significantly more compliant.

Further examination of the components of the stiffness tensor allows the degree of symmetry to be readily assessed. Samples for which the elastic moduli differ by less than the uncertainty are assumed to be isotropic because $C_{11} \approx C_{22} \approx C_{33}$ and $C_{44} \approx C_{55} \approx C_{66}$. The uncertainty in the host rock moduli is 5% for C11, C22, and C33 and 7% for C44, C55, and C66. In the fault rocks the uncertainty increases to 12% and 14% (Fig. 4.17). The greater uncertainty is produced by uncertainty in density measurements because the samples are not perfect cylinders. An isotropic symmetry was assigned to three of the samples: WR1, WQ1, and SMC2. Samples where two of the three moduli were equal within uncertainty ($C_{11} \approx C_{22} \neq C_{33}$ and $C_{44} \approx C_{55} \neq C_{66}$) were estimated to have transversely isotropic symmetry. TT1 can be described as transversely isotropic, in agreement with previous studies that indicated the Alpine Schist can be either orthorhombic or transversely isotropic [*Godfrey et al.*, 2000, 2002; *Christensen and Okaya*, 2007]. HM2, SC1, and HC1 also appear to be transversely isotropic. For orthorhombic and other more complex symmetries none of the diagonal components are equal ($C_{11} \neq C_{22} \neq C_{33}$ and $C_{44} \neq C_{55} \neq C_{66}$). This symmetry best describes GC1 and HM1. Additional measurements, including off-symmetry axis measurements, would be needed to fully derive the stiffness tensor and describe more complex symmetries [*Mah and Schmitt*, 2001, 2003]. Samples with only two directions measured are assigned two potential symmetries. For SC3, GC2, GC4, and GC5, both measurement directions provide similar stiffness coefficients; depending on the unmeasured third direction, the material could be either quasi-isotropic or transversely isotropic. The measurements for SC2 provided very different values so a third measurement could indicate it has either transversely isotropic or orthorhombic symmetry.

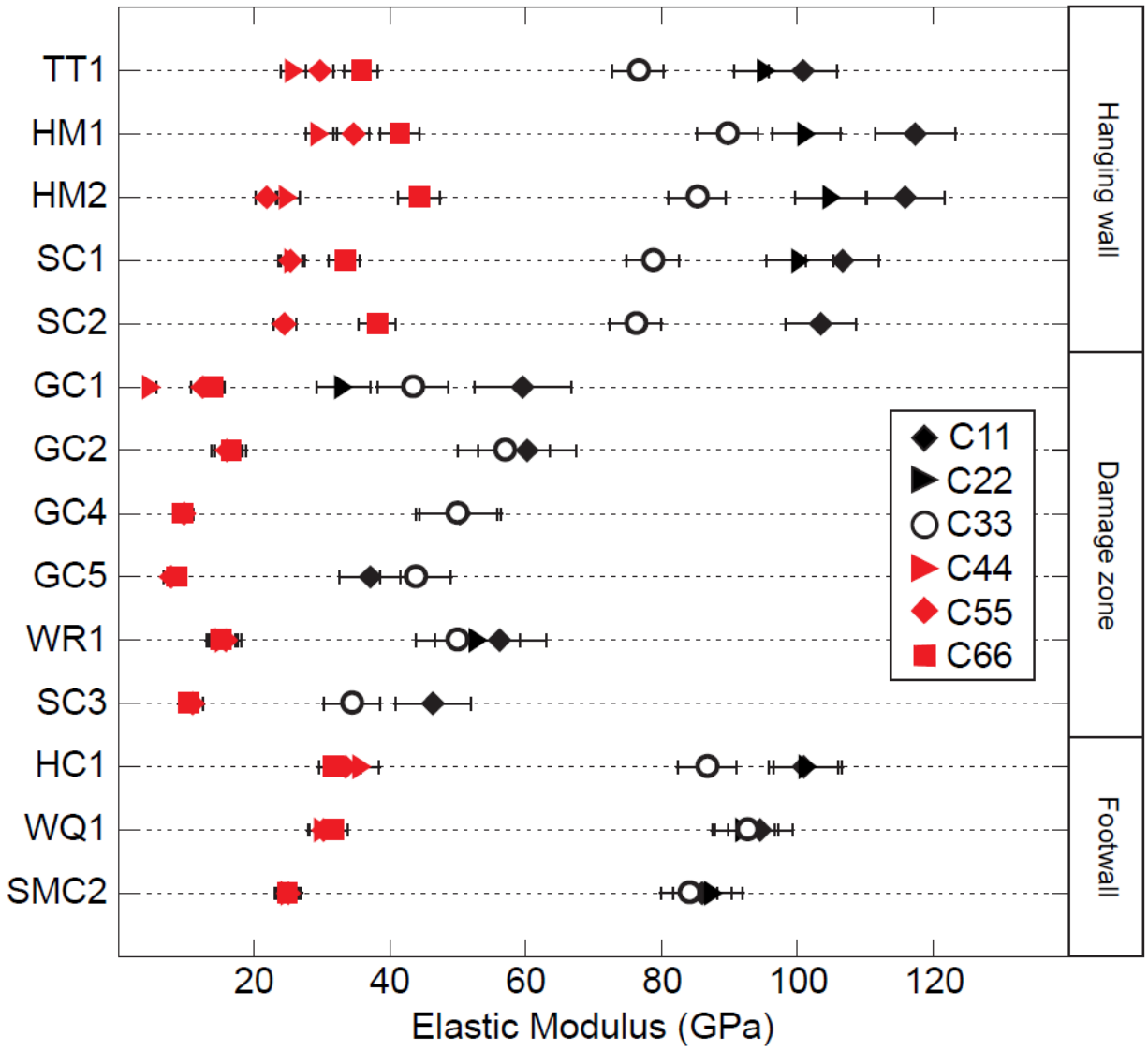

Figure 4.17: *Diagonal elastic coefficients of the stiffness tensor for Alpine Fault rocks. The cataclasites and gouges appear to be isotropic whereas the hanging wall rocks have transversely isotropic to orthorhombic symmetry.*

4.4.3 Scaling: lab to field

4.4.3.1 DFDP-1

I compare the laboratory measurements of velocity to the sonic log data from DFDP-1B by plotting the velocities measured on the DFDP-1 core samples at the depth where the sample was acquired (Fig. 4.18). As lab measurements on outcrop samples do not correlate to specific depths within the borehole, the range in measured velocities plus uncertainties are indicated by gray

boxes. As the fault core appears to be relatively isotropic, all measurement orientations were used to determine the velocity range shown. Velocities plotted were measured at an estimated *in situ* pressure of 2 MPa, determined based on average sample density and elevated fluid pressures measured in the borehole.

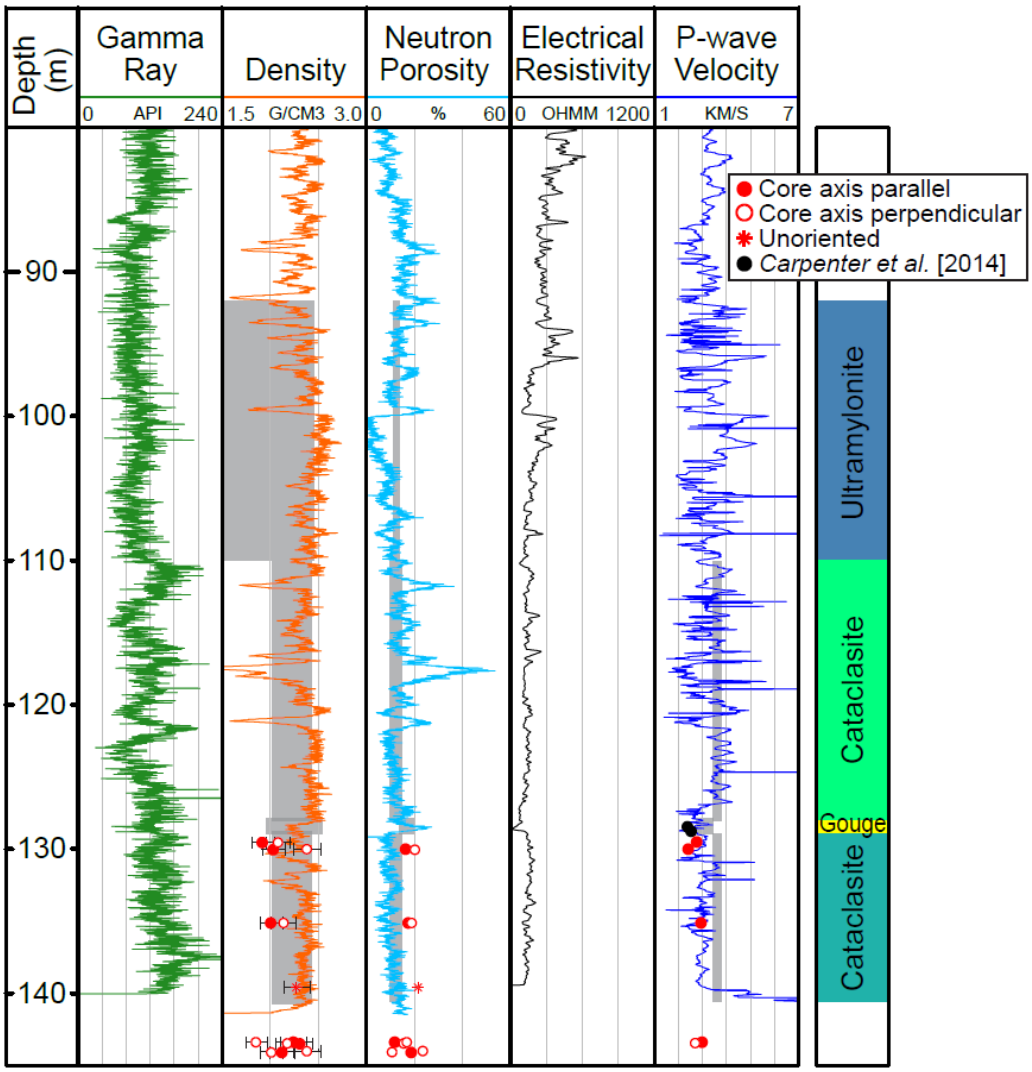

Figure 4.18: *Comparison of laboratory measurements and downhole geophysical logs from DFDP-1B. The range in data measured in the lab on outcrop samples in all directions is indicated by gray shaded regions. The velocity range of the ultramylonites is not available as data quality for the fractured ultramylonite sample at the estimated in situ pressure of 2 MPa is poor and the P-wave arrival could not be identified. Red symbols denote measurements made on DFDP-1 core samples and black circles denote measurements on core samples reported by Carpenter et al. [2014]. Error bars for the velocity and porosity measurements are smaller than the size of the symbol. In general the laboratory and log data are in good agreement.*

I find, as did *Carpenter et al.* [2014], that laboratory measurements of velocity on samples of the DFDP-1 core are in good agreement with the logging data. The outcrop samples are also in good agreement with the log data. This indicates that laboratory measurements of both core and outcrop samples, that have not been heavily weathered, can be used as proxies to estimate *in situ* velocities where sonic log measurements are not available. The agreement of the measurements obtained at different spatial and frequency scales indicates that the factors responsible for low velocity in the damaged rock are present at both lab and log scales. These factors must therefore be related to small-scale processes such as microfracturing, disaggregation, cataclastic grain-size reduction, and formation of authigenic clay minerals.

Lab-derived densities are lower than the log densities and lab-derived porosities are higher than the neutron porosity log values. This is expected due to exhumation and weathering of the outcrop samples and decompression cracking that occurs when core samples are brought to the surface.

4.4.3.2 DFDP-2

As with data from DFDP-1, I compare the borehole sonic log data to laboratory velocity measurements of waves propagating in the Z-direction (Fig. 4.19). The estimated *in situ* effective pressure incorporates the elevated pore pressure observed in the borehole [*Sutherland et al.*, 2017] and ranges from 5 to 15 MPa at depth. Laboratory velocities are 2 to 18% faster than the average log velocity. This difference in velocity could be due to anisotropy, differences in laboratory versus *in situ* conditions, frequency-dependent velocity dispersion, or a sampling bias. I examine these potential causes below.

Waves generated by the sonic logging tool propagate along the borehole wall. If foliation is perpendicular to the borehole then the orientation would be the same as the laboratory

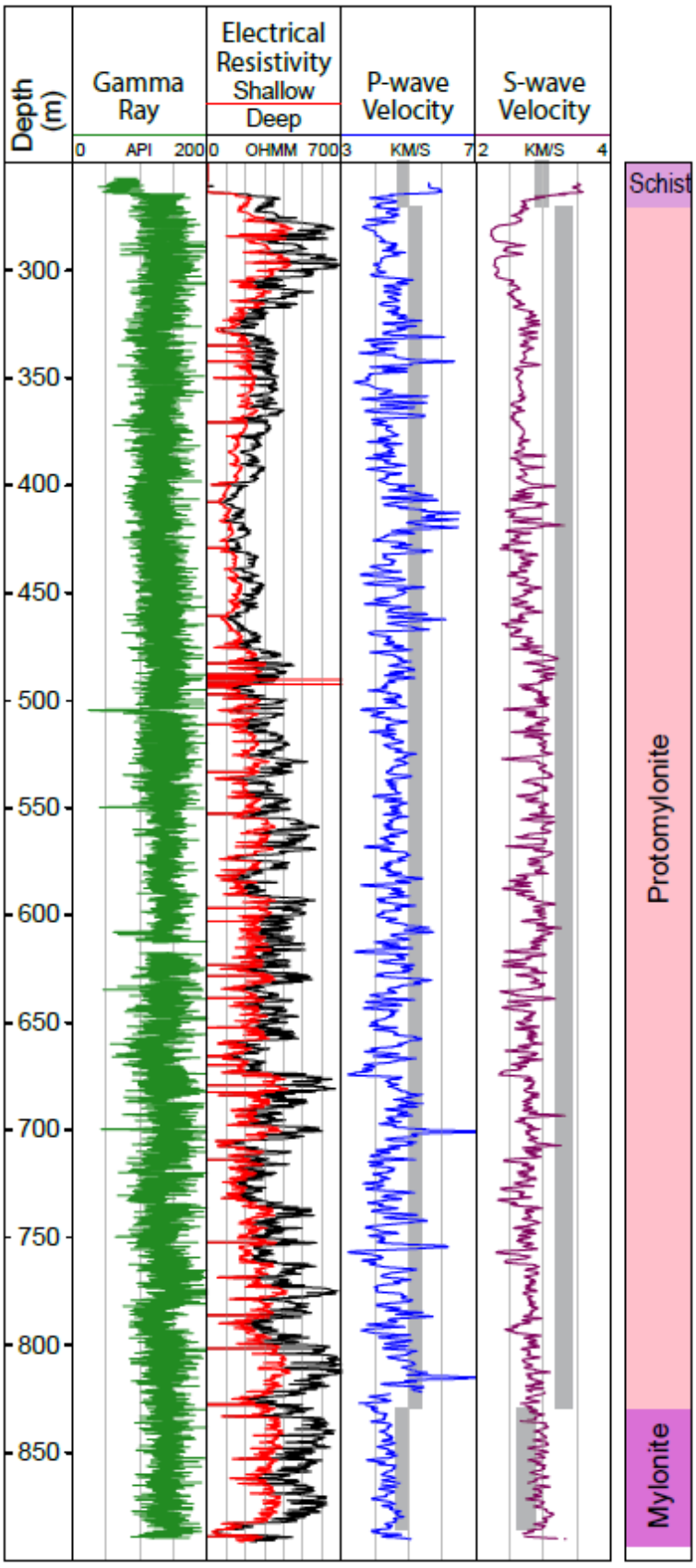

Figure 4.19: *Comparison of laboratory wavespeed measurement and downhole sonic logs from DFDP-2. The range in velocities measured in the lab on outcrop samples in the Z-direction is indicated by gray shaded regions. The velocities plotted were measured at estimated in situ effective pressures of 5 to 15 MPa. Lab-measured velocities are up to 18% faster than the average log velocity.*

measurements in the Z-direction. However, borehole images from the borehole televiewer logs indicate that foliation dips at an angle of 30˚ from the borehole axis near the top of the borehole, and increases to approximately 90˚ below 600 m measured depth due to the deviation of the borehole [*Massiot*, 2017]. As the hanging wall host rock is anisotropic, the velocity of waves propagating at 30˚ to foliation will be different from waves propagating at 90˚ to foliation. As waves propagating in the Z direction consistently produce the slowest velocities I anticipate that waves propagating at 30˚ to foliation would be faster and thus different propagation direction would only increase the difference between the laboratory and log velocities. Determining the wavespeed when propagation direction is at 30˚ to foliation requires knowledge of the full stiffness tensor. Lacking the full tensor, I used the transverse isotropy approximation of the Alpine Schist from *Godfrey et al.* [2000] (Table 4.4) to estimate the velocity at 30˚ to foliation. Measurements from *Godfrey et al*. [2000] were recorded at 100 MPa but, as the elastic properties of the schist are relatively pressure-independent, the measurements are similar to our results at lower pressures.

Using equations from *Thomsen* [1986] the velocities in different propagation directions can be calculated as:

$$\rho v_p^2(\theta) = \frac{1}{2}\left[C_{33} + C_{44} + (C_{11} - C_{33})\sin^2\theta + D(\theta)\right] \quad [12]$$

$$\rho v_{S1}^2(\theta) = \frac{1}{2}\left[C_{33} + C_{44} + (C_{11} - C_{33})\sin^2\theta - D(\theta)\right] \quad [13]$$

$$\rho v_{S2}^2(\theta) = C_{66}\sin^2\theta + C_{44}\cos^2\theta \quad [14]$$

where θ is the angle between the propagation direction and the axis of symmetry (60˚ in this case) and D(θ) is:

$$D(\theta) = \{(C_{33} - C_{44})^2 + 2[2(C_{13} + C_{44})^2 - (C_{33} - C_{44})(C_{11} + C_{33} - 2C_{44})]\sin^2\theta + [(C_{11} + C_{33} - 2C_{44})^2 - 4(C_{13} + C_{44})^2]\sin^4\theta\}^{1/2} \quad [15]$$

The resulting velocities are 5.64 km/s for the P-wave and 3.50 km/s and 4.38 km/s for the orthogonal S-waves. Waves propagating at 30˚ to foliation would be 22 to 46% faster than the log velocities. In this case, accounting for anisotropy does not resolve the difference between velocities measured at different scales but instead increases it.

Table 4.4: *Stiffness tensor of the transversely isotropic Alpine Schist from Godfrey et al. [2000].*

	ci1	ci2	ci3	ci4	ci5	ci6
c1j	100.805	24.362	7.895	0	0	0
c2j	24.362	100.805	7.895	0	0	0
c3j	7.895	7.895	72.453	0	0	0
c4j	0	0	0	26.002	0	0
c5j	0	0	0	0	26.002	0
c6j	0	0	0	0	0	38.2215

The second likely cause of the velocity difference is a difference between the actual *in situ* conditions and the conditions simulated in the lab. The pore fluid pressure measured in the borehole is about 10% above hydrostatic [*Sutherland et al.*, 2017]. This elevated fluid pressure was taken into account when estimating the *in situ* effective stress. At the lowest effective pressure examined (1 MPa), the laboratory P-wave velocity in the mylonite is only 4% faster than the log-measured velocity, but this corresponds to an overpressure ratio of 0.96. Near lithostatic pore pressure is not indicated by the drilling data.

There is also a difference in temperature between the lab and borehole conditions. Laboratory measurements were conducted at room temperature but the temperature measured at the bottom of the DFDP-2B borehole was 110.5˚C, resulting in an average geothermal gradient of 125 ±

55˚C/km [*Sutherland et al.*, 2017]. A decrease in velocity with increasing temperature has been documented in low porosity rock [*Bourbié et al.*, 1987; *Christensen*, 1989]. The change in velocity is usually less than 5% for a 100˚C increase in temperature. Accounting for temperature effects on the lab measurements would shift the measurements a little closer to the log data but is not likely to have a major effect at the depth of the DFDP-2B borehole. However, if the laboratory measurements are projected to greater depths the effect of temperature would need to be taken into account for both the host and damage zone rocks.

The velocity difference could be related to frequency-dependent velocity dispersion [*Winkler*, 1983, 1986]. In saturated, porous, attenuating media, a propagating wave causes the pore space to compress. At high (ultrasonic) frequencies, pore fluid may be trapped in the pore space causing the bulk modulus to increase and resulting in a relatively high measured velocity compared to lower (sonic or seismic) frequencies for which the pore fluid will have time to escape as pore space is compressed, resulting in a lower measured velocity. This effect is not expected to be significant in low porosity rocks such as the hanging wall schist and mylonites examined in this study. Using the Biot-Gassmann model [*Winkler*, 1986], I estimated the effect of velocity dispersion by predicting the low frequency water-saturated velocity in the hanging wall rock with the following equations:

$$v_s^2 = \frac{N}{\rho_c} \qquad [16]$$

$$\rho_c v_p^2 = \frac{(K_s - K_b)^2}{K_s\left(1 - \varphi - \frac{K_b}{K_s} + \varphi\frac{K_s}{K_f}\right)} + K_b + \frac{4}{3}N. \qquad [17]$$

Where ρ_c is the bulk density of the fluid-saturated rock, ρ_s is the density of the solid material, φ is the porosity, K_s is the bulk modulus of the solid material and K_f is the bulk modulus of the fluid.

N and K_b are the shear and bulk moduli, respectively, of the dry, solid, framework of the rock and are calculated as:

$$N = (1 - \varphi)\rho_s v_{s0}^2 \quad [18]$$

$$K_b = (1 - \varphi)\rho_s \left(v_{p0}^2 - \frac{4}{3} v_{s0}^2\right) \quad [19]$$

where v_{p0} and v_{s0} are P- and S-wave velocity measurements performed on dry samples. I obtained measurements under unsaturated conditions on a protomylonite sample in the Z-direction to carry out this calculation. At 10 MPa, the P- and S-wave velocities are 5.23 km/s and 3.23 km/s. At 60 MPa, the velocities are 5.45 km/s, 3.51 km/s, and 3.66 km/s. I simplified the calculation by assuming the solid part of the sample to be entirely quartz, with K_s and ρ_s of 37 GPa and 2.65 g/cm^3, respectively. The saturating fluid was fresh water, so K_f and ρ_f are 2.05 GPa and 1 g/cm^3, respectively. At 10 MPa, the dispersion would cause a 3% reduction in the P-wave velocity, increasing to 4% at 60 MPa. Saturation state does not significantly impact S-wave velocities, so the effect of dispersion would be 1% or less at both pressure steps. This difference is close to the experimental uncertainty. Velocity dispersion would have a greater effect in the higher porosity fault rock. In the gouges the estimated effect of dispersion at 60 MPa is a 17% or greater reduction in velocity.

An alternative, and preferred, hypothesis for the scale dependence of the velocity measurement is that it is the result of a sampling bias. From the borehole televiewer data it is apparent that the host rock is fractured [*Massiot*, 2017]. These fractures have apertures on the millimeter to centimeter-scale. The samples used in the laboratory measurements need to be relatively intact and do not contain mesoscale open fractures, joints, or faults. I propose that this bias in the

laboratory samples results in laboratory velocities that are faster than the *in situ* measurements, as the presence of fractures has been shown to decrease velocity [*Stierman and Kovach*, 1979; *Trippetta et al.*, 2010; *Jeanne et al.*, 2012; *Jeppson and Tobin*, 2015]. The fault rocks do not exhibit a similar velocity difference because brittle structures within the damage zone are present at multiple scales.

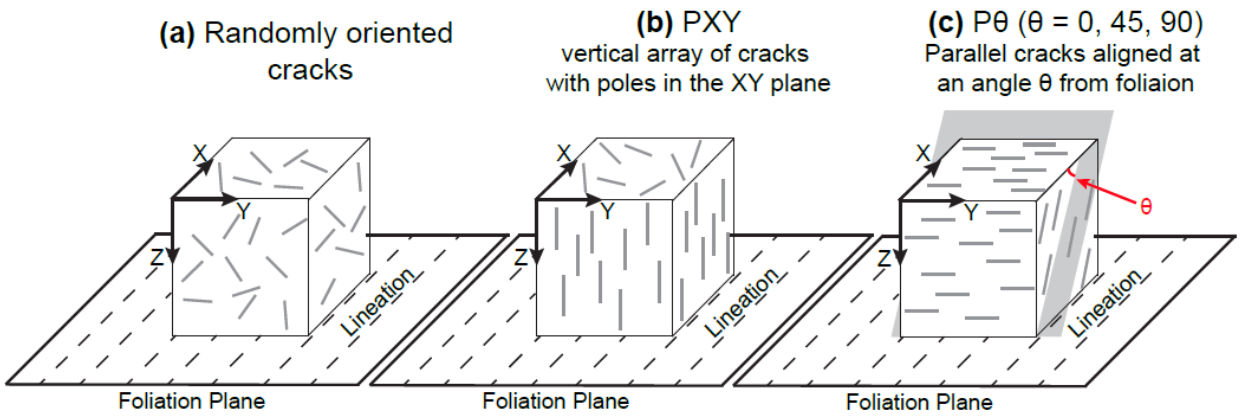

Figure 4.20: *Schematic diagrams of crack patterns used to examine the effect of crack density and orientation on wavespeed. The foliation plane forms the XY plane in the modeled reference frame. Fracture orientations examined are (a) randomly distributed, (b) cracks with all poles in the XY plane, (c) array of parallel cracks aligned at an angle θ from the foliation plane. Angles examined are 0˚, 45˚, and 90˚ from the foliation plane. Modified from Healy [2008].*

4.4.3.2.1 Effective Medium Theory

To test the hypothesis that mesoscale fracturing causes the log velocities to be slower than the lab velocities I use Effective Medium Theory (EMT) to calculate the effective velocity in a rock with a range of fracture densities and orientations. This method has been developed in detail in previous studies [*Sayers and Kachanov*, 1991, 1995; *Kachanov*, 1993; *Sayers*, 1998]. I use the dry crack formulation of EMT to remove the effects of frequency-dependent velocity dispersion. I assume the cracks present are flat and penny shaped, which allows a second-order crack density tensor to be defined as:

$$\alpha = \left({}^{1}/_{V}\right) \sum_{N} a^{3}\mathbf{nn} \qquad [20]$$

where V is the volume of interest, N is the number of cracks present in the volume, a is the radius of a circular crack, and **n** is the crack's unit normal. I examined the effects of five different crack patterns (Fig. 4.20): randomly oriented cracks, cracks with all poles in the XY plane (PXY), cracks aligned parallel to the foliation plane (P0), cracks aligned perpendicular to the foliation plane (P90), and aligned, parallel cracks inclined at an angle of 45˚ to the foliation plane (P45). These distributions are based on data from the borehole televiewer which indicates the presence of foliation-parallel fractures, joints oriented at 90˚ to the foliation, and subhorizontal (~45˚ from foliation plane) fractures [*Massiot*, 2017]. Using these different crack patterns, I estimate the change in material compliance due to the presence of fractures using the equations provided by *Sayers and Kachanov* [1995] and *Sayers* [1998]. Compliance is the inverse of stiffness, so the resulting compliance tensor is inverted and the P- and S-wave velocities are determined using equations 4 thru 9.

When wave propagation is in the Z-direction, the P-wave velocity is significantly reduced for the P0, P45, and random patterns (Fig. 4.21a). The greatest reduction occurs for P0, since propagation is perpendicular to the fracture plane. The P90 and PXY distributions produce only a very minor reduction in P-wave velocity: the velocity is reduced by less than 0.03 km/s for the PXY pattern and less than 0.02 km/s for the P90 pattern. For S-waves the P0 pattern does not affect the velocity because both vibration directions are in the fracture plane (Fig. 4.21b-c). The PXY and random patterns affect both vibration directions equally but the PXY distribution causes a greater velocity reduction because all the fractures are at a high angle to the vibration directions. The P45 and P90 patterns do not affect the Y-vibration direction because this is the rotation axis, so vibration is still parallel to the fracture. However, both of these crack

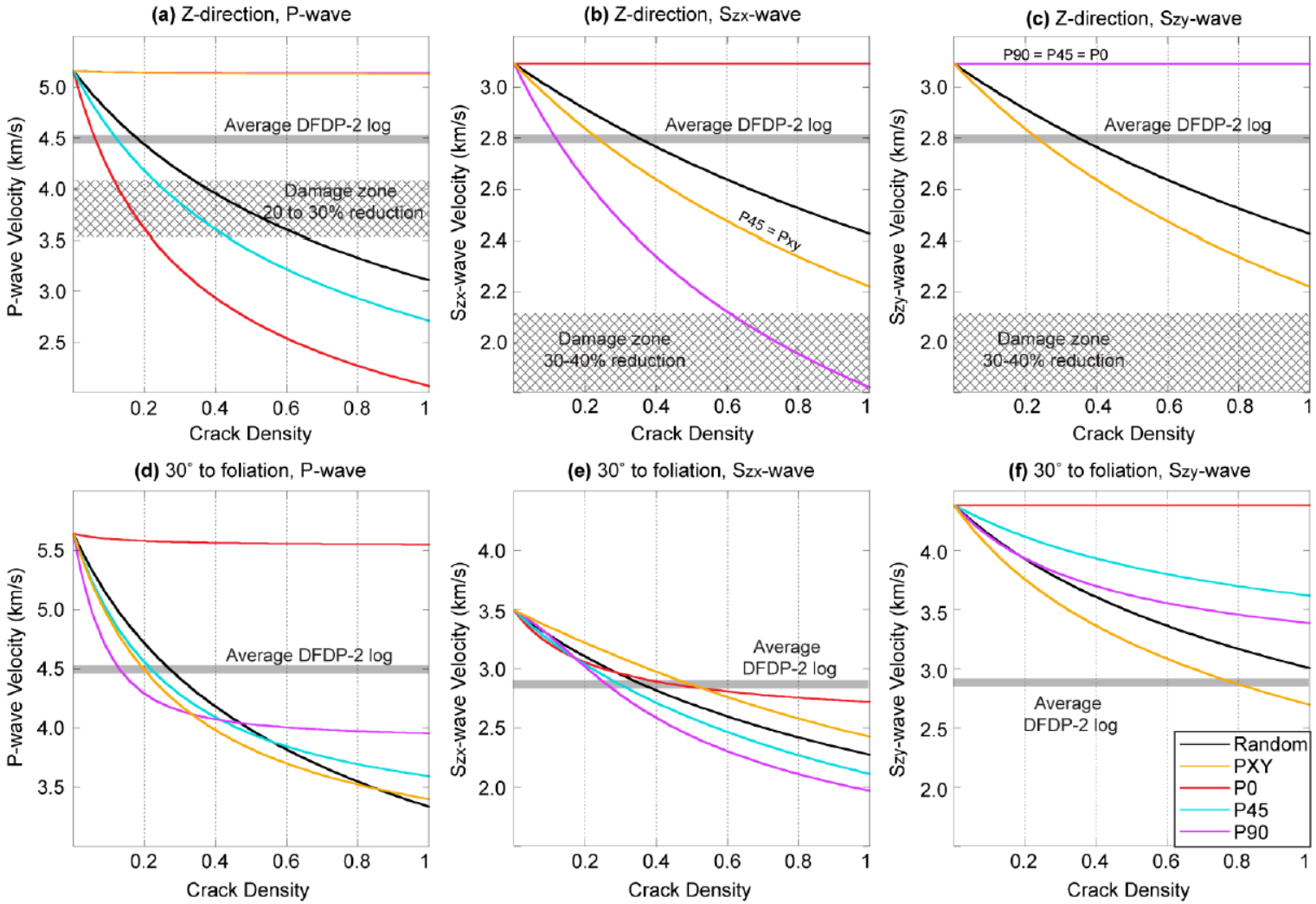

Figure 4.21: *P- and S-wave velocities as a function of crack density for the five crack distributions presented in figure 20. Variations are shown for P- and S-waves propagating (a-c) in the Z-direction and (d-f) at 30˚ to foliation consistent with the DFDP-2 sonic log. Average DFDP-2 sonic log velocities are denoted by the gray bars and the damage zone velocity reduction is indicated by the crosshatched regions.*

distributions cause velocity reduction when the vibration is in the X-direction. PXY causes a reduction equal to that caused by the P45 pattern. The P90 distribution results in the greatest velocity reduction observed for S-waves vibrating in the X-direction because the vibration direction is perpendicular to the fracture plane.

Rotating the reference frame on the Y-axis so waves are propagating at 30˚ to foliation, as is expected where the DFDP-2B borehole is vertical, causes the fractures to rotate, so wave propagation and vibration is never parallel to the fracture plane except for S-waves vibration in the Y-direction (Fig. 4.21d-f). The Y-vibration S-wave velocity remains constant for the P0 pattern because the reference frame was rotated on this axis, so the vibration direction is still parallel to the fracture.

Based on the results of the EMT models for waves propagating perpendicular to foliation, a crack density of 0.4 or less would be needed to obtain the velocities recorded by the DFDP-2 sonic log (Fig. 4.21a-c). For waves propagating at 30˚ to foliation (Fig. 4.21d-c) the P-wave and X-vibration S-wave would require a crack density of 0.5 or less to match the sonic log. However, the Y-vibration direction requires a much higher crack density for a match. The orientation of the sonic log S-wave vibration with respect to lineation is unknown, so it may be that the orientation is closer to the X-direction. The randomly oriented crack distribution is probably the closest to the actual crack density for the borehole wall rock, since fractures are present in multiple orientations in the televiewer data. The random crack model shows that a crack density of 0.2 to 0.4 is needed to match the sonic log. Lacking information on the dimensions of fractures observed in the borehole, I cannot calculate the actual fracture density in the wall rock. Estimates of crack density in other rock types indicate 0.4 is not an unreasonable estimate for host rock [e.g., *O'Connell and Budiansky,* 1974; *Hadley,* 1976; *Li et al.*, 2001]. The EMT models have

difficulty matching the velocity reduction documented in the damage zone, but the models do not account for increased clay content which will also affect the velocities.

4.4.3.3 Fault zone trapped waves

Trapped wave phases have been recorded on seismometers installed in the DFDP-1 boreholes [*Eccles et al.*, 2015]. These phases occur due to the contrast in the physical properties of the damage zone and host rock and have been observed at other major fault zones [e.g., *Li et al.*, 1990; *Li and Aki*, 1998; *Li and Vernon*, 2001; *Ben-Zion et al.*, 2003; *Li and Malin*, 2008]. Modeling of the phases observed by the DFDP seismometers indicates the presence of a 60 to 200-m wide waveguide where the S-wave velocity is reduced by 10 to 40% [*Eccles et al.*, 2015]. The size of the waveguide is broader than is indicated by field observations of the damage zone. The cataclasites occur within 30 m of the principal slip surface and the intensively fractured damage zone extends to 100 m from the principal slip surface [*Cooper and Norris*, 1994; *Norris and Cooper*, 2007]. The broader waveguide is likely due to the low frequency waves used in trapped waves studies. The magnitude of velocity reduction is consistent with the 30 to 40% reduction I observed in laboratory measurements of S-waves in the fault rocks and host rocks. *Li and Malin* [2008] found that fault-zone trapped wave phases indicated a similar velocity reduction of up to 40% in the damage zone surrounding the San Andreas Fault.

4.4.4 Implications for fault processes

Clay-rich gouges are found in up to 2-m thick zones surrounding principal slip surfaces within the active fault cores of both the Alpine and San Andreas Faults [e.g., *Bradbury et al.*, 2011; *Toy et al.*, 2015]. At both locations, this gouge is compliant, and the P- and S-wave velocities measured at simulated *in situ* pressure conditions in the gouges are less than 4.5 km/s and 2.3 km/s, respectively [*Jeppson and Tobin*, 2015; *this study]*. The wavespeeds in the gouges are 30 to 40% slower than the wavespeeds in the surrounding host rock. However, the gouges from the

San Andreas Fault appear to be more anisotropic than the Alpine Fault gouges. This anisotropy is due to a penetrative scaly fabric that probably developed as a result of creep on the San Andreas Fault [*Jeppson and Tobin*, 2015]. The Alpine Fault does not appear to creep [*Beavan and Ellis*, 2007; *Sutherland et al.*, 2007; *Beavan et al.*, 2010], which may explain the lack of a similar scaly fabric. The difference in anisotropy may also have implications for stress rotations surrounding the fault zones. *Healy* [2008, 2009] indicates that anisotropy in the fault core results in stress rotations. At the San Andreas Fault, where stress rotation appears to be needed in order for the fault to slip [e.g., *Zoback et al.*, 1987; *Rice*, 1992], the fault core is anisotropic whereas at the Alpine Fault, where stress rotations are not required for fault slip [*Leitner et al.*, 2001], the fault core is quasi-isotropic.

Both fault zones also have 100 to 200 m wide damage zone with a ~30 to 40% velocity reduction relative to the host rock that is observed at multiple scales [*Li and Malin*, 2008; *Jeppson et al.*, 2010; *Zoback et al.*, 2010; *Eccles et al.*, 2015]. However, due to a sampling bias in favor of intact samples, the velocity reduction was not seen at laboratory scales for samples of the San Andreas Fault damage zone [*Jeppson and Tobin*, 2015]. I only examined one Alpine Fault sample from within the damage zone but outside of the fault core. The velocity reduction observed at larger scales was observed at the laboratory scale for this sample, but the sample was collected near the boundary of the fault core. It is possible that at distances farther from the fault core, where micro-scale damage is not as prevalent, a scale dependence similar to that observed at the San Andreas Fault would be seen. The similarity in magnitudes and reductions in velocity observed at lab and field scales within the damage zone and fault core at both the Alpine and San Andreas Faults suggest that that the deformation and alteration processes occurring within major plate boundary fault zones produce similar fault rock properties with minor variations related to

protolith, fault regime, and slip behavior. However, more work would need to be done on other types of faults to evaluate this hypothesis.

4.4.5 Implications for seismic hazard

Modeling of dynamic rupture on a fault surrounded by a low velocity damage zone suggests that the presence of a low velocity zone slows rupture velocity, amplifies ground motion during rupture, and increases the final slip magnitude [*Cormier and Spudich*, 1984; *Harris and Day*, 1997; *Duan*, 2008; *Graves and Pitarka*, 2016]. Increased ground motion and peak accelerations have been observed within and near fault zones [e.g., *Marra et al.*, 2000; *Spudich and Olsen*, 2001; *Karabulut et al.*, 2007] and within basins containing unconsolidated sediment [e.g., *Borcherdt*, 1970; *Aki*, 1993; *Graves*, 1995; *Field et al.*, 1997; *Olsen*, 2000]. The amplification of ground motion can be understood in terms of Hooke's law which demonstrates that, for a given stress, a more compliant material will experience greater strain, This effect may be greater in fault zones due to constructive interference of trapped waves within the fault zone [*Marra et al.*, 2000; *Spudich and Olsen*, 2001; *Duan*, 2008].

4.5 Conclusions

Laboratory ultrasonic wavespeed measurements were performed on a comprehensive suite of samples of the host rock, damage zone and fault core of the Alpine Fault obtained in outcrop and drill core. These measurements show that the average velocity of the damage zone and fault core is reduced by 20 to 40% relative to the surrounding host rock. This decrease in velocity is associated with an increase in brittle deformation and clay content. Additionally, the hanging wall host rock is anisotropic whereas the fault core is quasi-isotropic, due to progressive disruption of mylonitic foliation by brittle structures.

Laboratory measurements of drill core and outcrop samples provide a good proxy for field-scale measurements as the velocity magnitudes and percent velocity reduction agree with borehole sonic log and fault-zone trapped wave data. This scale independence indicates that the velocity is controlled by microscale features, such as microfractures and clay content. However, comparison of laboratory measurement of host rock outcrop samples to DFDP-2 sonic logs indicates the laboratory measurements are, on average 2 to 18% faster than the sonic log. This difference cannot be explained by differences in laboratory and *in situ* pressure and temperature conditions or by frequency dispersion. However, there is a sampling bias toward intact rock for samples used in laboratory experiments. EMT models indicate that a mesoscopic crack density of 0.2 to 0.4 would account for the velocity difference.

Damage zone velocity reduction of similar magnitude to that observed at the Alpine Fault has been observed at multiple scales at the San Andreas Fault [e.g., *Li and Malin*, 2008; *Zoback et al.*, 2011; *Jeppson and Tobin*, 2015]. This similarity suggests that the deformation and alteration processes occurring within major plate bounding fault zones produce similar damage zone properties with minor differences related to variations in protolith, fault regime, and slip behavior. These processes produce a very compliant damage zone that is likely to accommodate high amplitude ground motions during earthquakes and slow rupture propagation.

Acknowledgements

Laboratory data used in this study were acquired at UW-Madison and are available from the author upon request. All sample information and data collected during DFDP is available upon request from the ICDP-hosted DFDP website at alpine.icdp-online.org. This work was funded by NSF grant EAR-1215711 to Harold Tobin. I would like to thank Jonathan Graham for running the XRD analysis. I also want to thank Michael Allen, Austin Boles, Carolyn Boulton, Brett Carpenter, Daniel Faulkner, Timothy Little, Catriona Menzies, Chance Morgan, David Prior, Virginia Toy, and Robert Valdez for their assistance with field work and sample collection.

References

Aki, K. (1993), Local site effects on weak and strong ground motion, *Tectonophysics*, *218*(1–3), 93–111, doi:10.1016/0040-1951(93)90262-i.

Alexandrov, K. S., and T. V Ryzhova (1961), Elastic properties of rock-forming minerals II: Layered silicates, *Bull. Acad. Sci. USSR Geophys. Ser. English Transl.*, *12*, 1165–1168.

Barnes, P. M. (2009), Postglacial (after 20 ka) dextral slip rate of the offshore Alpine fault, New Zealand, *Geology*, *37*(1), 3–6, doi:10.1130/G24764A.1.

Barth, N. C., C. Boulton, B. M. Carpenter, G. E. Batt, and V. G. Toy (2013), Slip localization on the southern Alpine Fault New Zealand, *Tectonics*, *32*(3), 620–640, doi:10.1002/tect.20041.

Beavan, J., and S. Ellis (2007), Kinematic constraints from GPS on oblique convergence of the Pacific and Australian plates, central South Island, New Zealand, *A Cont. Plate Bound. Tectonics South Island, New Zealand, Geophys. Monogr. Ser. 175*, 75–94.

Beavan, J., P. Denys, M. Denham, B. Hager, T. Herring, and P. Molnar (2010), Distribution of present-day vertical deformation across the Southern Alps, New Zealand, from 10 years of GPS data, *Geophys. Res. Lett.*, *37*(16), 7–11, doi:10.1029/2010GL044165.

Ben-Zion, Y., and C. G. Sammis (2003), Characterization of fault zones, *Pure Appl. Geophys.*, *160*, 677–715.

Ben-Zion, Y., Z. Peng, D. Okaya, L. Seeber, J. G. Armbruster, N. Ozer, A. J. Michael, S. Baris, and M. Aktar (2003), A shallow fault-zone structure illuminated by trapped waves in the Karadere-Duzce branch of the North Anatolian Fault, western Turkey, *Geophys. J. Int.*, *152*(3), 699–717, doi:10.1046/j.1365-246X.2003.01870.x.

Berge, P. A., and J. G. Berryman (1995), Realizability of negative pore compressibility in

poroelastic composites, *J. Appl. Mech.*, *62*, 1053–1062.

Berryman, K. R., U. A. Cochran, K. J. Clark, G. P. Biasi, R. M. Langridge, and P. Villamor (2012), Major earthquakes occur regularly on an isolated plate boundary fault., *Science.*, *336*, 1690–1693, doi:10.1126/science.1218959.

Birch, F. (1960), The velocity of compressional waves in rocks to 10 kilobars, part 1, *J. Geophys. Res.*, *65*(4), 1083–1102.

Birch, F. (1961), The Velocity of Compressional Waves in Rocks to 10 Kilobars , Part 2, *J. Geophys. Res.*, *66*(7), 2199–2224.

Boness, N. L., and M. D. Zoback (2006), A multiscale study of the mechanisms controlling shear velocity anisotropy in the San Andreas Fault Observatory at Depth, *Geophysics*, *71*(5), F131–F146, doi:10.1190/1.2231107.

Borcherdt, R. D. (1970), Effects of local geology on ground motion near San Francisco Bay, *Bull. Seismol. Soc. Am.*, *60*(1), 29–61.

Bos, B., and C. J. Spiers (2002), Fluid-assisted healing processes in gouge-bearing faults: Insights from experiments on a rock analogue system, *Pure Appl. Geophys.*, *159*, 2537–2566, doi:10.1007/s00024-002-8747-2.

Boulton, C., B. M. Carpenter, V. Toy, and C. Marone (2012), Physical properties of surface outcrop cataclastic fault rocks, Alpine Fault, New Zealand, *Geochemistry, Geophys. Geosystems*, *13*(1), doi:10.1029/2011GC003872.

Bourbié, T., O. Coussy, and B. Zinszner (1987), *Acoustics of Porous Media*, Editions Technip, Paris, France.

Bradbury, K. K., J. Evans, J. Chester, F. M. Chester, and D. Kirschner (2011), Lithology and internal structure of the San Andreas fault at depth based on characterization of Phase 3 whole-rock core in the San Andreas Fault Observatory at Depth (SAFOD) borehole, *Earth Planet. Sci. Lett.*, *310*, 131–144, doi:10.1016/j.epsl.2011.07.020.

Bruhn, R. L., W. T. Parry, W. a Yonkee, and T. Thompson (1994), Fracturing and hydrothermal alteration in normal fault zones, *Pure Appl. Geophys.*, *142*(3), 609–644, doi:10.1007/BF00876057.

Bull, W. B. (1996), Prehistorical earthquakes on the Alpine fault, New Zealand, *J. Geophys. Res.*, *101*(B3), 6037–6050.

Caine, J. S., J. P. Evans, and C. B. Forster (1996), Fault zone architecture and permeability structure, *Geology*, *24*, 1025–1028, doi:10.1130/0091-7613(1996)024<1025.

Carpenter, B. M., H. Kitajima, R. Sutherland, J. Townend, V. G. Toy, and D. M. Saffer (2014), Hydraulic and acoustic properties of the active Alpine Fault, New Zealand: Laboratory measurements on DFDP-1 drill core, *Earth Planet. Sci. Lett.*, *390*, 45–51, doi:10.1016/j.epsl.2013.12.023.

Castagna, J. P., M. L. Batzle, and R. L. Eastwood (1985), Relationships between compressional-wave and shear-wave velocities in clastic silicate rocks, *Geophysics*, *50*(4), 571–581.

Chan, J., and D. R. Schmitt (2015), Elastic anisotropy of a metamorphic rock sample of the Canadian Shield in Northeastern Alberta, *Rock Mech. Rock Eng.*, *48*(4), 1369–1385, doi:10.1007/s00603-014-0664-z.

Chester, F. M., and J. M. Logan (1987), Composite planar fabric of gouge from the Punchbowi Fault, California, *J. Struct. Geol.*, *9*(5), 621–634.

Chester, F. M., J. P. Evans, and R. L. Biegel (1993), Intemal Structure and Weakening Mechanisms of the San Andreas Fault, *J. Geophys. Res.*, *98*(B1), 771–786, doi:10.1029/92JB01866.

Cholach, P. Y., J. B. Molyneux, and D. R. Schmitt (2005), Flin Flon Belt seismic anisotropy: elastic symmetry, heterogeneity, and shear-wave splitting, *Can. J. Earth Sci.*, *42*(4), 533–554, doi:10.1139/e04-094.

Christensen, N. I. (1985), Measurement of dynamic properties of rock at elevated pressures and temperatures, *ASTM STP*, *869*, 93–107.

Christensen, N. I. (1989), Seismic velocities, in *Practical handbook of physical properties of rocks and minerals*, edited by R. S. Carmichael, pp. 431–546, CRC Press, Boca Raton.

Christensen, N. I., and D. A. Okaya (2007), Compressional and Shear Wave Velocities in South Island, New Zealand Rocks and Their Application to the Interpretation of Seismological Models of the New Zealand Crust, *A Cont. Plate Bound. Tectonics South Island, New Zeal.*, 123–155.

Cochran, E. S., Y.-G. Li, P. M. Shearer, S. Barbot, Y. Fialko, and J. E. Vidale (2009), Seismic and geodetic evidence for extensive, long-lived fault damage zones, *Geology*, *37*(4), 315–318, doi:10.1130/G25306A.1.

Cooper, A. F., and R. J. Norris (1994), Antatomy, structural evolution, and slip rate of a plate boundary thrust: The Alpine Fault at Gaunt Creek, Westland, New Zealand, *Geol. Soc. Am. Bull.*, *106*(May), 627--633, doi:10.1130/0016-7606(1994)106<0627:ASEASR>2.3.CO;2.

Cormier, V. F., and P. Spudich (1984), Amplification of ground motion and waveform complexity in fault zones: examples from the San Andreas and Calaveras Faults, *Geophys. J. Int.*, *79*(1), 135–152, doi:10.1111/j.1365-246X.1984.tb02846.x.

Cox, S. C., and R. Sutherland (2007), Regional Geological Framework of South Island, New Zealand, and its Significance for Understanding the Active Plate Boundary, *A Cont. Plate Bound. Tectonics South Island, New Zeal.*, 19–46.

Cox, S. J. D., and C. H. Scholz (1988), On the formation and growth of faults: an experimental study, *J. Struct. Geol.*, *10*(4), 413–430, doi:10.1016/0191-8141(88)90019-3.

Demets, C., R. G. Gordon, and D. F. Argus (2010), Geologically current plate motions, *Geophys. J. Int.*, *181*, 1–80, doi:10.1111/j.1365-246X.2009.04491.x.

Duan, B. (2008), Effects of low-velocity fault zones on dynamic ruptures with nonelastic off-fault response, *Geophys. Res. Lett.*, *35*, 1–6, doi:10.1029/2008GL033171.

Eberhart-Phillips, D., and S. Bannister (2002), Three-dimensional crustal structure in the Southern Alps region of New Zealand from inversion of local earthquake and active source data, *J. Geophys. Res.*, *107*(B10), doi:10.1029/2001JB000567.

Eccles, J. D., A. K. Gulley, P. E. Malin, C. M. Boese, J. Townend, and R. Sutherland (2015), Fault Zone Guided Wave generation on the locked, late interseismic Alpine Fault, New Zealand, *Geophys. Res. Lett.*, *42*(14), 5736–5743, doi:10.1002/2015GL064208.Received.

Faulkner, D. R., C. A. L. Jackson, R. J. Lunn, R. W. Schlische, Z. K. Shipton, C. A. J. Wibberley, and M. O. Withjack (2010), A review of recent developments concerning the structure, mechanics and fluid flow properties of fault zones, *J. Struct. Geol.*, *32*(11), 1557–1575, doi:10.1016/j.jsg.2010.06.009.

Field, E., P. Johnson, I. Beresnev, and Y. Zeng (1997), Nonlinear ground-motion amplification by sediments during the 1994 Northridge earthquake, *Nature*, *390*, 599–602, doi:10.1038/37586.

Godfrey, N. J., N. I. Christensen, and D. a. Okaya (2000), Anisotropy of schists: Contribution of crustal anisotropy to active source seismic experiments and shear wave splitting observations, *J. Geophys. Res.*, *105*(B12), 27991–28007, doi:10.1029/2000JB900286.

Godfrey, N. J., N. I. Christensen, and D. A. Okaya (2002), The effect of crustal anisotropy on reflector depth and velocity determination from wide-angle seismic data: A synthetic example based on South Island, New Zealand, *Tectonophysics*, *355*, 145–161, doi:10.1016/S0040-1951(02)00138-5.

Grapes, R. H., and T. Watanabe (1992), Metamorphism and uplift of Alpine Schist in the Franz Joseph-Fox Glacier area of the Southern Alps, New Zealand, *J. Metamorph. Geol.*, *10*, 171–180.

Graves, R., and A. Pitarka (2016), Kinematic ground-motion simulations on rough faults including effects of 3D stochastic velocity perturbations, *Bull. Seismol. Soc. Am.*, *106*(5), 2136–2153, doi:10.1785/0120160088.

Graves, R. W. (1995), Preliminary analysis of long-period basin respone in Los Angeles region from the 1994 Northridge earthquake, *Geophys. Res. Lett.*, *22*(2), 101–104.

Hadley, K. (1976), Comparison of calculated and observed crack densities and seismic velocities in Westerly granite, *J. Geophys. Res.*, *81*(20), 3484–3494.

Han, D., A. Nur, and D. Morgan (1986), Effects of porosity and clay content on wave velocities in sandstones, *Geophysics*, *51*(11), 2093–2107.

Harris, R. A., and S. M. Day (1997), Effects of a low-velocity zone on a dynamic rupture, *Bull. Seismol. Soc. Am.*, *87*(5), 1267–1280.

Healy, D. (2008), Damage patterns, stress rotations and pore fluid pressures in strike-slip fault

zones, *J. Geophys. Res. Solid Earth*, *113*(12), 1–16, doi:10.1029/2008JB005655.

Healy, D. (2009), Anisotropy, pore fluid pressure and low angle normal faults, *J. Struct. Geol.*, *31*(6), 561–574, doi:10.1016/j.jsg.2009.03.001.

Hofmann, R., X. Xu, M. L. Batzle, M. Prasad, A.-K. Furre, and A. Pillitteri (2005), Effective pressure or what is the effect of pressure?, *Lead. Edge*, *24*(12), 1256–1260.

Holdsworth, R. E., E. W. E. van Diggelen, C. J. Spiers, J. H. P. de Bresser, R. J. Walker, and L. Bowen (2011), Fault rocks from the SAFOD core samples: Implications for weakening at shallow depths along the San Andreas Fault, California, *J. Struct. Geol.*, *33*(2), 132–144, doi:10.1016/j.jsg.2010.11.010.

Jeanne, P., Y. Guglielmi, and F. Cappa (2012), Multiscale seismic signature of a small fault zone in a carbonate reservoir: Relationships between VP imaging, fault zone architecture and cohesion, *Tectonophysics*, *554–557*, 185–201, doi:10.1016/j.tecto.2012.05.012.

Jeppson, T., K. K. Bradbury, and J. Evans (2010), Geophysical properties within the San Andreas Fault Zone at the San Andreas Fault Observatory at Depth and their relationships to rock properties and fault zone structure, *J. Geophys. Res.*, *115*, doi:10.1029/2010JB007563.

Jeppson, T. N., and H. J. Tobin (2015), San Andreas fault zone velocity structure at SAFOD at core, log, and seismic scales, *J. Geophys. Res. Solid Earth*, *120*, 4983–4997, doi:10.1002/2015JB012043.

Johnston, J., and N. I. Christensen (1995), Seismic anisotropy of shales, *J. Geophys. …*, *100*(B4), 5991–6003.

Kachanov, M. (1993), On the effective moduli of solids with cavities and cracks, *Int. J. Fract.*, *59*(1), 17–21, doi:10.1007/BF00032223.

Karabulut, H., and M. Bouchon (2007), Spatial variability and non-linearity of strong ground motion near a fault, *Geophys. J. Int.*, *170*(1), 262–274, doi:10.1111/j.1365-246X.2007.03406.x.

Karner, S. L., C. Marone, and B. Evans (1997), Laboratory study of fault healing and lithification in simulated fault gouge under hydrothermal conditions, *Tectonophysics*, *277*, 41–55, doi:10.1016/S0040-1951(97)00077-2.

Katahara, K. W. (1996), Clay mineral elastic properties, *SEG Annu. Meet. Expand. Tech. Program. Abstr.*, Paper RP1.4, doi:10.1190/1.1826454.

Kern, H., and H. R. Wenk (1990), Fabric-related velocity anisotropy and shear wave splitting in rocks from the Santa Rosa Mylonite Zone, California, *J. Geophys. Res. Solid Earth*, *95*(B7), 11213–11223, doi:10.1029/JB095iB07p11213.

Kim, Y.-S., D. C. . Peacock, and D. J. Sanderson (2004), Fault damage zones, *J. Struct. Geol.*, *26*(3), 503–517, doi:10.1016/j.jsg.2003.08.002.

Kowallis, B. J., L. E. A. Jones, and H. F. Wang (1984), Velocity-porosity-clay content systematics of poorly consolidated sandstones, *J. Geophys. Res.*, *89*(B12), 355–364.

Langridge, R. M., P. Villamor, R. Basili, P. Almond, J. J. Martinez-Diaz, and C. Canora (2010), Revised slip rates for the Alpine fault at Inchbonnie: Implications for plate boundary kinematics of South Island, New Zealand, *Lithosphere*, *2*(3), 139–152, doi:10.1130/L88.1.

Leitner, B., D. Eberhart-Phillips, H. Anderson, and J. L. Nabelek (2001), A focused look at the Alpine fault, New Zealand: Seismicity, focal mechanisms, and stress observations, *J. Geophys. Res.*, *106*(2), 2193–2220.

Li, Y., P. Chen, E. S. Cochran, J. E. Vidale, and T. Burdette (2006), Seismic Evidence for Rock Damage and Healing on the San Andreas Fault Associated with the 2004 M 6.0 Parkfield Earthquake, *Bull. Geol. Soc. Am.*, *96*(4B), 349–363, doi:10.1785/0120050803.

Li, Y.-G., and K. Aki (1998), A delineation of the Nojima fault ruptured in the M7. 2 Kobe, Japan, earthquake of 1995 using fault zone trapped waves, *J. Geophys. Res.*, *103*(B4), 7247–7263.

Li, Y.-G., and P. E. Malin (2008), San Andreas Fault damage at SAFOD viewed with fault-guided waves, *Geophys. Res. Lett.*, *35*(8), L08304, doi:10.1029/2007GL032924.

Li, Y.-G., and F. L. Vernon (2001), Characterization of the San Jacinto fault zone near Anza, California, by the fault zone trapped waves, *J. Geophys. Res.*, *106*(B12), 30671–30688.

Li, Y.-G., P. Leary, K. Aki, and P. Malin (1990), Seismic trapped modes in the oroville and san andreas fault zones., *Science*, *249*(4970), 763–766, doi:10.1126/science.249.4970.763.

Li, Y.-G., F. M. Chester, and J. E. Vidale (2001), Shallow seismic profiling of the exhumed Punchbowl Fault Zone, Southern California, *Bull. Seismol. Soc. Am.*, *91*(6), 1820–1830.

Li, Y. G., J. E. Vidale, S. M. Day, D. D. Oglesby, and E. Cochran (2003), Postseismic fault healing on the rupture zone of the 1999 M 7.1 Hector Mine, California, earthquake, *Bull. Seismol. Soc. Am.*, *93*(2), 854–869, doi:10.1785/0120020131.

Little, T. a., S. Cox, J. K. Vry, and G. Batt (2005), Variations in exhumation level and uplift rate along the oblique-slip Alpine fault, central Southern Alps, New Zealand, *Geol. Soc. Am. Bull.*, *117*(5–6), 707–723, doi:10.1130/B25500.1.

Little, T. A., R. J. Holcombe, and B. R. Ilg (2002), Ductile fabrics in the zone of active oblique convergence near the Alpine Fault, New Zealand: identifying the neotectonic overprint, *J. Struct. Geol.*, *24*(1), 193–217, doi:10.1016/S0191-8141(01)00059-1.

Louis, L., C. David, P. Spacek, T. F. Wong, J. Fortin, and S. R. Song (2012), Elastic anisotropy of core samples from the Taiwan Chelungpu Fault Drilling Project (TCDP): Direct 3-D measurements and weak anisotropy approximations, *Geophys. J. Int.*, *188*, 239–252, doi:10.1111/j.1365-246X.2011.05247.x.

Lund Snee, J.-E., V. G. Toy, and K. Gessner (2014), Significance of brittle deformation in the footwall of the Alpine Fault, New Zealand: Smithy Creek Fault zone, *J. Struct. Geol.*, *64*,

79–98, doi:10.1016/j.jsg.2013.06.002.

Mah, M., and D. R. Schmitt (2001), Experimental determination of the elastic coefficients of an orthorhombic material, *Geophysics*, *66*(4), 1217–1225, doi:10.1190/1.1487068.

Mah, M., and D. R. Schmitt (2003), Determination of the complete elastic stiffnesses from ultrasonic phase velocity measurements, *J. Geophys. Res.*, *108*(B10), doi:10.1029/2003JB002710.

Marra, F., R. Azzara, F. Bellucci, A. Caserta, G. Cultrera, G. Mele, A. Palombo, A. Rovelli, and E. Boschi (2000), Large amplication of ground motion at rock sites within a fault zone in Nocera Umbra (central Italy), *J. Seismol.*, *4*(4), 543–565, doi:10.1023/A:1026559901378.

Martínez, J. M., and D. R. Schmitt (2013), Anisotropic elastic moduli of carbonates and evaporites from the Weyburn-Midale reservoir and seal rocks, *Geophys. Prospect.*, *61*(2), 363–379, doi:10.1111/1365-2478.12032.

Massiot, C. (2017), Fracture system characterisation and implications for fluid flow in volcanic and metamorphic rocks, Victoria University of Wellington.

Mavko, G., T. Mukerji, and J. Dvorkin (2009), *The Rock Physics Handbook: Tools for Seismic Analysis of Porous Media*, 2nd ed., Cambridge University Press, Cambridge.

Mooney, W. D., and A. Ginzburg (1986), Seismic measurements of the internal properties of fault zones, *Pageoph*, *124*.

Moore, D., and M. Rymer (2007), Talc-bearing serpentinite and the creeping section of the San Andreas fault, *Nature*, *448*, 795–797, doi:10.1038/nature06064.

Morrow, C., D. A. Lockner, and S. Hickman (2015), Low resistivity and permeability in actively deforming shear zones on the San Andreas Fault at SAFOD, *J. Geophys. Res. Solid Earth*, *120*(12), 8758–8773, doi:10.1002/2015JB012214.

Morrow, C. A., D. A. Lockner, D. E. Moore, and S. Hickman (2014), Deep permeability of the San Andreas Fault from San Andreas Fault Observatory at Depth (SAFOD) core samples, *J. Struct. Geol.*, *64*, 99–114, doi:10.1016/j.jsg.2013.09.009.

Norris, R. J., and A. F. Cooper (1997), Erosional control on the structural evolution of a transpressional thrust complex on the Alpine fault, New Zealand, *J. Struct. Geol.*, *19*(10), 1323–1342, doi:10.1016/S0191-8141(97)00036-9.

Norris, R. J., and A. F. Cooper (2001), Late Quaternary slip rates and slip partitioning on the Alpine Fault, New Zealand, *J. Struct. Geol.*, *23*(2–3), 507–520, doi:10.1016/S0191-8141(00)00122-X.

Norris, R. J., and A. F. Cooper (2003), Very high strains recorded in mylonites along the Alpine Fault, New Zealand: implications for the deep structure of plate boundary faults, *J. Struct. Geol.*, *25*(12), 2141–2157, doi:10.1016/S0191-8141(03)00045-2.

Norris, R. J., and A. F. Cooper (2007), The Alpine Fault, New Zealand: surface geology and

field relationships, *A Cont. Plate Bound. Tectonics South Island, New Zeal.*, 157–175.

Nur, A., and G. Simmons (1969), Stress-Induced Velocity Anisotropy in Rock: An Experimental Study, *J. Geophys. Res.*, *74*(27), 6667–6674.

O'Connell, R. J., and B. Budiansky (1974), Seismic velocites in dry saturated cracked solids, *J. Geophys. Res.*, *79*(35), 5413–5426.

Okaya, D., N. Christensen, D. Stanley, and T. Stern (1995), Crustal anisotropy in the vicinity of the Alpine Fault Zone , South Island , New Zealand, *New Zeal. J. Geol. Geophys.*, *38*(4), 579–583, doi:10.1080/00288306.1995.9514686.

Okaya, D. A., and N. I. Christensen (2002), Anisotropic effects of non-axial seismic wave propagation in foliated crustal rocks, *Geophys. Res. Lett.*, *29*(11), 1507, doi:10.1029/2001GL014285.

Olsen, K. B. (2000), Site amplification in the Los Angeles basin from three-dimensional modeling of ground motion, *Bull. Seismol. Soc. Am.*, *90*(6B), S77–S94, doi:10.1785/0120000506.

Olsen, M. P., C. H. Scholz, and A. Léger (1998), Healing and sealing of a simulated fault gouge under hydrothermal conditions: Implications for fault healing, *J. Geophys. Res.*, *103*(B4), 7421, doi:10.1029/97JB03402.

Pros, Z., T. Lokajicek, and K. Klima (1998), Laboratory approach to the study of elastic anisotropy on rock samples, *Pure Appl Geophys*, *151*, 619–629.

Rice, J. R. (1992), Fault stress states, pore pressure distriburitons, and the weakness of the San Andreas Fault, *Int. Geophys.*, *51*, 475–503.

Sayers, C. M. (1998), Misalignment of the orientation of fractures and the principal axes for P and S waves in rocks containing multiple non-orthogonal fracture sets, *Geophys. J. Int.*, *133*, 459–466.

Sayers, C. M., and M. Kachanov (1991), A simple technique for finding effective constants of cracked solids for arbitrary crack orientation statistics, *Int. J. Solids Struct.*, *27*(6), 671–680.

Sayers, C. M., and M. Kachanov (1995), Microcrack-induced elastic wave anisotropy of brittle rocks, *J. Geophys. Res.*, *100*(B3), 4149–4156.

Schleicher, A., R. Sutherland, J. Townend, V. Toy, and B. van der Pluijm (2015), Clay mineral formation and fabric development in the DFDP-1B borehole, central Alpine Fault, New Zealand, *New Zeal. J. Geol. Geophys.*, *58*(1), 13–21, doi:10.1080/00288306.2014.979841.

Sibson, R. (1977), Fault rocks and fault mechanisms, *J. Geol. Soc. London.*, *133*, 191–213.

Spudich, P., and K. B. Olsen (2001), Fault zone amplified waves as a possible seismic hazard along the Calaveras fault in central California, *Geophys. Res. Lett.*, *28*(13), 2533–2536.

Stern, T., D. Okaya, S. Kleffmann, M. Scherwath, S. Henrys, and F. Davey (2007), Geophysical Exploration and Dynamics of the Alpine Fault Zone, *A Cont. Plate Bound. Tectonics South*

Island, New Zeal., 207–233.

Stierman, D. J., and R. L. Kovach (1979), An in situ velocity study: The Stone Canyon Well, *J. Geophys. Res.*, *84*(B2), 672, doi:10.1029/JB084iB02p00672.

Suggate, R. P. (1961), Rock-stratigraphic names for the South Island schists and undifferentiated sediments of the New Zealand geosyncline, *New Zeal. J. Geol. Geophys.*, *4*(4), 392–399, doi:10.1080/00288306.1961.10420127.

Sutherland, R. (2014), DFDP-2 Whataroa River, *GNS Sci.* Available from: https://wiki.gns.cri.nz/DFDP/DFDP-2_Whataroa_River (Accessed 14 August 2014)

Sutherland, R. et al. (2007), Do great earthquakes occur on the Alpine fault in central South Island, New Zealand?, *A Cont. Plate Bound. Tectonics South Island, New Zeal.*, 235–251.

Sutherland, R. et al. (2012), Drilling reveals fluid control on architecture and rupture of the Alpine fault, New Zealand, *Geology*, *40*(12), 1143–1146, doi:10.1130/G33614.1.

Sutherland, R. et al. (2015), *Deep Fault Drilling Project (DFDP), Alpine Fault Boreholes DFDP-2A and DFDP-2B Technical Completion Report*, Wellington.

Sutherland, R., J. Townend, V. G. Toy, P. Upton, J. Coussens, and DFDP2 Science Team (2017), Extreme hydrothermal conditions at an active plate-bounding fault, *Nature*, doi:10.1038/nature22355.

Tenthorey, E., S. F. Cox, and H. F. Todd (2003), Evolution of strength recovery and permeability during fluid-rock reaction in experimental fault zones, *Earth Planet. Sci. Lett.*, *206*(1), 161–172, doi:10.1016/S0012-821X(02)01082-8.

Thomsen, L. (1986), Weak elastic anisotropy, *Geophysics*, *51*(10), 1954–1966, doi:10.1190/1.1442051.

Tosaya, C., and A. Nur (1982), Effects of Diagenesis and clays on compressional velocities in rocks, *Geophys. Res. Lett.*, *9*(1), 5–8.

Tosaya, C. A. (1982), Acoustical properties of clay-bearing rocks, Stanford University.

Townend, J., R. Sutherland, and V. Toy (2009), Deep Fault Drilling Project - Alpine Fault, New Zealand, *Sci. Drill.*, *8*, 75–82, doi:10.2204/iodp.sd.8.12.2009.

Townend, J., R. Sutherland, V. G. Toy, J. D. Eccles, C. Boulton, S. C. Cox, and D. McNamara (2013), Late-interseismic state of a continental plate-bounding fault: Petrophysical results from DFDP-1 wireline logging and core analysis, Alpine Fault, New Zealand, *Geochemistry, Geophys. Geosystems*, *14*(9), 3801–3820, doi:10.1002/ggge.20236.

Toy, V. (2007), Rheology of the Alpine Fault mylonite zone: deformation processes at and below the base of the seismogenic zone in a major plate boundary structure, University of Otago.

Toy, V., R. Sutherland, J. Townend, and DFDP2 Science Team (in review), Bedrock geology of DFDP-2B, Central Alpine Fault, New Zealand, *New Zeal. J. Geol. Geophys.*,

doi:10.1080/09500693.2010.511297.

Toy, V. G., D. J. Prior, and R. J. Norris (2008), Quartz fabrics in the Alpine Fault mylonites: Influence of pre-existing preferred orientations on fabric development during progressive uplift, *J. Struct. Geol.*, *30*(5), 602–621, doi:10.1016/j.jsg.2008.01.001.

Toy, V. G., D. J. Prior, R. J. Norris, A. F. Cooper, and M. Walrond (2012), Relationships between kinematic indicators and strain during syn-deformational exhumation of an oblique slip, transpressive, plate boundary shear zone: The Alpine Fault, New Zealand, *Earth Planet. Sci. Lett.*, *333–334*, 282–292, doi:10.1016/j.epsl.2012.04.037.

Toy, V. G. et al. (2015), Fault rock lithologies and architecture of the central Alpine fault, New Zealand, revealed by DFDP-1 drilling, *Lithosphere*, *7*(2), 155–173, doi:10.1130/L395.1.

Trippetta, F., C. Collettini, S. Vinciguerra, and P. G. Meredith (2010), Laboratory measurements of the physical properties of Triassic Evaporites from Central Italy and correlation with geophysical data, *Tectonophysics*, *492*, 121–132, doi:10.1016/j.tecto.2010.06.001.

Vanorio, T., M. Prasad, and A. Nur (2003), Elastic properties of dry clay mineral aggregates, suspensions and sandstones, *Geophys. J. Int.*, *155*, 319–326.

Velde, B. (1995), *Origin and Mineralogy of Clays*, Springer-Verlag Berlin Heidelburg.

Vermilye, J. M., and C. H. Scholz (1998), The process zone: A microstructural view of fault growth, *J. Geophys. Res.*, *103*(B6), 12223–12237.

Vidale, J. E., and Y. G. Li (2003), Damage to the shallow Landers fault from the nearby Hector Mine earthquake, *Nature*, *421*(6922), 524–526, doi:10.1038/nature01354.

Wang, C.-Y., D. A. Okaya, C. Ruppert, G. A. Davis, T.-S. Guo, Z. Zhong, and H.-R. Wenk (1989), Seismic reflectivity of the Whipple Mountain shear zone in southern California, *J. Geophys. Res.*, *94*(B3), 2989–3005.

Wang, Z. Z., H. Wang, and M. E. Cates (2001), Effective elastic properties of solid clays, *Geophysics*, *66*(2), 428–440.

Warr, L. N., and S. Cox (2001), Clay mineral transformations and weakening mechanisms along the Alpine Fault, New Zealand, *Geol. Soc. London, Spec. Publ.*, *186*(1), 85–101, doi:10.1144/GSL.SP.2001.186.01.06.

Wellman, H. W. (1955), New Zealand quaternary tectonics, *Geol. Rundschau*, *43*(1), 248–257.

Williams, J. N., V. G. Toy, D. D. Mcnamara, and T. Wang (2016), Damaged beyond repair? Characterising the damage zone of a fault late in its interseismic cycle, the Alpine Fault, New Zealand, *J. Struct. Geol.*, *90*, 76–94, doi:10.1016/j.jsg.2016.07.006.

Winkler, K. (1983), Frequency dependent ultrasonic properties of high-porosity sandstones, *J. Geophys. Res.*, *88*(B11), 9493–9499.

Winkler, K. (1986), Estimates of velocity dispersion between seismic and ultrasonic frequencies, *Geophysics*, *51*(1), 183–189.

Yasuhara, H., C. Marone, and D. Elsworth (2005), Fault zone restrengthening and frictional healing: The role of pressure solution, *J. Geophys. Res. B Solid Earth*, *110*(B06310), doi:10.1029/2004JB003327.

Zhao, D., H. Kanamori, H. Negishi, and D. Wiens (1996), Tomography of the source area of the 1995 Kobe Earthquake: Evidence for fluids at the hypocenter?, *Science*, *274*, 1891–1894.

Zoback, M., S. H. Hickman, and W. Ellsworth (2005), Overview of SAFOD phases 1 and 2: Drilling, sampling and measurements in the San Andreas Fault Zone at Seismogenic Depth, *Eos Trans. AGU*, *86*(52), Fall Meet. Suppl., Abstract T23E-01.

Zoback, M., S. Hickman, and W. Ellsworth (2010), Scientific drilling into the San Andreas Fault Zone, *Eos (Washington. DC).*, *91*(22), 197–204.

Zoback, M., S. Hickman, W. Ellsworth, and S. S. Team (2011), Scientific drilling Into the San Andreas Fault Zone — an overview of SAFOD's first five years, *Sci. Drill.*, *11*, 14–28, doi:10.2204/iodp.sd.11.02.2011.

Zoback, M. D. et al. (1987), New evidence on the state of stress of the San Andreas Fault System, *Science*, *238*(4830), 1105–1111.

4.6 Appendix

4A.1 Supplementary material

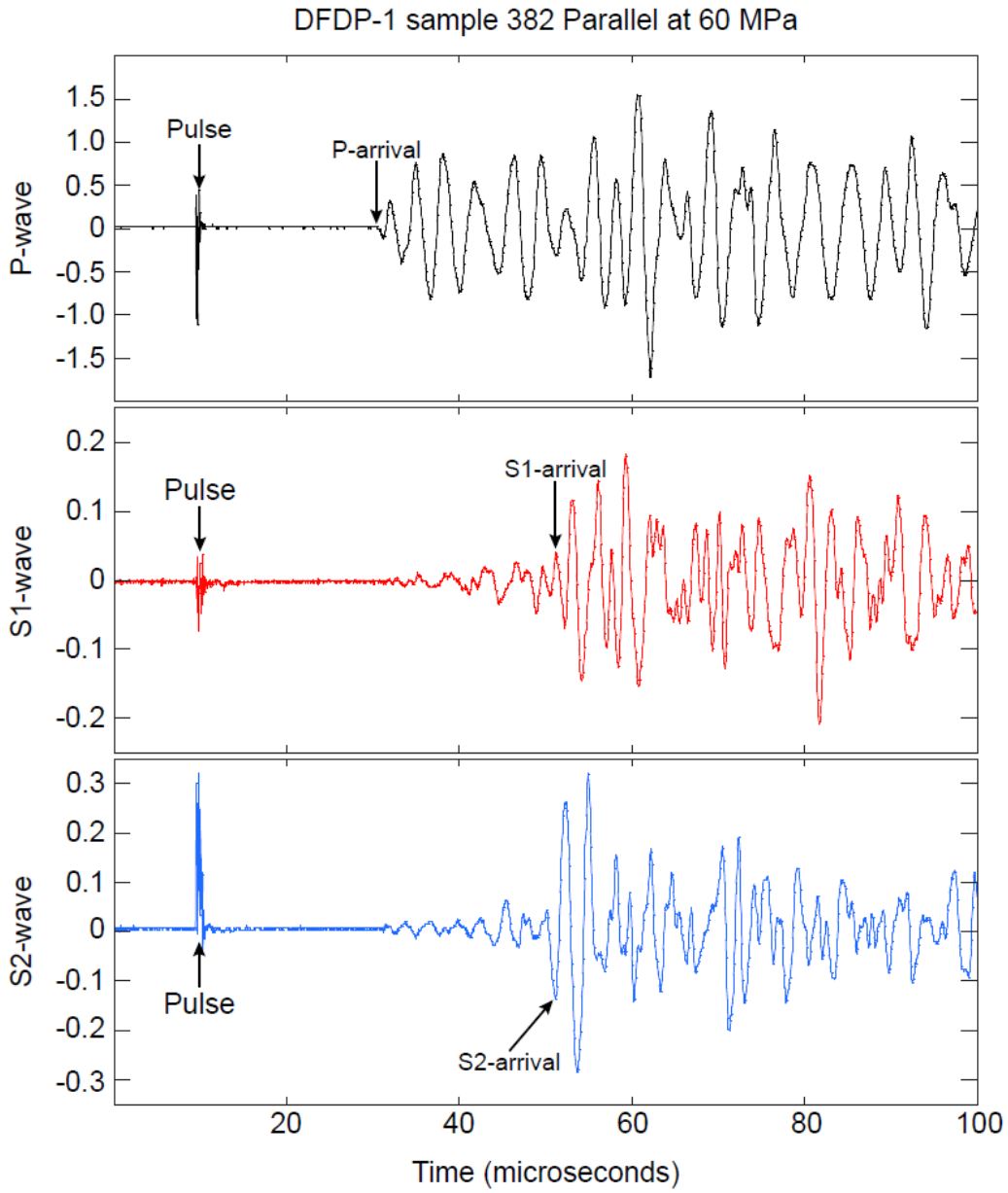

Figure 4A.1.1: Example of raw waveforms measured at the University of Wisconsin-Madison on DFDP-1 drill core sample 382 parallel at 60 MPa. The P- and S2 waveforms are examples of good quality waveforms while the S1-waveform is intermediate quality.

5 Laboratory measurements quantifying elastic properties of accretionary wedge sediments: Implications for slip to the trench during the 2011 M_w 9.0 Tohoku-Oki earthquake

Abstract

The 11 March 2011 (M_w 9.0) Tohoku-Oki earthquake ruptured through the shallowest part of the subduction zone plate boundary fault, producing tens of meters of displacement at the seafloor and a devastating tsunami. Because elastic and mechanical properties of faults and wallrocks are controlling factors in earthquake generation and propagation, information on these properties is essential to understanding and accurately modeling earthquake rupture and tsunami generation. Laboratory ultrasonic velocity measurements of samples of rock surrounding the Tohoku earthquake principal fault zone recovered by drilling during IODP Expedition 343 (JFAST) show that, under *in situ* conditions, materials in the frontal accretionary prism are slow and compliant, with P-wave velocities of 2.0-2.4 km/s, S-wave velocities of 0.8-1.0 km/s, and shear modulus of 1.0-2.3 GPa. In order to better understand the elastic properties of shallow subduction zone sediments, we compare our measurements from the Japan Trench to values from analogous shallow subduction zone drill core samples from other locations. We find that shallow subduction zone accretionary prism sediments in general have shear modulus values an order of magnitude lower than what is commonly used in earthquake rupture simulation models. We present a model of the shear modulus of the Japan Trench outer forearc based on laboratory and field measurements that can be adapted for use at other subduction zones and used in dynamic rupture models to improve seismic and tsunami hazard estimates.

5.1 Introduction

Rock properties are a major controlling factor in frictional behavior of faults and earthquake rupture dynamics [*Scholz*, 2002]. The shear modulus, or modulus of rigidity, is of particular interest as it describes a rock's resistance to shear deformation and influences earthquake rupture velocity and fault slip. Low shear modulus materials in the shallow regions of subductions zones have been cited as the cause of the shallow aseismic zone [e.g., *Byrne et al.*, 1988] and of greater than expected tsunami wave heights experienced during tsunami earthquakes [e.g., *Kanamori*, 1972; *Fukao*, 1979; *Pelayo and Wiens*, 1992; *Bilek and Lay*, 1999a]. Earthquake data have been used to estimate shear modulus variations with depth [*Dziewonski and Anderson*, 1981; *Bilek and Lay*, 1998, 1999a, 1999b] but these earthquake-scale studies do not estimate shear modulus in the upper ~ 5 km of a subduction zone, so shallow shear modulus variations remain poorly constrained and are typically ignored in megathrust studies in general.

Numerical models of dynamic rupture processes by *Lotto et al.* [2017] have explored the effect of accretionary prisms composed of compliant sedimentary material on subduction zone earthquakes. They found that a compliant prism can slow rupture velocity, increase shallow slip, and increase tsunami height relative to models without a compliant prism. The degree to which velocity, slip, and wave height are altered depends on the size of the prism, contrast in shear modulus between the prism and surrounding material, and basal friction. The effect of a prism on subduction zone earthquakes is complex, so a better understanding of the elastic properties of prisms at convergent margins is needed to fully characterize seismic and tsunami hazard.

We have performed laboratory measurements of ultrasonic wavespeed and density on samples of drill core obtained during Integrated Ocean Drilling Program (IODP) Expedition 343, known as the Japan Trench Fast Drilling Project (JFAST). These measurements allow us to compute the

dynamic elastic moduli of the frontal prism of the Japan Trench. Dynamic elastic moduli, rather than static, are most relevant to this study as we are interested in the processes occurring during the rapid propagation of fault rupture and slip, which occurs at speeds close to the shear wave velocity. In this paper we show that the Japan Trench frontal prism is very compliant relative to standard crustal model values and explore global variations in shallow subduction zone elastic moduli. In addition, we used the laboratory data with wide-angle refraction data from the Japan Trench [*Miura et al.,* 2001, 2005] to create a 2D shear modulus model of the Japan Trench that is applicable to compliant prisms globally and can be used to explore their role in coseismic shallow slip and tsunami generation.

5.1.1 Japan Trench

At the Japan Trench subduction zone off the northeastern coast of Japan, the Pacific plate subducts beneath Honshu Island at a shallow angle of 5° to 15° (Fig. 5.1) [*von Huene and Langseth*, 1982; *Apel et al.*, 2006; *Ide et al.*, 2011; *Satake et al.*, 2013]. The Pacific plate is composed of basaltic rocks overlain by a chert unit and a sequence of pelagic clay and hemipelagic mudstone all cut by high-angle normal faults [*Arthur and Adelseck,* 1980; *Chester et al.*, 2013; *Nakamura et al.*, 2014]. A relatively small frontal accretionary prism has formed landward of the trench. The prism is acoustically chaotic and composed of Neogene sediments, specifically hemipelagic mudstones and underthrust terrigenous mudstones and pelagic clays [*Chester et al.,* 2013; *Nakamura et al.*, 2014; *Kirkpatrick et al.*, 2015; *Moore et al.*, 2015]. The backstop of the prism is formed by a sequence of Cretaceous rocks which are separated from Neogene slope cover sediments by an erosional surface [*von Huene and Culotta*, 1989; *von Huene and Lallemand,* 1990; *von Huene et al.,* 1994]. This sequence was sampled at Deep Sea Drilling Program (DSDP) Site 439 [*Murauchi and Ludwig*, 1980].

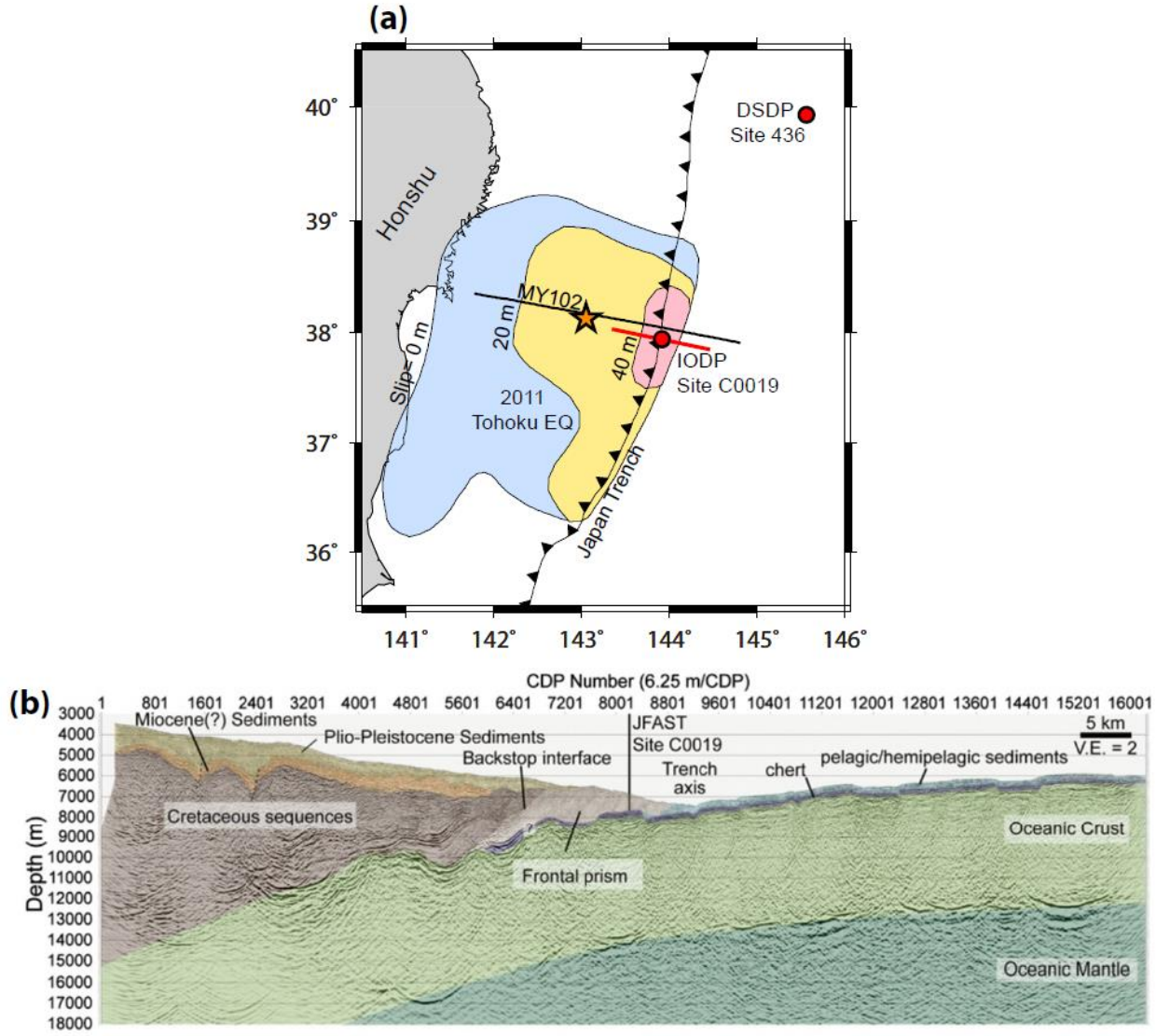

Figure 5.1: *(a) Location of the JFAST drill site. Red dots indicate ocean drilling sites, the black line shows the location of the MY 102 seismic line referred to in figure 5.9, and the red line shows the location of the JFD1 seismic line. Modified from Miura et al. [2005] and Chester et al. [2013]. The orange star shows the location of the 2011 Tohoku-Oki epicenter and contours show coseismic slip magnitudes over the fault area as compiled by Chester et al. [2013]. (b) Interpreted seismic profile (line JFD1) showing the location of Site C0019. From Nakamura et al., [2014].*

The Japan Trench megathrust fault hosted the Tohoku-Oki (M_W 9.0) earthquake on 11 March 2011. There is evidence that the rupture reached the seafloor at the trench with up to 60 m of displacement at shallow depths and produced a large tsunami [*Ammon et al.*, 2011; *Fujii et al.*, 2011; *Ide et al.*, 2011; *Ito et al.*, 2011; *Koper et al.*, 2011; *Lay et al.*, 2011; *Kodaira et al.*, 2012].

Previous to this earthquake, it was generally assumed that the velocity-strengthening frictional properties and low strength of sediments in shallow parts of subduction zones would cause megathrust slip to dissipate rather than grow as rupture traveled through this energy-absorbing, compliant, and velocity-strengthening material. Thus the large shallow slip of the Tohoku-Oki earthquake raised many questions about potentially anomalous frictional and elastic properties of the Japan Trench subduction zone.

One year after the Tohoku-Oki earthquake, JFAST drilling was undertaken. The main goal of JFAST was to understand the physical mechanisms and dynamics of the large slip earthquake [*Mori et al.*, 2012]. Three boreholes were drilled in the frontal prism of the Japan Trench subduction zone at Site C0019, located about 200 km east of the Oshika Peninsula (Fig. 5.1). Drilled to depths of about 845 to 855 m below the seafloor (mbsf), the boreholes were used to (1) collect geophysical well logs (natural gamma ray and resistivity), (2) retrieve core samples, and (3) install a temperature observatory [*Expedition 343/343T Scientists*, 2013]. Based on changes in log signature and bedding orientation observed in borehole logging data from Hole C0019B, the plate-boundary fault was interpreted to be located around 820 mbsf.

Coring in Hole C0019E targeted the probable fault location identified in the log data. Seven lithologic units were identified in the recovered core: (1) olive-gray mudstone (176.5 to 185.2 mbsf), (2) brown and bluish gray mudstone (648.0 to 659.7 mbsf), (3) gray mudstone (688.5 to 820.1 mbsf), (4) sheared clay (821.5 to 822.5 mbsf), (5) brown mudstone (824 to 832.9 mbsf), (6) pelagic clay (832.9 to 833.5 mbsf), and (7) chert (833.5 to 836.8 mbsf). Unit 4, sheared clay, is interpreted to represent the plate boundary décollement zone [*Expedition 343/343T Scientists*, 2013].

Table 5.1: *Clay content from Kameda et al. [2015] and laboratory measurements of physical properties at an estimated in situ effective pressure of 5 MPa. Porosity is within the normal range for clay-rich marine sediment from the upper kilometer of the crust [e.g., Bray and Karig, 1985; Gettemy and Tobin, 2003; Hashimoto et al., 2010].*

Sample	Depth (mbsf)	Density (g/cm^3)	Porosity (%)	Total Clay content in bulk sample (wt.%)	Smectite content in bulk sample (wt.%)	P-wave velocity (km/s)	S-wave velocity (km/s)	Shear Modulus (GPa)	Bulk Modulus (GPa)	Poisson's Ratio†
4R2	690.40	1.54 ± 0.09	38.3 ± 2.68	19.2	9.1	2.00 ± 0.08	0.85 ± 0.03	1.13 ± 0.16	4.70 ± 0.75	0.39 ± 0.11
6R1	704.03	2.06 ± 0.12	32.9 ± 2.30	15.7	10.9	2.20 ± 0.09	0.99 ± 0.04	2.00 ± 0.28	7.35 ± 1.18	0.38 ± 0.10
7R1	713.20	1.91* ± 0.11	41.9 ± 2.93	29.8	19.6	2.29 ± 0.09	1.09 ± 0.04	2.29 ± 0.32	7.01 ± 1.12	0.35 ± 0.10
8R2	720.83	1.80 ± 0.11	47.9 ± 3.35	24.0	15.4	2.03 ± 0.08	0.95 ± 0.04	1.63 ± 0.23	5.29 ± 0.85	0.36 ± 0.10
15R1	817.45	1.91 ± 0.11	42.8 ± 2.99	23.9	17.7	2.36 ± 0.09	1.04 ± 0.04	2.05 ± 0.29	7.87 ± 1.26	0.38 ± 0.10
16R1	818.50	2.19 ± 0.13	32.7 ± 2.29	25.3	14.3	2.44 ± 0.10	1.03 ± 0.04	2.31 ± 0.32	9.90 ± 1.58	0.39 ± 0.11
19R2	827.90	2.11 ± 0.13	32.8 ± 2.30	36.4	21.4	2.15 ± 0.09	0.83 ± 0.03	1.46 ± 0.21	7.80 ± 1.25	0.41 ± 0.11

* Density from shipboard measurement of core

†High uncertainty in Poisson's Ratio is due to error propagation. It is highly unlikely that Poisson's ratio in this material would exceed 0.50 or fall below 0.30.

5.2 Methods

5.2.1 Samples

Laboratory high-pressure experiments to measure ultrasonic wave velocity were performed on seven samples from the JFAST site C0019E borehole (Table 1). Cylindrical specimens with diameters of 25.4 mm were extracted from the JFAST cores with the axis of the specimen oriented perpendicular to the drill core axis. All lab samples were prepared by hand using precision knives and

sandpaper due to the delicate nature of the sample material. Six of the samples are of the Unit 3 gray mudstone located above the plate boundary fault. The seventh sample comes from the underthrust brown mudstone of lithologic unit 5.

5.2.2 Ultrasonic velocity measurements

Following pulse-transmission techniques adapted from *Birch* [1960, 1961] and *Christensen* [1985] velocity measurements were performed on the cylindrical specimens under elevated confining and pore pressure conditions (Table 1).

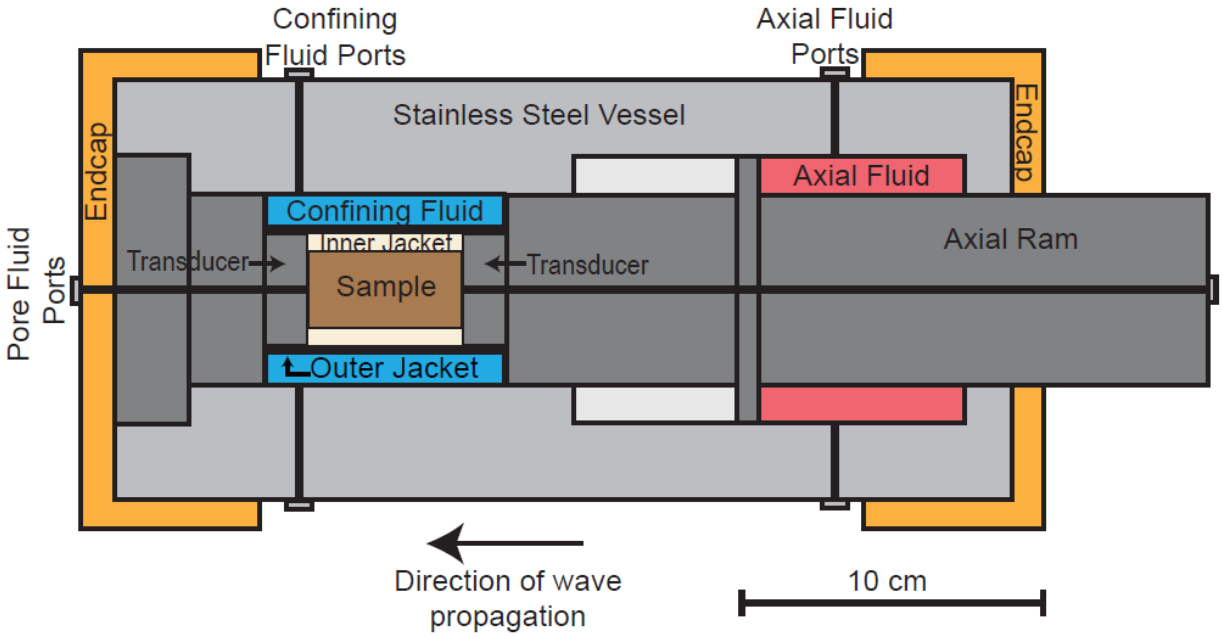

Figure 5.2: *Schematic of the triaxial pressure vessel used at the University of Wisconsin-Madison; Kochi University vessel is similar.*

All samples except 7R1 were measured at the University of Wisconsin-Madison Rock Physics Laboratory in the Department of Geoscience. Sample 7R1 was measured at Kochi University. At the University of Wisconsin, samples were loaded into a standard triaxial vessel (Fig. 5.2) with sintered metal filters at both ends to prevent extrusion of the sample material into the pore pressure ports when pressure is applied. Six 500 kHz central frequency piezoelectric transducers

embedded in the endcaps of the vessel (three in each endcap) were used as source-receiver pairs. These transducers generate the P-wave and two mutually perpendicular S-wave vibration directions used in the wave propagation experiments.

During our experiments, confining pressure, axial stress, and pore fluid pressure were independently controlled using three syringe pumps; salt water (salinity of 35 ppt) was used as a saturating fluid. The axial and confining pressures were simultaneously increased to 2 MPa and 1.8 MPa, respectively. The 0.2 MPa difference between axial stress and confining pressure was maintained throughout the experiment to ensure good coupling between the sample liner and endcap. The specimen was then saturated by creating a pressure differential across the sample. One side of the sample was left open to atmospheric pressure and a 1 MPa pore pressure was applied at the other side. Once water began flowing out the open end of the sample that side was connected to the syringe pump so the saturating fluid flowed into both ends of the sample. Pore space gas should be minimal as core samples were stored in conditions that limited drying so samples were still wet when placed in the vessel. Pore fluid pressure of 1 MPa was maintained through the experiments so that any remaining pore space gas was kept in solution, ensuring 100% saturation. The specimen was allowed to saturate for $\geq$ 24 hours before the first ultrasonic velocity measurement was made. We then simultaneously increased the confining and axial pressure to obtain an effective pressure of 2 MPa and allowed the sample to equilibrate. Ultrasonic measurements were conducted at regular intervals between 1 MPa and 70 MPa. Following each pressure step, the sample was allowed to equilibrate, as monitored by continuous measurements of sample length and pore volume change, before an ultrasonic measurement was made. Measurements were made during both increasing and decreasing pressure paths. P- and S-wavespeeds were determined from time-of-flight measurements and the measured sample length.

At Kochi University, sample 7R1 was measured using a similar procedure but pore pressure was held constant at 0.5 kPa and confining pressure was only increased to 18 MPa. Additionally only one source-receiver pair of identical S-wave polarized 500 kHz transducers was used, similar to the method described in *Gettemy and Tobin* [2003]. This transducer arrangement yields only one waveform instead of the three individual waveforms recorded at Wisconsin. This increases the uncertainty in determining the S-wave arrival. Preliminary analysis of the data indicated that the S-wave measured at Kochi was noticeably different from the S-waves measured at Wisconsin and resulted in an unrealistic Poisson's ratio that decreased with pressure. For this reason, we only used the P-wave measurement from this sample.

Initial picking of the wave arrivals had a high level of uncertainty, particularly in the S-wave at low pressures. We have decreased that uncertainty by cross-correlating waveforms acquired at low pressures with those recorded at higher pressures. This improved the wave arrival pick at low pressures where poor sample-transducer coupling leads to greater uncertainty. Overall there is a 1% uncertainty in picking the P-wave arrival and a 2% uncertainty in the S-wave arrival. Additional uncertainty in the velocity arises from non-parallel core faces and associated uncertainties in initial length measurements. The core faces can usually be smoothed and made parallel so there is less than 0.5 mm variability leading to 2% uncertainty in the length of the sample. The total uncertainty in the velocity measurement is less than 4%.

Final porosity and density were determined through direct measurement of sample volume and wet and dry mass. These measurements, combined with the axial displacement, were used to estimate porosity and density changes during the experiment. The total sample volume was determined using both linear measurements using a vernier caliper and volumetric displacement methods. Because the samples are fragile and must be prepared by hand the sample diameter is

not uniform. This results in a relatively high uncertainty of 6% in the density measurements and 7% in the porosity measurements.

We calculated the shear (μ) and bulk moduli (K) and Poisson's ratio (ν) for all samples from the measured wave speeds and densities. The bulk density (ρ) at each pressure step was estimated from the bulk density measured at the end of each test and the measured sample volume changes at each pressure step. Assuming elastic isotropy, the dynamic elastic moduli are given by:

$$\mu = \rho v_s^2 \qquad [1]$$

$$K = \lambda + \frac{2\mu}{3} \qquad [2]$$

$$\nu = \frac{\lambda}{2(\lambda + \mu)} \qquad [3]$$

where v_p and v_s are the P- and S-wave velocities, respectively, and λ is Lame's constant:

$$\lambda = \rho\left(v_p^2 - 2v_s^2\right) \qquad [4]$$

5.3 Results and discussion

5.3.1 P- and S-wavespeeds

Velocity was measured over a cycle as effective pressure was increased from 1 to 70 MPa and then decreased back to 1 MPa (Fig. 5.3). The pressure curves indicate that the sediments are very compliant. The samples experience permanent axial strains of up to 14%. The shallowest sample, 4R2, is the most compliant. There is also hysteresis in the velocity curves: at 15 MPa there is an 8 to 19% difference in the P-wave velocity and a 13 to 24% change in the S-wave velocity between the loading and unloading values. The velocity values increase with increasing effective pressure for all samples measured.

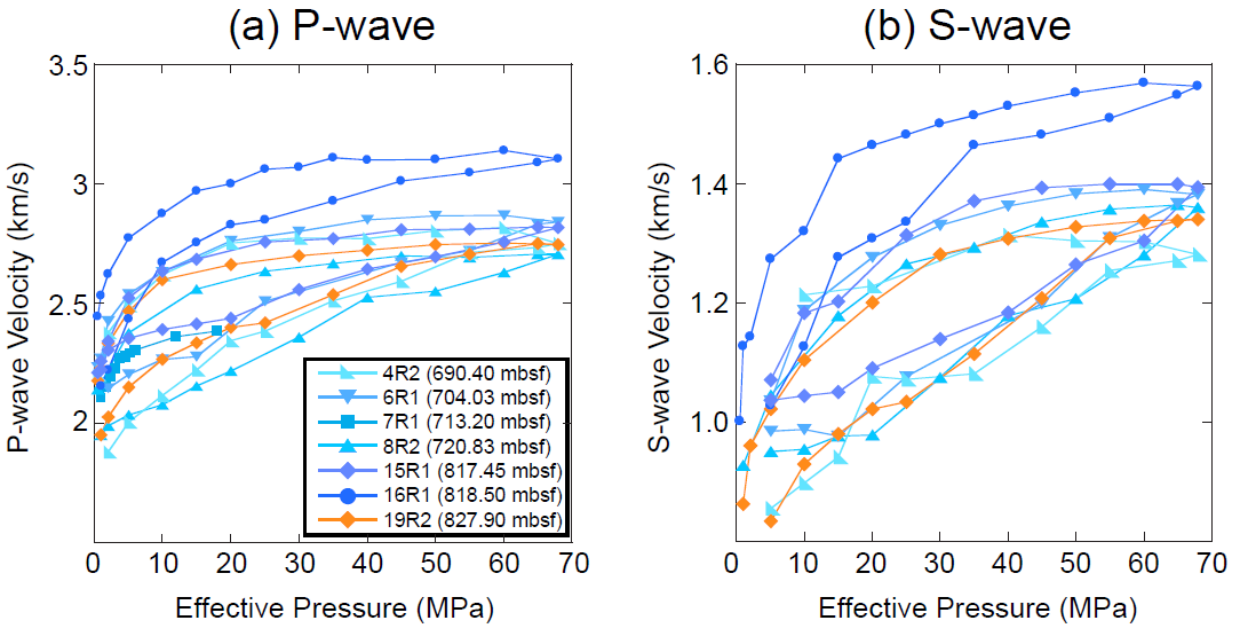

Figure 5.3: *Variations in (a) P-wave and (b) S-wave velocity measurements with effective pressure for JFAST core samples. The two orthogonal S-wave measurements showed little to no anisotropy so only one S-wave vibration direction is shown here. The sample from unit 5 (orange) is similar to the samples from unit 3 (blue).*

The measured wavespeeds are low (v_p <3.2 km/s, v_s <1.6 km/s) and similar in both the unit 5 underthrust brown mudstone specimen and the unit 3 gray mudstone samples. The lab velocities are consistent with seismic reflection models that indicate the velocity should range between 1.5 to 3.0 km/s in the frontal prism sediments in the Japan Trench [*Murauchi and Ludwig*, 1980; *Miura et al.*, 2001, 2005; *Nakamura et al.*, 2014]. They also agree with ultrasonic wavespeed measurements of prism sediments from other subduction zones [*Carson and Bruns*, 1980; *Tobin et al.*, 1994, 1995; *Tobin and Moore*, 1997; *Gettemy and Tobin*, 2003; *Hashimoto et al.*, 2010; *Raimbourg et al.*, 2011; *Schumann et al.*, 2014]. For the purposes of this study we are mainly interested in the average elastic properties of the prism. Because of this, and the limited number of samples available for this study, fine-scale variations are only briefly discussed in the following paragraphs.

In the unit 3 gray mudstone samples examined here, an overall trend of increasing velocity with sample depth is apparent. However, sample 8R2 deviates from that trend as it has a slower velocity than samples located at shallower depths. The lower velocity could be due to a higher porosity, as velocity typically has an inverse relationship with porosity [*Nafe and Drake*, 1957; *Kowallis et al.*, 1984; *Han et al.*, 1986; *Klimentos*, 1991; *Hashimoto et al.*, 2010]. A porosity of 48% was measured for sample 8R2; this is the highest porosity we measured for the unit 3 samples. Comparison of our porosity measurements to porosities measured during the JFAST expedition on the same cores [*Expedition 343/343T Scientists*, 2013] shows that the porosities differ by less than 10% for samples collected at depths greater than 713 mbsf. However, the porosities measured for our two shallowest samples (4R2 and 6R1) are 15% less than the on-expedition measurements, indicating that our measurements of these two samples may be in error. The expected porosity range for 4R2 and 6R1 is between 48 and 53% (Fig. 5.4.) which is greater than or equal to the porosity of 8R2 so porosity variations may not explain the low velocity of 8R1.

Based on XRD analysis by *Kameda et al.* [2015] on samples less than one meter away from the samples examined in this study, the clay content in 8R2 is 5% greater than in 4R2 and 6R1. Velocity has been shown to have an inverse relationship with clay content so the decrease in velocity could be due to clay [*Tosaya and Nur*, 1982; *Kowallis et al.*, 1984; *Castagna et al.*, 1985; *Han et al.*, 1986; *Klimentos*, 1991]. However, if velocity was controlled solely by clay we would also expect 7R1, 15R1, and 16R1 to have a lower velocity than 6R1 and 4R2, yet these samples follow the trend of increasing velocity with depth. Detailed microstructural analyses would be required to evaluate potential microstructural and diagenetic controls on the velocity.

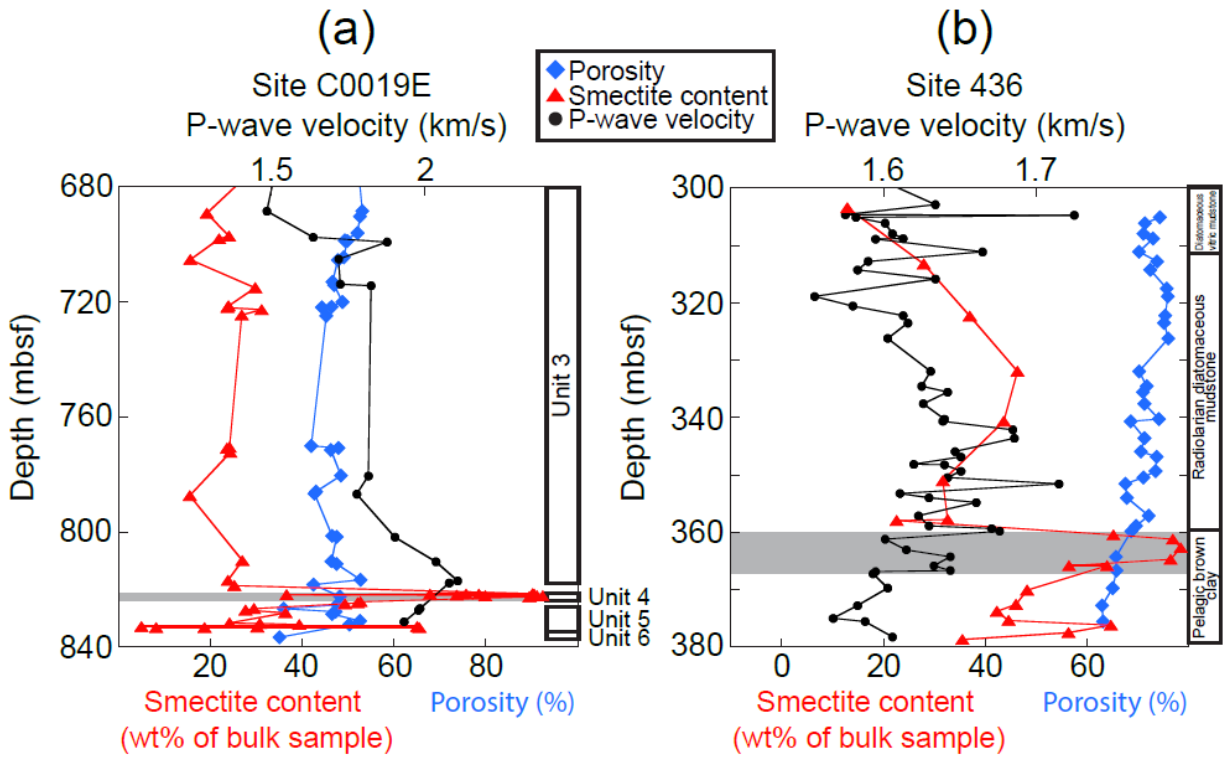

Figure 5.4: *Measurements of dry, unconfined P-wave velocity (black) and porosity (blue) with depth for core samples from (a) IODP Site C0019E (depth interval 680 to 840 mbsf; data from Expedition 343/343T Scientists [2013]) and (b) ODP Site 436 (depth interval 300 to 380 mbsf, data from Carson and Bruns [1980]) shown with smectite content (red) from quantitative XRD work by Kameda et al. [2015]. Smectite-rich horizons identified at both sites are highlighted by gray boxes. A decrease in velocity is observed within and below this horizon due to the increase in clay content.*

The unit 5 brown mudstone sample (19R2) is the deepest sample but it has a slower velocity than the samples directly above it (15R1 & 16R1). An examination of discrete velocity measurements acquired during the JFAST expedition on unsaturated, unconfined samples, shows a general trend of increasing velocity with depth in unit 3 but a decrease in velocity in the unit 5 underthrust sediments relative to the basal wedge sediments of unit 3 (Fig. 5.4a) [*Expedition 343/343T Scientists*, 2013]. Porosity is variable but generally decreases with depth so the porosity variations do not explain the decrease in velocity. Based on XRD analysis by *Kameda et al.* [2015], unit 5 has greater clay content then unit 3. The smectite content in unit 3 remains relatively constant with an average of 13 wt.% of the bulk samples, whereas in unit 5 the average

smectite content is 18 wt.% of the bulk sample [*Kameda et al.*, 2015] suggesting that the lower velocity in unit 5 is due to higher clay content.

The dependence of velocity on clay content is also seen in data from DSDP Site 436 (Fig. 5.4b) [*Carson and Bruns*, 1980]. XRD data from *Kameda et al.* [2015] shows a smectite-rich horizon at both sites (gray shaded regions in figure 5.4). Immediately below the top of this horizon, the velocity decreases relative to the velocities above even though porosity is decreasing. Although the smectite content is greater at Site 436 then at C0019E and there are several age reversals with depth at Site C0019E due to folding and faulting [*Chester et al.*, 2013; *Moore et al.*, 2015], the smectite content below the clay-rich horizon is greater than in the sediments above the horizon at both sites. Although the sediments at Site C0019E are not in the same stratigraphic sequence as those from Site 436, similar dependence of velocity on clay content is observed.

5.3.2 Elastic moduli

The frontal prism sediments from the Japan Trench are characterized by low bulk modulus, low shear modulus, and high Poisson's ratio (Fig. 5.5). The moduli vary systematically with effective pressure, as reflected in increased P- and S-wavespeeds with effective pressure. At an effective pressure of 5 MPa on the loading curve, which is comparable to *in situ* conditions, the bulk modulus ranges from 4.7 to 9.9 GPa, shear modulus ranges from 1.1 to 2.3 GPa, Poisson's ratio ranges from 0.33 to 0.41, and v_p/v_s ratio ranges from 1.99 to 2.58. This is consistent with other evidence that indicates the shallowest parts of subduction zones have low shear moduli relative to crustal rocks (shear modulus ~30 GPa), which numerous workers have suggested causes an updip limit to the seismogenic zone [e.g., *Fukao*, 1979; *Bray and Karig*, 1985; *Byrne et al.*, 1988; *Satake*, 1994; *Lay and Bilek*, 2007].

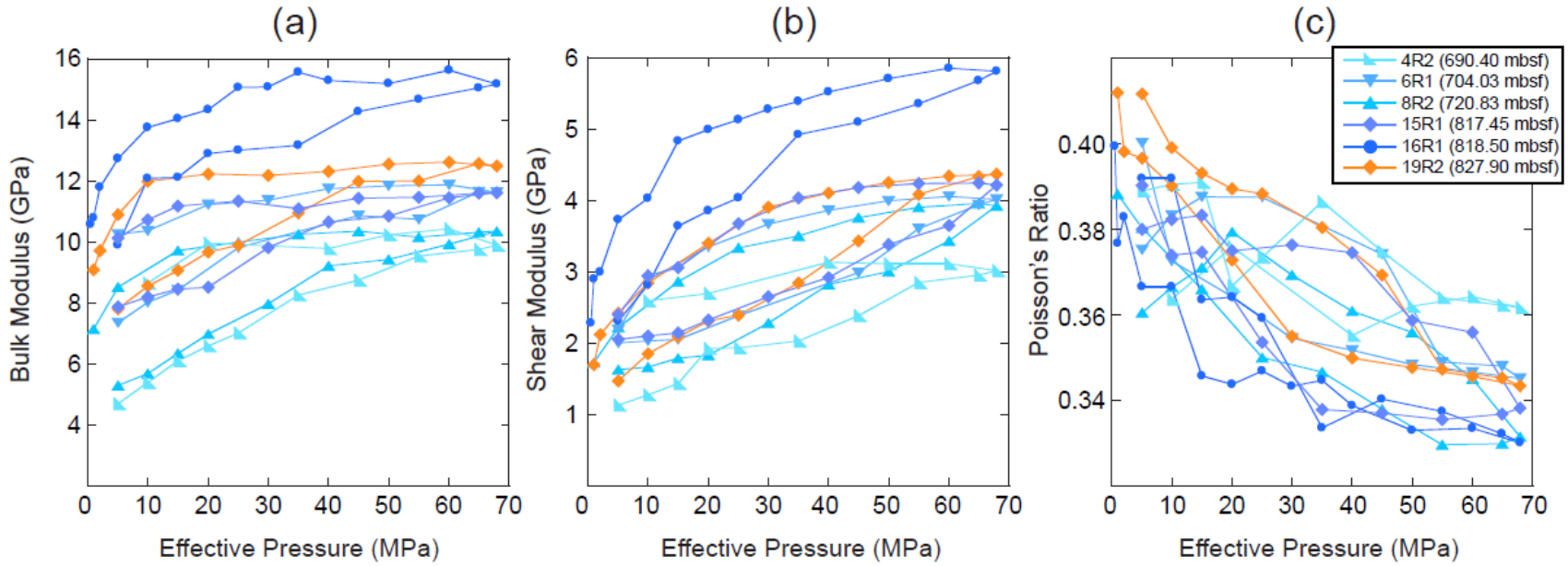

Figure 5.5: *Variations in (a) bulk modulus, (b) shear modulus, and (c) Poisson's ratio with effective pressure calculated from laboratory velocity and density data show that the sediments are very compliant.*

5.3.3 Comparison of global subduction zone elastic moduli

The large magnitude of shallow coseismic slip to the trench during the 2011 (M_w 9.0) Tohoku earthquake was unexpected due to the predicted low modulus of rigidity and velocity strengthening properties of sediments near the trench. At other subduction zones it has been suggested that the occurrence of shallow coseismic slip is due to the presence of unusually competent and strong sediments which allow the accumulation and release of elastic energy [*Gulick et al.*, 2011]. To test this hypothesis, we examined ultrasonic velocity measurements that have been collected on shallow accretionary prism sediments retrieved from other subduction

zone margins by IODP, DSDP, and Ocean Drilling Program (ODP) projects [*Tobin et al.*, 1994, 1995; *Tobin and Moore*, 1997; *Gettemy and Tobin*, 2003; *Hashimoto et al.*, 2010; *Raimbourg et al.*, 2011; *Schumann et al.*, 2014]. We compared our computed elastic properties to published data from other accretionary prisms to address whether a difference in the elastic properties could account for the occurrence of coseismic slip to the trench during the Tohoku earthquake.

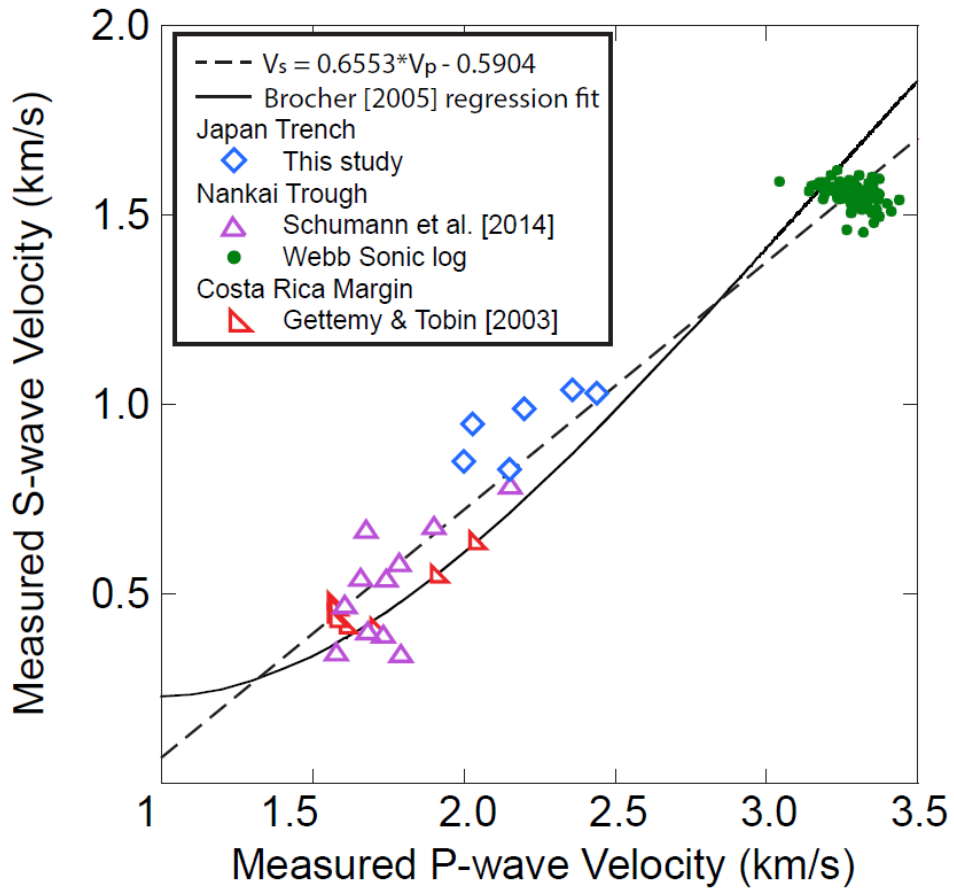

Figure 5.6: *Relationship between P- and S-wave velocities in accretionary prisms based on data from the Japan Trench, Nankai Trough [Schumann et al., 2014], and Costa Rica margin [Gettemy and Tobin, 2003] (dashed line). Log data were averaged over 10 m intervals to avoid biasing the fit with a large number of log measurements. The resulting fit is similar to the regression fit from Brocher [2005] (solid black line).*

Many of these published studies did not report S-wavespeed or densities for accretionary prism materials. To estimate the S-wavespeed for the prism materials of other convergent margins, we

used the data from this study, *Gettemy and Tobin's* [2003] data from the Costa Rica margin, *Schumann et al.'s* [2014] data from the Nankai Trough, and sonic log data from the NantroSEIZE project Site C0002P (S. Webb, personal communication, 2017) to derive a linear v_p-v_s relationship (Fig. 5.6). This relationship was then used to estimate S-wave velocity for the datasets where only P-wave velocity had been measured. Where density was not reported, IODP, DSDP, and ODP databases of shipboard measurements were used to obtain the nearest neighbor (less than 1.5 m) density measurement. To calculate elastic moduli we used the velocity recorded at the estimated *in situ* pressure for each sample. The results of this comparison are shown in figure 5.7.

The Japan Trench data fit in the overall depth trend of the other subduction zone moduli. The Japan Trench has lower Poisson's ratio than most of the samples acquired at other subduction zones, but without more data at depths greater than 600 msbf, it cannot be determined if the Japan Trench or Nankai Trough data are more representative of global accretionary prisms. While it is difficult to identify distinct rigidity-depth trends in the data there are some differences among the prisms. The majority of data presented in figure 5.7 come from the Nankai Trough, where multiple boreholes have been drilled at different locations in the accretionary prism as part of the NantroSEIZE project. These data show variations in elastic moduli related to the setting from which each sample was taken within the accretionary prism volume. The variations appear to be controlled by differences in composition, grain size, and history. For example, at the same depth below the seafloor, samples from the prism toe are less compliant than samples from the upper accretionary prism (Supp. Fig. 5A.1.3) and contain 5 to 10 wt.% less smectite clay [*Guo and Underwood*, 2012]. The lower clay content may explain the greater elastic moduli of the prism toe samples. Underthrust samples have smectite content similar to the upper accretionary

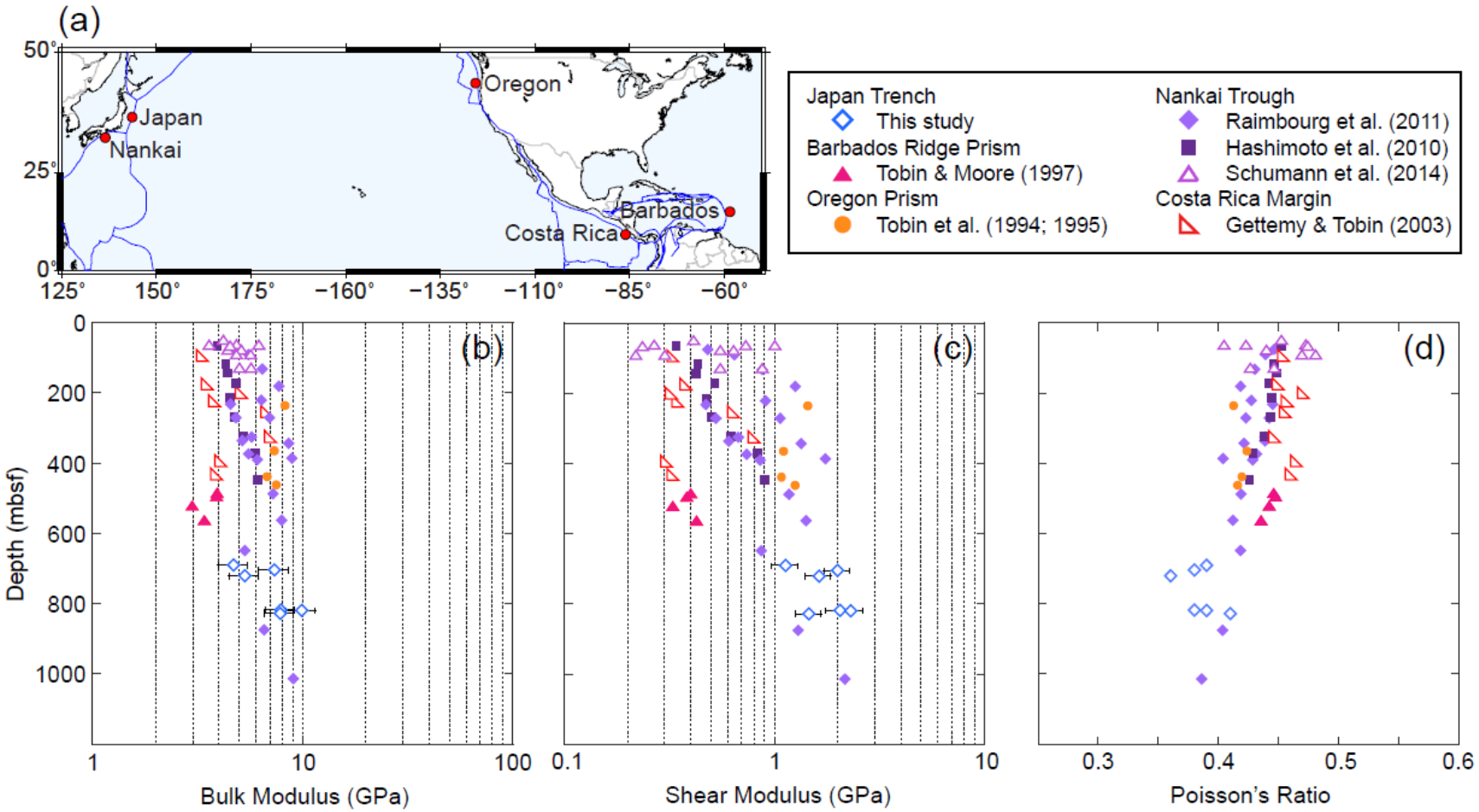

Figure 5.7: *(a) Map of convergent margins where prism sediments examined in this study were obtained (red dots). Blue lines show locations of plate boundaries. Global variations in (b) bulk modulus, (c) shear modulus, and (d) Poisson's ratio with depth. Moduli calculated from measured S-wave velocities are indicated by open symbols whereas calculated S-waves are indicated by solid symbols. Although there are variations in the elastic properties of sediments from different margins, distinct margin specific trends cannot be identified.*

prism and appear to lie on a similar rigidity-depth trend. If the apparent rigidity-depth trends of the prism toe and upper accretionary prism were projected to greater depths, both types of sediment would be more rigid than the forearc basin sediments. Clay content in the forearc basin is similar to that of the prism toe [*Guo and Underwood*, 2012], but the forearc basin sediments have not experienced the tectonic stresses and deformation that sediments from other regions of the prism have experienced. These stresses and deformation are expected to cause greater compaction leading to less compliant prism sediments.

Most of the samples from the Oregon prism and Costa Rica margin have elastic properties similar to those of the Nankai accretionary prism sediments but the Barbados Ridge samples are more compliant. Total clay content in the Barbados Ridge samples ranges from 50 to 80 wt.% whereas at Nankai it ranges from 30 to 70 wt.% [*Underwood and Deng*, 1997; *Guo and Underwood*, 2012]. The greater clay content may explain the more compliant nature of the Barbados Ridge samples.

Overall, variations in the elastic properties among the different subduction zones are small. Without a more complete dataset, we cannot define a substantial difference between the elastic properties of the Japan Trench and the other margins examined here. This contradicts the hypothesis that anomalously rigid elastic properties of the Japan Trench permitted anomalously shallow coseismic slip.

5.3.4 Shear modulus variation with depth at the Japan Trench

Laboratory data are not available to constrain the elastic properties of the subduction zone at depths greater than a few kilometers below the seafloor. Although samples have been subjected to greater stresses in the lab (up to 70 MPa) to simulate greater depths, the geologic modifications of diagenesis are not duplicated in such experiments. The shear modulus at greater

depths in the crust has been estimated by inverting seismic normal mode data and body wave travel times [*Dziewonski and Anderson*, 1981], and shear modulus specifically along subduction zone megathrust faults has been estimated based on rupture duration and source depth [*Bilek and Lay*, 1999b]. Figure 5.8 shows that different datasets used to estimate the shear moduli at a variety of scales (lab, log, and earthquake) are not inconsistent with each other, but if the megathust rigidity-depth relationship of *Geist and Bilek* [2001] or the preliminary reference earth model (PREM) [*Dziewonski and Anderson*, 1981] was projected to the surface, the shear modulus of the prism would be overestimated by up to 20 GPa.

To better characterize the shallow shear modulus variations in the Japan Trench we combined our laboratory results with data from a wide-angle refraction study [*Miura et al.*, 2001, 2005] to create a cross section of shear modulus variation within the Japan Trench. The refraction data were acquired on the MY 102 seismic line, located north of Site C0019 (Fig. 5.1). Density was estimated based on laboratory data and an existing density model developed by *Miura et al.* [2005]. In the Neogene slope cover sequence, Cretaceous marginal wedge, upper crust, lower crust, and incoming sediment layers the *Brocher* [2005] regression fit was used to estimate S-wave velocity from refracted P-wave velocities. The Brocher fit could also have been used to estimate the S-wave velocity in the prism, but we used the linear v_p-v_s relationship discussed in section 3.3 as it provides a better fit to the laboratory data (Fig. 5.6). In ocean layers 2 and 3, S-wave velocity was estimated using the *Brocher* [2005] mafic line equation. The *Brocher* [2005] v_p-v_s relationships result in v_p/v_s ratios similar to those found in other studies for similar materials [e.g., *Christensen*, 1989; *Hole et al.*, 1991; *Holbrook et al.*, 1992; *Zhao et al.*, 1992, 2010; *Planke and Cambray*, 1998; *Barclay et al.*, 2001; *Nakajima et al.*, 2001]. For the mantle we

assumed a v_p/v_s ratio of 1.77 based on previous studies [*Birch*, 1964; *Jordan*, 1976; *Duffy and Anderson*, 1989; *Zhao et al.*, 1992; *Nakajima et al.*, 2001].

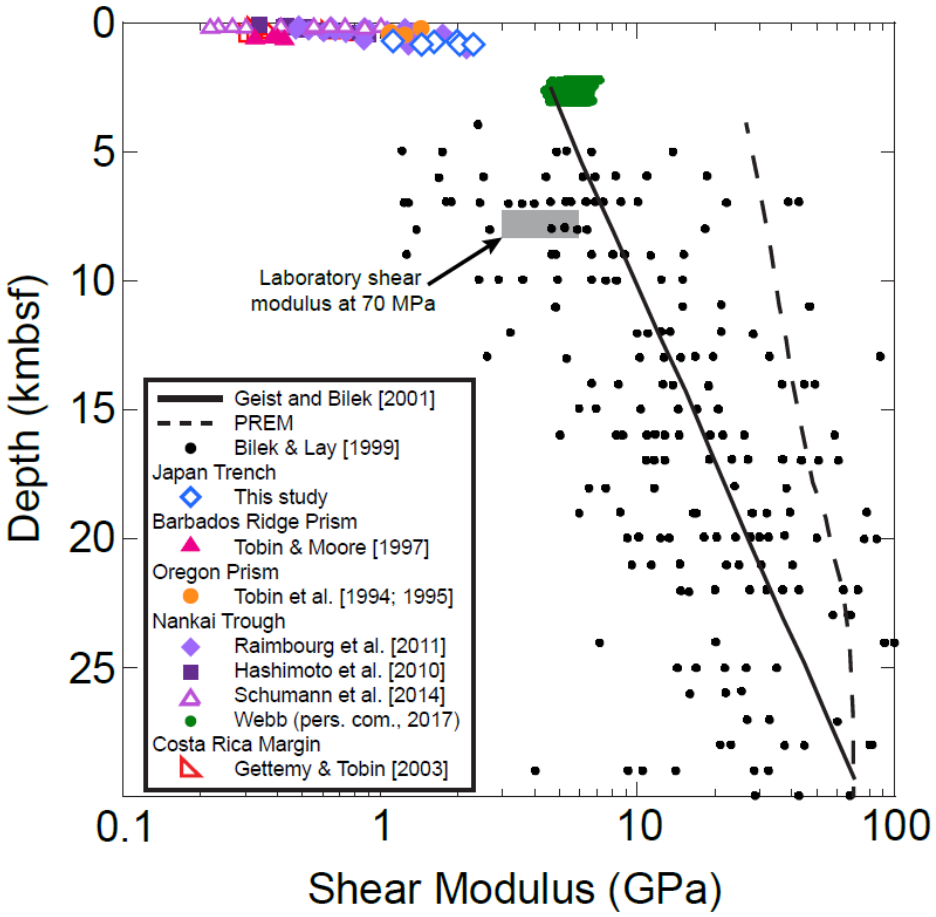

Figure 5.8: *Shear modulus computed from lab (colored points), log (green dots), and earthquake (black circles) data with rigidity-depth relationships from Geist and Bilek [2001] (solid black line) and PREM [Dziewonski and Anderson, 1981] (dashed black line). Estimates of rigidity at different scales are not inconsistent with each other but existing rigidity-depth relationships would greatly overestimate shallow rigidity. The gray box indicates the range in shear modulus calculated from laboratory S-wave velocities measured at 70 MPa effective pressure.*

The resulting shear modulus cross section (Fig. 5.9) shows that the frontal prism, Neogene cover sequence, and incoming sediments all have very low shear moduli on the order of 1 GPa. There are discrete boundaries at the top of the Cretaceous marginal wedge and ocean layer 2 where the shear modulus abruptly increases to 25 GPa. A depth transect through the prism indicates the

PREM relationship provides a good estimate of the shear modulus except in the prism and Neogene cover sequence (Fig. 5.9b), suggesting that a different rigidity-depth relationship is appropriate for poorly consolidated sediments.

We lack measurements of samples from the megathrust fault itself, and the fault is too narrow to be resolved by the wide-angle refraction data, so we cannot provide any constraints on shear modulus within the megathrust. Assuming that the properties of the sub-prism megathrust are similar to the material properties in the hanging and foot walls, then the *Geist and Bilek* [2001] relationship would overestimate the shear modulus of the fault. Shear moduli computed using the sonic log from IODP expedition 348 from depths of 2 to 3 km in the Nankai Trough accretionary prism (S. Webb, personal communication, 2017) are well described by the *Geist and Bilek* [2001] relationship (Fig. 5.8), suggesting that it may be more applicable to subduction zones with a larger accretionary prism.

5.3.5 Implications for tsunami generation and slip to the trench

The frontal prism of the Japan Trench is a volumetrically small component of the subduction zone, and is therefore commonly ignored in numerical simulations of earthquake rupture. Most models assume a constant shear modulus on the order of 30 GPa and a Poisson's ratio of 0.25 throughout the subduction zone [e.g., *Ide et al.*, 1993; *Liu and Rice*, 2005; *Loveless and Meade*, 2011]. This is comparable to the PREM shear modulus and is suitable for most crustal rocks. However, tsunamigenic earthquakes have been linked to the presence of low shear moduli material in the shallow subduction zone, and quantitative models indicate a low shear modulus is required to match model results to observations of tsunami amplitude [*Kanamori*, 1972; *Fukao*, 1979; *Okal*, 1988; *Pelayo and Wiens*, 1992; *Kanamori and Kikuchi*, 1993; *Satake*, 1994, 1995; *Tanioka and Satake*, 1996; *Heinrich et al.*, 1998; *Satake and Tanioka*, 1999]. In most

tsunamigenic earthquake models, the shear modulus is only reduced to 10 to 20 GPa and the prism is not included in the models. Although waves propagating in a low shear modulus materials are attenuated more rapidly than in higher shear modulus materials, Hooke's Law shows that the stress generated by the wave will result in greater strain. Incorporation of a compliant prism in earthquake models may therefore lead to an amplification of simulated fault slip and tsunami wave height. This effect might explain where and how the largest tsunamis are generated.

Numerical models of *Lotto et al.* [2017] examined the effect of variations in prism size, shear modulus, and sub-prism friction on shallow slip magnitude and tsunami wave height. In these models, it is apparent that rupture velocity slows dramatically in the prism to a velocity close to the prism S-wave velocity. The presence of a small (less than 10 km wide) compliant prism results in local enhancement of shallow slip that is amplified if the shear modulus is on the order of 2 GPa or if the basal frictional properties are velocity weakening. The presence of a large prisms (greater than 20 km wide) increases shallow slip if the frictional properties are velocity-weakening, but decreases shallow slip if the frictional properties are velocity-strengthening. This effect is amplified if the prism has very low shear modulus. Small, velocity-strengthening prisms have relatively little effect on tsunami wave height, but if the prism is velocity-weakening or larger in size, the effect on tsunami wave height is greater. Thus, although the effect of a prism is clearly complex, the presence of a compliant prism does influence fault slip and tsunami generation.

For a small prism similar to the frontal prism of the Japan Trench, where S-wave velocity is around 1 km/s and sub-prism friction is neutral to velocity-strengthening [*Ikari*, 2015; *Ikari et al.*, 2015], the results of *Lotto et al.* [2017] predict a 7 to 21 m increase in slip at the trench

relative to a model where there is no prism. The tsunami wave height would change by 0.5 m or less. Dynamic rupture simulations of the 2011 M_w 9.0 Tohoku-Oki earthquake predicted about 30 m of slip at the toe of the trench if velocity-strengthening friction extends 30 km down dip from the trench or 40 m of slip if velocity-strengthening friction only extends to 15 km [*Kozdon and Dunham*, 2013]. These simulations did not account for the effects of a compliant prism, and did not match the displacements observed nearest the trench. Incorporating a compliant frontal prism, consistent with our measurements of *in situ* material properties, could produce the additional displacement needed to match the 50 to 60 m near trench slip [*Fujii et al.*, 2011; *Ide et al.*, 2011; *Ito et al.*, 2011; *Lay et al.*, 2011; *Kodaira et al.*, 2012] that was observed during the Tohoku-Oki earthquake.

5.4 Conclusions

Laboratory ultrasonic wavespeed measurement of seven samples from the JFAST core helps quantify the elastic moduli of the shallow subduction zone. Comparison to data from other subduction zone margins shows that the elastic properties of the Japan Trench frontal prism are similar to those of frontal prisms at other margins. For all samples we examined, the bulk modulus, shear modulus, and Poisson's ratio range from 3 to10 GPa, 0.2 to 3 GPa, and 0.35 to 0.5, respectively, at estimated *in situ* pressures. This indicates that anomalous material properties are not responsible for the unexpected large magnitude slip to the trench experienced during the 2011 Tohoku earthquake. Furthermore by logical extension, it is likely that Tohoku-like slip to the trench behavior is also not anomalous.

Shallow coseismic slip extending all the way to the seafloor has been observed at the Japan Trench [*Fujii et al.*, 2011; *Ide et al.*, 2011; *Ito et al.*, 2011; *Lay et al.*, 2011; *Kodaira et al.*, 2012], Sunda Trench [*Henstock et al.*, 2006; *Gulick et al.*, 2011], and Peru-Chile Trench [*Yue et*

al., 2014]. Evidence of past coseismic slip to the trench has also been found at the Nankai Trough [*Sakaguchi et al.*, 2011] and Cascadia margin [*Satake et al.*, 2003]. As the compliant elastic properties of subduction zone prisms have been linked to increased shallow slip and greater tsunami amplitudes, incorporation of shallow shear modulus variations is necessary for accurate simulations of earthquake wave propagation and displacement through the shallow subduction zone. Laboratory, borehole log, and earthquake estimates of shear modulus from global subduction zones are not inconsistent with one another, but rigidity-depth relationships based solely on earthquake-scale estimates overestimate the shear modulus of the frontal prism. We anticipate that incorporation of the shallow shear modulus variations in the Japan Trench, presented in this study, into simulations of the 2011 Tohoku-Oki earthquake will produce a better fit to observations of shallow, near-trench slip. Incorporating compliant prisms into numerical simulations of other subduction zones is similarly expected to provide better estimates of the seismic hazard posed by different margins through an improved understanding of the magnitude of coseismic slip to the trench and the mechanics of tsunami earthquakes.

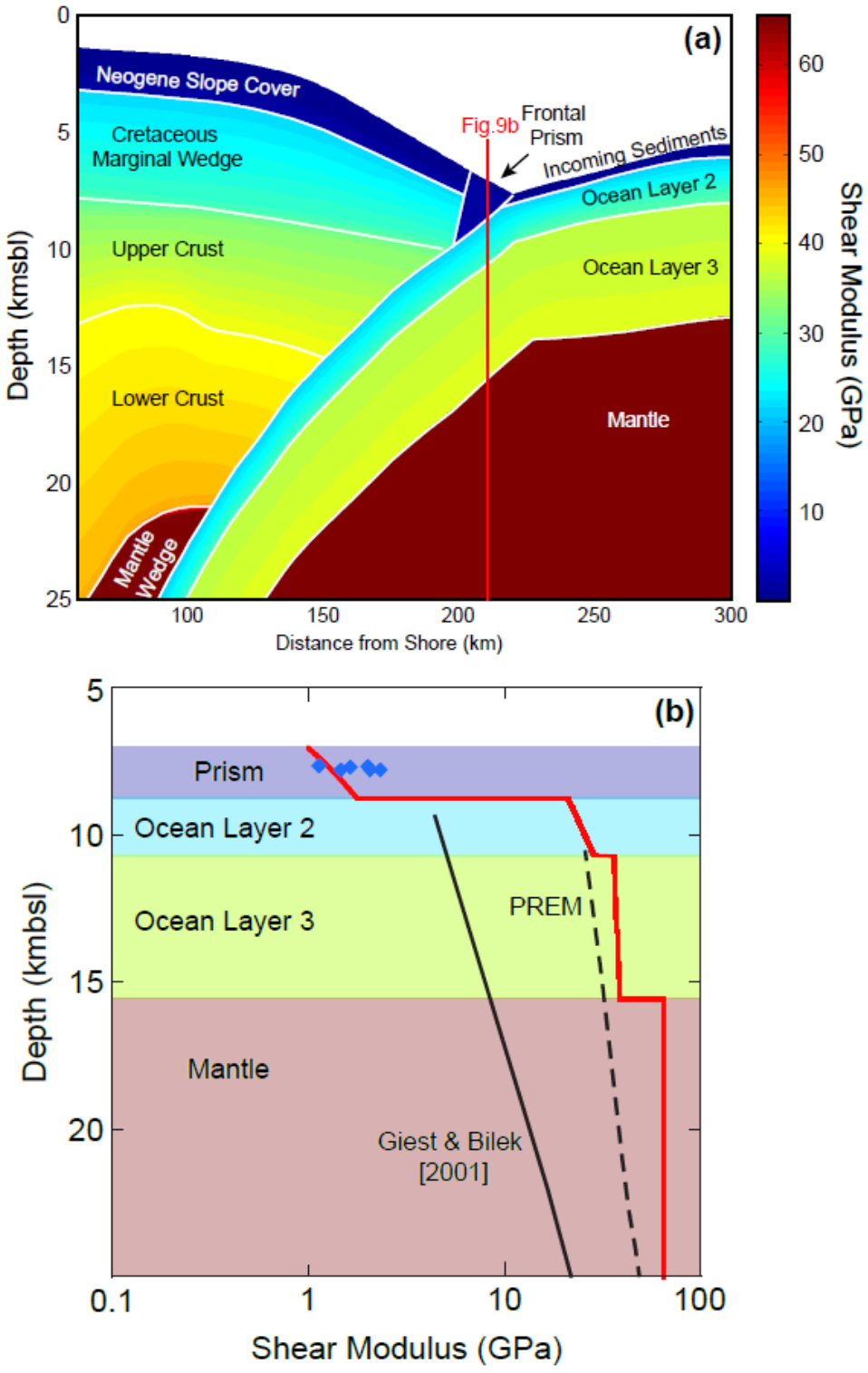

Figure 5.9: *(a) Rigidity structure of the Japan Trench based on laboratory and wide-angle refraction data (line MY 102 in figure 1). (b) A depth transect through the prism, location indicated by red line in figure 9a, shows that the prism is much more compliant than the surrounding material. PREM (dashed line) provides a good estimate of rigidity in crustal layers. Blue diamonds are shear modulus values calculated from the data presented in this study.*

Acknowledgments

Laboratory data used in this study were acquired at UW-Madison and Kochi University. These data and the elastic property models are available from the author upon request. We thank the science party of Expedition 343/343T and the staff of the Drilling Vessel Chikyu for their dedication and assistance with the project. Thanks to Gabriel Lotto, Eric Dunham, and Ludmila Adam for reviewing an early version of this manuscript. This work was funded by a U.S. Scientific Support Program Post-Expedition award to Jeppson.

References

Ammon, C. J., T. Lay, H. Kanamori, and K. M. Cleveland (2011), A rupture model of the 2011 off the Pacific coast of Tohoku Earthquake, Earth, Planets Sp., 63(7), 693–696, doi:10.5047/eps.2011.05.015.

Apel, E. V., R. Bürgmann, G. Steblov, N. Vasilenko, R. King, and a. Prytkov (2006), Independent active microplate tectonics of northeast Asia from GPS velocities and block modeling, Geophys. Res. Lett., 33(11), L11303, doi:10.1029/2006GL026077.

Arthur, M. A., and C. G. Adelseck (1980), Acknowledgements, introduction, and explanatory notes: The Japan Trench Transect, Legs 56 and 57, Deep Sea Drilling Project, in Scientific Party, Init. Repts., DSDP, 56, 57 (Pt. 1), pp. 3–21, U.S. Govt. Printing Office, Washington, D.C.

Barclay, A. H., D. R. Toomey, and S. C. Solomon (2001), Microearthquake characteristics and crustal Vp/Vs structure at the Mid-Alantic Ridge, 35˚N, J. Geophys. Res., 106(B2), 2017–2034.

Bilek, S. L., and T. Lay (1998), Variation of Interplate Fault Zone Properties with Depth in the Japan Subduction Zone, Science, 281(5380), 1175–1178, doi:10.1126/science.281.5380.1175.

Bilek, S. L., and T. Lay (1999a), Comparison of Depth Dependent Fault Zone Properties in the Japan Trench and Middle America Trench, Pure Appl. Geophys., 154, 433–456, doi:10.1007/s000240050238.

Bilek, S. L., and T. Lay (1999b), Rigidity variations with depth along interplate megathrust faults in subduction zones, Nature, 400, 443–446.

Birch, F. (1960), The velocity of compressional waves in rocks to 10 kilobars, part 1, J. Geophys. Res., 65(4), 1083–1102.

Birch, F. (1961), The Velocity of Compressional Waves in Rocks to 10 Kilobars , Part 2, J. Geophys. Res., 66(7), 2199–2224.

Birch, F. (1964), Density and composition of mantle and core, J. Geophys. Res., 69(20), 4377–4388, doi:10.1029/JZ069i020p04377.

Bray, C. J., and D. E. Karig (1985), Porosity of sediments in Accrectionary prisms and some implications of dewatering processes, J. Geophys. Res., 90(B1), 768–778.

Brocher, T. M. (2005), Empirical Relations between Elastic Wavespeeds and Density in the Earth's Crust, Bull. Seismol. Soc. Am., 95(6), 2081–2092, doi:10.1785/0120050077.

Byrne, D. E., D. M. Davis, and L. R. Sykes (1988), Loci and maximum size of thrust earthquakes and the mechanics of the shallow region of subduction zones, Tectonics, 7(4), 833–857, doi:10.1029/TC007i004p00833.

Carson, B., and T. R. Bruns (1980), Physical properties of sediments from the Japan Trench margin and outer trench slope: Results from Deep Sea Drilling Project legs 56 and 57, in Init. Rep. DSDP 56 and 57 (part 2), pp. 1187–1199, DSDP.

Castagna, J. P., M. L. Batzle, and R. L. Eastwood (1985), Relationships between compressional-wave and shear-wave velocities in clastic silicate rocks, Geophysics, 50(4), 571–581.

Chester, F. M. et al. (2013), Structure and composition of the plate-boundary slip zone for the 2011 Tohoku-Oki earthquake, Science, 342(6163), 1208–1211, doi:10.1126/science.1243719.

Christensen, N. I. (1985), Measurement of dynamic properties of rock at elevated pressures and temperatures, ASTM STP, 869, 93–107.

Christensen, N. I. (1989), Seismic velocities, in Practical handbook of physical properties of rocks and minerals, edited by R. S. Carmichael, pp. 431–546, CRC Press, Boca Raton.

Duffy, T. S., and D. L. Anderson (1989), Seismic velocities in mantle minerals and the mineralogy of the upper mantle, J. Geophys. Res., 94(B2), 1895–1912, doi:10.1029/JB094iB02p01895.

Dziewonski, A. M., and D. L. Anderson (1981), Preliminary reference Earth model, Phys. earth Planet. Inter., 25, 297–356, doi:10.1016/0031-9201(81)90046-7.

Expedition 343/343T Scientists (2013), Site C0019, in Prod. IODP, 343/343T, vol. 343, edited by F. M. Chester, J. Mori, N. Eguchi, S. Toczko, and Expedition 343/343T Scientists, Integrated Ocean Drilling Program Management International, Inc, Tokyo.

Fujii, Y., K. Satake, S. Sakai, M. Shinohara, and T. Kanazawa (2011), Tsunami source of the 2011 off the Pacific coast of Tohoku Earthquake, Earth, Planets Sp., 63(7), 815–820, doi:10.5047/eps.2011.06.010.

Fukao, Y. (1979), Tsunami earthquakes and subduction processes near deep-sea trenches, J. Geophys. Res., 84(B5), 2303–2314, doi:10.1029/JB084iB05p02303.

Geist, E. L., and S. L. Bilek (2001), Effect of depth-dependent shear modulus on tsunami generation along subduction zones shallow depths in comparison to standard earth, Geophys. Res. Lett., 28(7), 1315–1318.

Gettemy, G. L., and H. J. Tobin (2003), Tectonic signatures in centimeter-scale velocity-porosity relationships of Costa Rica convergent margin sediments, J. Geophys. Res., 108(B10), 2494, doi:10.1029/2001JB000738.

Gulick, S. P. S., J. A. Austin, L. C. McNeill, N. L. B. Bangs, K. M. Martin, T. J. Henstock, J. M. Bull, S. Dean, Y. S. Djajadihardja, and H. Permana (2011), Updip rupture of the 2004 Sumatra earthquake extended by thick indurated sediments, Nat. Geosci., 4(7), 453–456, doi:10.1038/ngeo1176.

Guo, J., and M. B. Underwood (2012), Data report: clay mineral assemblages from the Nankai Trough accretionary prism and the Kumano Basin, IODP Expeditions 315 and 316, NanTroSEIZE Stage 1, in Proceedings of the Integrated Ocean Drilling Program, vol. 314/315/31, edited by M. Kinoshita, H. J. Tobin, J. Ashi, G. Kimura, S. Lallemant, E. J. Screaton, D. Curewitz, H. Masago, K. T. Moe, and E. Scientists, Intergrated Ocean Drilling Program Management International, Inc., Washington, DC.

Han, D., A. Nur, and D. Morgan (1986), Effects of porosity and clay content on wave velocities in sandstones, Geophysics, 51(11), 2093–2107.

Hashimoto, Y., H. J. Tobin, and M. W. Knuth (2010), Velocity-porosity relationships for slope apron and accreted sediments in the Nankai Trough Seismogenic Zone Experiment, Integrated Ocean Drilling Program Expedition 315 Site C0001, Geochemistry Geophys. Geosystems, 11, doi:10.1029/2010GC003217.

Heinrich, P., F. Schindele, S. Guibourg, and P. F. Ihmle (1998), Modeling of the February 1996 Peruvian tsunami, Geophys. Res. Lett., 25(15), 2687–2690, doi:10.1029/98GL01780.

Henstock, T. J., L. C. McNeill, and D. R. Tappin (2006), Seafloor morphology of the Sumatran subduction zone: Surface rupture during megathrust earthquakes?, Geology, 34(6), 485, doi:10.1130/22426.1.

Holbrook, W. S., W. D. Mooney, and I. C. Nicolas (1992), The seismic velocity structure of the deep continental crust, in Continental Lower Crust, edited by D. M. Fountain, R. Arculus, and R. Kay, pp. 1–34, Elsevier, Amsterdam.

Hole, F., G. J. Iturrino, N. I. Christensen, S. Kirby, and M. H. Salisbury (1991), Seismic velocities and elastic properties of oceanic gabbroic rocks from Hole 735B, in Proceedings of the Ocean Drilling Program, Scientific Results, vol. 118, edited by R. P. Von Herzen and P. T. Robinson, pp. 227–244, Ocean Drilling Program, Colle.

Ide, S., F. Imamura, Y. Yoshida, and K. Abe (1993), Source characteristics of the Nicaraguan Tsunami Earthquake of September 2, 1992, Geophys. Res. Lett., 20(9), 863–866, doi:10.1029/93GL00683.

Ide, S., A. Baltay, and G. C. Beroza (2011), Shallow dynamic overshoot and energetic deep rupture in the 2011 Mw 9.0 Tohoku-Oki earthquake., Science, 332(6036), 1426–1429, doi:10.1126/science.1207020.

Ikari, M. J. (2015), Data report: rate- and state-dependent friction parameters of core samples from Site C0019, IODP Expedition 343 (JFAST) - 343, Proc. Ocean Drill. Progr., 343/343T.

Ikari, M. J., J. Kameda, D. M. Saffer, and A. J. Kopf (2015), Strength characteristics of Japan Trench borehole samples in the high-slip region of the 2011 Tohoku-Oki earthquake, Earth Planet. Sci. Lett., 412, 35–41, doi:10.1016/j.epsl.2014.12.014.

Ito, Y., T. Tsuji, Y. Osada, M. Kido, D. Inazu, Y. Hayashi, H. Tsushima, R. Hino, and H. Fujimoto (2011), Frontal wedge deformation near the source region of the 2011 Tohoku-Oki earthquake, Geophys. Res. Lett., 38(15), L00G05, doi:10.1029/2011GL048355.

Jordan, T. H. (1976), Mineralogies, densities and seismic velocites of garnet lherzolites and their geophyiscal implications, in The Mantle Sample: Inclusion in Kimberlites and Other Volcanics, edited by F. R. Boyd and H. O. A. Meyer, pp. 1–14, American Geophysical Union, Washington D.C.

Kameda, J., M. Shimizu, K. Ujiie, T. Hirose, M. Ikari, J. Mori, and K. Oohashi (2015), Pelagic smectite as an important factor in tsunamigenic slip along the Japan Trench, Geology, 43(2), 155–158, doi:10.1130/G35948.1.

Kanamori, H. (1972), Mechanism of tsunami earthquakes, Phys. earth Planet. Inter., 6, 246–259.

Kanamori, H., and M. Kikuchi (1993), The 1992 Nicaragua earthquake: a slow tsunami earthquake associated with subduction sediments, Nature, 363, 714–716.

Kirkpatrick, J. D. et al. (2015), Structure and lithology of the Japan Trench subduction plate boundary fault, Tectonics, 34(1), 53–69, doi:10.1002/2014TC003695.

Klimentos, T. (1991), The effects of porosity-permeability-clay content on the velocity of compressional waves, Geophysics, 56(12), 1930–1939.

Kodaira, S., T. No, Y. Nakamura, T. Fujiwara, Y. Kaiho, S. Miura, N. Takahashi, Y. Kaneda, and A. Taira (2012), Coseismic fault rupture at the trench axis during the 2011 Tohoku-oki earthquake, Nat. Geosci., 5(9), 646–650, doi:10.1038/ngeo1547.

Koper, K. D., A. R. Hutko, T. Lay, C. J. Ammon, and H. Kanamori (2011), Frequency-dependent rupture process of the 2011 Mw 9.0 Tohoku Earthquake: Comparison of short-period P wave backprojection images and broadband seismic rupture models, Earth, Planets Sp., 63(7), 599–602, doi:10.5047/eps.2011.05.026.

Kowallis, B. J., L. E. A. Jones, and H. F. Wang (1984), Velocity-porosity-clay content systematics of poorly consolidated sandstones, J. Geophys. Res., 89(B12), 355–364.

Kozdon, J. E., and E. M. Dunham (2013), Rupture to the Trench: Dynamic Rupture Simulations of the 11 March 2011 Tohoku Earthquake, Bull. Seismol. Soc. Am., 103(2B), 1275–1289, doi:10.1785/0120120136.

Lay, T., and S. Bilek (2007), Anomalous earthquake ruptures at shallow depths on subduction zone megathrusts, in The Seismogenic Zone of Subduction Thrust Faults, edited by T. H. Dixion and C. Moore, pp. 476–511, Columbia University Press, New York.

Lay, T., C. Ammon, H. Kanamori, L. Xue, and M. Kim (2011), Possible large near-trench slip during the great 2011 Tohoku (Mw 9.0) earthquake, Earth Planets Sp., 63, 687–692, doi:10.5047/eps.2011.05.033.

Liu, Y., and J. R. Rice (2005), Aseismic slip transients emerge spontaneously in three-dimensional rate and state modeling of subduction earthquake sequences, J. Geophys. Res., 110, doi:10.1029/2004JB003424.

Lotto, G. C., E. M. Dunham, T. N. Jeppson, and H. J. Tobin (2017), The effect of compliant prisms on subduction zone earthquakes and tsunamis, Earth Planet. Sci. Lett., 458, 213–222, doi:10.1016/j.epsl.2016.10.050.

Loveless, J. P., and B. J. Meade (2011), Spatial correlation of interseismic coupling and coseismic rupture extent of the 2011 Mw = 9.0 Tohoku-oki earthquake, Geophys. Res. Lett., 38(17), doi:10.1029/2011GL048561.

Miura, S., N. Takahashi, A. Nakanishi, A. Ito, S. Kodaira, T. Tsuru, and Y. Kaneda (2001), Seismic velocity structure off Miyagi fore-arc region, Japan Trench, using ocean bottom seismographic data, Front. Res. Earth Evol., 1, 337–340.

Miura, S., N. Takahashi, A. Nakanishi, T. Tsuru, S. Kodaira, and Y. Kaneda (2005), Structural characteristics off Miyagi forearc region, the Japan Trench seismogenic zone, deduced from a wide-angle reflection and refraction study, Tectonophysics, 407, 165–188, doi:10.1016/j.tecto.2005.08.001.

Moore, J. C., T. A. Plank, F. M. Chester, P. J. Polissar, and H. M. Savage (2015), Sediment provenance and controls on slip propagation: Lessons learned from the 2011 Tohoku and other great earthquakes of the subducting northwest Pacific plate, Geosphere, 2(3), 533–541, doi:10.1130/GES01099.1.

Mori, J., F. M. Chester, N. Eguchi, and S. Toczko (2012), Expedition 343 Scientific Prospectus Japan Trench Fast Earthquake Drilling Project (JFAST), Washington D.C.

Murauchi, S., and W. J. Ludwig (1980), Crustal structure of the Japan Trench: the effect of subduction of the ocean crust, Initial Rep. Deeo Sea Drill. Proj., 56/57, 463–470.

Nafe, J. E., and C. L. Drake (1957), Variation with depth in shallow and deep water marine sediments of porosity, density, and the velocities of compressional and shear waves, Geophysics, XXII(3), 523–552.

Nakajima, J., T. Matsuzawa, A. Hasegawa, and D. Zhao (2001), Three-dimensional structure of Vp, Vs, and Vp/Vs beneath northeastern Japan: Implications for arc magmatism and fluids, J. Geophys. Res., 106(B10), 21843–21857, doi:10.1029/2000JB000008.

Nakamura, Y., S. Kodaira, B. J. Cook, T. Jeppson, T. Kasaya, Y. Yamamoto, Y. Hashimoto, M. Yamaguchi, K. Obana, and G. Fujie (2014), Seismic imaging and velocity structure around the JFAST drill site in the Japan Trench: low Vp, high Vp/Vs in the transparent frontal prism, Earth, Planets Sp., 66(121).

Okal, E. A. (1988), Seismic parameters controlling far-field tsunami amplitudes: A review, Nat. Hazards, 1(1), 67–96, doi:10.1007/BF00168222.

Pelayo, A. M., and D. A. Wiens (1992), Tsunami earthquakes: slow thrust faulting events in the accretionary wedge, J. Geophys. Res., 97, 15321–15337.

Planke, S., and H. Cambray (1998), Seismic properties of flood basalts From Hole 917A downhole data, southeast Greenland volcanic margin, in Proceedings of the Ocean Drilling Program, Scientific results, vol. 152, edited by A. D. Saunders, H. C. Larsen, and S. W. J. Wise, pp. 453–462, Ocean Drilling Program, College Station, TX.

Raimbourg, H., Y. Hamano, S. Saito, M. Kinoshita, and A. Kopf (2011), Acoustic and mechanical properties of Nankai accretionary prism core samples, Geochemistry, Geophys. Geosystems, 12(4), doi:10.1029/2010GC003169.

Sakaguchi, A. et al. (2011), Seismic slip propagation to the updip end of plate boundary subduction interface faults: Vitrinite reflectance geothermometry on integrated ocean drilling program nantro SEIZE cores, Geology, 39(4), 395–398, doi:10.1130/G31642.1.

Satake, K. (1994), Mechanism of the 1992 Nicaragua Tsunami Earthquake, Geophys. Res. Lett., 21(23), 2519–2522, doi:10.1029/94GL02338.

Satake, K. (1995), Linear and nonlinear computations of the 1992 Nicaragua earthquake tsunami, Pure Appl. Geophys., 144(3–4), 455–470, doi:10.1007/BF00874378.

Satake, K., and Y. Tanioka (1999), Sources of tsunami and tsunamigenic earthquakes in subduction zones, Pure Appl. Geophys., 154(3–4), 467–483, doi:10.1007/s000240050240.

Satake, K., K. Wang, and B. F. Atwater (2003), Fault slip and seismic moment of the 1700 Cascadia earthquake inferred from Japanese tsunami descriptions, J. Geophys. Res., 108(B11), 2535, doi:10.1029/2003JB002521.

Satake, K., Y. Fujii, T. Harada, and Y. Namegaya (2013), Time and Space Distribution of Coseismic Slip of the 2011 Tohoku Earthquake as Inferred from Tsunami Waveform Data, Bull. Seismol. Soc. Am., 103(2B), 1473–1492, doi:10.1785/0120120122.

Scholz, C. H. (2002), The Mechanics of Earthquakes and Faulting, 2nd ed., Cambridge University Press, New York.

Schumann, K., M. Stipp, J. H. Behrmann, D. Klaeschen, and D. Schulte-Kortnack (2014), P and S wave velocity measurements of water-rich sediments from the Nankai Trough, Japan, J. Geophys. Res. Solid Earth, 119(2), 787–805, doi:10.1002/2013JB010290.

Tanioka, Y., and K. Satake (1996), Fault parameters of the 1896 Sanriku tsunami earthquake estimated from tsunami numerical modeling, Geophys. Res. Lett., 23(13), 1549–1552.

Tobin, H. J., and J. C. Moore (1997), Variations in ultrasonic velocity and density with pore pressure in the decollement zone, Northern Barbados Ridge accretionary prism, edited by T. H. Shipley, Y. Ogawa, P. Blum, and J. M. Bahr, Proc. Ocean Drill. Program, Sci. Results, 156, 125–135.

Tobin, H. J., J. C. Moore, and G. F. Moore (1994), Fluid pressure in the frontal thrust of the Oregon accretionary prism: Experimental constraints, Geology, 22, 979–982, doi:10.1130/0091-7613(1994)022<0979.

Tobin, H. J., J. C. Moore, and G. F. Moore (1995), Laboratory measurement of velocity vs. effective stress in thrust faults in the Oregon accretionary prism: implications for fault zone overpressure, Proc. Ocean Drill. Program, Sci. Results, 146(1).

Tosaya, C., and A. Nur (1982), Effects of Diagenesis and clays on compressional velocities in rocks, Geophys. Res. Lett., 9(1), 5–8.

Underwood, M. B., and X. Deng (1997), Clay mineralogy and clay geochemistry in the vicinity of the decollement zone, Northern Barbados Ridge, in Proceeding of the Ocean Drilling Program, Scientific Results, vol. 157, edited by T. H. Shipley, Y. Ogawa, P. Blum, and J. M. Bahr, Ocean Drilling Program, College Station, TX.

Yue, H., T. Lay, L. Rivera, C. An, C. Vigny, X. Tong, and J. C. Báez Soto (2014), Localized fault slip to the trench in the 2010 Maule, Chile M_w = 8.8 earthquake from joint inversion of high-rate GPS, teleseismic body waves, InSAR, campaign GPS, and tsunami observations, J. Geophys. Res. Solid Earth, 119(10), 7786–7804, doi:10.1002/2014JB011340.

von Huene, R., and R. Culotta (1989), Tectonic erosion at the front of the Japan Trench convergent margin, Tectonophysics, 160(1–4), 75–90, doi:10.1016/0040-1951(89)90385-5.

von Huene, R., and S. Lallemand (1990), Tectonic erosion along the Japan and Peru convergent margins, Geol. Soc. Am. Bull., 102(6), 704–720, doi:10.1130/0016-7606(1990)102<0704.

von Huene, R., and M. Langseth (1982), A summary of Cenozoic tectonic history along the IPOD Japan Trench transect, Geol. Soc. Am. Bull., 93(9), 829–846, doi:10.1130/0016-7606(1982)93<829.

von Huene, R., D. Klaeschen, and B. Cropp (1994), Tectonic structure across the accretionary and erosional parts of the Japan Trench margin, J. Geophys. Res., 99(B11), 22349–22361, doi:10.1029/94JB01198.

Zhao, D., A. Hasegawa, and S. Horiuchi (1992), Tomographic Imaging of P and S Wave Velocity Structure Beneath Northeastern Japan, J. Geophys. Res., 97(B13), 19909–19928, doi:10.1029/92JB00603.

Zhao, M., X. Qiu, S. Xia, H. Xu, P. Wang, T. K. Wang, C. S. Lee, and K. Xia (2010), Seismic structure in the northeastern South China Sea: S-wave velocity and Vp/Vs ratios derived from three-component OBS data, Tectonophysics, 480(1–4), 183–197, doi:10.1016/j.tecto.2009.10.004.

5.5 Appendix

5A.1 Supplementary material

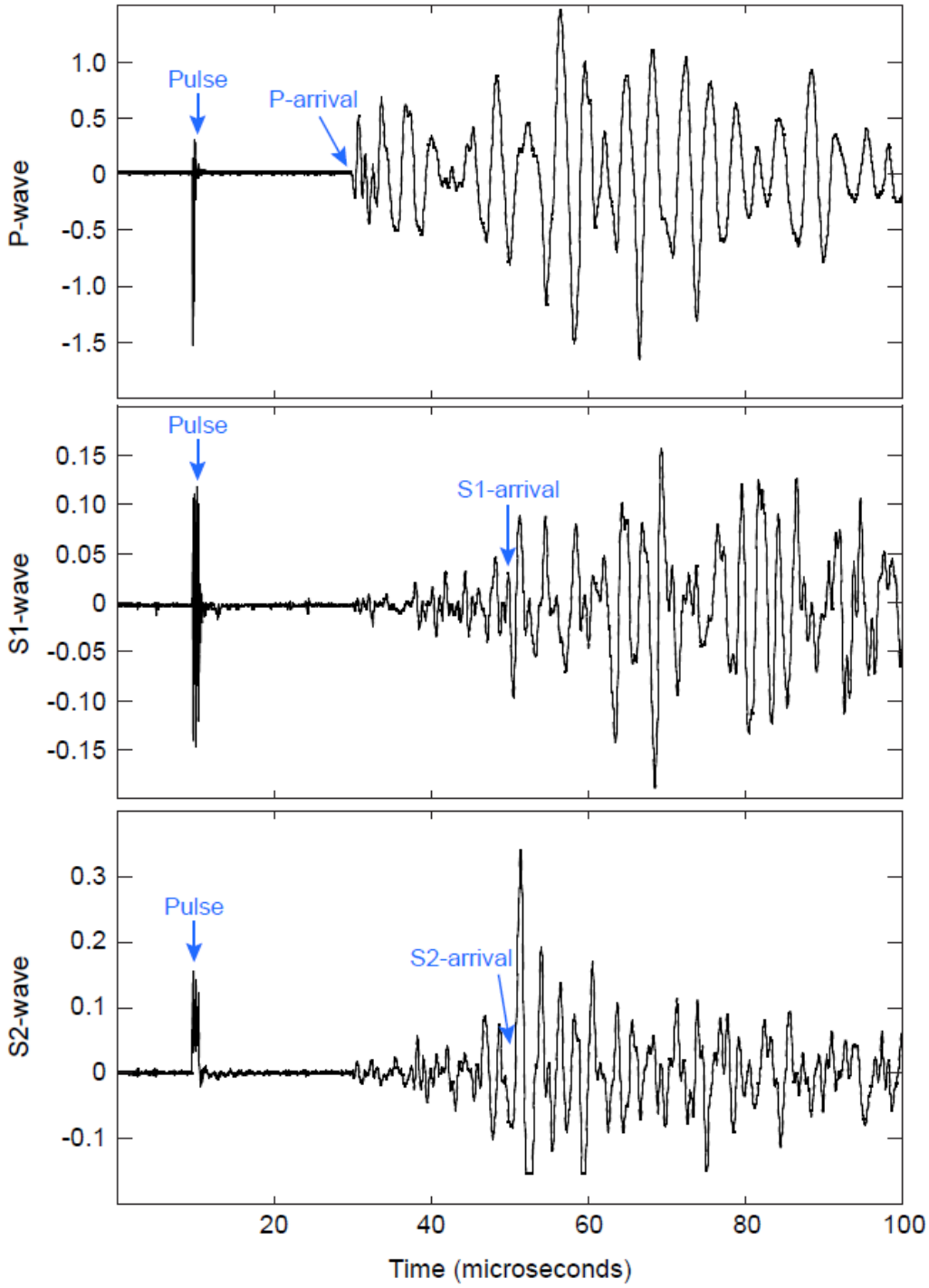

Figure 5A.1.1: *Example of raw waveforms acquired at the University of Wisconsin - Madison on sample 15R1 at 68 MPa.*

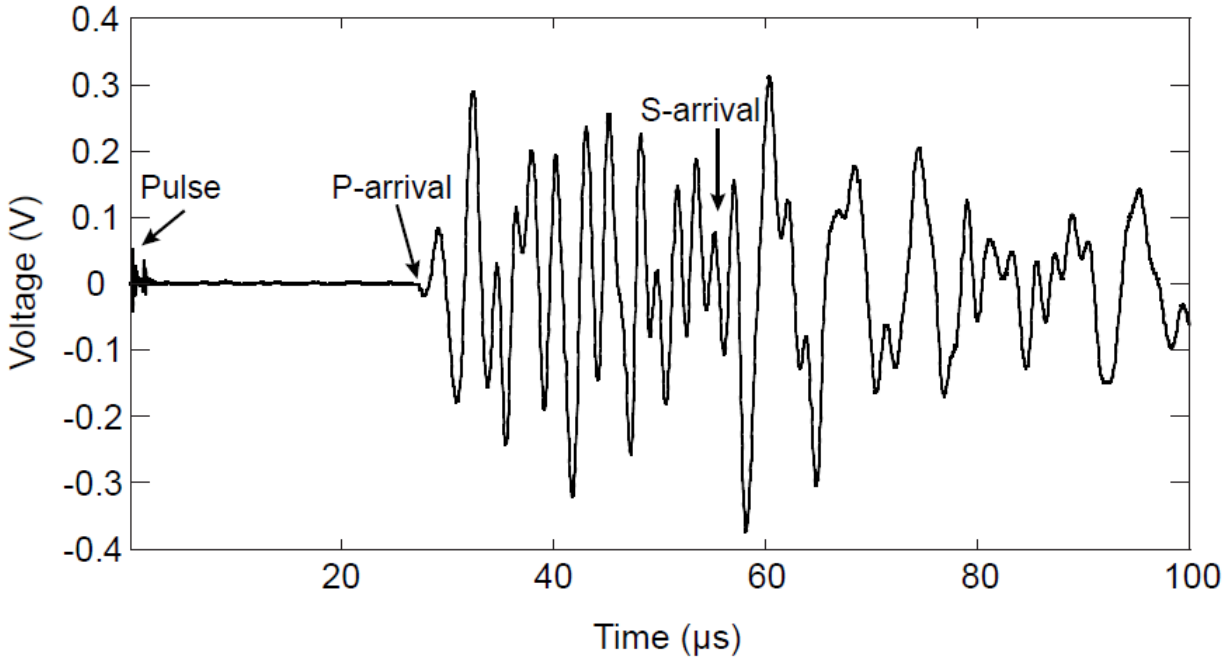

Figure 5A.1.2: *Example of raw waveforms acquired at Kochi University for sample 7R1 at 18 MPa.*

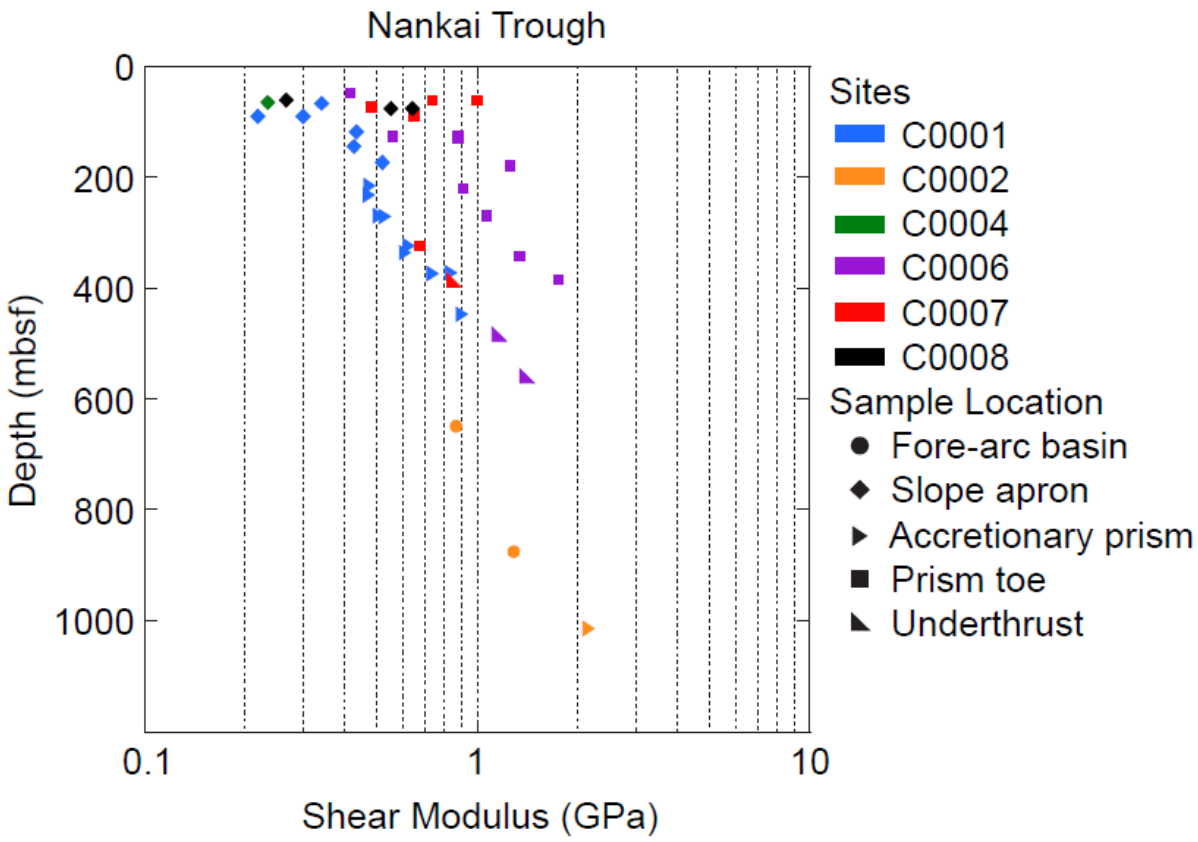

Figure 5A.1.3: *Variations in shear modulus with depth in sediments from the Nankai Trough indicate that samples with different histories follow slightly different rigidity-depth trends. Data from Hashimoto et al. [2010], Raimbourg et al. [2011], and Schumann et al. [2014].*

6 Appendix

6A.1 TEMCO triaxial pressure vessel maintenance and operation

1. Safety

- Wear safety glasses when the system is pressurized
- Do not open valves if pressure is above 70 to 100 kPa
- If you need to stop the pumps immediately for any reason (in any mode) press the red stop button on the control panel twice and then button d on the pump controller.

2. Maintenance

2.1 ISCO pumps

The user manual for the Teledyne ISCO pumps can be found at http://www.teledyneisco.com/en-us/pumpproducts/Pumps%20Documents/Manuals/D-Series%20Syringe%20Pumps%20User%20Manual.pdf

This manual contains full details on the operation and care of the pumps. Maintenance checks should be performed at least once a year. Standard checks include:

1. Seal cleaning and replacement
2. Checking the motor brushes (rarely need to be replace but should be checked regularly)
3. Lubricating the ball screw and lube wheel (may need to be done more often depending on use)

Details on how to perform these tasks are provided in section 9 of the user manual. When reassembling the pumps never-seez should be applied on all screw connections.

If salt water is used in the pumps make sure to empty pump and flush with fresh water after each experiment. Do not leave salt water in pump when it is not actively being used. Additionally if pumps are not in regular use all pumps should be emptied.

2.1.1 Leaks

Regularly check the system for leaks at all connections. If the leak is slow you may not be able to visually observe it. As a result, pump flow rate and volume need to be closely monitored during each experiment as changes in these will notify you of leaks in the system.

As of June 2017, there is a slow leak in pump B. This leak is only observed at pressures greater than ~20 to 40 MPa. The exact location/cause of the leak is currently unknown and may indicate the wear ring needs to be replaced. The leak is slow (~0.1 ml/hour) and does not prevent the pump from maintaining pressure during experiments.

2.2 Vessel

Every year the piston endcap should be removed from the body of the vessel so the endcaps and vessel can be cleaned. O-ring and backup rings should be cleaned and replaced every 1 to 2 years. Replacement rings can be ordered from Global O-Ring and Seal, LLC. We use the Dupont Viton O-rings and spiral

Teflon backup rings. Before reattaching the endcaps smear a small amount of silicone O-ring lubricant to the O-rings and make sure the endcaps are completely clean. Also spread a small amount of anti-scoring extreme pressure lube to the screw threads on the vessel before attaching the endcaps. Old lube will periodically need to be cleaned off and new lube applied on the end with the fixed plug, as dust will accumulate in the threads making it harder to screw and unscrew the vessel. To clean the threads, use dish soap, water, and a soft brush.

The vessel body should also be thoroughly cleaned and dried. Currently, the interior cylinder of the vessel contains many small pits due to an accumulation of water that was trapped behind the piston plug for many years and caused corrosion. These pits have been polished and do not affect the seal. Additionally there are several deeper scratches due to grains of hard material becoming trapped between the piston plug and vessel body. These have also been polished down and do not appear to affect the seal. If a similar problem occurs again; polish the interior of the vessel with fine emery paper following the curve of the vessel with motions parallel to the opening to grind down any edges associated with the pits or scratches. Do not polish with perpendicular motions, as the O-rings will have difficulty sealing scratches in this direction.

3. Operation

3.1 Sample preparation

The vessel can accommodate samples with 2.54 or 3.81 cm diameters and lengths from ~1.9 to 5.0 cm. The ends of the sample should be made parallel and polished using the surface grinder in the Sample Preparation Lab in Engineering Hall. Use sandpaper on softer samples. Note: Paralleling and polishing is especially critical for hard rock samples. For soft mudstones, clays, and friable sandstones, polishing will likely only remove material and is not necessarily helpful. Contact Hiroki Sone to use the surface grinder or drill press in Engineering Hall or Basil Tikoff to use the drill press in the basement of Weeks Hall. Once a sample is prepared, be sure to measure its length, diameter, and mass. The porosity can also be measured using the porosimeter in the rock mechanics lab (Weeks B138).

2.54 cm diameter samples will need to be jacketed with clear pvc tubing that has a ~1.5” outer diameter (OD) and ~1” inner diameter (ID). This jacket should be cut slightly shorter than the length of the sample, with ends approximately parallel. I found the best way to do cut tubing was to make initial cuts with pipe cutters then use to belt sander in the Weeks machine shop to the parallel ends of the jacket. The tubing can be ordered from United States Plastic Corp. I used the 1" ID x 1-1/2" OD x 1/4" Wall Tygon® S3™ B-44-3 Beverage Tubing.

3.2 Vessel Preparation

1. Prepare the left side of the vessel, where the axial fluid chamber is located. Start by ensuring that the axial ram is at the proper extension for your sample. The axial ram moves to accommodate different sample lengths, and if you do not know its level of extension, your sample might be crushed by the action of closing the vessel. If you do not know the length of the most recently measured sample be sure to extend the axial ram fully. To do so, drain the axial chamber of all fluid, and use the brass extender to push it back. To prevent wear and scratches on the

transducer, it is best to do this as rarely as possible, so *start with your longest samples and work smaller*.

2. Attach the aluminum ring with the displacement transducer to the axial ram, so that the transducer is just barely in contact with the back of the vessel (allowing the full 10 mm of travel on the metal bar).
3. To perform any experiment in the ultrasonic vessel, the sample needs to be enclosed in the black rubber tube outer jacketing of an appropriate length. The jacket should be about 3 cm longer then the sample. The length does not need to be exact, and it is better to err on the longer side. However, if the jacket is too long it will bulge and cause problems with your experiment. Once you have selected the jacket that is appropriate for your sample, slide the outer jacket into the vessel so that it fits over transducers on the axial ram. Then slide the sample into the outer jacket, pushing it snugly against the axial ram transducer stack.
    a. The outer jacket material can be ordered from Dudadiesel.com. You want the fluoroelastomer Hose grade A with an inner diameter of 1.5 inches and outer diameter of 1.75 inches.
4. You can now attach the other endcap. To get the best signal, the transducers need to be aligned. To accomplish this, the pore pressure ports on the endcaps need to be aligned. I have also marked a red line on the exterior of both endcaps. If these lines are vertical and pore pressure ports are aligned, then transducers are aligned, and the S1-transducer (red) has a vertical vibration direction and S2 (green) vibration is horizontal.
5. Reattach the transducer cords (red, blue, and green cords bound together). Turn on the switching box (black box near pulse generator), pulse generator, and oscilloscope.
6. Turn on syringe pumps, then turn on pump control box. For experiments under dry conditions, turn on only pumps A (confining) and B (axial). For wet conditions, turn on pumps A, B, & C (pore fluid). It is a good idea to give the pumps a little time to equilibrate so you might want to turn them on when you start setting up the vessel.

    The pumps will need to be zeroed. If they are not already filled you will need to fill them first (open file Temco controller.lvproj then the Panel file and see below for more information). Once pumps are filled, close the valves to the reservoir and open valves to the vessel. If you opened the Labview software, make sure to shut it down, then on the pump controller; press stop > zero pressure > select the pump you want to zero. *If Labview is open when you press stop it is likely to cause problems later on.*

4. Starting the acquisition system

1. Open the file Temco controller.lvproj (on desktop), and open the file Ramp.vi within that folder. Then open file temco acquisition.vi on desktop. *The files must be opened in this order or they will not work.*
2. In the temco acquisition (TA) window on the sample tab, input your sample information. Click the white arrow at the top left and wait for the Panel window to update. Return to the TA window and check the scope, ISCO, and Scope tabs to make sure the displacement, pump information, and oscilloscope data are all being recorded. If you don't see data being recorded on

any of these tabs, you will need to restart labview and possibly the entire computer. Once everything is up and running, you are ready to start the experiment.

5. Running an experiment

5.1 Bring endcaps into contact with sample

1. On the Panel window, change pump B to constant flow and set the flow rate to 25 ml/min. Make sure the line from pump to reservoir is closed, and the line from pump to vessel and axial outflow valves are open. Start the pump (click button that says "stopped – press to run"). When fluid begins to flow from the outflow port, stop the pump and close the outflow valve. Stop the pump. If the volume of fluid remaining in the pump is less than 25 ml, I suggest refilling the pump from the reservoir at this time.
   Switch to constant pressure and set pressure to 500 to 600 kPa. restart the pump and closely watch pressure. You should see the pressure gradually start to increase then level off as the piston starts to move. The pressure will oscillate around this pressure and pump flow rate will increase. If flow rate is allowed to increase unchecked the pressure will suddenly spike as the transducer plug on the piston comes into contact with the sample. You do not want to see this spike as the sudden increase in pressure could crush your sample. So when the pump rate is high, periodically stop and start the pump so you don't overshoot the pressure by too much. 500 kPa is usually the pressure required to overcome the vessel seal and get the vessel to close up around the sample. Sometime 500 kPa is not quite enough, and you may need to increase the pressure to 600 kPa. During this process, also watch the displacement transducer readings. If the displacement gets close to 10 mm, stop the pump and move the transducer back on the piston. *Exceeding 10 mm will break the transducer and you will need to connect a new one.*

   Q: How to do I know if the vessel has closed up?

   A: Ideally, you should have some idea of how much the vessel needs to close up if you know the length of the previously run sample. If you know this value, watch the displacement plot. If you have reached 500 kPa and know there is more space that needs to be closed up, increase the pressure.

   a. If you've reach 500 kPa you aren't sure if more space needs to be closed up here are some ways to tell:Leave the axial pump on a constant pressure for a while and watch the displacement plot. If you are not in contact the displacement will continue to increase over time if the axial load is 500 kPa but if you are in contact, it will start to oscillate around a constant value.

   b. Turn off the axial pump and watch the pressure reading. If it drops off quickly you are not in contact with the sample. Increase the pressure setting and try again.

Once the vessel is closed up, leave it running on constant pressure and move on to step 2.

2. Switch pump A to constant flow. Make sure the line from the pump to the reservoir is closed and the line from the pump to vessel and confining outflow lines are open. Start pump A. When fluid

begins to flow from the outflow port, stop the pump and close the outflow valve. Refill the pump from the reservoir if needed. Switch to constant pressure and set pressure to 500 kPa. Start the pump and closely watch pressure. Stop the pump periodically as pressure increases especially as the pressure approaches 500 kPa so you don't overshoot. Do not allow the confining pressure to exceed the axial pressure as this could cause the sample jacket to gap, allowing the confining fluid to leak into the sample. While increasing the pressure, observe the pore fluid port on the right hand side of the vessel. If fluid begins to flow from that port, stop the pump - there is a leak due to problems with the liner. You will need to open the vessel back up and reload the sample.

3. Allow the system to equilibrate. Adjust the displacement transducer on the axial ram, so that the transducer is just barely in contact with the back of the vessel (allowing the full 10 mm of travel on the metal bar). Then tighten the screw to secure. Once pressure has equilibrated and displacement has leveled off, zero the displacement measurement by pressing the "autozero" button on the sample tab.

6. Saturating the sample

If running under dry conditions skip this step.

1. Connect the pore pressure lines on both sides of the vessel. Make sure the pump C to reservoir and downstream valves are closed. Open the upstream and drain/outflow valves. Switch pump C to constant flow and decrease the flow rate. I recommend starting between 1 and 5 ml/min and maybe lower for low permeability samples. Start the pump and monitor pressure while waiting for fluid to come out of the outflow port. If pressure gets close to 100 kPa, stop the pump, switch to a constant pressure, and start the pump again. Let sit until water comes out of the outflow valve. When you start getting a regular drip from the pore drain valve, stop the pump, close the pore drain valve, and open the downstream line valve. Set pump to constant pressure of 100 kPa.
2. At this point you may wish to increase the pump pressures to match your desired first pressure step. Section 7 describes how to do this. Regardless of whether you increase the pressure or remain at the current low pressure, make sure you allow time for the sample to saturate and the system to equilibrate. This usually requires 12+ hours. When the sample is saturated and the system has equilibrated you are ready take a measurement.
   Q: How will I know if it has equilibrated?
   A: Monitor changes in volume of fluid in the pumps and sample displacement to determine when the system has equilibrated, they should be oscillating around zero. You can also record waveforms at regular intervals to see if the velocity is changing over time, indicating sample has not equilibrated.

   If your sample has very low permeability, you will never see any outflow. In this case, run water through the pore pressure lines before connecting them to the vessel to remove air. Close the drain valve and open both upstream and downstream lines. Set the pump to 100 kPa and start. *Never let pore pressure exceed your confining and axial pressures*.

7. Acquiring data and changing pressure

7.1 Changing Pressure

You will first need to determine your target pressures. Note: there is a mechanical advantage in the system that causes the axial load felt by the sample to be slightly greater than what the pump is set to. To calculate the pressure the pump needs to be set at to achieve the desired pressure on the sample, use the Labview program "Temco sigma to pump." You can input your desired pressures (sigmas) and sample dimensions, then hit the white arrow and the program will calculate the required pump pressures.

Once you have determined the pressure steps **make sure the pumps are set to constant pressure**, and open the ramp window. This module increases the pressure incrementally so you don't overshoot the target pressures. Input your target pressure for pumps A and B, then input the time to complete the step and the number of steps or increments. 30 steps over 60 seconds are usually good values but if you are doing a large pressure step you will need to increase both the number of steps and the time. A notification window will pop up if the increment you chose requires a step greater than 500 kPa. Hit run and then the white arrow and wait for your target pressure to be reached.

If running with pore pressure, once target pressures for pumps A and B have been reached you can go to the panel window to change the pump C pressure. Just stop the C pump and change your target pressure, then start the pump again, starting and stopping occasionally so as not to exceed the target pressure.

Monitor the pump information for any evidence of leaks. If there is a significant leak, you will see a flow rate that does not oscillate around zero. Small, slow leaks can only be observed by looking at the data over a longer period of time.

Once your sample has equilibrated you can record waveforms.

7.2 Recording waveforms

Open scope tab and click capture. Wait for waveform to be recorded and continue. It is a good idea to record the waveforms several times at each pressure step.

7.2.1 Troubleshooting

The scope often has time out and other errors that prevent waveforms from being recorded. If this happens, the plot on the scope tab will be blank and the retry will be highlighted. If this happens, there are several things to try:

1. Disconnect and then reconnect the USB A/B cable at the back of the oscilloscope. The waveforms should reappear on the scope screen within ~30 seconds
2. The oscilloscope may reset to its default setting (if this happens you may see one waveform on the plot instead of three). Press the "save/recall" button on the oscilloscope, then use the top button to the right of the screen to cycle through the actions until you see "recall setup." I have saved the current settings as setup 1, 2, & 3. Press the button corresponding to "recall."
3. If the previous steps have not worked, restart the oscilloscope, signal generator, and switch box.

8. Completion

Once you have finished your pressure steps, reduce the pore pressure to 70 kPa, turn off pump C and open the pore drain. Leave the sample for a period of time, so the internal pore pressure can bleed off and you don't end up hydro-fracturing your sample when you remove the confining pressure. I usually left my sample for 12 hours. If your sample is very strong or very permeable, you will not need as much time.

Reduce confining and axial pressure to 70 kPa. Turn off pumps and open outflow valves. Set pumps to refill and start. Once pumps are full, close to vessel and open to reservoir. Set pumps to constant flow and run. When empty, close to reservoir, open to vessel and refill again. You may need to repeat this 2 to 3 times before opening the vessel up and removing your sample.

Once the vessel is empty, run water through pore pressure lines to make sure no sediment grains are stuck in the plumbing. If you are using a salt water solution, empty the pore pressure pump then fill it with fresh water and flush out the lines. *Do not leave salt water in the pump!*

Shut down the program by clicking quit on the Panel window then Stop on the acquisition window. Now you can close the windows. There is no need to save changes.

Dry the interior of the vessel with a soft towel. Then squirt some acetone and methanol into the vessel to aid in the evaporation of any remaining water.

9. Miscellaneous information and important reminders

1. If you are working with poorly consolidated, compliant sedimentary rock, you must use a filter between your sample and the transducers. This prevents your sample from extruding into the pore pressure ports. I recommend using sintered metal filters or very fine wire mesh, both of which are currently available in the lab. The metal filters are reusable, but if you need more, take the sintered metal sheets to the physics machine shop to have more filters cut. Make sure they do not polish the flat surfaces, as this will close off the pores. The wire meshes tend to get stuck to the sample, so are difficult to reuse.
2. *Do not let confining pressure exceed axial pressure* as this will cause gaps and leaks between the sample liner and endcap. Also do not let pore pressure exceed confining and axial pressure unless you are trying to fracture your sample.
3. *Make sure pumps are set to constant pressure before running ramp*! If not, you could cause the pumps to flow out of control.
4. Actively check the data for evidence of leaks while running each experiment. *If the flow rate is not oscillating around zero, you have a leak*! It may be internal, but be sure to check all the connections. If it is internal, depending on location and severity, you may be able to finish the experiment, but keep an eye on it, because increasing the pressure could cause the leak to worsen and if the pumps cannot keep up they will shut down.
5. The Knuth color system for wire labels is blue = P-wave, green = S1, and pink = S2
6. Isopar-H is used as a confining and axial fluid.
7. All valves are right-tight left-loose and visibly "in" when closed and "out" when open.
8. If windows or Labview crashes the ISCO pumps will continue with their last orders indefinitely. The data you were collecting should be saved as a backup .lvm file.

10. Picking wave arrivals

All data acquired are saved on the C-drive > data > Temco. Three files should be saved. Notes.txt contains the sample information you input at the start; for an unknown reason this file does not always save. Temco.txt contains all the pump and displacement information that is continuously recorded throughout the experiment. Scope.bin contains all the record waveforms. To view this file, open the "TemcoPicker" Labview file. Ignore the load summary warning, then click the white arrow and navigate to the file you want to open. Use the event index to move through the recorded waveforms. The displacement, pressures, and pump information are documented on the left side of the picker window. The waveform index determines if you are looking at the P, S1 or S2 wave. Waveform index 0 corresponds to coax channel 0 and scope channel 1; this is the P-wave. Waveform index 4 is the S1 (Coax 1, scope 2) and waveform index 8 is S2 (coax 2, scope 3). The other waveforms are combinations of P and S transducers as source and receiver. Pick the arrival by moving the yellow cursor line to the location of the arrival. The corresponding arrival time is displayed in the X box in seconds. You can zoom by selecting the magnifying glass icon.

If you want to export the waveform data to plot in a different program, right click on the displayed waveform and select one of the export options. You will need to do this for each waveform individually.

6A.2 UW Thesis collection reference numbers

Table 6A.2.0.1: *Alpine Fault outcrop samples in UW collection.*

UW number	Manuscript number	Field number	Orientation w.r.t foliation & lineation	Sample Type	Description	Location	Figured in
UW2037/1.1	TT1	1119_001A	Perpendicular, N/A	Mini-core	Schist	Tartare tunnels, West Coast, South Island, New Zealand	Fig. 4.4 & 4.7
UW2037/1.2	TT1	1119_001B	Parallel, Perpendicular	Mini-core	Schist	Tartare tunnels, West Coast, South Island, New Zealand	Fig. 4.4 & 4.7
UW2037/1.3	TT1	1119_001C	Parallel, Parallel	Mini-core	Schist	Tartare tunnels, West Coast, South Island, New Zealand	Fig. 4.4 & 4.7
UW2037/1.4	TT1	1119_001XY	XY plane	Billet	Schist	Tartare tunnels, West Coast, South Island, New Zealand	Fig. 4.4 & 4.7
UW2037/1.5	TT1	1119_001XY	XY plane	Thin section	Schist	Tartare tunnels, West Coast, South Island, New Zealand	Fig. 4.4 & 4.7
UW2037/1.6	TT1	1119_001XZ	XZ plane	Billet	Schist	Tartare tunnels, West Coast, South Island, New Zealand	Fig. 4.4 & 4.7
UW2037/1.7	TT1	1119_001XZ	XZ plane	Thin section	Schist	Tartare tunnels, West Coast, South Island, New Zealand	Fig. 4.4 & 4.7

UW2037/1.8	TT1	1119_001YZ	YZ plane	Billet	Schist	Tartare tunnels, West Coast, South Island, New Zealand	Fig. 4.4 & 4.7
UW2037/1.9	TT1	1119_001YZ	YZ plane	Thin section	Schist	Tartare tunnels, West Coast, South Island, New Zealand	Fig. 4.4 & 4.7
UW2037/2.1	HM1	1113_014A	Perpendicular, N/A	Mini-core	protomylonite	Hare Mare Creek, West Coast, South Island, New Zealand	Fig. 4.4 & 4.7
UW2037/2.2	HM1	1113_014B	Parallel, Perpendicular	Mini-core	protomylonite	Hare Mare Creek, West Coast, South Island, New Zealand	Fig. 4.4 & 4.7
UW2037/2.3	HM1	1113_014XY	XY plane	Billet	protomylonite	Hare Mare Creek, West Coast, South Island, New Zealand	Fig. 4.4 & 4.7
UW2037/2.4	HM1	1113_014XY	XY plane	Thin section	protomylonite	Hare Mare Creek, West Coast, South Island, New Zealand	Fig. 4.4 & 4.7
UW2037/2.5	HM1	1113_014XZ	XZ plane	Billet	protomylonite	Hare Mare Creek, West Coast, South Island, New Zealand	Fig. 4.4 & 4.7
UW2037/2.6	HM1	1113_014XZ	XZ plane	Thin section	protomylonite	Hare Mare Creek, West Coast, South Island, New Zealand	Fig. 4.4 & 4.7
UW2037/2.7	HM1	1113_014YZ	YZ plane	Billet	protomylonite	Hare Mare Creek, West Coast, South Island, New Zealand	Fig. 4.4 & 4.7
UW2037/2.8	HM1	1113_014YZ	YZ plane	Thin section	protomylonite	Hare Mare Creek, West Coast, South Island, New Zealand	Fig. 4.4 & 4.7
UW2037/3.1	HM2	1113_016A	Perpendicular, N/A	Mini-core	tranistional mylonite	Hare Mare Creek, West Coast, South Island, New Zealand	Fig. 4.4 & 4.7
UW2037/3.2	HM2	1113_016C	Parallel, Parallel	Mini-core	tranistional mylonite	Hare Mare Creek, West Coast, South Island, New Zealand	Fig. 4.4 & 4.7
UW2037/4.1	SC1	1111_005A	Parallel, Parallel	Mini-core	mylonite, blocky metasandstone	Stoney Creek, West Coast, South Island, New Zealand	Fig. 4.4 & 4.7
UW2037/4.2	SC1	1111_005B	Parallel, Perpendicular	Mini-core	mylonite, blocky metasandstone	Stoney Creek, West Coast, South Island, New Zealand	Fig. 4.4 & 4.7
UW2037/4.3	SC1	1111_005C	Perpendicular, N/A	Mini-core	mylonite, blocky metasandstone	Stoney Creek, West Coast, South Island, New Zealand	Fig. 4.4 & 4.7
UW2037/4.4	SC1	1111_005XY	XY plane	Billet	mylonite, blocky	Stoney Creek,	Fig. 4.4

					metasandstone	West Coast, South Island, New Zealand	& 4.7
UW2037/4.5	SC1	1111_005XY	XY plane	Thin section	mylonite, blocky metasandstone	Stoney Creek, West Coast, South Island, New Zealand	Fig. 4.4 & 4.7
UW2037/4.6	SC1	1111_005XZ	XZ plane	Billet	mylonite, blocky metasandstone	Stoney Creek, West Coast, South Island, New Zealand	Fig. 4.4 & 4.7
UW2037/4.7	SC1	1111_005XZ	XZ plane	Thin section	mylonite, blocky metasandstone	Stoney Creek, West Coast, South Island, New Zealand	Fig. 4.4 & 4.7
UW2037/4.8	SC1	1111_005YZ	YZ plane	Billet	mylonite, blocky metasandstone	Stoney Creek, West Coast, South Island, New Zealand	Fig. 4.4 & 4.7
UW2037/4.9	SC1	1111_005YZ	YZ plane	Thin section	mylonite, blocky metasandstone	Stoney Creek, West Coast, South Island, New Zealand	Fig. 4.4 & 4.7
UW2037/5.1	SC2	1111-004A	Parallel, Parallel	Mini-core	ultramylonite	Stoney Creek, West Coast, South Island, New Zealand	Fig. 4.4 & 4.7
UW2037/5.2	SC2	1111-004B	Perpendicular, N/A	Mini-core	ultramylonite	Stoney Creek, West Coast, South Island, New Zealand	Fig. 4.4 & 4.7
UW2037/5.3	SC2	1111-004YX	YZ plane	Billet	ultramylonite	Stoney Creek, West Coast, South Island, New Zealand	Fig. 4.4 & 4.7
UW2037/5.4	SC2	1111-004YX	YZ plane	Thin section	ultramylonite	Stoney Creek, West Coast, South Island, New Zealand	Fig. 4.4 & 4.7
UW2037/10.1	GC3	1012_003	---	Billet	foliated green cataclasite	Gaunt Creek, West Coast, South Island, New Zealand	Fig. 4.5 & 4.8
UW2037/10.2	GC3	1012_003	Z plane	Thin section	foliated green cataclasite	Gaunt Creek, West Coast, South Island, New Zealand	Fig. 4.5 & 4.8
UW2037/11.1	GC2	1124_002	Z plane	Billet	Protocataclasite	Gaunt Creek, West Coast, South Island, New Zealand	Fig. 4.5 & 4.8
UW2037/11.2	GC2	1124_002	Z plane	Thin section	Protocataclasite	Gaunt Creek, West Coast, South Island, New Zealand	Fig. 4.5 & 4.8
UW2037/11.3	GC2	1124_002	Z plane	Thin section	Protocataclasite	Gaunt Creek, West Coast, South Island, New Zealand	Fig. 4.5 & 4.8
UW2037/12.1	GC4	1124_003	Z plane	Billet	Gouge	Gaunt Creek, West Coast, South	Fig. 4.5 & 4.8

						Island, New Zealand	
UW2037/12.2	GC4	1124_003	Z plane	Thin section	Gouge	Gaunt Creek, West Coast, South Island, New Zealand	Fig. 4.5 & 4.8
UW2037/12.3	GC4	1124_003	Z plane	Thin section	Gouge	Gaunt Creek, West Coast, South Island, New Zealand	Fig. 4.5 & 4.8
UW2037/13.1	GC1	1124_004	XZ plane	Billet	black brecciated ultramylonite	Gaunt Creek, West Coast, South Island, New Zealand	Fig. 4.5 & 4.8
UW2037/13.2	GC1	1124_004	XZ plane	Thin section	black brecciated ultramylonite	Gaunt Creek, West Coast, South Island, New Zealand	Fig. 4.5 & 4.8
UW2037/14.1	WR1	1024_005	Z plane	Billet	Gouge	Waikukupa River, West Coast, South Island, New Zealand	Fig. 4.5 & 4.8
UW2037/14.2	WR1	1024_005	Z plane	Thin section	Gouge	Waikukupa River, West Coast, South Island, New Zealand	Fig. 4.5 & 4.8
UW2037/14.3	WR1	1024_005	Z plane	Thin section	Gouge	Waikukupa River, West Coast, South Island, New Zealand	Fig. 4.5 & 4.8
UW2037/14.4	WR1	1024_005	Z plane	Thin section	Gouge	Waikukupa River, West Coast, South Island, New Zealand	Fig. 4.5 & 4.8
UW2037/15.1	SC3	1111_001	Z plane	Billet	Gouge	Stoney Creek, West Coast, South Island, New Zealand	Fig. 4.5 & 4.8
UW2037/15.2	SC3	1111_001	Z plane	Thin section	Gouge	Stoney Creek, West Coast, South Island, New Zealand	Fig. 4.5 & 4.8
UW2037/6	SMC1	1113_007A	Perpendicular, N/A	Mini-core	Ultracataclasite	Smithy Creek, West Coast, South Island, New Zealand	Fig. 4.6
UW2037/16.1	GC5	1124_001B	Z plane	Billet	Gouge	Gaunt Creek, West Coast, South Island, New Zealand	Fig. 4.5 & 4.8
UW2037/16.2	GC5	1124_001B	Z plane	Thin section	Gouge	Gaunt Creek, West Coast, South Island, New Zealand	Fig. 4.5 & 4.8
UW2037/16.3	GC5	1124_001B	Z plane	Thin section	Gouge	Gaunt Creek, West Coast, South Island, New Zealand	Fig. 4.5 & 4.8
UW2037/16.4	GC5	1124_001B	Z plane	Thin section	Gouge	Gaunt Creek, West Coast, South Island, New	Fig. 4.5 & 4.8

						Zealand	
UW2037/7.1	HC1	1018-001A	Parallel, Parallel	Mini-core	FW mylonite	Harold Creek, West Coast, South Island, New Zealand	Fig. 4.6 & 4.9
UW2037/7.2	HC1	1018-001B	Parallel, Perpendicular	Mini-core	FW mylonite	Harold Creek, West Coast, South Island, New Zealand	Fig. 4.6 & 4.9
UW2037/7.3	HC1	1018-001C	Perpendicular, N/A	Mini-core	FW mylonite	Harold Creek, West Coast, South Island, New Zealand	Fig. 4.6 & 4.9
UW2037/7.4	HC1	1018-001XZ	XZ plane	Billet	FW mylonite	Harold Creek, West Coast, South Island, New Zealand	Fig. 4.6 & 4.9
UW2037/7.5	HC1	1018-001XZ	XZ plane	Thin section	FW mylonite	Harold Creek, West Coast, South Island, New Zealand	Fig. 4.6 & 4.9
UW2037/7.6	HC1	1018-001YZ	YZ plane	Billet	FW mylonite	Harold Creek, West Coast, South Island, New Zealand	Fig. 4.6 & 4.9
UW2037/7.7	HC1	1018-001YZ	YZ plane	Thin section	FW mylonite	Harold Creek, West Coast, South Island, New Zealand	Fig. 4.6 & 4.9
UW2037/8.1	SMC2	1113_008A	Horizontal	Mini-core	Monzonite	Smithy Creek, West Coast, South Island, New Zealand	Fig. 4.6 & 4.9
UW2037/8.2	SMC2	1113_008B	Horizontal	Mini-core	Monzonite	Smithy Creek, West Coast, South Island, New Zealand	Fig. 4.6 & 4.9
UW2037/8.3	SMC2	1113_008C	Vertical	Mini-core	Monzonite	Smithy Creek, West Coast, South Island, New Zealand	Fig. 4.6 & 4.9
UW2037/8.4	SMC2	1113_008J	---	Billet	Monzonite	Smithy Creek, West Coast, South Island, New Zealand	Fig. 4.6 & 4.9
UW2037/8.5	SMC2	1113_008J	---	Thin section	Monzonite	Smithy Creek, West Coast, South Island, New Zealand	Fig. 4.6 & 4.9
UW2037/8.6	SMC2	1113_008I	---	Billet	Monzonite	Smithy Creek, West Coast, South Island, New Zealand	Fig. 4.6 & 4.9
UW2037/8.7	SMC2	1113_008I	---	Thin section	Monzonite	Smithy Creek, West Coast, South Island, New Zealand	Fig. 4.6 & 4.9
UW2037/9.1	WQ1	1115_002B	Parallel, Perpendicular	Mini-core	Granitic L-tectonite	Whataroa Upper Quarry, , West Coast, South Island, New	Fig. 4.6 & 4.9

						Zealand	
UW2037/9.2	WQ1	1115_002C	Parallel, Parallel	Mini-core	Granitic L-tectonite	Whataroa Upper Quarry, , West Coast, South Island, New Zealand	Fig. 4.6 & 4.9
UW2037/9.3	WQ1	1115_002XZ	XZ plane	Billet	Granitic L-tectonite	Whataroa Upper Quarry, , West Coast, South Island, New Zealand	Fig. 4.6 & 4.9
UW2037/9.4	WQ1	1115_002XZ	XZ plane	Thin section	Granitic L-tectonite	Whataroa Upper Quarry, , West Coast, South Island, New Zealand	Fig. 4.6 & 4.9
UW2037/9.5	WQ1	1115_002YZ	YZ plane	Billet	Granitic L-tectonite	Whataroa Upper Quarry, , West Coast, South Island, New Zealand	Fig. 4.6 & 4.9
UW2037/9.6	WQ1	1115_002YZ	YZ plane	Thin section	Granitic L-tectonite	Whataroa Upper Quarry, , West Coast, South Island, New Zealand	Fig. 4.6 & 4.9
UW2037/9.7	WQ2	1115_002YZ	YZ plane	Thin section	Granitic L-tectonite	Whataroa Upper Quarry, , West Coast, South Island, New Zealand	Fig. 4.6 & 4.9

Table 6A.2.2: *DFDP-1 Samples in UW collection.*

Archive Number	Manuscript Number	Orientation w.r.t. core axis	Hole	Run	Section	Measured Depth (m)	Sample Type	Description	Location	Figured in
ICDP5052ESQAGU2_7-16/1	198A	Parallel	B	60	1	129.5	Mini-core	Cataclasite	DFDP-1 borehole, Gaunt Creek, West Coast, South Island, New Zealand	n/a
ICDP5052ESQAGU2_7-16/2	198B	Perpendicular	B	60	1	129.5	Mini-core	Cataclasite	DFDP-1 borehole, Gaunt Creek, West Coast, South Island, New Zealand	n/a
ICDP5052ESSAGU2_0-6/1	382A	Parallel	B	60	2	130.01	Mini-core	Cataclasite	DFDP-1 borehole, Gaunt Creek, West Coast, South Island, New Zealand	n/a
ICDP5052ESSAGU2_0-6/2	382B	Perpendicular	B	60	2	130.01	Mini-core	Cataclasite	DFDP-1 borehole, Gaunt	n/a

									Creek, West Coast, South Island, New Zealand	
ICDP5052ESCBGU2_2.5-13/1	130A	Parallel	B	64	1	135.125	Mini-core	Cataclasite	DFDP-1 borehole, Gaunt Creek, West Coast, South Island, New Zealand	n/a
ICDP5052ESCBGU2_2.5-13/2	130B	Perpendicular	B	64	1	135.125	Mini-core	Cataclasite	DFDP-1 borehole, Gaunt Creek, West Coast, South Island, New Zealand	n/a
ICDP5052ESSBGU2_5-8/1	316	Not oriented	B	67	1	139.59	Mini-core	Cataclasite	DFDP-1 borehole, Gaunt Creek, West Coast, South Island, New Zealand	n/a
ICDP5052ES2CGU2_5-9/1	960A	Perpendicular	B	69	2	143.39	Mini-core	Foliated cataclasite	DFDP-1 borehole, Gaunt Creek, West Coast, South Island, New Zealand	n/a
ICDP5052ES2CGU2_5-9/2	960B	Parallel	B	69	2	143.39	Mini-core	Foliated cataclasite	DFDP-1 borehole, Gaunt Creek, West Coast, South Island, New Zealand	n/a
ICDP5052ES2CGU2_11-15/1	410A	Parallel	B	69	2	143.45	Mini-core	Foliated cataclasite	DFDP-1 borehole, Gaunt Creek, West Coast, South Island, New Zealand	n/a
ICDP5052ES2CGU2_11-15/2	410B	Perpendicular	B	69	2	143.45	Mini-core	Foliated cataclasite	DFDP-1 borehole, Gaunt Creek, West Coast, South Island, New Zealand	n/a
ICDP5052ES2CGU2_66-71/1	428	Perpendicular	B	69	2	144	Mini-core	Cataclasite	DFDP-1 borehole, Gaunt Creek, West Coast, South Island, New Zealand	n/a

ICDP5052ES2CGU2_66-71/2	384A	Parallel	B	69	2	144.1	Mini-core	Proto-cataclasite	DFDP-1 borehole, Gaunt Creek, West Coast, South Island, New Zealand	n/a
ICDP5052ES2CGU2_76-78/1	384B	Perpendicular	B	69	2	144.1	Mini-core	Proto-cataclasite	DFDP-1 borehole, Gaunt Creek, West Coast, South Island, New Zealand	n/a